University Of Surrey

Molecular Dynamics Simulations of Water Transport Properties and Magnetic Resonance Relaxation in Cement Nanopores

Author:
Serge-Henri Cachia

Supervisors:
Prof. Peter McDonald
Dr. David Faux

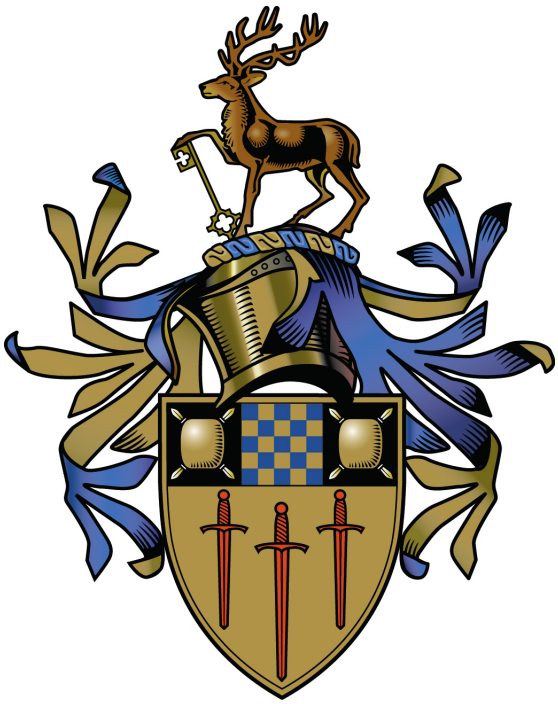

Submitted for the degree of Doctor of Philosophy

April 20, 2016

Acknowledgement

I would like to thank my two supervisors Peter McDonald and David Faux who helped me so much in the completion of this thesis. Their expertise, motivation, guidance and patience made this work possible. I would like also to thank Andre Nonat and Sergei Churakov who helped me to build the MD models. In the same way, the expertise of my colleagues Jayesh Bhatt and Nick Howlett was important for the development of the algorithms I used. I would like also to thank my PhD friends from TRANSCEND project for all these days when we spoke about science and life and for all the amazing moments we shared.

I am also very grateful to all my relatives and friends, with a special thought for C.N., who supported me during these years when I doubted about myself. Their kindness, care and support helped me so much.

Finally, I would like to acknowledge the sponsorship from European Commission for Marie-Curie Initial Training Network Transcend "The Understanding TRANSport for Concrete which is Eco friendly, iNnovative and Durable" (EP7/2007-2013).

Declaration of Authorship

This thesis and the work to which it refers are the results of my own efforts. Any ideas, data, images or text resulting from the work of others (whether published or unpublished) are fully identified as such within the work and attributed to their originator in the text, bibliography or in footnotes. This thesis has not been submitted in whole or in part for any other academic degree or professional qualification.

I agree that the University has the right to submit my work to the plagiarism detection service TurnitinUK for originality checks. Whether or not drafts have been so-assessed, the University reserves the right to require an electronic version of the final document (as submitted) for assessment as above.

Abstract

Water transport properties in cement are important for the cement industry. At the nanoscale, a nondestructive experimental method, ^{1}H nuclear magnetic resonance [NMR] relaxometry, can be used to quantify these properties. However, recent results have proven difficult to reconcile with current understanding of cement. The purpose of this work is to use Molecular Dynamics [MD] simulations to try and better understand water in cement and hence better interpret some of the NMR data. In particular, MD simulations are used to investigate water dynamics in two sizes of nanopores in analogues of calcium-silicate-hydrate [C-S-H], which is the active phase of cement paste. These pores are gel pores (3-5 nm) and interlayer spaces (1 nm).

First, a bulk water system is studied and the water diffusion coefficient and NMR relaxation times are calculated. The results are compared to literature values and used to validate the methods. Then, different C-S-H analogues based on SiO_2 α-quartz crystal, tobermorite 11Å and modified tobermorite 14Å are presented. Two different sets of interatomic potentials are used for these model simulations: CLAY_FF+SPC/E and Freeman+TIP4P. These simulations are then compared. A model called MD4 which is based on modified tobermorite 14Å and using CLAY_FF+SPC/E potentials is selected for further work.

The density profile of water oxygen in MD4 is used to identify four water layers with different properties in the gel pore (L1, L2, TL and B) and one water layer in the interlayer pore (IL). Diffusivity and desorption analyses are performed on water populations related to these layers. The importance of the calcium ions close to the surface is highlighted. The NMR dipolar correlation function is generated for water using data from the MD4. This function underpins relaxation analysis.

These outputs are compared to Korb's single water layer model of surface NMR relaxation. Korb's model is not supported by the new data. However, a new relaxation model of surface relaxation that takes into account water in two layers is supported by the data. Exchange is possible between these layers and is important for diffusivity as well as relaxation.

Simulations are carried out as a function of temperature and used to calculate water transport activation energies in bulk and in MD4.

Finally, the analysis of water exchange between the interlayer and gel pores is performed. It is shown that the exchange time in simulations is ≈69000 times smaller than measured experimentally. Some possible failings in the model that would account for this are discussed.

Contents

Acknowledgement i

Declaration of Authorship ii

Abstract iii

Contents vi

List of Figures xviii

List of Tables xx

1 Introduction 1
1.1 Cement study and TRANSCEND project . . . 1
1.1.1 The Impact of Concrete and Cement . . . 1
1.1.2 TRANSCEND Project . . . 3
1.2 NMR and Numerical Simulation . . . 3
1.2.1 NMR and Cement . . . 3
1.2.2 NMR Modelling . . . 5
1.3 Cement Pastes Nanostructure: C-S-H . . . 5
1.3.1 Powers'Model . . . 5
1.3.2 Feldman and Sereda's Model . . . 6
1.3.3 Jennings' Model . . . 7
1.4 Aims . . . 8

2 Theory 9
2.1 Basics of ^{1}H NMR Relaxometry . . . 9
2.1.1 Preamble to NMR . . . 9
2.1.2 Resonance, Longitudinal and Transverse Relaxations . . . 11
2.2 The BPP theory . . . 12
2.2.1 Correlation Function and Spin Sets . . . 13
2.2.2 Spin Selection, Homo/Heteronuclear and Intra/Intermolecular Interaction, Relaxation Times Calculation . . . 15
2.2.3 Behaviour of T_1 and T_2 in Bulk . . . 16
2.3 Basics of Diffusion . . . 17
2.4 Exchange Theory and Desorption . . . 19
2.4.1 Simple Theory of Population Exchange . . . 20

2.4.2 Population Exchange and Gaussian Propagator . . . 21
2.4.3 Fast exchange and NMR Relaxation Times . . . 22
2.5 Korb's Model of Surface Relaxation . . . 23
2.6 An Improved Model . . . 24
2.7 The Arrhenius Law . . . 24

3 Methodology **26**
3.1 Preamble: Conceptual Cement Structure at the Nanoscale . . . 26
3.2 Simulation Techniques for Water Dynamics Analysis . . . 27
3.2.1 Density Functional Theory . . . 27
3.2.2 Thermodynamics . . . 27
3.2.3 Molecular Dynamics (MD) Simulations . . . 28
3.2.4 Dynamic Monte Carlo Simulations . . . 29
3.2.5 Fluid Dynamics Simulations . . . 30
3.3 Molecular Dynamics using DL_POLY . . . 30
3.3.1 A Sample of DL_POLY Functions . . . 31
3.3.2 Interatomic Potential . . . 33
3.3.3 Periodic Boundary Conditions . . . 37
3.4 Water Transport Properties and NMR Relaxation Analysis . . . 38
3.4.1 Water Density . . . 38
3.4.2 Selection of Water Populations . . . 38
3.4.3 Diffusion and Desorption Analysis . . . 40
3.4.4 Calculation of the Correlation Function . . . 40
3.4.5 Numerical Calculation of the Spectral Density Function and Relaxation Times . . . 43

4 Validation Of Methods In 3D Bulk Water **45**
4.1 Bulk Water System . . . 45
4.1.1 A Bulk Water Simulation Box . . . 45
4.1.2 Water Representation and Atomistic Potentials . . . 46
4.2 Data Analysis . . . 47
4.2.1 Diffusion Coefficient . . . 47
4.2.2 Propagator Analysis . . . 48
4.2.3 NMR Relaxation . . . 50

5 Choice Of The C-S-H Analogue Model **54**
5.1 C-S-H Structure . . . 54
5.2 Structural Models . . . 56
5.2.1 Previous C-S-H Analogues . . . 58
5.2.2 MD4 to MD9 Models: Modified Tobermorite 14 Å . . . 59
5.3 Atomistic Potentials . . . 63
5.3.1 CLAY_FF and SPC/E . . . 63
5.3.2 Modified Freeman and TIP4P Potentials . . . 64
5.4 Simulation Details . . . 66
5.5 Model Selection . . . 66
5.5.1 Density Profiles and Surface Desorption . . . 66

5.5.2 Summary and Choice of the Model for Further Study 73

6 MD4 Analysis **74**
6.1 Density Profile Analysis and Layers Definition: L1, L2, TL, bulk and IL . . . 74
6.1.1 Calcium Effect on Water Molecules 76
6.2 Diffusion Analysis 80
6.2.1 $D_{\{B>B>B\}}$ Validation 80
6.2.2 $D_{\{L1>SL>L1\}}$ 81
6.2.3 $D_{\{L2>\Omega-B>L2\}}$ 82
6.2.4 $D_{\{TL>TL>TL\}}$ 82
6.2.5 $D_{\{IL>IL>IL\}}$ 83
6.2.6 Diffusion Summary 84
6.3 Desorption Analysis 85
6.3.1 Desorption of {L1>SL>SL} 85
6.3.2 Desorption of {L2>L2+δ>L2+δ} and {SL>SL+δ>SL+δ} 85
6.3.3 Desorption of Gel Calcium First Hydration Shell 87
6.3.4 Desorption Summary 88
6.4 ^{1}H NMR Relaxometry Analysis: Correlation Function 89
6.5 To a New Model for the Interpretation of NMR Relaxometry in Hydrated Porous Silicate Materials 90
6.6 Summary Conclusion 93

7 Temperature Influence and Activation Energy **94**
7.1 Influence of Temperature on Bulk Water System 94
7.1.1 Presentation of the Simulations 94
7.1.2 Diffusion and Activation Energy 95
7.1.3 NMR Relaxation Times and Activation Energy 97
7.2 Influence of Temperature on MD4 Model 98
7.2.1 Model Preparation 98
7.2.2 Diffusion and Activation Energy 99
7.2.3 Desorption and Activation Energy 100
7.2.4 Correlation Functions 102
7.2.5 Experimental NMR Relaxation Times of White Cement Paste 103

8 Water Exchange between the Interlayer and the Gel Pores **104**
8.1 Gel-Interlayer Exchange Model 104
8.2 Desorption, Exchange Time and Tortuosity 105
8.2.1 Interlayer Desorption 105
8.2.2 Interlayer Diffusion versus Long Desorption Times 108
8.2.3 Possible Water Behaviour in the Interlayer 109

9 Discussion And Further Work **112**

Appendices **115**

Bibliography **127**

List of Figures

1.1 Concrete is a cheap material with good physical features, which explains an enormous demand worldwide (adapted from [4]) 1
1.2 Embodied energy and CO_2 emission produced per kg of concrete is negligible compared to other materials (adapted from [5]) 2
1.3 Characteristic degradation of a concrete bridge pylon in the Pimpama River, southeast Queensland [7] 2
1.4 TRANSCEND project can be seen as a matrix of projects where simulation and experiments are used to understand water transport properties in cement and concrete from the nano to the meso and macroscale. This thesis project is red circled. (adapted from [6]) 3
1.5 An histogram of the T_2 ^{1}H NMR relaxation time highlights white cement pore size distribution. Calcium-Silicate-Hydrates Interlayer size is $\approx$ 1 nm, C-S-H Gel size is $\approx$ 3 nm and Interhydrate size is $\approx$ 9 nm [8]. The abscissa is the spin-spin relaxation time T_2 and will be discussed in chapter 2. 4
1.6 This picture represents Powers' C-S-H model (adapted from [19]). The large grey zones represent capillary water. In the dark grey zone that is zoomed (circle), black lines represent Gel particles and non-evaporating water, and the white lines represent the physically bound Gel water. 6
1.7 This picture represents Feldman and Sereda C-S-H model (adapted from [20]). Black lines represent crystal sheets, red crosses represent the interlayer water and the full blue disks represent the absorbed water. 6
1.8 These pictures represent Jennings CM-I model with different densities of C-S-H: on the left the low density one and on the right the high density one. A C-S-H globule is circled in red. 7
1.9 CM-II C-S-H Jennings model (adapted from [24]). The globule floc size is $\approx$ 50 nm, the Larger Gel Pore (LGP) size is $\approx$ 3 to 12 nm, the Small Gel Pore (SGP) size is $\approx$ 1 to 3 nm and the InterGlobular Pore (IGP) size is $\leq$ 1 nm. 7

2.1 Magnetic moment μ aligns with ($\uparrow$) or against($\downarrow$) the magnetic field $\overrightarrow{B_0}$. The two populations have different energy level, split by the presence of the magnetic field. 10
2.2 The orientation of magnetic dipole moments $\overrightarrow{\mu}$ that are precessing about an external magnetic field is shown here. The sum of all the dipoles gives the magnetization vector $\overrightarrow{M}$. 11

2.3 A perpendicular and rotating magnetic field $\overrightarrow{B_1}$ is turned on at time $t = 0$. As a consequence, the magnetisation vector is rotating until $\overrightarrow{B_1}$ is turned off (here after a rotation of angle $\frac{\pi}{2}$). This representation is made in the rotating frame. 11
2.4 After a $\frac{\pi}{2}$-pulse, two relaxation processes occur. Top: classical picture of the spin-lattice relaxation; magnetisation vector (red) is returning to its original position in a typical time T_1 (ie: aligned to B_0. Bottom: classical picture of the spin-spin relaxation; the magnetic moments (green) coherence is less and less effective because of the effect of some local magnetic fields after a typical time T_2. The spin-spin relaxation is quicker than the spin-lattice relaxation as shown by the blue arrow ($T_2 \leq T_1$). 13
2.5 The spatial parameters used to generate $G^{(m)}_{I,J}(t)$ function, where t is time, are shown here: $\overrightarrow{r_{ij}}$ the vector between spins i and j, polar angles θ_{ij} and ϕ_{ij} at time $t = 0$ and $t > 0$ in the reference frame where $\overrightarrow{B_0} = B_0 \overrightarrow{k}$ 14
2.6 A water proton can interact with the second proton in the same water molecule (dash blue line), with a proton in another water molecule (double solid blue line, with a surface Fe (solid green line) or with a surface hydroxyl O-H (solid red line). 15
2.7 The behaviour of NMR relaxation times T_1 and T_2 is a function of the correlation time for a bulk system. This figure is extracted from [40]. 17
2.8 2D Brownian motion for three particles that move of a vector distance $\overrightarrow{\delta r}$ in a time δt. This displacement is randomly oriented: the ballistic behaviour of such a process is quickly lost to let the diffusion rule this displacement. These three particles trajectories are shown in solid black line, blue dash line and red dash line. Grey solid lines represent the local trajectories of other particles before and after collision. 18
2.9 The Gaussian distribution shape is shown here for different time values ($t = 1$ in black, $t = 4$ in red and $t = 9$ in blue in arbitrary units) with $D = 1$ to show its evolution with time for a particle at $x = 0$ at $t = 0$. 19
2.10 The system Ω shown here is composed of a gel pore GP (big pore) and an interlayer pore IP (small pore). A water molecule in one can move to the other as its trajectory shows: solid blue line in the GP and dash red line in the IP. 20
2.11 Two populations A and B respectively composed of n^0_A and n^0_B spins at $t = 0$, n_A and n_B at a time $t > 0$ are exchanging with exchange rates $k_{A\to B}$ and $k_{B\to A}$. 20
2.12 A population A composed of n^0_A spins at $t = 0$ and n_A at a time $t > 0$ is giving spins to another population X with exchange rate $k_{A\to X}$. Population X does not give any spin to population A, which can be formally seen as an exchange rate $k_{X\to A} = 0$. 21
2.13 The probability a spin, in bulk, that was at time $t = 0$ in the space volume defined by the interval $[-a,a]$ is in the same interval at time $t > 0$ is shown here with $a = 1$ and the diffusion coefficient $D = 1$. 22

2.14 Korb's model focuses on the first surface proton water spin layer. Three trajectories are shown. A full black disk represent the absorption of a water molecule whereas an empty black disk represent its desorption. In this model, Fe^{3+} ions are embedded in the crystal surface and water molecules cannot penetrate a volume around it specified by a disk of radius δ. Desorption is ruled by the surface desorption time τ_s and the surface diffusion is ruled by the hopping time τ_m. 24

3.1 The schematic cement nanostructure is composed of two kind of pores: the interlayer pore (IP) and the gel pore (GP). "W" stands for water molecules, Ca stands for calcium ions and the broken line stands for SiO_2 tetrahedral silicate chains. 26
3.2 Bulk water system is a simulation box full of water molecules (W). 27
3.3 Molecular Dynamics simulations descritise the Newton's law of motion and generate the coordinates of an ensemble of atoms at a time $t+\delta t$ as a function of their coordinates at time t and the interaction between all the atoms. . . . 28
3.4 DL_POLY needs input files (on the left) to generate a simulation that produces output files (on the right). The most used files are presented in this figure. The ones with an asterisk are not mandatory. 31
3.5 The Buckingham potential is plotted with $A_{ij} = 1$, $\rho_{ij} = 1$ and $C_{ij} = 1$. . . . 34
3.6 The n-m potential is plotted with $E^0_{ij} = 1$, $r_{ij} = 1$ and both (n,m)=(12,6) (black solid line) and (9,6) (red solid line). 35
3.7 The Morse potential is plotted with $E^0_{ij} = 1$, $k_{ij} = 1$ and $r_{ij} = 1$. 35
3.8 The screened harmonic potential parameters are shown here where i, j, k are three atoms, r_{ij} and r_{ik} are the distances between i and j and i and k respectively and θ is the angle $\widehat{ijk}$. This figure is adapted from [73]. 36
3.9 The screened harmonic potential is plotted with $k = 1$, $\theta_0 = \frac{\pi}{3}$, $r_{ij} = r_{ik}$ and $\rho_1 = \rho_2 = 1$. 36
3.10 The PBC replicate the simulation cell infinitely in the plane. When the position of an atom i is calculated after a time δt, this atom is replaced in the original simulation cell at the same place it would be in the copied cell. 37
3.11 A schematic representation of the probability density of water molecules (or more generally of an atom). The shape of the curve can be used to define layers where the water molecules have different behaviours. 38
3.12 The process to select the waters belonging to the ensemble $\{A > B > C\}$ is shown here. Every time a water molecule goes outside zone B, it is removed from the ensemble. At time t, only waters in zone C are considered for the calculation. Three trajectories , that start from the cross and are at the full circle at time t, are shown and belong to a specific (smallest) population: $\{L_1 > L_1 > L_1\}$ in red ($A = L_1$, $B = L_1$ and $C = L_1$), $\{L_1 > \Omega > L_2\}$ in green ($A = L_1$, $B = \Omega$ and $C = L_2$) and $\{L_2 > L_2 + L_3 > L_2\}$ in blue ($A = L_2$, $A = L_2 + L_3$ and $A = L_2$). 39
3.13 In 2D, the simulation cell is surrounded by 8 ghost cells. All the spins whose distance to a spin i are in the disc of radius $min_{d\in\{1,2,3\}} \frac{Cell[d]}{2}$ (where $Cell[d]$ is the length of the cell in the d^{th} direction) is in the its neighbour list. 41

4.1 Pure Bulk water (white and red sticks) and simulation box. SPC/E water (red oxygens and white hydrogens) was used here. The simulation box size is $25 \times 25 \times 25$ Å^3. 45
4.2 In this study, two representations of water have been considered. On both models, O stands for oxygen and H for hydrogen. On the left: SPC/E water is a three points model. On the right: TIP4P water is a four points model where M represents a pseudo atom where the oxygen charge is shifted on the bisector of $\widehat{HOH}$. 46
4.3 Bulk water simulated mean square displacement (black crosses) is proportional with time (t) and the slope of this curve is linked to the diffusion coefficient. It can be fitted (red full line) to a straight line. The diffusion coefficient found is $D_{sim} = 2.66 \times 10^{-9}$ m^2.s^{-1} with a standard error of 0.01×10^{-9} m^2.s^{-1}. The error bars were calculated were calculated in the mean over the average of all time starts. 48
4.4 Water (red oxygens and white hydrogens) propagation from a box. Top: $t =$ 0 ns; middle: $t = 0.5$ ns; bottom: $t = 1.5$ ns. 49
4.5 Water propagation curve versus time (t) from MD simulation (black crosses) can be fitted by the analytical formula in equation 2.28 (red solid line). This fit is good and shows the propagator is Gaussian. The varying parameter is the diffusion coefficient and is found to be $D = 2.763 \pm 0.004 \times 10^{-9}$ m^2.s^{-1}. 50
4.6 Correlation function simulated components G_{NN} (black crosses with its standard error bars), G_{NF} (red crosses and its standard error bar) and the analytical G_{FF} (blue crosses) versus time (t) in log-log space. The correlation time is $\tau_c = 9 \pm 1 \times 10^{-12}$ s. 51
4.7 Spectral density functions J_{NN} (black crosses), J_{NF} (red crosses) and J_{FF} (blue crosses) versus frequency are shown with their respective standard errors with a frequency between 1 and 100 MHz. 52
4.8 NMR relaxation time components T_1^{NN} (black crosses), T_1^{NF} (red crosses) and T_1^{FF} (blue crosses) versus frequency shown with their respective standard error. 53

5.1 Blue triangles represent silicate tetrahedra. In tobermorite 9 Å and anomalous tobermorite 11 Å, the two silica chains are close enough to join. As a result, some silica tetrahedra are linking the two previous chains: these are the Q_3 silicates. The dots denote an infinite crystal. 55
5.2 Blue triangles represent for silicate tetrahedra. In normal tobermorite 11 Å and tobermorite 14 Å, the two silicate chains are separated. As a result, there is no Q_3 silicates and only Q_2 (a lot for long chains) and Q_1 (a small amount as they only are at the extremities of the silica chains) silicates tetrahedra are present in such a structure. The dots denote an infinite crystal. 55
5.3 Blue triangles stand for silicate tetrahedra. In C-S-H, the Q_1 silicons are the most important silicate population. As the C/S ratio increases (some silicon tetrahedra are removed and replaced by calcium ions. Here, a Q_0 silicon is shown also. However, the number of Q_0 in such a structure is really small. The dots denote an infinite crystal. 56

5.4 A SiO_2 α-quartz system with protonated surface creates a gel pore filled with water molecules. Red and yellow lattice: the SiO_2 crystal; red and white balls: surface hydroxyls; red and white sticks: water molecules. Here, this is a snapshot of MD2 as suggested by the protonated surface that is highlighted by the green rectangles. The white line refers to the size of the gel pore of 1 nm. 58
5.5 An anomalous tobermorite 11 Å system with protonated surface creates a gel pore filled with water molecules. Four pores are shown: three interlayer pores and one gel pore (that wraps around the end of the simulation cell as drawn). Red and yellow lattice: the SiO_2 crystal; red and white balls: surface hydroxyls (highlighted by the green rectangles); red and white sticks: water molecules; green ball: hydrated calcium ions. The white line refers to the size of the interlayer pore of 1.1 nm. 59
5.6 This figure is a simple illustration of the transformation of tobermorite 14 Å to the system with good Q_n and C/S ratio values. Dark blue triangles represent silicon tetrahedra; red balls are oxygens, light blue balls are calciums in layers and "Ca" in circles represent the hydrated calcium ions added to the system. The silicate dimer chains can then be easily seen. Here, this chain is infinite (ie: PBC means periodic boundary conditions). This figure is adapted from Richardson [45] 60
5.7 A snapshot of the simulation of the basic modified tobermorite 14 Å system is shown here (here, this is MD4 but the structure is the same for MD4f, MD5 and MD5f). Red and yellow chains are silicate dimer chains; blue balls are calciums and red and white sticks are water molecules. The gel pore is on the left and the interlayer pore on the right. The white line refers to the size of the interlayer pore of 1.4 nm. 61
5.8 The previous modified tobermorite 14 Å system is modified here: the surface is protonated, this is MD8. As a consequence, the positive calcium ions are repelled to the bulk by the negative surface hydroxyls. The meaning of the different forms and colors are the same as in previous figure and red and white balls represent surface hydroxyls and green balls calcium ions (highlighted by green rectangles). The white line refers to the size of the interlayer pore of 1.4 nm. 61
5.9 The previous modified tobermorite 14 Å system is modified here: the number of hydrated calcium ions is increased by a factor 2. Here this is a snapshot of model MD6 but the same behaviour is obtained with MD6f, MD7 and MD7f. The meaning of the different forms and colors are the same as in previous figure. The hydrated calcium ions that cannot find a stable position close to the surface (forming a negatively charged plan) are repulsed to the center of the pore. Surface stable calcium ions and the one rejected to the center of the pore are highlighted by green rectangles. The white line refers to the size of the interlayer pore of 1.4 nm. 62
5.10 The previous modified tobermorite 14 Å system is modified here: hydroxide groups charge balance the hydrated calcium ions. This is MD9. The meaning of the different forms and colors are the same as in previous figure but here red and white balls are hydroxides. The white line refers to the size of the interlayer pore of 1.4 nm. 62

5.11 MD4f: Modified tobermorite 14 Å simulation with the whole crystal atoms positions fixed and CLAY_FF potential used. Left: density profile; right: surface desorption. $\tau_S = 5.15 \pm 0.02$ ns as listed in table 5.1. On the left, yellow stands for silicate, green stands for calcium, red stands for water oxygen and black stands for water hydrogen. On the right, black crosses are the simulated desorption data and the solid red line is its exponential fit. The surface layers (SL) are limited by the silicate peaks and the bars on the abscissa. 67
5.12 MD5f: Modified tobermorite 14 Å simulation with the whole crystal atoms positions fixed and modified Freeman potentials used. Left: density profile; right: surface desorption. $\tau_S = 7.17 \pm 0.01$ ns as listed in table 5.1. On the left, yellow stands for silicate, green stands for calcium, red stands for water oxygen and black stands for water hydrogen. On the right, black crosses are the simulated desorption data and the solid red line is its exponential fit. The surface layers (SL) are limited by the silicate peaks and the bars on the abscissa. 68
5.13 MD4: Modified tobermorite 14 Å simulation with only silicate atoms positions fixed and CLAY_FF potential used. Left: density profile; right: surface desorption. $\tau_S = 3.09 \pm 0.01$ ns as listed in table 5.1. On the left, yellow stands for silicate, green stands for calcium, red stands for water oxygen and black stands for water hydrogen. On the right, black crosses are the simulated desorption data and the solid red line is its exponential fit. The surface layers (SL) are limited by the silicate peaks and the bars on the abscissa. 68
5.14 MD5: Modified tobermorite 14 Å simulation with ony silicate atoms positions fixed and modified Freeman potentials used. Left: density profile; right: surface desorption. $\tau_S = 0.14 \pm 0.01$ ns as listed in table 5.1. On the left, yellow stands for silicate, green stands for calcium, red stands for water oxygen and black stands for water hydrogen. On the right, black crosses are the simulated desorption data and the solid red line is its exponential fit. The surface layers (SL) are limited by the silicate peaks and the bars on the abscissa. 69
5.15 MD6f: Modified tobermorite 14 Å simulation with the whole crystal atoms positions fixed and CLAY_FF potential used and additional hydrated calcium ions. Left: density profile; right: surface desorption. $\tau_S = 5.80 \pm 0.01$ ns as listed in table 5.1. On the left, yellow stands for silicate, green stands for calcium, red stands for water oxygen and black stands for water hydrogen. On the right, black crosses are the simulated desorption data and the solid red line is its exponential fit. The surface layers (SL) are limited by the silicate peaks and the bars on the abscissa. 70
5.16 MD7f: Modified tobermorite 14 Å simulation with the whole crystal atoms positions fixed and modified Freeman potentials used and additional hydrated calcium ions. Left: density profile; right: surface desorption. $\tau_S = 6.84 \pm 0.01$ ns as listed in table 5.1. On the left, yellow stands for silicate, green stands for calcium, red stands for water oxygen and black stands for water hydrogen. On the right, black crosses are the simulated desorption data and the solid red line is its exponential fit. The surface layers (SL) are limited by the silicate peaks and the bars on the abscissa. 70

5.17 MD6: Modified tobermorite 14 Å simulation with only silicate atoms positions fixed and CLAY_FF potential used and additional hydrated calcium ions. Left: density profile; right: surface desorption. $\tau_S = 4.21 \pm 0.02$ ns as listed in table 5.1. On the left, yellow stands for silicate, green stands for calcium, red stands for water oxygen and black stands for water hydrogen. On the right, black crosses are the simulated desorption data and the solid red line is its exponential fit. The surface layers (SL) are limited by the silicate peaks and the bars on the abscissa. 71
5.18 MD7: Modified tobermorite 14 Å simulation with ony silicate atoms positions fixed and modified Freeman potentials used and additional hydrated calcium ions. Left: density profile; right: surface desorption. $\tau_S = 0.12 \pm 0.01$ ns as listed in table 5.1. On the left, yellow stands for silicate, green stands for calcium, red stands for water oxygen and black stands for water hydrogen. On the right, black crosses are the simulated desorption data and the solid red line is its exponential fit. The surface layers (SL) are limited by the silicate peaks and the bars on the abscissa. 71
5.19 MD8: Modified tobermorite 14 Å simulation with the whole crystal atoms positions fixed and CLAY_FF potential used and surface protonated. Left: density profile; right: surface desorption. $\tau_S = 0.18 \pm 0.01$ ns as listed in table 5.1. On the left, yellow stands for silicate, green stands for calcium, red stands for water oxygen and black stands for water hydrogen. On the right, black crosses are the simulated desorption data and the solid red line is its exponential fit. The surface layers (SL) are limited by the silicate peaks and the bars on the abscissa. 72
5.20 MD9: Modified tobermorite 14 Å simulation with the whole crystal atoms positions fixed and CLAY_FF potential used and hydroxide groups. Left: density profile; right: surface desorption. $\tau_S = 6.36 \pm 0.02$ ns as listed in table 5.1. On the left, yellow stands for silicate, green stands for calcium, red stands for water oxygen and black stands for water hydrogen. On the right, black crosses are the simulated desorption data and the solid red line is its exponential fit. The surface layers (SL) are limited by the silicate peaks and the bars on the abscissa. 73

6.1 A density profile shows that MD4 can be split into multiple zones: L1, L2, TL, Bulk and IL (IL-B and IL-S). C stands for the crystal layer. The behavior of water molecules can be studied in each of these zones. Crystal layers have a strong influence on water by itself. The crystal also attracts indirectly water molecules thanks to calcium ions' influence. The calcium ions later split the surface layer into two sub layers L1 and L2 and have a strong influence on the water molecules in their surrounding. The color code is as follows: yellow line refers to silicon atoms, green line refers to calcium ions, red line refers to water oxygen atoms and black line to water hydrogen atoms. 75

6.2 This figure represents a slice of the crystal layer silicon dimers and the gel calcium layer in the xy axis for $z \in \{SL+C\}$ as defined in figure 6.1. Calcium ions (bluish balls) are placed between silica tetrahedra dimers (yellow [for silicons] and red [for oxygens] structures) and replace the former bridging silica tetrahedra of the tobermorite 14 Å as shown in figure 5.6. These calcium ions (Ca^{2+}) create a stable lattice of a positively charged plane that splits the surface layer of water molecules into L1 and L2. The position of the gel pore calcium ions is the same as the position of the wells that split the surface layers into L1 and L2 in the density profile in figure 6.1. The white line refers to the size of a silicon dimer in the crystal layer which is 0.31 nm. 76

6.3 The radial distribution function that links calcium ions and the water molecules that surround them is shown here for calcium ions in the MD4 gel pore (red dash line) and in pure bulk water (black dash line). The number of water molecules in the first hydration shell is also shown for MD4 (red dot line) with ≈5 water molecules and for bulk water (black dot line) with 8 water molecules. The radial distribution function that links calcium ions to other calcium ions in MD4 gel lattices is also shown (green dash line) and the number of close calcium ions neighbours too (green dot line). It is clear here that in MD4, the average distance between two calcium ions is larger than twice the average distance between a calcium and a water molecule. 77

6.4 The probability of presence of water molecules in the different zones is shown here. Pink means a water molecule is not likely to stay at this position. Yellow means this is a stable position for water. White means the position is highly improbable. Green means a calcium ion can be in that position but it will be more probably in blue positions. The behaviour of water molecules is highly influenced by hydrated calcium ions that are trapped close to the surface. Top left map is for L1, top right map is for L2, middle left map is for TL, middle right map is for Bulk and bottom map is for IL. 79

6.5 On the left, the 2D mean square displacement and its standard error (black crosses) are generated for a {B>B>B} set of water molecules. The data can be only analysed during a small time interval because of the exchange between bulk and the TL. For the same reason, the statistics become less and less accurate with time because of the decreasing population taken into account in the calculation (right). This is why a fit is done for early times (ref line). As a result, a diffusion coefficient $D_{Bulk} = 2.96 \pm 0.01 \times 10^{-9} m^2/s$ is found. . . . 80

6.6 On the left, the 2D mean square displacement and its standard error (black crosses) are calculated for {L1>SL>L1} set of water molecules. These water molecules can do a hop via L2. But this hop is not straighforward and before doing it, water molecules are vibrating (black dash line). This is the reason why the curve is not considered during the short time to evaluate the diffusion process. These data are compared to {L1>L1>L1} set of water molecules to show the importance of hops (blue crosses represent for the 2D mean square displacement and its standard error). The populations taken into account in the calculation are also shown (right). As a result, the {L1>SL>L1} left curve is fitted by a straight line (black line) and a diffusion coefficient $D_{S1} = 1.98 \pm 0.01 \times 10^{-13} m^2/s$ is found. 81

6.7 On the left, the 2D mean square displacement and its standard error (black crosses) are calculated for a {L2>Ω-B>L2} set of water molecules. These water molecules can stay in TL as long as they do not go to bulk where they lose any L2 influence. The idea is to only include jumps in TL to go to another position in L2. On the right, the decreasing {L2>Ω-B>L2} population is shown. The diffusion analysis cannot be carried out for too short times (ie: less than 1 ns) to avoid vibration effects. The curve is fitted by a straight line from 1 to 6 ns and the diffusion coefficient is calculated: $D_{L2} = 6.01 \pm 0.01 \times 10^{-12} m^2/s$. . . 82
6.8 On the left, the 2D mean square displacement and its standard error (black crosses) are calculated for the {TL>TL>TL} set of water molecules. All the comments for bulk are valid for the TL. On the right, the decreasing {TL>TL>TL} population is shown. The diffusion analysis can only be done for short times (ie: less than 0.16 ns) because of the quick decrease of the number of water molecules taken into account in the calculation (right). A fit is made (red solid line on the left) and the diffusion coefficient can be calculated: $D_{TL} = 1.42 \pm 0.01 \times 10^{-9} m^2/s$. 83
6.9 The motion of six IL water molecules randomly chosen was investigated. For each of them, three positions are allowed: left surface (top), middle bulk (middle) and right surface (bottom). The exchange between surface and bulk is fast and the residency time is varying a lot, which is a property of a Levy walk. 83
6.10 On the left, the 2D mean square displacement and its standard error (black crosses) are calculated for the {IL>IL>IL} set of water molecules. There is no decrease of the {TL>TL>TL} population because the IL is a close system in MD4: there is no exchange with other layers, the number of water molecules taken into account in the calculations is constant (right). The diffusion analysis is straightforward: a fit (red line) can easily be made and a diffusion calculation gives $D_{IL} = 9.44 \pm 0.01 \times 10^{-11} m^2/s$. 84
6.11 A desorption curve (black crosses), a one component exponential fit (red line) and a two component expoonential fit (blue line) show L1 waters that are accepted in L2 and desorb from SL. The one component exponential gives in a typical desorption time $\tau_s = 11.74 \pm 0.01$ ns. A two component exponential fit gives a fast desorption time $\tau_{s,L1,fast} = 1.52 \pm 0.01$ ns and a slow desorption time $\tau_{s,L1,slow} = 15.94 \pm 0.01$ ns. 86
6.12 A desorption curve (black crosses), a one component exponential fit (red line) and a two component expoonential fit (blue line) show L2 water molecules desorption. The one component exponential gives in a typical desorption time $\tau_s = 0.75 \pm 0.01$ ns. A two component exponential fit gives a fast desorption time $\tau_{s,L2,fast} = 0.22 \pm 0.01$ ns and a slow desorption time $\tau_{s,L2,slow} = 1.17 \pm 0.01$ ns. 86
6.13 A desorption curve (black crosses), a one component exponential fit (red line) and a two component expoonential fit (blue line) show SL water molecules desorption. The one component exponential gives in a typical desorption time $\tau_s = 6.65 \pm 0.02$ ns. A two component exponential fit gives a fast desorption time $\tau_{s,SL,fast} = 1.13 \pm 0.03$ ns and a slow desorption time $\tau_{s,SL,slow} = 10.79 \pm 0.02$ ns. 87

6.14 A desorption analysis is done on the calcium first hydration shell for waters in L1 (black crosses), in L2 (red crosses) and SL (blue circles) with fits by a one component exponential (respectively black, red and blue lines) and a two component exponential for the FHS-SL (blue dash line). Typical desorption times found this way are $\tau_{s,FHS-L1} = 21.02 \pm 0.03$ ns, $\tau_{s,FHS-L2} = 2.01 \pm 0.01$ ns and $\tau_{s,FHS-SL} = 6.44 \pm 0.02$ or $\tau_{s,FHS-SL,slow} = 21.24 \pm 0.15$ ns and $\tau_{s,FHS-SL,fast} = 1.05 \pm 0.01$ ns. 88
6.15 MD4 correlation function is split in a like-spin component G_{II} (top dash black line) and an unlike-spin component G_{IS} (bottom dash dark-grey line). These curves are compared to a simulated Quasi 2D bulk water slab of thickness 1.3 nm (red solid line). The initial value for the G_{IS} curve depends on the Fe^{3+} density. 89
6.16 The Faux model considers two layers of water (respectively L2 and B_{eq}) distant from the surface crystal (respectively by distances d_{L2} and $d_{B_{eq}}$ with hopping rates (related to the diffusion coefficient in each of these layers). Adapted from Faux [13] 90
6.17 This figure represents schematically the behaviour of a water molecule in a porous media: here, the water trajectory (red solid line) start on the surface layer (ie: L2, purple zone), diffuse slowly and then goes to a bulk layer (ie: Beq, green zone) and go on diffusing, faster. Paramagnetic iron ions are represented in the surface by orange balls. This figure was extracted from a presentation by Peter McDonald. 91
6.18 This figure represents schematically the Levy walk a water molecule performs between the two layers (dark blue plane for the surface layer and light blue plane for the bulk like layer). The three black and white pictures are extracted from [36] and represent the Korb's surface process. The dark blue line is the water trajectory that uses the bulk like layer to jump to another surface position. This figure was extracted from a presentation by Peter McDonald. . 91
6.19 Longitudinal relaxation rates T_1^{-1} were recorded versus frequency (black squares). These data were fitted by Korb's model (dash black line) and the Faux model (solid black line). This figure is extracted from [13]. 92

7.1 Water density versus temperature is shown in this graph. The simulation values (black crosses) seem to decrease faster than the the values obtained by a fit of the experiments [95] (red solid line). This can be explained by the relatively small number of water molecules and hence the small simulation cell sizes considered here. 95
7.2 The Arrhenius law can be used to calculate the water diffusion activation energy. The natural logarithm of diffusion coefficient (simulation in red crosses and experiment in black crosses) is plotted versus the inverse of temperature in K^{-1}. The slope of the fitting straight line of these data (red solid line for simulation and black dash line for literature) is the activation energy divided by the gas constant. As a result, the water diffusion activation energy for the range of temperature 270-370 K found thanks to the 11 bulk water simulations is $E_{a,sim}^{dif} = 14.69 \pm 0.76$ kJ/mol, which is close to the activation energy from experiment $E_{a,exp}^{dif} = 16.08 \pm 0.45$ kJ/mol. 96

7.3 The Arrhenius law can be used to calculate the NMR relaxation time T_1 activation energy. The natural logarithm of T_1 (black crosses for simulation and red crosses for experiment [80]) is plotted versus the inverse of temperature (in K^{-1}). A straight line fits these data points (black line) and the slopes are the activation energies divided by the gas constant (black line for simulation and red line for experiment). As a result, the NMR relaxation time T_1 activation energy for the range of temperature 270-370 K found thanks to the 11 bulk water simulations is $E_{a,sim}^{T_1} = 14.89 \pm 0.30$ kJ/mol and $E_{a,exp}^{T_1} = 16.51 \pm 0.14$ kJ/mol 98
7.4 The natural logarithm of the diffusion coefficients of the different water populations are shown here. Crosses and circles represent the simulated values and the solid lines their fits by straight lines. The color code is as follows: black stands L2, purple for TL and red, just behind the green curves, for Ω, green for Bulk and blue for IL. 100
7.5 The natural logarithm of the desorption times of the different water populations are shown here. The dash lines represent the simulated values and the solid lines their fits by straight lines. The color code is as follows: black stands for L1, red stands for L2 and blue stands for SL=L1+L2. 101
7.6 The correlation functions for MD4 model at different temperatures have been generated (dash lines). The color code is as follows: blue stands for T= $293.15K$, green stands for T= $313.15K$, red stands for T= $333.15K$ and black stands for T= $353.15K$. 102

8.1 This model is composed of two interlayer pores (whose length is ≈5.5 nm) connected with a gel pore (whose length is ≈3.5 nm). The connections allow exchange between the two pores. The color code is as for MD4 model: yellow (silicon) and red (silicon oxygen) chains stand for the silica dimer chains, white (water hydrogen) and red (water oxygen) triangles stand for water molecules and blue balls stand for calcium ions. The interlayer is split into three parts: two interlayer border zones (IL_E) and one interlayer center zone IL_C. 105
8.2 The desorption analysis of the {IL>IL>IL} set of water molecules is performed. This yields to a decaying curve (black crosses) that is fitted by an exponential function (black line) with a decaying time $\tau = 4.94 \pm 0.02$ ns and an offset of 429 water molecules (ie: $fit(t) = 105.72e^{-\frac{t}{4.94}} + 429.25$ waters). 106
8.3 The desorption analysis of the {IL_C>IL>IL_C} (red crosses) and {IL_C>IL_C>IL_C} (black crosses) set of water molecules is carried out. The first one does not decay in the analysis time range since a water molecule in the center of the interlayer needs ≈ 7 ns to reach the gel. The second one is fitted (black line) by an exponential $fit(t) = 80.34e^{-\frac{t}{9.52}} + 92.71$ waters. 107
8.4 The desorption analysis of the {IL_E>IL>IL_E} (red crosses) and {IL_E>IL_E>IL_E} (black crosses) set of water molecules is performed. The first one is fitted (red line) by $fit(t) = 49.7e^{-t/4.32} + 125.91$ waters and the second one is fitted (black line) by $fit(t) = 69.84e^{-t/3.27} + 102.57e^{-t/49.09}$ waters. 107
8.5 The desorption coefficient in the interlayer is not the same everywhere because of the exchange between the interlayer and the gel pore. A simple idea is to consider the gel influence is not limited to the edge of the interlayer. 109

8.6 The desorption of the interlayer water molecules can be disturbed by the presence of other crystal layers obstructing the end of the interlayer. In this figure, red lines represent the crystal layers, black crosses mean water exchange is difficult whereas green double arrows show easier exchange zones. 110
8.7 The desorption of the interlayer water molecules can be disturbed by the chemical composition of the end of the interlayer pore. However, the actual chemical structure of such a system is not well known. The red lines represent the crystal layers and the warning triangles at the ends of the interlayers suggest an unknown structure. 110
8.8 The desorption of the interlayer water molecules can be disturbed by the collapse of the crystal layers that create the interlayer pore. The black arrows represent such collapses at different places of the model that would reduce the water exchange and the green double arrows represent an easier exchange where there is no layer collapse. 111

List of Tables

4.1 The different parameters necessary for SPC/E and TIP4P/2005 water potentials are presented in this table: distances ($r_{OH,OM}$), angles ($\widehat{HOH}$), charges ($q_{O,H,M}$), masses ($M_{O,H}$) and Lennard-Jones parameters (ϵ and σ). Note that the Lennard-Jones potential is only considering the oxygens of two different water molecules. 47

5.1 List of MD simulations with surface conditions (OH_s for surface hydroxyl group), different hydrated calcium ion (Ca^{2+}) densities, effect of hydroxide groups (OH_l), atomistic potentials and values of surface desorption times τ_S. 57

5.2 The species used in the models are defined in this table. Their CLAY_FF molar masses M and charges q are given. 63

5.3 The potential interactions between the different atoms involved in this study "CLAY_FF" simulations are shown here. Only the Lennard-Jones (lj) potential is used where E_0, in [eV], stands for the dissociation energy between the two atoms interacting and r_0, in [Å], is the equilibrium bond distance as described in equation 3.3. Here, {OX}={OSm or OSf or Ohs or OW}. 63

5.4 The hydroxide ion features are defined here: molar masses M and charges q are shown. The total charge of an hydroxide is -1 in such a way that two of them can charge balance the hydrated Ca^{2+} ions that have an integer +2 charge. 64

5.5 The potential interactions between the hydroxide and the different atoms involved in this study simulations using CLAY_FF potential are listed. Only the Lennard-Jones (lj) potential is used where E_0, in [eV], stands for the dissociation energy between the two atoms interacting and r_0, in [Å], is the equilibrium bond distance as described in equation 3.3. 64

5.6 The species used in the models are defined in this table. Their "Freeman" molar masses M and charges q are listed. 65

5.7 The potential interactions between the different atoms involved in the simulations using modified Freeman potentials are shown here. For the Buckingham potential, A is in [eV], ρ is in [Å] and C is in [eV/Å^6]. For the $n-m$ potential, E_0 is in [eV], r_0 is in [Å] and n and m are integers with no unit. For the Lennard-Jones potential, E_0 is in [eV] and r_0 is in [Å]. For the Morse potential, E_0 is in [eV], r_0 is in [Å] and k is in [Å^{-1}]. Finally, for the screened harmonic angular potential, $\rho_{1,2}$ are in [Å], r_c is the cutoff distance for this interaction in [Å], θ is in [degree] and k is in [degree^{-2}]. Details of all these parameters can be found in chapter 3 section 3.3.2. 65

6.1 The sizes of different layers in this model are recorded here. As a comparison, the typical water size is ≈ 0.27 nm. There are two of each layer exept for bulk and IL-B because of the pores symmetry. 75
6.2 A diffusion analysis for each MD4 layer is done and diffusion cefficients are recorded in this table. 84
6.3 A desorption analysis for each layer is done and desorption times are recorded in this table. 88
6.4 This table shows the differences between Korb's single layer and Faux two layer models. 92
6.5 This table shows the similarities between Korb's single layer and Faux two layer models. 92

7.1 11 NVT simulations were used to generate the water mean square displacement and then to calculate the associated water diffusion coefficients D_{sim} and its standard error. These diffusion coefficients were compared with experimental ones D_{exp} [44]. This yields to the behaviour of water diffusion versus temperature. 96
7.2 11 NVT simulations were used to generate the NMR relaxation times T_1 (the T_2 is the same for this range of frequency). These results can be used to calculate the NMR relaxation time T_1 activation energy. 97
7.3 Four NVT simulations were used to generate different water populations (L2={L2>Ω-B>L2},TL={TL>TL>TL},B={B>B>B}, Ω={Ω>Ω>Ω} and IL={IL>IL>IL}, where {A>B>C} means that water molecules start in A, can go to B and are considered in the calculation at time t if in C) mean square displacement and to calculate the diffusion coefficients associated. They will be ploted in figure 7.4. 99
7.4 The diffusion activation energies were generated for the five different water populations (L2,TL,Bulk,Ω and IL) taking into account four temperatures from 293 to 253 K. The date presented in figure 7.4 were fited by straight lines whose slopes are the activation energies divided by the gaz constant for each water populations. 100
7.5 4 NVT simulations were used to generate L1, L2 and SL desorptions and the desorption times τ_s are listed here. 101
7.6 The desorption activation energies were generated for the three different surface water populations taking into account four temperatures from 293 to 253 K. . 102
7.7 The T_1 activation energies [AE] for C-S-H interlayer and gel pores water were measured. The values are shown for a 28 days hydration and a 90 days hydration samples are shown. These results are extracted from A. Gajewicz thesis [96]. 103

8.1 The slow and fast desorption times of the four water populations {IL_C>IL_C>IL_C}, {IL_C>IL>IL_C}, {IL_E>IL_E>IL_E} and {IL_E>IL>IL_E} are shown in this table. When existing according to the analysis, the fast decaying time is in the range of [0,10] ns whereas nothing can be said about the slow decaying time but it is bigger than 40 ns. 108

Chapter 1

Introduction

1.1 Cement study and TRANSCEND project

1.1.1 The Impact of Concrete and Cement

Concrete is nowadays one of the most used man-made building materials in the world. An estimation is that almost three tons of this material are used per year per human being [1]. Its success is due to many causes: it is a cheap material as shown in figure 1.1, it can be made easily everywhere, it is a liquid stone and can take any shape, it is durable, strength and water-tightness.
Note that contrary to the usual bad feeling about concrete in society, architects can use the very latest new concrete materials to create some astonishing buildings like MuCem in Marseille [2] or the Louis Vuitton Foundation in Paris [3] .

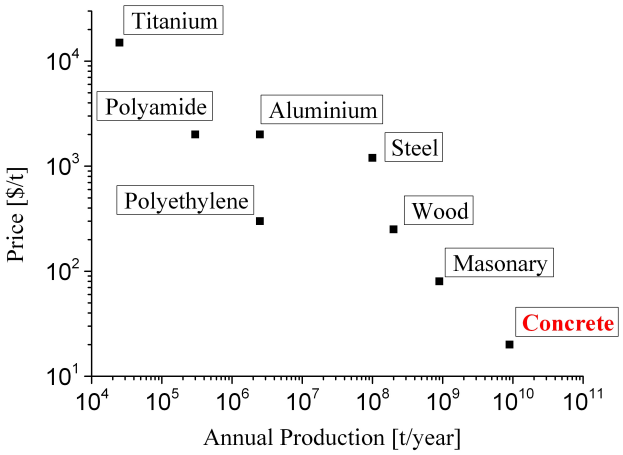

Figure 1.1: Concrete is a cheap material with good physical features, which explains an enormous demand worldwide (adapted from [4])

Concrete is a porous material. It is composed of aggregates, sand, water and cement. The latter, after some chemical reactions with water, becomes its binder, also porous.

Even if it is an eco friendly material according to the small amount of CO_2 emission generated per kilogram, the huge amount of concrete used in the world produces $\approx 5\%$ of the CO_2 footprint. Indeed, the process to create cement (burn fuel to heat limestone and the breakdown of limestone itself) is the main factor of such a global warming impact.

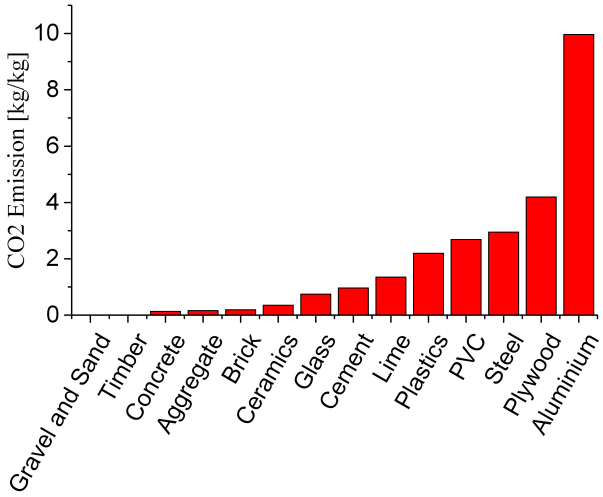

Figure 1.2: Embodied energy and CO_2 emission produced per kg of concrete is negligible compared to other materials (adapted from [5])

Hence, a better understanding of the different physical processes involved in cement and concrete productions are important. Indeed, for instance, water transport properties are significant for durability: chemical agents can move with water into the pores and damage the structure. This study of water displacement at different lengthscales is the purpose of the TRANSCEND project [6].

Figure 1.3: Characteristic degradation of a concrete bridge pylon in the Pimpama River, southeast Queensland [7]

1.1.2 TRANSCEND Project

TRANSCEND project (ie: TRANSport for Concrete which is Eco friendly, iNnovative and Durable) is a network funded by the European Union (Marie-Curie Initial Training Network). The goal of such a project is to understand water transport properties in cement and concrete from the nanoscale to the meso-macroscale using experiments and simulation technique as shown in figure 1.4. The project is separated into three main themes: theme A is about computer modelling from the nanoscale to the macroscale and uses a range of simulation methods (especially Molecular Dynamics), theme B is about experimental work whose goal is to give input data to theme A and theme C is about the validation of theme A.

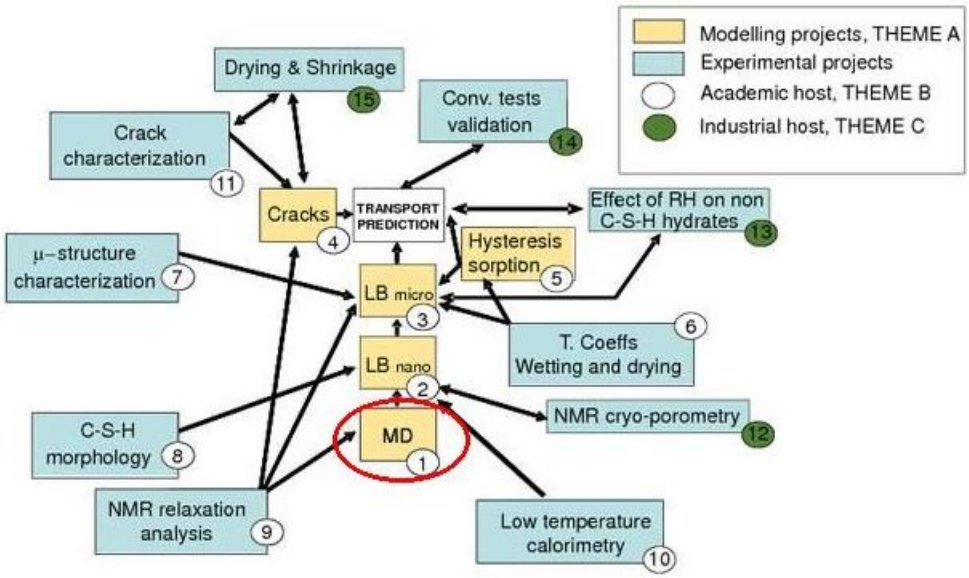

Figure 1.4: TRANSCEND project can be seen as a matrix of projects where simulation and experiments are used to understand water transport properties in cement and concrete from the nano to the meso and macroscale. This thesis project is red circled. (adapted from [6])

This thesis presents the theories, methodologies and results of a project in Theme A that is about the water transport properties in cement at the nanoscale and the ^{1}H NMR simulation in such a system.

1.2 NMR and Numerical Simulation

1.2.1 NMR and Cement

As said previously, concrete and cement are porous materials (cement nanostructure will be discussed in next section) and these pores contain water. A powerful technique to investigate this structure and also the water transport properties in it is ^{1}H Nuclear Magnetic Resonance

(NMR) relaxometry. Actually, all the fluid containing protons can be analysed with ^{1}H NMR. Such a technique is non-invasive and non-destructive. It does not affect the dynamics of the studied fluid. It can be repeated easily in a very short time that allows a dynamical study of transport properties (ie: if the fluid is subject to a chemical reaction with its surrounding and loses some ^{1}H, it can be seen).

^{1}H NMR has already been used with other materials like clays, rocks, porous glasses, zeolites or polymers. The idea is to use ^{1}H nuclei as a probe to analyse the material. According to the local environment, the ^{1}H will move in a different way and its behavior will be recorded in NMR data. For instance, thanks to NMR relaxometry, it has been shown that concrete is formed of pores that have specific sizes: the pore size distribution is discrete and not continuous [8]. Indeed, the outputs of such a technique are relaxation times as it will be explained later. The distribution of the relaxation times highlights the presence of different proton populations (depending on their surrounding) and these populations associated to different pores whose the size can be calculated.

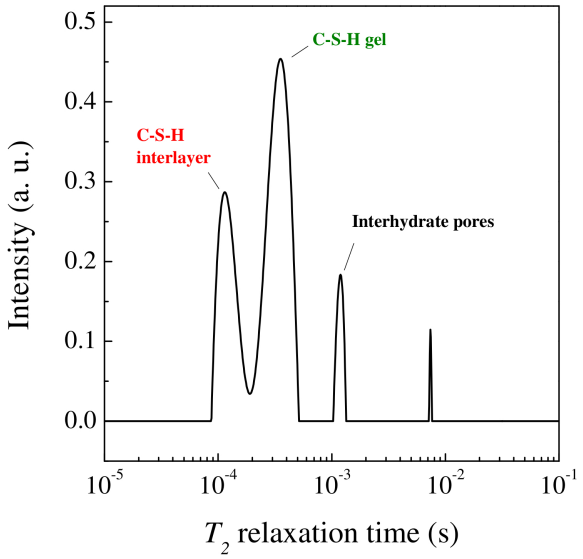

Figure 1.5: An histogram of the T_2 ^1H NMR relaxation time highlights white cement pore size distribution. Calcium-Silicate-Hydrates Interlayer size is ≈ 1 nm, C-S-H Gel size is ≈ 3 nm and Interhydrate size is ≈ 9 nm [8]. The abscissa is the spin-spin relaxation time T_2 and will be discussed in chapter 2.

The interesting pores for this study are the nanopores (first and second peaks on figure 1.5). They are associated with the cement binding phase: the Calcium-Silicate-Hydrates (C-S-H). The morphology of such a phase is not well understood and different models exist as it will be seen later. NMR relaxometry signals give good data to analyse these different models (NMR can be used in other techniques for the determination of silicate tetrahedral coordination analysis thanks to ^{29}Si NMR which is important to discriminate the different cement nanostructure models [9, 10]). These signals are interpreted using theoretical models that will be used later to fit the data.

1.2.2 NMR Modelling

Experimentalists need to fit their data to theoretical models based on proton spin dynamics in order to interpret ^{1}H NMR signals. The outputs of these models are NMR relaxation times. These NMR relaxation times (or their inverse: the NMR relaxation rates) are frequency dependent and can be compared and fitted to the frequency dependence of the considered models.

The first significant stone was placed by Bloembergen, Purcell and Pound in 1948 [11] (the so called BPP theory). It considers an auto-correlation function (referred as G) based on the dipolar interaction of spin pairs. This G function can be Fourrier transformed to get a spectral density function (referred as J) from which relaxation times are calculated. This theory assumed that the auto-correlation function G is proportional to a decaying exponential with an argument τ_c that represents the correlation time of the dipolar coupling. Unfortunately, such a description can be used only for simple systems (bulk water for instance). Cement systems, as will be discussed later, are composed of different surrounding (like the surface and the bulk) that can exchange.

However, another significant stone was set up in the porous medium community to avoid this problem. In 1997, Korb et al. [12] published a model that considers that the relaxation mechanism is dominated by the interaction between the water molecules absorbed on the pore crystal and the paramagnetic impurities (Fe^{3+}). Indeed, the proton-proton interaction is ruled by their gyromagnetic ratio only whereas the proton-Fe^{3+} interaction is also ruled by the electron gyromagnetic ratio that is far higher than the proton one ($\gamma_{Fe^{3+}} \approx 658.21\gamma_{proton}$). This model also takes into account other parameters but will be discussed later The simulations of this thesis helped to design a new improved model developed by Faux et al. [13] .

The incredible growth of computer calculation capacities over the last decades offered a new way to tackle problems in Physics. Indeed, now, the spin dynamics can be simulated in any system considered, here cement, in order to calculate the auto-correlation function G from the generated trajectories. In 1953, Torrey [14] was the first to do this and used a Monte Carlo simulation method, Translational Diffusion, where each spin can move to a neighbour site depending on a known probability. In 1981, Sholl [15] worked on analytical solutions for the spectral densities in 1, 2 and 3 dimensions for the translational diffusion of like spins in the low and high frequency limits. In 1986, Faux [16] used this work to simulate the spin diffusion in a cubic lattice and calculate the auto-correlation function. This kind of technique can be applied to other simulation methods. Indeed, Molecular Dynamics outputs are trajectories, and auto-correlation functions can be calculated based on Faux and Sholl works, as done by Faux [17] and Bhatt [18].

1.3 Cement Pastes Nanostructure: C-S-H

1.3.1 Powers'Model

In 1958, Powers et al. [19] proposed a first model of the C-S-H morphology based on the adsorption outputs they produced. Powers took into account different parameters such as the high specific surface area (about 200 m^2/g) and the size (about 3 nm) of the gel pore and

the unit cell size (less than 14 nm) and proposed a model composed of some colloids where water cannot evaporate. Later, he detailed the C-S-H gel as some sorts of fibers thanks to electron microscopy where a lattice of rigid particles blocks made of parallel layers embeds the gel water as shown in figure 1.6. C-S-H has chemical similarities to mineral phases such as tobermorite and jennite.

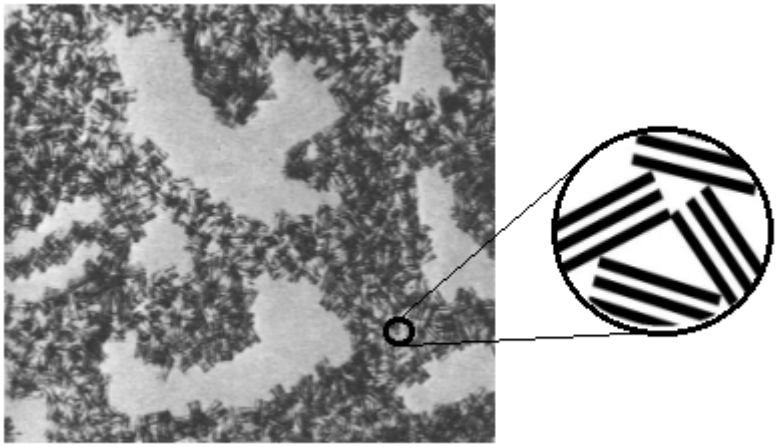

Figure 1.6: This picture represents Powers' C-S-H model (adapted from [19]). The large grey zones represent capillary water. In the dark grey zone that is zoomed (circle), black lines represent Gel particles and non-evaporating water, and the white lines represent the physically bound Gel water.

1.3.2 Feldman and Sereda's Model

In 1968, Feldman and Sereda [20, 21] proposed another model for C-S-H morphology thanks to sorption experiment. They suggested that C-S-H is composed of silica tetrahedra layers surrounding calcium and water layers. In this model, the silica layers are highly connected. Different populations of water can be identified: water highly confined between two layers of silica tetrahedra (the so called interlayer water), and water in bigger pores (the so called gel pore) comprising the bulk (free water), and the surface absorbed water (combined water). Figure 1.7 shows the surface and interlayer waters.

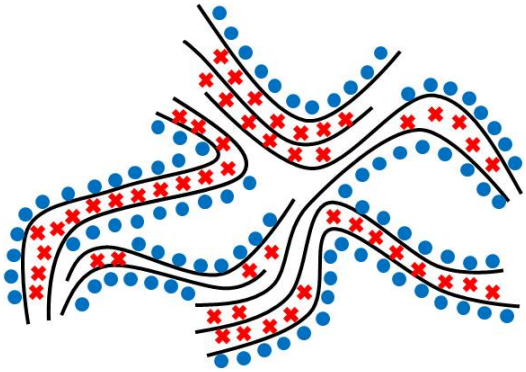

Figure 1.7: This picture represents Feldman and Sereda C-S-H model (adapted from [20]). Black lines represent crystal sheets, red crosses represent the interlayer water and the full blue disks represent the absorbed water.

1.3.3 Jennings' Model

In 2000, Jennings and Tennis made a first colloidal model [22, 23]. They suggested there were two types of C-S-H: a low density one and a high density one as shown in figure 1.8. They considered some C-S-H with layers that regroup in capillary pores to form C-S-H globules. Thanks to this model, they proposed a calculation of the cement phase composition by fitting experimental values of specific surface area and porosity.

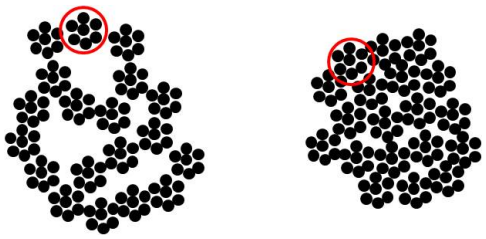

Figure 1.8: These pictures represent Jennings CM-I model with different densities of C-S-H: on the left the low density one and on the right the high density one. A C-S-H globule is circled in red.

In 2008, Jennings improved his previous model into a CM-II model [24]. He suggested that his CM-I C-S-H units are formed of layers with a thickness of about 4.2 nm [25]. He considered two locations for water: in the interlayer pores and in the intra-globule pores. The globules stuck together form some clusters and small gel pores (size $\approx$ 3 nm) and these clusters are packed together form globule flocs and large gel pores (size $\approx$ 3 to 12 nm) as shown in figure 1.9.

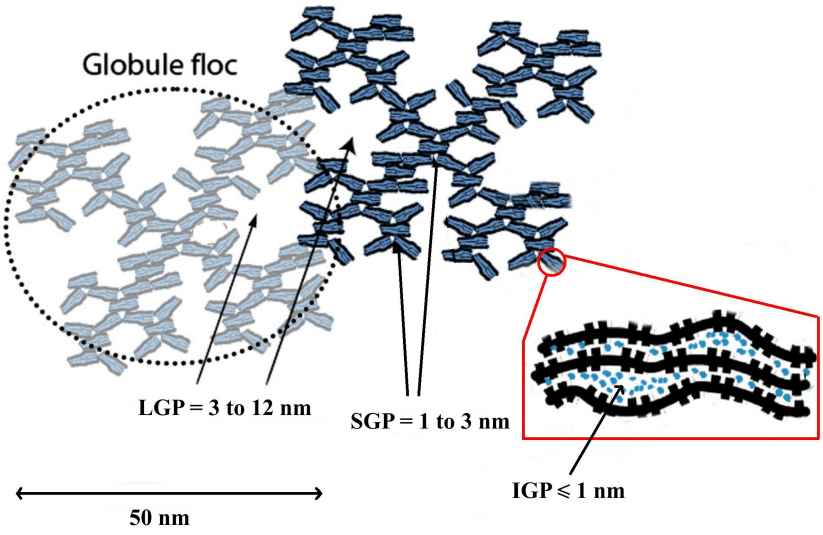

Figure 1.9: CM-II C-S-H Jennings model (adapted from [24]). The globule floc size is $\approx$ 50 nm, the Larger Gel Pore (LGP) size is $\approx$ 3 to 12 nm, the Small Gel Pore (SGP) size is $\approx$ 1 to 3 nm and the InterGlobular Pore (IGP) size is $\leq$ 1 nm.

1.4 Aims

The purpose of this work is to understand in a better way how water molecules move inside the cement paste at the nanoscale, particularly in order to improve the knowledge of the ^{1}H NMR relaxation processes involved in C-S-H systems. This work is based on numerical simulations such as Molecular Dynamics in order to learn about relaxation directly from the water hydrogens trajectories. The outputs of these simulations are compared to experimental data and provide a new point of view to interpret the latter. A better understanding of C-S-H structure is not the purpose of this work.

Chapter 2

Theory

The purpose of this chapter is to present the different elements of theory used in this work. The basics of quantum mechanics are not tackled here but the reader can find more information about this, upon which the NMR phenomena rely, in the bibliography [26, 27].

2.1 Basics of ^{1}H NMR Relaxometry

2.1.1 Preamble to NMR

NMR is the consequence of the existence of a pure nuclear or electronic quantum parameter, the intrinsic angular momentum: the spin of a particle $\overrightarrow{s}$. The spin value S is an integer or half an integer and the angular momentum is $|\overrightarrow{s}| = \sqrt{S(S+1)}\hbar$, where $\hbar$ is the Planck constant divided by 2π. For instance, the ^{1}H nucleus and Fe^{3+} electron spin values are respectively $I = s_{\mathrm{H}} = \frac{1}{2}$ and $S = s_{\mathrm{Fe}} = \frac{5}{2}$. Conventionally, I is used for nucleus spins and S for electron spins. All particles that have a spin also have a magnetic dipole moment $\overrightarrow{\mu}$ proportional to the spin $\overrightarrow{s}$ (in this study the spin quantum operator and the spin vector will be noted the same way) with a proportionality constant γ called the gyromagnetic ratio (different for each particle type):

$$\overrightarrow{\mu} = \gamma \overrightarrow{s} \tag{2.1}$$

If a spin experiences a magnetic field $\overrightarrow{B_0}$, the Hamiltonian of the interaction between them is:

$$H = -\overrightarrow{\mu} \cdot \overrightarrow{B_0} \tag{2.2}$$

Conventionally, the applied magnetic field $\overrightarrow{B_0}$ in NMR defines the z axis: $\overrightarrow{B_0} = (0, 0, B_0)$.

A second quantum number m_s appears when the magnetic field is not equal to zero: it represents the z-component of the angular momentum. For instance, for a proton, the energy of interaction is split into two levels $E_+ = \frac{\gamma\hbar B_0}{2}$ and $E_- = -\frac{\gamma\hbar B_0}{2}$ (the eigenvalues of the Hamiltonian) and the magnetic dipole μ can only align with the field ($\uparrow$) or against the field ($\downarrow$) as shown in figure 2.1.

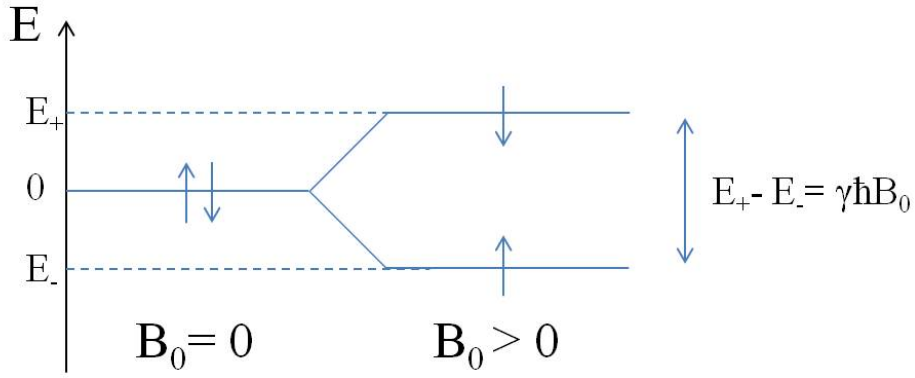

Figure 2.1: Magnetic moment μ aligns with ($\uparrow$) or against($\downarrow$) the magnetic field $\overrightarrow{B_0}$. The two populations have different energy level, split by the presence of the magnetic field.

At equilibrium, these two populations have respectively $N_\uparrow$ and $N_\downarrow$ spins linked by the ratio $\frac{N_\uparrow}{N_\downarrow} \approx e^{-\frac{E}{k_B T}}$ where k_B is the Boltzmann factor and T the temperature. Hence, the sum of all these dipole moments (ie the magnetisation vector $\overrightarrow{M}$) is non zero and can be observed. For instance, the difference of the population as a fraction of the total population for a sample of protons at room temperature $T = 300K$ in the presence of a magnetic field $\overrightarrow{B_0}$ of intensity $B_0 = 1$ T is $\frac{N_\uparrow - N_\downarrow}{N_\uparrow + N_\downarrow} \approx 10^{-6}$.

The classical standpoint is similar to the Bloch-Torrey equations [28]. If a dipole $\overrightarrow{\mu} = (\mu_x, \mu_y, \mu_z)$ is placed in a magnetic field $\overrightarrow{B_0} = B_0 \overrightarrow{k}$, the turning force is equal to the rate of change of the angular momentum:

$$\frac{d\overrightarrow{\mu}}{dt} = \gamma \overrightarrow{\mu} \times \overrightarrow{B_0} \tag{2.3}$$

As, by convention, the magnetic field is aligned to the z axis, this leads to:

$$\begin{cases} \mu_x = \mu_{xy} \times \cos(\gamma B_0 t) \\ \mu_y = \mu_{xy} \times \sin(\gamma B_0 t) \\ \mu_z = \text{ constant } = \sqrt{\mu^2 - \mu_{xy}^2} \end{cases} \tag{2.4}$$

where μ_{xy} is constant.
The Larmor frequency can be defined as:

$$\omega_0 = -\gamma B_0 \tag{2.5}$$

The dipole is precessing around the magnetic field at the frequancy ω_0 as shown in figure 2.2.

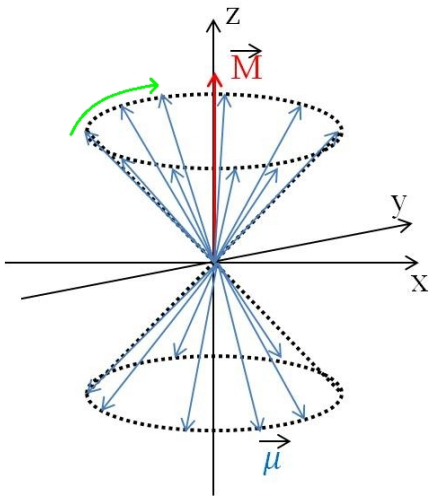

Figure 2.2: The orientation of magnetic dipole moments $\overrightarrow{\mu}$ that are precessing about an external magnetic field is shown here. The sum of all the dipoles gives the magnetization vector $\overrightarrow{M}$.

In a system of $\approx 10^{26}$ spins, the spins are not precessing in phase and, as a consequence, no macroscopic magnetisation in the (xy) plane can be observed as the external magnetic field is said to be on the z axis. However, the resonance effect of a radio frequency excitation pulse of electromagnetic radiation introduced in the next section induces a coherence and hence a magnetisation in this plane.

2.1.2 Resonance, Longitudinal and Transverse Relaxations

This precession is the equilibrium state as long as the magnetic field $\overrightarrow{B_0}$ is turned on. However, it can be disturbed with another magnetic field $\overrightarrow{B_1}$. In NMR experiments, $\overrightarrow{B_1}$ is perpendicular to the main magnetic field $\overrightarrow{B_0} = B_0 \overrightarrow{k}$ and is rotating at the resonance frequency (ie: Larmor frequency) ω_0: $\overrightarrow{B_1} = B_1(cos(\omega_0 t)\overrightarrow{i} + sin(\omega_0 t)\overrightarrow{j})$. The effect of this $\overrightarrow{B_1}$ magnetic field is to rotate the magnetisation vector around the rotating vector $\overrightarrow{x'}(t) = cos(\omega_0 t)\overrightarrow{i} + sin(\omega_0 t)\overrightarrow{j}$ during a specific time t (what is usually referred to as a pulse length) as shown in figure 2.3. For this reason, much of NMR is described in a rotating reference frame $x'y'z'$, rotating about z at the Larmor frequency.

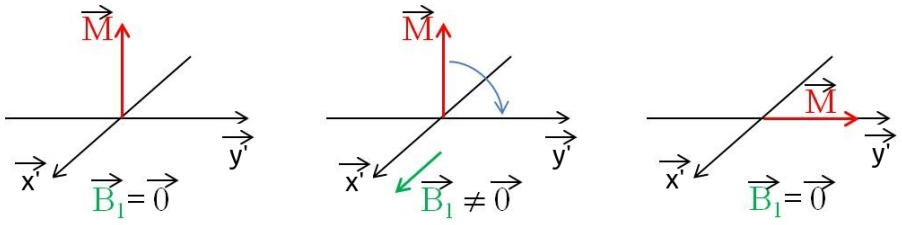

Figure 2.3: A perpendicular and rotating magnetic field $\overrightarrow{B_1}$ is turned on at time $t = 0$. As a consequence, the magnetisation vector is rotating until $\overrightarrow{B_1}$ is turned off (here after a rotation of angle $\frac{\pi}{2}$). This representation is made in the rotating frame.

The main idea of NMR is to apply such a pulse in order to disturb the equilibrium and initiate a coherent precession and then to let the magnetisation vector return to its equilibrium position: this phenomenon is the relaxation. There are two relaxation processes in such an experiment.

The first relaxation process is the transverse relaxation [29] (also called the spin-spin relaxation). When the pulse stops, the spins that were precessing coherently about $\overrightarrow{B_1}$ stop and they start to precess coherently about $\overrightarrow{B_0}$. They also experience a loss of coherence of precession in (xy) about $\overrightarrow{B_0}$ because of a local magnetic field that is not the same for each spin. Hence, some spins will precess faster than others until no clear orientation is favoured. This is characterized by a relaxation time called the spin-spin or transverse relaxation time T_2.

The second relaxation process is the longitudinal relaxation (also called the spin-lattice relaxation, the lattice referring to the environment where the spin is). When the pulse stops, the magnetisation vector is going to return to its equilibrium position. This is characterized by a relaxation time called the spin-lattice or longitudinal relaxation time T_1.

The local magnetic field has three origins. First, it is due to the inhomogeneity in the applied field. Appropriate experiments (for instance CPMG pulse sequences [30, 31]) overcome this problem. Second, it is due to spin-spin interactions (the field of a spin acting on another) that give some information about the spin dynamics. Third, it can be due to the heterogeneity of the sample magnetic susceptibility (this is the case in porous material); this can be seen as a special case of either of the other two.

Figure 2.4 shows the two relaxation mechanisms. A $\frac{\pi}{2}$-pulse is considered here.

These relaxation times can be computed. This is the object of the next section.

2.2 The BPP theory

BPP theory [11, 29, 32, 33] (named after Bloembergen, Purcell and Pound who first derived the analysis) gives the relaxation rates T_1^{-1} and T_2^{-1}, inverse of the relaxation times, as a linear combination of some specific values of the averaged spectral density of the spin-spin interaction (or, more loosely, the local magnetic field) function as it will be shown in the next section. This function (that is the Fourier transform of the correlation function) contains all the information necessary to describe the NMR relaxation. Actually, it relies on the study of the local magnetic field (B_{loc}) which varies according of the environment where the spin is moving and which can influence the energy state of the spin at the frequency of resonance.

All the relevant relaxation details of the system are recorded in the spectral density function $J^{(m)}(\omega)$, where m is the order of coherence describing the coherence between the magnetic quantum numbers m_s and ω is the experimental NMR frequency. $J^{(m)}(\omega)$ is the Fourrier Transform of the auto-correlation function and represents the average energy of the dipolar interaction of spins coupled to their varying local magnetic field $B_{loc}(t)$ as a function of time.

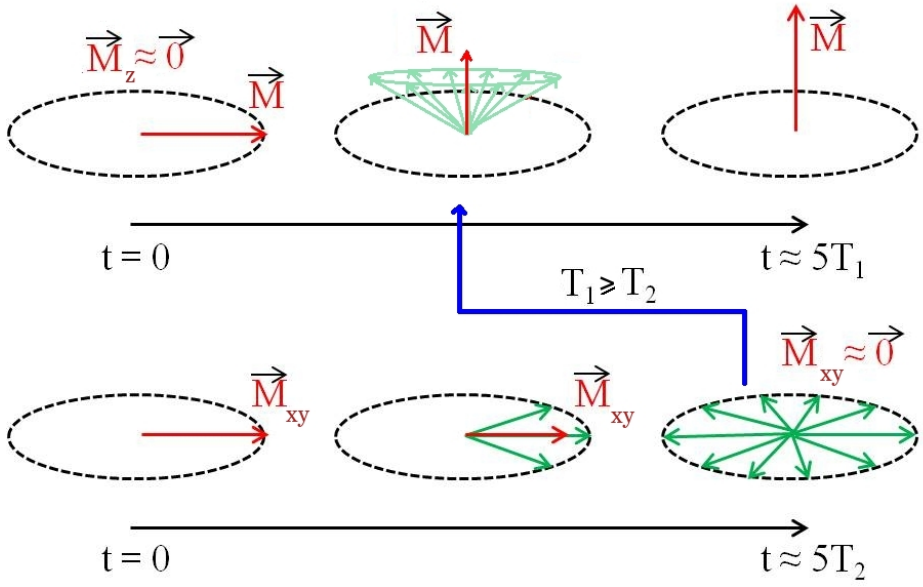

Figure 2.4: After a $\frac{\pi}{2}$-pulse, two relaxation processes occur. Top: classical picture of the spin-lattice relaxation; magnetisation vector (red) is returning to its original position in a typical time T_1 (ie: aligned to B_0. Bottom: classical picture of the spin-spin relaxation; the magnetic moments (green) coherence is less and less effective because of the effect of some local magnetic fields after a typical time T_2. The spin-spin relaxation is quicker than the spin-lattice relaxation as shown by the blue arrow ($T_2 \leq T_1$).

The relaxation times can then be generated thanks to the values of $J^{(m)}(\omega)$ at different specific frequencies.

The next sections will show how to generate the correlation function $G^{(m)}(t)$, the spectral density function $J^{(m)}(\omega)$ and the NMR relaxation times $T_{1,2}$.

2.2.1 Correlation Function and Spin Sets

The average correlation can be defined for a specific set of spin pair formed of a spin of type I and a spin of type J (nb: I can be equal to J). Such a function is calculated per spin and is noted $G^{(m)}_{I,J}(t)$. It is given by [29]:

$$G^{(m)}_{I,J}(t) = \left(\frac{\mu_0}{4\pi}\right)^2 \frac{4\pi}{5}\hbar^4\gamma_I^2\gamma_J^2 \left\langle \frac{\bar{Y}_2^{(m)}(\theta_{ij}(0),\phi_{ij}(0))}{r_{ij}^3(0)} \frac{Y_2^{(m)}(\theta_{ij}(t),\phi_{ij}(t))}{r_{ij}^3(t)} \right\rangle_{pair} \tag{2.6}$$

where μ_0 is the vacuum permeability, $\hbar$ the Planck constant divided by 2π, γ_I the gyromagnetic ratio of species I, t is time, $Y_2^m(\theta,\phi)$ is the spherical harmonic of order two, considering that $\overrightarrow{B_0} = B_0\,\overrightarrow{k}$, θ_{ij} and ϕ_{ij} are polar angles of vector $\overrightarrow{r_{ij}}$ between spin i and spin j with a norm of r_{ij} in such a reference frame. These parameters are shown in figure 2.5. $\bar{Y}$ is the complex conjugate of Y and $\langle\cdot\rangle_{pair}$ represents the average process over all the spin pairs [1].

[1] In practice, in the simulations, correlation functions can be generated from different initial times, hence, an average over all the different initial times can be done.

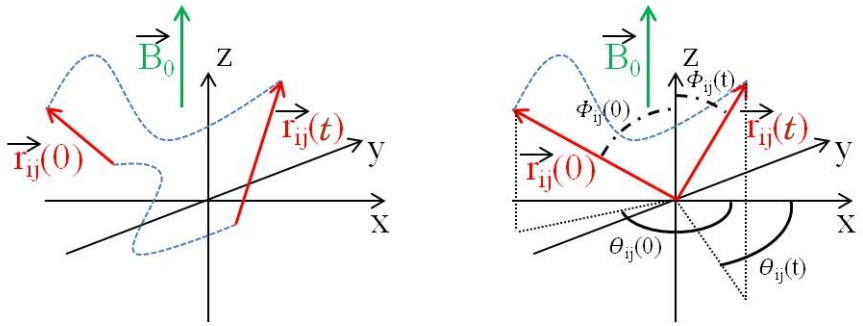

Figure 2.5: The spatial parameters used to generate $G^{(m)}_{I,J}(t)$ function, where t is time, are shown here: $\overrightarrow{r_{ij}}$ the vector between spins i and j, polar angles θ_{ij} and ϕ_{ij} at time $t = 0$ and $t > 0$ in the reference frame where $\overrightarrow{B_0} = B_0 \overrightarrow{k}$.

This expression can be highly simplified according to certain hypotheses. From now, the I and J indexes will be removed and $\langle\cdot\rangle_{pair}$ will be replaced by $\langle\cdot\rangle$ and the pre factor $\left(\frac{\mu_0}{4\pi}\right)^2 \frac{4\pi}{5}\hbar^4\gamma_I^2\gamma_J^2$ omitted in order to lighten the expressions.

If the equilibrium system is time reversal invariant, then [32]:

$$G^{(m)}(t) = G^{(-m)}(t) \tag{2.7}$$

Hence, thanks to this simplification, m can take only three values (0, 1 and 2). New constants can be defined:

$$\alpha^{(0)} = \frac{48\pi}{15} \quad , \quad \alpha^{(1)} = \frac{8\pi}{15} \quad , \quad \alpha^{(2)} = \frac{32\pi}{15} \tag{2.8}$$

This leads to:

$$G^{(m)}(t) = \alpha^{(m)} \left\langle \frac{\bar{Y}_2^{(m)}(\theta_{ij}(0), \phi_{ij}(0))}{r_{ij}^3(0)} \frac{Y_2^{(m)}(\theta_{ij}(t), \phi_{ij}(t))}{r_{ij}^3(t)} \right\rangle \tag{2.9}$$

If the average of $G^{(m)}(t)$ is taken over all the possible orientations of the main magnetic field $\overrightarrow{B_0}$ orientations, for a 2D, Quasi-2D [17] or 3D [34] system, the correlation function becomes:

$$G^*(t) = \left\langle \frac{P_2[\cos(\Phi)]}{r_{ij}^3(0) r_{ij}^3(t)} \right\rangle = \left\langle \frac{\frac{1}{2}(3\cos^2(\Phi) - 1)}{r_{ij}^3(0) r_{ij}^3(t)} \right\rangle \tag{2.10}$$

where P_2 is the Legendre Polynomial of order 2 (ie: $P_2(t) = \frac{1}{2}(3t^2 - 1)$) and Φ the angle between $r_{ij}(0)$ and $r_{ij}(t)$. It is interesting to note that the action of the spin pairs (i, j) and (j, i) have exactly the same influence in this formula because the cos function is even. Hence, in practice, the average is only made on half the spin pairs in the system. The m index can be simplified as:

$$\forall m \in \{0, 1, 2\} \ , \ G^*(t) = \frac{4\pi G^{(m)}(t)}{\alpha^{(m)}} \tag{2.11}$$

Note that the average can be made over all the possible orientations for the magnetic field

$\overrightarrow{B_0}$ because of the nature of cement [12, 35]. Indeed, locally, the cement structure is ordered but macroscopically, this order is lost: the orientation of the cement crystal layers is random. Hence, the angle between these layers and the applied magnetic field is random. Such an average is called the "powder average".

All these approximations are valid for this work. Hence, the only function that one needs to generate using numerical simulations is the $G^*(t)$ correlation functions (or $G^*_{I,J}(t)$ to refer to the spin populations I and J).

2.2.2 Spin Selection, Homo/Heteronuclear and Intra/Intermolecular Interaction, Relaxation Times Calculation

The $G^*_{I,J}(t)$ function estimates the correlation, per spin, between two sets of spins I and J. There are different ways to consider these two populations in this study. The first one is to consider that I and J refer to the same population, for instance: all the protons in a bulk water system. The second way is to consider that I and J refer to two subsets of a same population with different spatial properties, for instance: the protons trapped on a crystal surface (I) and the free protons in bulk water (J). The two previous possibilities are about the same type of spins, are homonuclear interactions and are noted $I-I$. The third option is to consider two populations of different spin type, for instance: the interaction between the water protons (I) and some iron impurities (J) embedded on a crystal surface [29, 36] (nb: this interaction will be really relevant to this study because this is the case in cement paste and that $\gamma_{Fe^{3+}} \approx 658.21\gamma_{proton}$). This third possibility is heteronuclear interaction and is noted $I-S$.

These distinctions are important since the expressions of T_1 and T_2 are different for $I-I$ and $I-S$ as it will be shown in equations 2.13 and 2.14.

A further categorisation also allows to consider the intra and inter-molecular interactions as shown in figure 2.6 for proton spins in a water system:

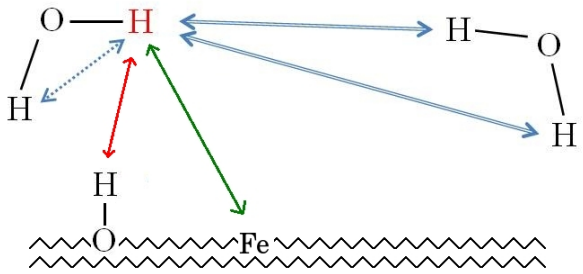

Figure 2.6: A water proton can interact with the second proton in the same water molecule (dash blue line), with a proton in another water molecule (double solid blue line, with a surface Fe (solid green line) or with a surface hydroxyl O-H (solid red line).

Finally, considering these kinds of interactions, different correlation functions for homonu-

clear interactions $G^*_{I-I}(t)$ and for heteronuclear interactions $G^*_{I-S}(t)$ can be calculated. [2] These correlation functions can also be split between their intra-molecular part $G^*_{I-X,rot}(t)$ and inter-molecular part $G^*_{I-X,trans}(t)$ (where X refers to I or S). The intra-molecular part only represents a rotational behaviour and inter-molecular part is composed of both translational and rotational behaviour but, at long times, the intra-molecular part can be associated mainly to a translational behaviour.

Then, each G^* function can be Fourier transformed to generate the spectral density functions J^*.

$$J^*(\omega) = \int_{\mathbb{R}} G^*(t) e^{j\omega t} dt \tag{2.12}$$

Finally, the averaged relaxation times T_1 and T_2 can be written as the inverse of a sum of weighted values of the spectral density function [29]:

$$\begin{cases} \left\langle \frac{1}{T_{1,I-I}(\omega_I)} \right\rangle = \frac{1}{5} C_{I-I} [J^*_{I-I}(\omega_I) + 4J^*_{I-I}(2\omega_I)] \\ \\ \left\langle \frac{1}{T_{2,I-I}(\omega_I)} \right\rangle = \frac{1}{10} C_{I-I} [3J^*_{I-I}(0) + 5J^*_{I-I}(\omega_I) + 2J^*_{I-I}(2\omega_I)] \end{cases} \tag{2.13}$$

and

$$\begin{cases} \left\langle \frac{1}{T_{1,I-S}(\omega_I)} \right\rangle = \frac{1}{3} C_{I-S} [3J^*_{I-S}(\omega_I) + 7J^*_{I-S}(\omega_S)] \\ \\ \left\langle \frac{1}{T_{2,I-S}(\omega_I)} \right\rangle = \frac{1}{6} C_{I-S} [4J^*_{I-S}(0) + 3J^*_{I-S}(\omega_I) + 13J^*_{I-S}(\omega_S)] \end{cases} \tag{2.14}$$

respectively for $I-I$ and $I-S$ interactions where ω_I and ω_S refer to spins I and S respectively and where the two coefficients C_{I-I} and C_{I-S} that were previously omitted from equation 2.6 are given by:

$$\begin{cases} C_{I-I} = \left(\frac{\mu_0}{4\pi}\right)^2 \hbar^4 \gamma_I^4 I(I+1) \\ \\ C_{I-S} = \left(\frac{\mu_0}{4\pi}\right)^2 \hbar^4 \gamma_I^2 \gamma_S^2 S(S+1) \end{cases} \tag{2.15}$$

where I and S are the values of spins I and S.

These sums are for one kind of interaction (ie $I-I$ or $I-S$) but the actual observed rate the sum of all the rates. For instance, for $T_{1,I}$:

$$\frac{1}{T_{1,I}} = \frac{1}{T_{1,II}} + \frac{1}{T_{1,IJ}} \tag{2.16}$$

2.2.3 Behaviour of T_1 and T_2 in Bulk

For simple Brownian motion and rotation, such as in bulk water, the auto-correlation function is a simple decaying exponential and the spectral density function is proportional to a Lorentzian function [37, 38]:

$$J^*(\omega) \propto \frac{2\tau_c}{1+\omega^2\tau_c^2} \tag{2.17}$$

[2] In this study, only the proton-iron heteronuclear interaction is considered but this could be used for other couples of type of spins

where τ_c is the correlation time of the motion in the bulk system.

With equation 2.13, the dependence of $T_{1,2}$ on the correlation time, which describe the molecular motion of the system, can be evaluated and plotted as in figure 2.7. At the Larmor frequency ω_0, the behaviour of T_1 and T_2 can be split into two different regimes. When $\omega_0\tau_c \ll 1$, this is the fast motion regime where both T_1 and T_2 decrease when τ_c increases. When $\omega_0\tau_c \gg 1$, this is the slow motion regime where T_1 increases while T_2 decreases when τ_c increases. The minimum of T_1 is for $\omega_0\tau_c = 0.62$ [39]. BPP theory does not work when $\gamma\Delta B_{loc}\tau_c \approx 1$, where ΔB_{loc} is the spread of the local magnetic field. In this case, the dipolar interactions do not average to zero over time: this is the rigid lattice limit. This behaviour is summarized in figure 2.7.

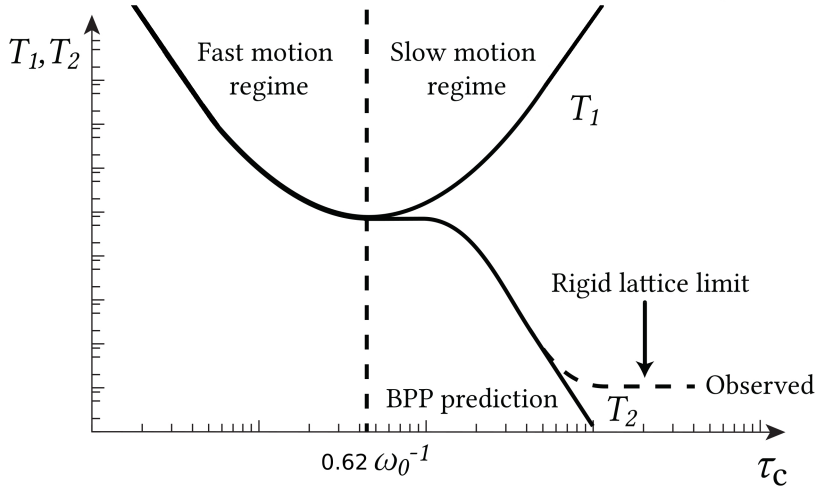

Figure 2.7: The behaviour of NMR relaxation times T_1 and T_2 is a function of the correlation time for a bulk system. This figure is extracted from [40].

2.3 Basics of Diffusion

The diffusion process is strongly linked with the concept of Brownian motion [41]. If an ensemble of particles (for instance protons) in an isotropic and homogeneous medium is considered, it is difficult to look at a single trajectory. Indeed, for a very short time, the particle is free (ie: the ballistic trajectory) but at a certain point, it will encounter another particle. Because of the repulsion effect, these particles will move in another direction until they encounter other particles etc... (the diffusive trajectory).

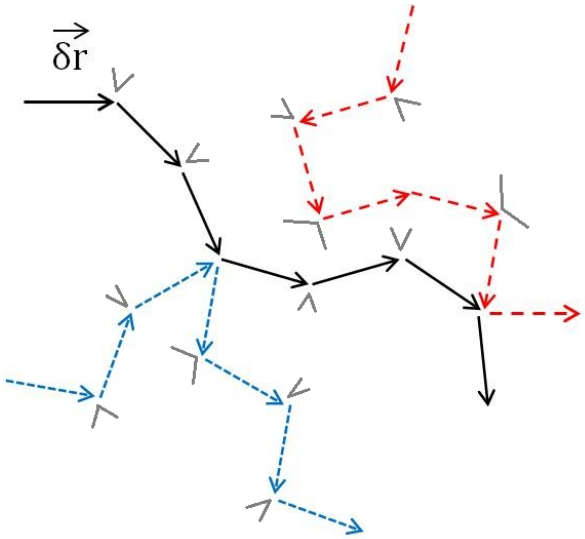

Figure 2.8: 2D Brownian motion for three particles that move of a vector distance $\overrightarrow{\delta r}$ in a time δt. This displacement is randomly oriented: the ballistic behaviour of such a process is quickly lost to let the diffusion rule this displacement. These three particles trajectories are shown in solid black line, blue dash line and red dash line. Grey solid lines represent the local trajectories of other particles before and after collision.

Because of the enormous amount of information needed to track all the particles, the problem can be treated with probabilities and, more precisely, because of the ignorance of the state of each particle at a time t, such a motion can be characterized as random: that is as a stochastic process (random with time).

During the ballistic period, the displacement of the particle is proportional to time. During the diffusive period, that is not the case, indeed the square of the displacement is then proportional with time and the proportionality coefficient is a function of the dimensionality of the system:

$$\left\langle x^2 \right\rangle = 2dDt \tag{2.18}$$

where x is the particle displacement, d is the dimension of the system (1, 2 or 3), t is time and D is the diffusion coefficient.

It can be interesting to notice that the diffusion coefficient depends on temperature, if the temperature increases the velocity of particles will also increase and *de facto* the diffusion coefficient will increase too. It also depends on other parameters, but this is not in the scope of this study.

Finally, the probability a particle moves a distance x in one direction during a time t can be defined as:

$$p(x,t) = \frac{1}{\sqrt{4\pi Dt}} e^{-\frac{x^2}{4Dt}} \tag{2.19}$$

The shape of such a Gaussian distribution is shown in figure 2.9 for different values.

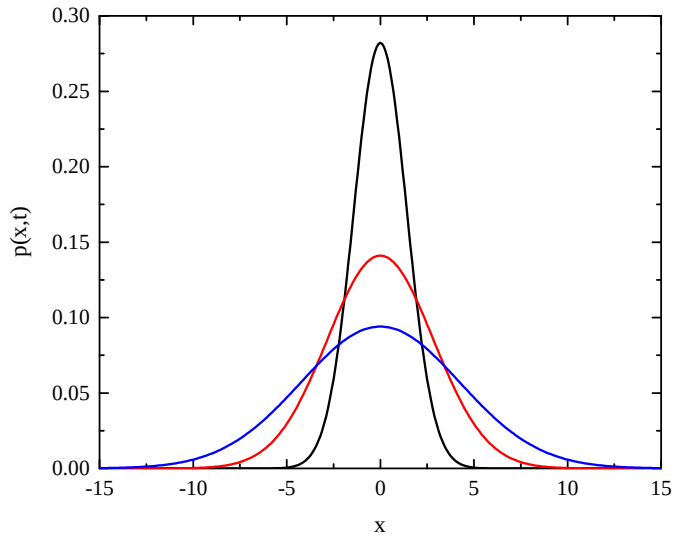

Figure 2.9: The Gaussian distribution shape is shown here for different time values ($t = 1$ in black, $t = 4$ in red and $t = 9$ in blue in arbitrary units) with $D = 1$ to show its evolution with time for a particle at $x = 0$ at $t = 0$.

This equation is a specific case of the probability a particle is at a position x at a time t knowing that it was at a position x_0 at a positive time $t_0 < t$:

$$p(x_0, t_0|x_t, t) = \frac{1}{\sqrt{4\pi D(t - t_0)}} e^{-\frac{(x_t - x_0)^2}{4D(t-t_0)}} \tag{2.20}$$

This formula is valid for only one dimension, but in dimension d, it is only necessary to multiply the probabilities in each dimension in such a way that:

$$P(\overrightarrow{x}, t) = \prod_{i=0}^{d} p(x_i, t) \quad , \quad \overrightarrow{x} = (x_0, x_1, \cdots, x_d) \tag{2.21}$$

2.4 Exchange Theory and Desorption

In this study, the discussed models can be seen as a system (say Ω) composed of different spin reservoirs. The spins within each of them can exchange. For instance, water may be in a large gel pore or in small interlayer spaces and individual molecules may move/exchange by diffusion from one to the other as shown in figure 2.10.

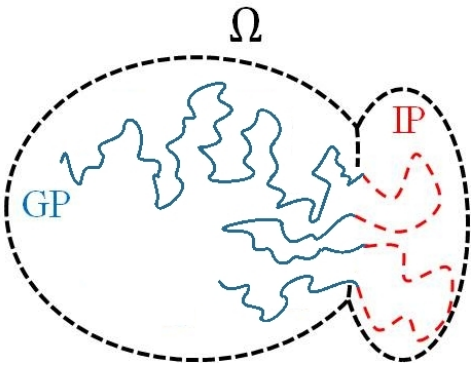

Figure 2.10: The system Ω shown here is composed of a gel pore GP (big pore) and an interlayer pore IP (small pore). A water molecule in one can move to the other as its trajectory shows: solid blue line in the GP and dash red line in the IP.

2.4.1 Simple Theory of Population Exchange

The idea here is to consider a simple model of exchange. Populations are defined by a number (n_I: the amount of elements in population I) and the exchange between two populations is defined by another number ($k_{I,J}$: the exchange rate from population I to population J). Two basic systems are discussed here.

The first system is only composed of two populations that are exchanging in both directions as shown in figure 2.11. The only information known is the populations at $t = 0$: n_A^0 and n_B^0. Note that there is no exchange with any other populations (closed system).

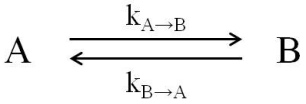

Figure 2.11: Two populations A and B respectively composed of n_A^0 and n_B^0 spins at $t = 0$, n_A and n_B at a time $t > 0$ are exchanging with exchange rates $k_{A\to B}$ and $k_{B\to A}$.

During a small time interval dt, population A gives $k_{A\to B} \cdot n_A \cdot dt$ spins to population B and population B gives $k_{B\to A} \cdot n_B \cdot dt$ spins to population A. Hence, these variations of the spins in populations A and B leads to a system of differential equations:

$$\begin{cases} \frac{dn_A}{dt} = -k_{A\to B}n_A + k_{B\to A}n_B \\ \\ \frac{dn_B}{dt} = k_{A\to B}n_A - k_{B\to A}n_B \end{cases} \tag{2.22}$$

Because the system Ω is closed, $\forall t,\ n_A(t) + n_B(t) = n_A^0 + n_B^0 = N_\Omega$. The solutions of these equations are two decaying exponentials with offsets:

$$\begin{cases} n_A(t) = C_1 e^{-Kt} + C_2 \\ \\ n_B(t) = -C_1 e^{-Kt} + C_3 \end{cases} \tag{2.23}$$

where

$$\begin{cases} K = k_{A\to B} + k_{B\to A} \\ C_1 = \frac{k_{A\to B} n_A^0 - k_{B\to A} n_B^0}{K} \\ C_2 = \frac{k_{B\to A}}{K} N_\Omega \\ C_3 = \frac{k_{A\to B}}{K} N_\Omega \end{cases} \tag{2.24}$$

The second system is only composed of one population A that contains n_A^0 elements at time $t = 0$. Every time interval δt, the population A is giving $k_{A\to X}$ to the rest of the system Ω ($X = \Omega - A$), but the rest of the system does not supply population A as shown in figure 2.12.

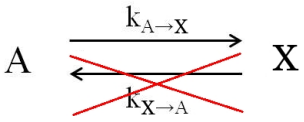

Figure 2.12: A population A composed of n_A^0 spins at $t = 0$ and n_A at a time $t > 0$ is giving spins to another population X with exchange rate $k_{A\to X}$. Population X does not give any spin to population A, which can be formally seen as an exchange rate $k_{X\to A} = 0$.

This leads to a much simpler differential equation:

$$\frac{dn_A}{dt} = -k_{A\to X}\ n_A \tag{2.25}$$

The solution of such an equation is a simple decaying exponential with no offset:

$$n_A(t) = n_A^0 e^{-k_{A\to X} t} \tag{2.26}$$

For instance, A can represent the water ^{1}H spin population on the C-S-H surface at time $t = 0$ and X the bulk zone and $n_A(t)$ is then the number of the *original* population remaining at time t.

Finally, in the general case, in a system of $p + 1$ populations, if a population composed of n_I^0 spins at $t = 0$ is exchanging with a set P composed by p other populations, it can be shown mathematically that the number of spins n_I at time $t > 0$ is a sum of p exponentials plus an offset:

$$n_A(t) = C_0 + \sum_{l=1}^{p} C_l e^{-\frac{t}{\tau_l}} \tag{2.27}$$

where all the τ_l and C_l are functions of the exchange rates $k_{i\to j}$, $i \neq j$, $(i, j) \in P$, between the different populations and the initial number of spins in these populations n_i^0, $i \in P$.

2.4.2 Population Exchange and Gaussian Propagator

If a population A is defined as the set of spins in a specific spatial zone (say $x_0 \in [-a, a]$) at a time $t = 0$, it is interesting to look at the probability a spin in population A is in this same

zone ($x_t \in [-a, a]$) at a time $t > 0$. This probability is the same as the desorption probability (with previous notations, it would correspond to the curve $\frac{n_A(t)}{n_A^0}$). It is given by thanks to the Gaussian propagator:

$$\mathcal{P}(t) = \int_{x_t=-a}^{a} \int_{x_0=-a}^{a} \frac{p(x_0, 0|x_t, t)}{2a} dx_0 dx_t = \text{erf}\left(\sqrt{\frac{a^2}{Dt}}\right) + \sqrt{\frac{Dt}{\pi a^2}}(e^{-\frac{a^2}{Dt}} - 1) \tag{2.28}$$

where D is the diffusion equation of spin population A. The factor $\frac{1}{2a}$ was included in order to account the uniform distribution of positions of a spin at time $t = 0$ in the zone $x \in [-a, a]$.

This will be of interest for theoretical fits to numerical simulation data for method validation using bulk water in chapter 4 section 4.2.2 but it will not be used elsewhere because the models that will be discussed later will not respect the homogeneous and isotropic hypotheses. The typical shape of this curve for $a = 1$ and $D = 1$ is shown in figure 2.13:

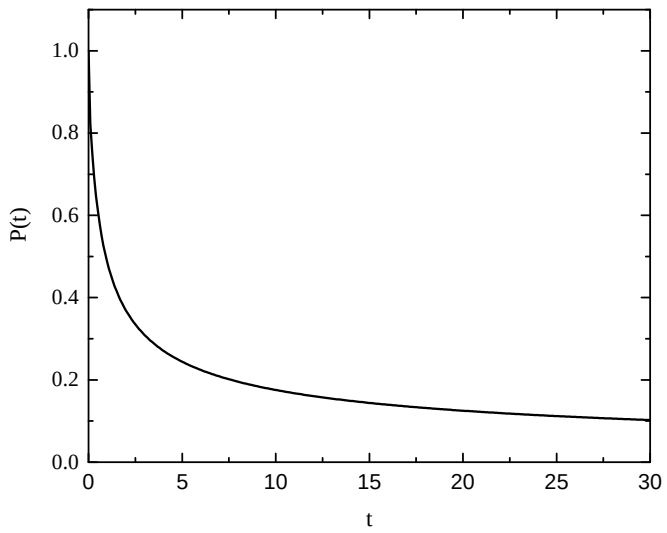

Figure 2.13: The probability a spin, in bulk, that was at time $t = 0$ in the space volume defined by the interval [−a,a] is in the same interval at time $t > 0$ is shown here with $a = 1$ and the diffusion coefficient $D = 1$.

2.4.3 Fast exchange and NMR Relaxation Times

A key element of NMR theory in population exchange is the fast exchange model [42]. If a system of two populations of spins, say A and B, is considered, the effect of the exchange of these two populations can influence the relaxation times. Indeed, if there is no exchange or a very slow exchange ($k << 1$, for instance some protons can exchange in a pore P_A and a pore P_B with no connection between the two pores or a very tiny one), the experimentalist will measure two different values for the relaxation times T_A and T_B. However, if the two populations experience a fast exchange ($k >> 1$, for instance some protons weakly trapped on

a surface and bulk water protons that move freely [43]), the experimentalist will only measure one relaxation time T_{msr} that is a weighted average of the two pores relaxation times:

$$\frac{1}{T_{msr}(\omega)} = \frac{N_A}{N_A + N_B}\frac{1}{T_A(\omega)} + \frac{N_B}{N_A + N_B}\frac{1}{T_B(\omega)} \tag{2.29}$$

where N_A and N_B are respectively the number of spins of populations A and B. If populations A and B refer respectively to the bulk and the surface layer populations, this equation can be written as a function of the crystal surface S, the surface layer thickness ϵ and the gel pore/bulk volume V. This gives a good way to estimate the pore size [36].

$$\frac{1}{T_{msr}(\omega)} = \frac{V - \epsilon S}{V}\frac{1}{T_{bulk}(\omega)} + \frac{\epsilon S}{V}\frac{1}{T_{surf}(\omega)} \approx \frac{\epsilon S}{V}\frac{1}{T_{surf}(\omega)} \tag{2.30}$$

The last approximation comes from the fact that the surface layer volume is negligible versus the bulk volume ($V >> \epsilon S$) and that the bulk relaxation time is negligible versus the surface layer one as it will be shown in the next section ($T_{surf} >> T_{bulk}$). Hence, if the shape of the pore is said to be a sphere or a cylinder for instance, the ratio $\frac{\epsilon S}{V}$ can be used to estimate the pore size. Note that these relaxation times can be either the spin-lattice relaxation time (T_1) either the spin-spin relaxation time (T_2).

2.5 Korb's Model of Surface Relaxation

Korb's model [12] was established to analyse NMR relaxometry in a system of spins composed of a surface layer (trapped spins) and a bulk zone (free spins). It gives a value for the correlation function $G^*(t)$ and is usually relevant for systems where the relaxation mechanism is mainly due to the interaction between some static spins (S) uniformly distributed on a crystal surface and other spins (I) moving in a 2D random walk in the same surface. In this study, the moving spins are water protons and static spins are iron impurities embedded in the cement layers surface. Note that the probability a water proton encounters an iron impurity is greater in 2D than in 3D because of the properties of the random walk. This implies that $G^*(t) \approx G^*_{I-S}(t)$ and $G^*_{I-I}(t) \approx 0$. Indeed, $\gamma_{Fe^{3+}} \approx 658.21\gamma_{proton}$ and the pre factor $\left(\frac{\mu_0}{4\pi}\right)^2 \frac{4\pi}{5}\hbar^4\gamma_I^2\gamma_J^2$ in equation 2.6 explain that $G^*_{I-I}(t)$ can be neglected. A constraint in the model is that the moving spins cannot approach the static spins closer than a distance δ that corresponds to the typical size of a water molecule as shown in figure 2.14, a parameter that has a influence on the correlation function. However, the primary contribution to G^* and hence $T_{1,2}$ is due to the $I-S$ interaction between the static spins S and the I spins contained in the same layer. Indeed, for $t >> 1$, $G^*_{I-S,surface}(t) \to \frac{1}{t}$ whereas $G^*_{I-S,bulk}(t) \to \frac{1}{t^2}$. As a result, $G^*(t) \approx \frac{A}{t}$ (A is a constant). The problems come when this correlation function is to be Fourier transformed simply because $f(x) = \frac{1}{x}$ cannot be Fourier transformed. In order to avoid this problem, the model assumes that some moving spins I desorb from the surface and are then removed from the calculation with a typical desorpton time τ_s. Finally, the model gives a correlation function as:

$$G^*_{I-S,Korb}(t) = \frac{A}{t}\left[\frac{e^{-\frac{t}{\tau_s}} - e^{-\frac{t}{\tau_m}}}{\frac{1}{\tau_m} - \frac{1}{\tau_s}}\right] \tag{2.31}$$

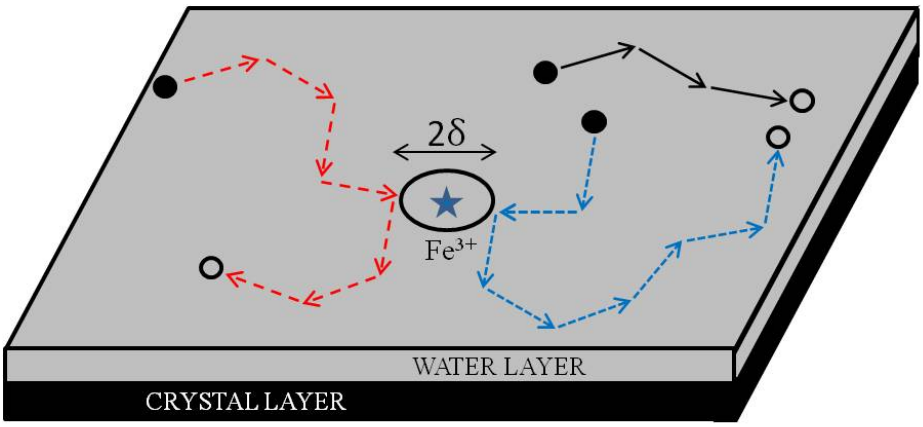

Figure 2.14: Korb's model focuses on the first surface proton water spin layer. Three trajectories are shown. A full black disk represent the absorption of a water molecule whereas an empty black disk represent its desorption. In this model, Fe^{3+} ions are embedded in the crystal surface and water molecules cannot penetrate a volume around it specified by a disk of radius δ. Desorption is ruled by the surface desorption time τ_s and the surface diffusion is ruled by the hopping time τ_m.

where τ_m is the typical displacement time for a moving spin on the surface ($\tau_m = \frac{\delta^2}{4D}$, D is the diffusion coefficient of spins I on the surface), τ_s the surface desorption time and A a constant. This correlation function can be Fourier transformed which allows to calculate the relaxation times.

2.6 An Improved Model

An improved model has been developed by Faux et al. thanks to the results of this study. It will be discussed in chapter 6 section 6.5 and more details are provided in an appendix.

2.7 The Arrhenius Law

The influence of temperature on water transport in C-S-H nanostructure is also studied in this work. Indeed, diffusion, desorption and NMR relaxation times can change with temperature. The Arrhenius law is used to quantify these changes.

The Arrhenius equation is a formula that links the constant rate of a reaction k with temperature T:

$$k = Ae^{-\frac{E_A}{RT}} \tag{2.32}$$

where A is a prefactor, E_A is the activation energy (in J), R is the gas constant ($R = 8.31$ J.K^{-1}.mol^{-1}) and T is temperature (in K). This law is also valid for diffusion coefficients [44]. Moreover, since the desorption times as defined in equations 2.22 and 2.25 is the inverse of the exchange rates, desorption times follow a similar Arrhenius law:

$$\tau_s = Ae^{+\frac{E_A}{RT}} \tag{2.33}$$

This is the same for the correlation time τ_c of molecular motion that causes relaxation. According to BPP theory, the relaxation rates are proportional to the spectral density functions and for simple Brownian diffusion (in bulk system) are as written in equation 2.12:

$$\frac{1}{T_1} \propto J(\omega) \propto \frac{2\tau_c}{1+\omega^2\tau_c^2} \tag{2.34}$$

The NMR relaxation time T_1 is a function of τ_c and shows a minimum for $\omega_0\tau_c \approx 1$ where ω_0 is the Larmor frequency, as shown in figure 2.7. Two behaviours can be seen:

$$\omega_0\tau_c \ll 1 \implies \ln\left(\frac{1}{T_1}\right) = C + \frac{E_A}{RT} \quad \text{and} \quad \omega_0\tau_c \gg 1 \implies \ln\left(\frac{1}{T_1}\right) = C - \frac{E_A}{RT} \tag{2.35}$$

where C is a constant.

Chapter 3

Methodology

The purpose of this chapter is to describe the simulation technique and method of data analysis used in this work. Before a brief description of the different simulation methods that could be considered for use in this study, the conceptual overview of the cement structure of interest will be presented. Then, the software code used for the chosen simulation method (Molecular Dynamics) will be explored in more detail. Finally, how the analysis of water dynamics is used for NMR relaxation calculations will be highlighted.

3.1 Preamble: Conceptual Cement Structure at the Nanoscale

First, it is imperative to identify the cement nanostructure model that will be used. This description is not specially about the chemical composition, rather just about the structure itself. Nuclear magnetic resonance relaxation experiments show that cement is a porous medium with a discrete distribution of pore sizes. At the nanoscale, within the active C-S-H phase of the gel, there are two pore types: the inter-layer pore ($\approx$ 1 nm) and the gel pore ($\approx$ 3.5 nm). The inter-layer spaces occur between sheets of calcium and oxygen atoms sandwiched with planes of silica tetrahedra either side. The planes are locally ordered (semi-crystalline) at this scale. Gel pores occur between regions of locally aggregated sheets [45]. This information leads to the schematic structure shown in figure 3.1.

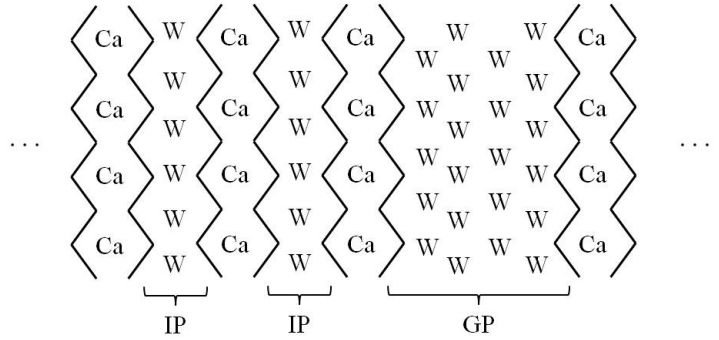

Figure 3.1: The schematic cement nanostructure is composed of two kind of pores: the interlayer pore (IP) and the gel pore (GP). "W" stands for water molecules, Ca stands for calcium ions and the broken line stands for SiO_2 tetrahedral silicate chains.

For the purpose of the validation of the different methods that will be explored in chapters 4, 5, 6, 7 and 8, a pure bulk water system is introduced. This system is a box full of water molecules. Such a system is homogenous and isotropic.

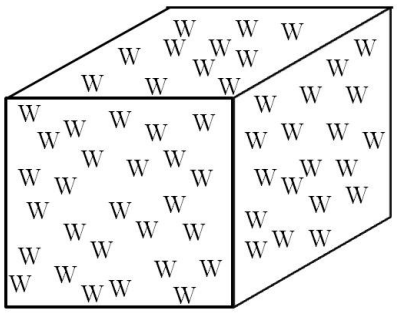

Figure 3.2: Bulk water system is a simulation box full of water molecules (W).

3.2 Simulation Techniques for Water Dynamics Analysis

Different methodologies can be used to study water dynamic properties. However, their range of action is limited by the time scales and length scales of interest in the study.

3.2.1 Density Functional Theory

Density Functional Theory [46] (commonly called DFT) is an *ab initio* quantum method that solves the Schrödinger equation for a N-body system comprising many atoms. The number of equations to solve is 3N but the efficiency of this method relies on the fact that only the electron density is considered and then the number of equations to solve reduces to just 3. Although it is computationally very accurate when compared to experiment, the main drawback of such a method is its computational cost: a very long time is needed to generate even short trajectories for a few hundreds of atoms.

Jennite and tobermorite crystals are often considered as analogues of C-S-H and hence are often studied. For instance, S. V. Churakov et al [47] investigated the protonation scheme and the hydrogen bond connectivity in the structure of jennite using DFT in order to compare it to Bonaccorsi et al protonation scheme [48] that was based on spectroscopic studies, they confirmed the scheme proposed by Bonaccorsi.

3.2.2 Thermodynamics

Thermodynamics provides useful information about the phase composition of a cement given a starting mixture of anhydrous materials and water. However, it does not give information about the nano structure. It is interesting for the understanding of cement science and in this case especially for the Fe^{3+} surface density but it is not applicable to the main purpose of this study.

B. Lothenbach et al [49] designed a thermodynamic model of the composition of the phase assemblage and the pore solution of hydrated Portland cements. It could be used to study the influence of composition and temperature on the hydrated assemblage and on the composition of the pore solution. For instance, it could be shown that Portland cements have a ratio $Al_2O_3/SO_3 > 1.3$. It could also show above 50°C, monosulphate and monocarbonate are present. Moreover, it gives a good correlation between porosity and measured compressive force.

D. A. Kulik et al [50] coded the GEMS-PSI package (GEMS for Gibb Energy Minimisation Selector) in order to calculate many interesting properties such as sorption, co-precipitation, re-crystallisation and other thermodynamics properties. This code was developed by PSI (Paul Scherrer Institute close to Zurrich) and was used extensively in studies related to nuclear waste disposal. This package is still in development: for instance, G. D. Miron and D. A. Kulik [51] coded the GEMSFITS package that was used to fit internally consistent input parameter of the GEM models against various types of experimental data.

3.2.3 Molecular Dynamics (MD) Simulations

Molecular Dynamics [52] is a simulation technique that solves numerically Newton's law of motion for a N-body system of many atoms. It considers the initial configuration of these N atoms and the different interactions between them. A set of coordinates of the atoms $\mathcal{C}(t+\delta t)$ at a discrete time $t+\delta t$ is a function of their coordinates $\mathcal{C}(t)$ at time t ($\mathcal{C}(t+\delta t) = f[\mathcal{C}(t)]$) as shown in figure 3.3.

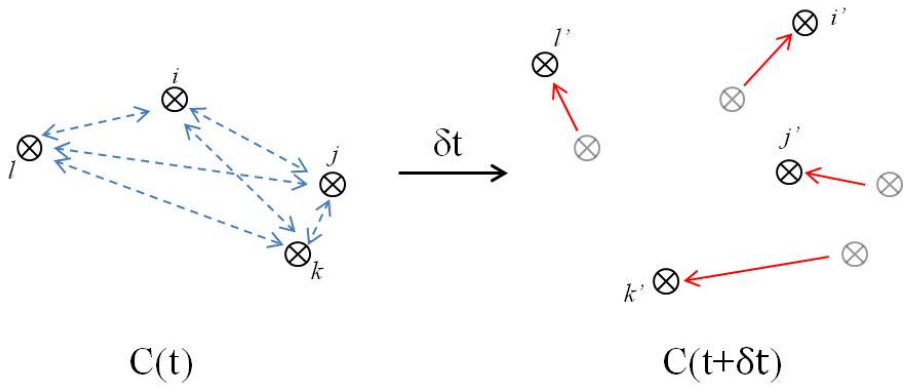

Figure 3.3: Molecular Dynamics simulations descritise the Newton's law of motion and generate the coordinates of an ensemble of atoms at a time $t+\delta t$ as a function of their coordinates at time t and the interaction between all the atoms.

The relationship between these two sets of coordinates is directly taken from the discretisation of Newton's equation $\sum_{ext} \overrightarrow{F}(t) = -\vec{\nabla}U = m\frac{\overrightarrow{d^2r}}{dt^2}$, where $\overrightarrow{F}(t)$ is the force applied to the considered element, U is the potential related to this force, m is its mass, $\overrightarrow{r}$ is its position and $\frac{\overrightarrow{d^2r}}{dt^2}$ its acceleration.

The typical timescale of such a simulation time on a good desktop computer is $\approx$ 10ns for a number of atoms of the order of 10^3 to 10^4. MD can also give useable atomic trajectories. Note that the trajectories generated this way are not strictly correct. Indeed, even if optimized integration schemes such as the Verlet leapfrog algorithm [52] are used, the timestep δt of such a simulation involves computational errors (this scheme is accurate to the second power of the time interval δt). Another source of errors is the approximations in the potentials that are fitted to simple formulae. However it generally gives good averaged results.
Notwithstanding these problems, the analysis of the trajectories can lead to the observation of dynamics over ns timescales for reasonable system sizes (nm) and despite a less accurate description of the system than with DFT, MD generates coordinates for a time long enough for the purpose of this research.

A. G. Kalinichev et al [53] used MD simulations to look at the behavior of water close to the surface. He investigated more precisely the water structure in nano-confinement and at fluid/solid interfaces, especially on the surface of tobermorite. These simulations give information on the structure, the dynamics and the energetics of these water molecules. For tobermorite, he found a strong structuring of water in the channels between the silicate chains. He also could see such structures above the surface because of a H-bond network. He could finally calculate a diffusion coefficient for the surface water that was close to that measured experimentally.

3.2.4 Dynamic Monte Carlo Simulations

Dynamic Monte Carlo (MC) simulations [52] are a class simulation method based on the probability an atom in at a position r on a lattice being able to move to another position $r+\delta r$ in a time δt. In practice, in 3D for a surface centered lattice, the atom in a lattice voxel can go to one of its 6 neighbour voxels or stay in its current position (δr can be equal to 0 or a , where a is the lattice unity). The probability of displacement is a function of the local environment. In bulk, the diplacement is equiprobable in all the directions (homogeneous) whereas close to a crystal surface, this is not the case. This hopping process is constrained by whether or not the target voxel is occupied by another atom. The typical time τ and length scales associated with such a simulation are related by the diffusion coefficient ($\tau_m = \frac{\delta r^2}{2nD}$ where D is the diffusion coefficient and n is the dimensionality of the system) or by the desorption time τ_s if the atom goes to or from a surface.

The MC technique is interesting because it can access a larger number of atoms and a longer timescale than MD. However, it needs a set of parameters usually derived from experimental or lower level simulation data). The drawback is a lack of precision of the displacement at small distances due to the discretisation of the lattice.

N. C. Howlett et al [40] used MC simulations in quasi-two dimensional pores C-S-H models in order to understand in a better way the validity of analytical models of water NMR relaxation and dynamics in cement pastes. He used different pore sizes and surface conditions such as Fe^{3+} impurities density embedded in the surface. His work demonstrated the validity of Faux's analytical results that showed the limitations of Korb's model of relaxation in cement pastes.

A. G. Kalinichev and S. V. Churakov [54] also used MC simulations in order to examine the structure of supercritical water and get some information about the formation of small molecular clusters in high temperature water vapor. More precisely, they investigated the statistics of the size and topolgy distribution of hydrogen-bonded water clusters over wide ranges of temperatures and densities. They found that H-bonded molecular clusters containing open chain-like or tree-structures are much more present than clusters containing cyclic ring-like elements that were predicted by *ab initio* calculations.

3.2.5 Fluid Dynamics Simulations

Fluid dynamics simulations are useful to understand meso/macroscopic behavior of water in cement pores and are based on continuum mechanics expressed in differential forms such as the Navier Stokes or diffusion equations. Different methods are available to solve such a problem. One is the Lattice Boltzmann (LB) method [55] that has been used in related projects. LB uses fictitious particles to simulate a fluid. These particles are able to propagate and to collide over a discrete lattice. Such a method can deal with complex boundary conditions which is the case for cement meso and micro structures.

M. Zalzale et al [56] used LB simulations to investigate the permeability of microstructures of cement pastes (based on numerical models like CEMHYD3D [57] and μIC [58]). He found that the permeability decreases with increasing hydration and decreasing water to cement ratio in agreement with experiment (even if the simulated permeability is larger than the experimental one). He also investigated the liquid/vapor capillary adsorption and desorption isotherms.

3.3 Molecular Dynamics using DL_POLY

In this study, Molecular Dynamics simulations will be used. It is the most effective method for studying water dynamics properties in cement at the nanoscale. It is clearly less accurate and detailed than Density Functional Theory and cannot reach the same time/length scale as Monte Carlo simulations but it is a good compromise.

Open-access and commercial software packages exist to perform MD simulations. Examples include LAMMPS [59], Amber [60], GROMACS [61] and DL_POLY [62]. DL_POLY was selected because there is a huge active community in the UK who uses this stable package. Also, previous work was started with DL_POLY in the team and thus local expertise was available.

DL_POLY requires the user to parameterise a series of input files (three mandatory ones and one optional) prior to a simulation. Also, once the simulation runs, four output files are created as shown in figure 3.4.

The first input file is the CONFIG file where the initial coordinates of all the atoms are written in a specific format (the velocities and forces applied to the considered atom may also be specified). The second input file is the FIELD file where all the interaction potentials

between the different atoms are written. Different interactions can be implemented as it will be seen in the next sections. The third input file is the CONTROL file where all the different parameters necessary for the simulations are recorded like the length of the simulation and the timestep.

There are other optional input files and one of them that is important is the REVOLD file. It contains statistics arrays from previous simulation job and is necessary if the **restart** directive in the CONTROL file (the simulation starts from the end of a previous simulation).

The first output file is the OUTPUT file where the simulation progression with statistics can be seen especially.

The second output file is the HISTORY file where the atomic coordinates (and also velocities and forces are optional). This file is optional but very important to analyse the system after the simulation. This file will be used for all the different methods that will be developped in the next chapters.

There are other output files. Two are really useful when the **restart** directive in the CONTROL file is written: the REVCON file where the last set of coordinates is recorded that will replace the CONFIG file and the REVIVE file that contains the accumulated statistical data and will be named REVOLD.

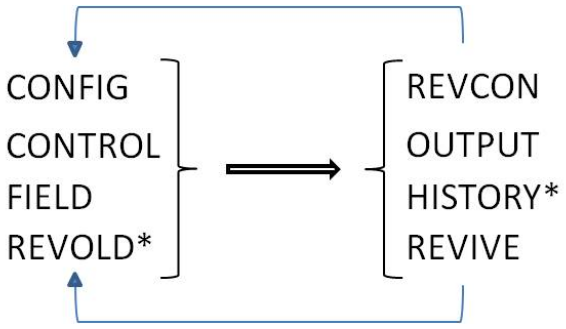

Figure 3.4: DL_POLY needs input files (on the left) to generate a simulation that produces output files (on the right). The most used files are presented in this figure. The ones with an asterisk are not mandatory.

The next section is about the different parameters used in the CONTROL and FIELD files that refer to some specific functions in DL_POLY package.

3.3.1 A Sample of DL_POLY Functions

As said previously, the CONTROL input file is where all the different parameters used in the DL_POLY functions needed are recorded. The critical ones are presented here.

The very first function is the one that defines which algorithm will be used in the simulation. A MD program solves numerically the Newton's law of motion for a N-body system. The algorithm chosen in this work to discretise these differential equations is the Verlet-Leapfrog

algorithm [52] as shown in equation 3.1. This numerical scheme is a second order method whereas the Euler integration is a first order one for the same number of function evaluations per step. Moreover, this is a time reversal algorithm, it conserves angular momentum and is symplectic (it conserves energy of dynamical systems).

$$\begin{cases} v\left(t+\frac{1}{2}\Delta t\right) \leftarrow v\left(t-\frac{1}{2}\Delta t\right)+\Delta t\frac{F(t)}{m} \\ r(t+\Delta t) \leftarrow r(t)+v\Delta t\left(t+\frac{1}{2}\Delta t\right) \\ v(t)=\frac{1}{2}\left[v\left(t-\frac{1}{2}\Delta t\right)+v\left(t+\frac{1}{2}\Delta t\right)\right] \end{cases} \tag{3.1}$$

where $r(t)$ is the position, $v(t)$ is the velocity and Δt is the simulation timestep.

It is also important to define the system ensemble. Indeed, different ensembles like NVT or NPT can be chosen. Here N stands for the number of atoms, V for the volume or simulation cell sizes, T for the temperature and P for the pressure.

In a NVT simulation, N and V are kept constant and T targets a chosen value thanks to a thermostat whereas P varies. In order to keep the temperature constant, a thermostat is needed. The algorithm used in this work is the Berendsen thermostat that basically forces the temperature to relax to the chosen value by re-scaling the atomistic velocities at each timestep. Note that such a thermostat breaks the time reversal property of Newton's law of motion. However, the trajectories produced still give reasonable results.

In a NPT simulation, N and V are kept constant and P targets a chosen value thanks to a barostat whereas T varies. In order to keep the pressure constant, a barostat is needed. The Berendsen barostat algorithm, that scale the lengths in the system, can be used here. However, in this study, because of the hypotheses of the structures, NPT simulations will not be used as explained later.

The simulation length and timestep have to be chosen. For initial configurations, a small simulation is usually run with a very small timestep in order to avoid the system numerically diverging when it is far from dynamic equilibrium. Usually, in this case, once the simulation converges, a timestep of 1 fs is set. The maximum length of these simulation is 20 ns (or 20 millions timesteps).

The cut-off distance that limits the spin interactions to compute also has to be specified. If an atom pair has a distance smaller than this cut-off distance, then the interactions between them are calculated. Otherwise, they are assumed to be negligible. The choice of such a distance is a function of the desired accuracy (the bigger the number of atoms in the calculation, the more accurate trajectories) and the time available for the simulation (a bigger number of atoms involved in the calculation implies a bigger compute time per timestep). This choice is also limited by the simulation cell sizes that are specified for each simulation.

In all this study simulations, the system will be considered as infinite or more precisely periodic as it will be explained later. Such a condition allows an Ewald summation [63] of

the electrostatic forces. Indeed, DL_POLY can use either direct summation or Ewald method that considers the short ranged interactions and the long ranged ones. These sums can be respectively calculated in an efficient way in the real space and in the reciprocal space thanks to the Fourier series method. As a result, Ewald summation replaces a potentially infinite sum by two finite sums.

The time interval Δt between two sets of coordinates has to be specified. Coordinates are then recorded in the HISTORY output file every Δt. Usually, coordinates are written every 1 ps.

The SHAKE algorithm [64] is also important here. It re-scales the distance between two atoms when the distance is defined as constant. For instance, in these simulations, the distance $O_{water} - H_{water}$ is constant. Note that when the system tries to converge for initial configurations, it is necessary to allow a big tolerance to this constraint because of the forces applied to the water molecules and crystal atoms (re-scale the tolerance factor chosen in the CONTROL file).

3.3.2 Interatomic Potential

The FIELD file specified all the interatomic force functions and their parameters. This is where all the interaction between the different atoms of the system are recorded. Different types of basic potentials were used here: constant distances constraints, Buckingham potentials [65], Lennard-Jones 12-6 [66], or in the general case n-m potentials [67], the intramolecular Morse potentials [68] and the screened harmonic potential [62]. These potentials are functions of some constants that depend on the type of the considered atoms that interact with each other. In the simulations, they were grouped into two sets of different (crystal-water) potentials : CLAYFF-SPC/E [69, 70] and Freeman-TIP4P [71].

The choice of the potentials is critical to the performance of MD simulation. However, it is important to be aware that these potentials are only approximations of actual ones: one can approximate in a good way a physical property like the diffusion coefficient but another will be more accurate for the thermodynamic properties for instance. Hence, there is no "best" potential description. These potentials are simple as they usually need 2 to 3 parameters. Many other forms of potential exist but in this work, only the previous ones will be used.

The choice of the potential for the different models (CLAYFF-SPC/E and Freeman-TIP4P) will be discussed later.

Buckingham Potential

The Buckingham potentials are of the form:

$$U_{Buck}(i,j) = A_{ij} e^{-\frac{r_{ij}}{\rho_{ij}}} - \frac{C_{ij}}{r_{ij}^6} \tag{3.2}$$

where r_{ij} is the distance between two atoms of type i and j, the first term on the right ($A_{ij}e^{-\frac{r_{ij}}{\rho_{ij}}}$) is a repulsion term and the second term ($-\frac{C_{ij}}{r_{ij}^6}$) is an attraction term. The shape of such a potential for $A_{ij} = 1$, $\rho_{ij} = 1$ and $C_{ij} = 1$ is shown in figure 3.5.

A_{ij}, ρ_{ij} and C_{ij} are inputs for the DL_POLY FIELD file.

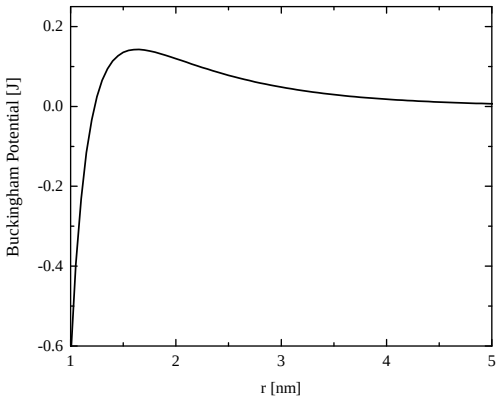

Figure 3.5: The Buckingham potential is plotted with $A_{ij} = 1$, $\rho_{ij} = 1$ and $C_{ij} = 1$.

Lennard-Jones $n - m$ Potential

The Lennard-Jones n-m potentials are of the form:

$$U_{L-J}^{n-m}(i,j) = \frac{E_{ij}^0}{n-m}\left(m\left(\frac{r_{ij}^0}{r_{ij}}\right)^n - n\left(\frac{r_{ij}^0}{r_{ij}}\right)^m\right) \tag{3.3}$$

where n and m are (n,m)=(12,6) and (n,m)=(9,6), r_{ij} is the distance between two atoms of type i and j, E_{ij}^0 is the dissociation energy and r_{ij}^0 is the equilibrium bond distance. These parameters respect the Laurentz-Berthelot mixing rules [72] $E_{ij}^0 = \sqrt{E_{ii}^0 E_{jj}^0}$ and $r_{ij}^0 = \frac{r_{ii}^0 + r_{jj}^0}{2}$. The shape of such a potential for $E_{ij}^0 = 1$, $r_{ij} = 1$ and both (n,m)=(12,6) and (9,6) is shown in figure 3.6.

E_{ij}^0 and r_{ij}^0 are inputs for the DL_POLY FIELD file.

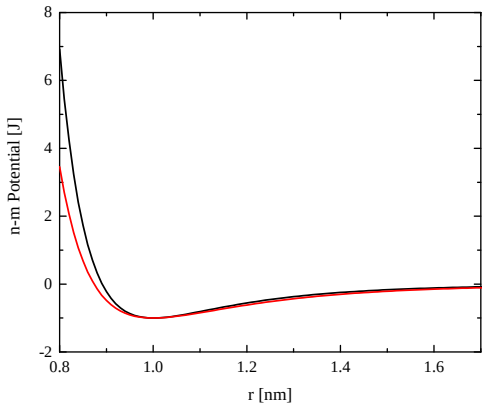

Figure 3.6: The n-m potential is plotted with $E_{ij}^0 = 1$, $r_{ij} = 1$ and both (n,m)=(12,6) (black solid line) and (9,6) (red solid line).

Intramolecular Morse Potential

The intramolecular Morse potentials are of the form:

$$U_{Morse}(i,j) = E_{ij}^0 \left[\left(1 - e^{-k_{ij}(r_{ij} - r_{ij}^0)} \right)^2 - 1 \right] \tag{3.4}$$

where r_{ij} is the distance between atoms i and j, E_{ij}^0 is the dissociation energy, r_{ij}^0 is the equilibrium bond distance and $k_{ij} = \sqrt{\frac{f_{ij}^0}{2E_{ij}^0}}$ where f_0 is the force constant at the minimum of the well. The shape of such a potential for $E_{ij}^0 = 1$, $k_{ij} = 1$ and $r_{ij} = 1$ is shown in figure 3.7.

E_{ij}^0, k_{ij} and r_{ij}^0 are inputs for the DL_POLY FIELD file.

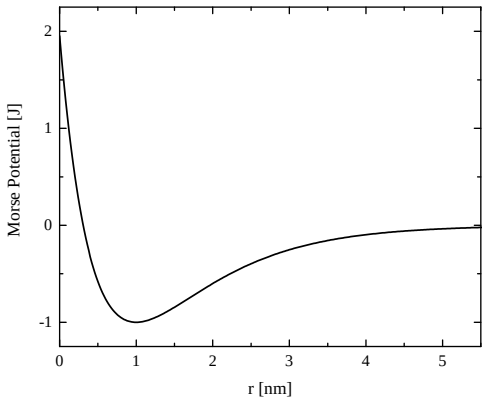

Figure 3.7: The Morse potential is plotted with $E_{ij}^0 = 1$, $k_{ij} = 1$ and $r_{ij} = 1$.

Screened Harmonic Potential

The screened harmonic potentials (shrm) are of the form:

$$U_{shrm}(\theta_{jik}) = \frac{k}{2}\left(\theta_{jik} - \theta_0\right)^2 e^{-\left(\frac{r_{ij}}{\rho_1} + \frac{r_{ik}}{\rho_2}\right)} \tag{3.5}$$

where r_{ij} and r_{ik} are respectively the distances between atoms i and j and atoms i and k, k is the "spring" constant, θ_0 is the equilibrium angle and ρ_1 and ρ_2 are respectively the stable distances between atoms i and j and atoms i and k. The shape of such potential for $k = 1$, $\theta_0 = \frac{\pi}{3}$, $r_{ij} = r_{ik} = 1$ and $\rho_1 = \rho_2 = 1$ is shown in figure 3.9. If r_{ij} is larger than ρ_1 then the potential is smaller (indeed, the atoms are far from each other) and if r_{ij} is smaller than ρ_1 the potential is stronger because of the proximity of the atoms, which is consistent. The same reasoning is valid for r_{ik} and ρ_2.

k, θ_0, r_{ij}, r_{ik}, ρ_1 and ρ_2 are inputs for the DL_POLY FIELD file and are shown in figure 3.8.

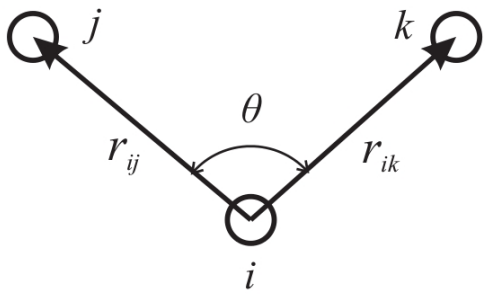

Figure 3.8: The screened harmonic potential parameters are shown here where i, j, k are three atoms, r_{ij} and r_{ik} are the distances between i and j and i and k respectively and θ is the angle $\widehat{ijk}$. This figure is adapted from [73].

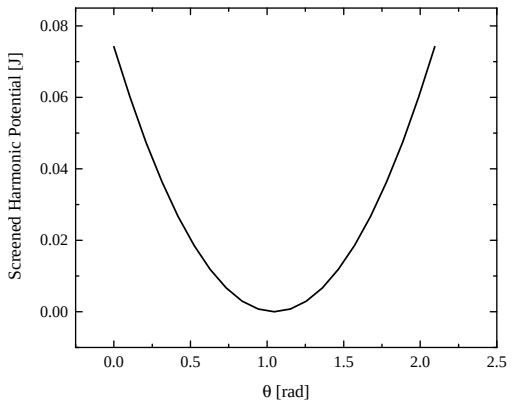

Figure 3.9: The screened harmonic potential is plotted with $k = 1$, $\theta_0 = \frac{\pi}{3}$, $r_{ij} = r_{ik}$ and $\rho_1 = \rho_2 = 1$.

3.3.3 Periodic Boundary Conditions

The Periodic Boundary Conditions (PBC) [52] are a method to generate an "infinite" space with the overall characteristics as the simulation cell. The idea is that when a water molecule moves out from one side of the simulation cell, it re-enters into it on the other side with the same conditions. The space is periodic. That can be interpreted as if the entire universe was composed of a lattice of cells that are an exact copy of the simulation cell as shown in figure 3.10 in 2D.
Before doing any analysis on the trajectories, the PBC have to be removed and atom displacement updated, otherwise, their trajectories will be discontinuous which is an artefact that would give wrong results. This is why, before any analysis that will be tackled in this chapter, the PBC will be removed.

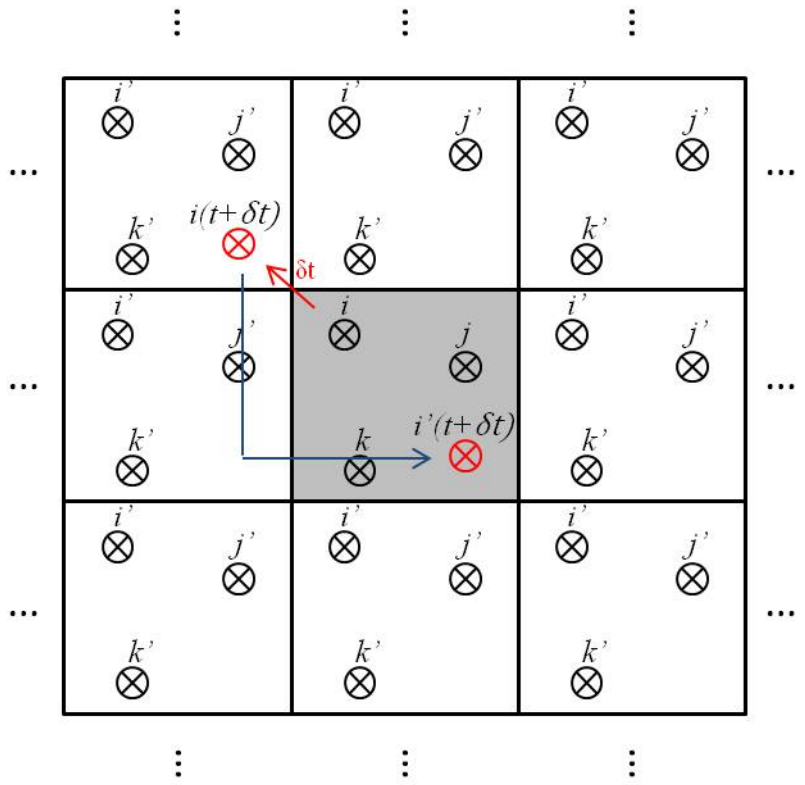

Figure 3.10: The PBC replicate the simulation cell infinitely in the plane. When the position of an atom i is calculated after a time δt, this atom is replaced in the original simulation cell at the same place it would be in the copied cell.

3.4 Water Transport Properties and NMR Relaxation Analysis

This section describes some of the key methods for analysing the properties of water confined to a pore.

3.4.1 Water Density

In this model, C-S-H nanostructure is composed of quasi-crystal layers. These solid layers divide space into different volumes: the nanopores. Water molecules occupy these pores and their behavior is a function of their position: the water molecules close to the crystal will move less freely than the water molecules away from it.

The MD data are used to generate a probability density curve for water in the pore space. This is normally calculated in the z direction orthogonal to the quasi-crystal layers and so gives the probability of finding a water at a distance z from the pore surface. Examination of the probability density will reveal that water becomes structured near the surface in layers as shown in figure 3.11. Each layer can be studied and compared.

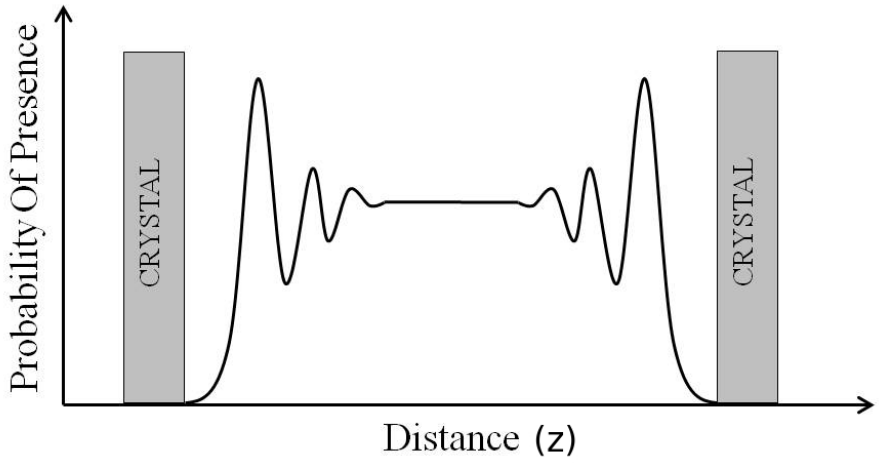

Figure 3.11: A schematic representation of the probability density of water molecules (or more generally of an atom). The shape of the curve can be used to define layers where the water molecules have different behaviours.

3.4.2 Selection of Water Populations

The layers of water are a function of only the position in the z axis. Hence, physical properties of water molecules in this system will change according to their distance from a pore surface. However, it is not straightforward to calculate these properties because water can move from one layer to another (for instance desorption from the surface layer to bulk).

Determining the population of interest for the calculation of a physical property in a specific layer can be difficult because of this exchange. Hence, a method that selects the water

molecules has been designed for this work. The idea is to select all the water molecules in a zone $\{A\}$ at the initial time, to follow them as long as they are in a second zone $\{B\}$ and then to calculate the property at time t for only the ones that are in zone $\{C\}\subset\{B\}$. Note that a zone can be a set of one or more layers and that the same layer can be in two different zones: for instance, a layer L_1 can be in $\{A\}$ and also in $\{B\}$.

The notation used for such a water population is $\{A > B > C\}$. Examples of populations of water are shown in figure 3.12. In this figure, Ω represents the whole space (for this Example, Ω contains all the layers in the pore: $\Omega = L_1 + L_2 + L_3$). Three trajectories are shown. For the red one, a water starts in $\{L_1\}$ and stays in it during the whole observation time. This water is in the population $\{L_1 > L_1 > L_1\}$. It is also in the population $\{L_1 + L_2 > L_1 + L_2 > L_1 + L_2\} \supset \{L_1 > L_1 > L_1\}$ and more generally this water is in population $\{(L_1 \text{ or } L_1 + L_2 \text{ or } L_1 + L_3 \text{ or } \Omega) > (L_1 \text{ or } L_1 + L_2 \text{ or } L_1 + L_3 \text{ or } \Omega) > (L_1 \text{ or } L_1 + L_2 \text{ or } L_1 + L_3 \text{ or } \Omega)\}$ ($4^4 = 64$ possibilities). However, in these 64 possibilities, some are redundant like $\{L_1 > L_1 + L_3 > L_1\}$=$\{L_1 > L_1 > L_1\}$ since there is no connection between L_1 and L_3 (ie L_2 is not considered here). In the same way, because of the lack of connection, the population $\{L_1 > L_3 > L_1\}$=$\emptyset$ by definition.
However, in figure 3.12, only the smallest sets containing the trajectories are written: for the red trajectory, the population is $\{L_1 > L_1 > L_1\}$, for the green trajectory, the population is $\{L_2 > \Omega > L_1\}$ and for the blue trajectory, the population is $\{L_2 > L_2 + L_3 > L_2\}$.

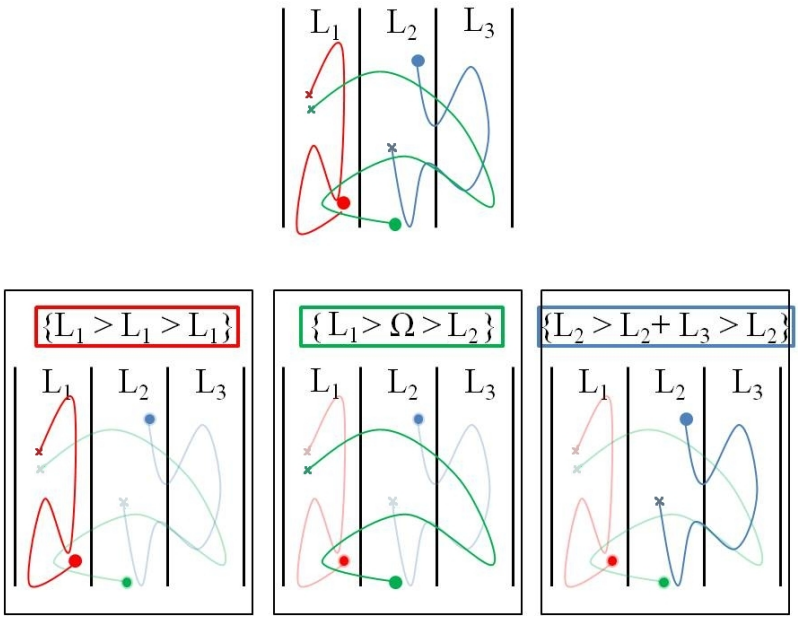

Figure 3.12: The process to select the waters belonging to the ensemble $\{A > B > C\}$ is shown here. Every time a water molecule goes outside zone B, it is removed from the ensemble. At time t, only waters in zone C are considered for the calculation. Three trajectories , that start from the cross and are at the full circle at time t, are shown and belong to a specific (smallest) population: $\{L_1 > L_1 > L_1\}$ in red ($A = L_1$, $B = L_1$ and $C = L_1$), $\{L_1 > \Omega > L_2\}$ in green ($A = L_1$, $B = \Omega$ and $C = L_2$) and $\{L_2 > L_2 + L_3 > L_2\}$ in blue ($A = L_2$, $A = L_2 + L_3$ and $A = L_2$).

From now, B refers to bulk and S refers to the surface. A system containing a bulk zone and a surface layer (ie $\Omega = S + B$) can be considered here. If only the water molecules that were in bulk during the whole simulation time, then the population that is taken into account is $\{B > B > B\}$. In this case, this population will have the same properties as a population of water in a pure bulk simulation as shown in figure 3.2. Waters in population $\{S > S > S\}$ will contain the water molecules that only stayed in the surface during the whole simulation. Waters in population $\{S > \Omega > S\}$ will contain the water that started on the surface, moved anywhere in the pore (in the surface and in bulk too) and came back to the surface.

It is interesting to remark that the border between the different zones (like surface/bulk border in the previous case) is not clear. Even if the density profile is a good tool to define them, one has to be careful about the difference between real exchange and vibration around this border. Hence, in practice, water molecules are allowed to "fluctuate" outside a zone by half the size of a water molecule ($\frac{2.7}{2} = 1.35\text{Å}$).

3.4.3 Diffusion and Desorption Analysis

The diffusion analysis relies on the calculation of the diffusion coefficient of water molecules (or protons). The calculation of the diffusion coefficient is straightforward if the PBC have been removed. Then, the equation 2.18 is used on a specific population as described in the previous section. For instance, to calculate the diffusion coefficient of the surface, the considered population is $\{S > S > S\}$. For bulk, the considered population is $\{B > B > B\}$.

The desorption analysis is straightforward too. The idea is to look at the number $N_S(t)$ of water molecules in population $\{S > S > S\}$ versus time. Because of the exchange between the surface and the rest of the pore, $N_S(t)$ is a decaying exponential function which allows a decay time, or desorption time, to be defined.

3.4.4 Calculation of the Correlation Function

The correlation function $G^*_{I-J}(t)$ between two sets of spins I and J can be generated (for instance between all the protons and Fe^{3+} impurities on the surface). In practice, it would be too long to calculate all the spin pairs interactions in the model, and still, as the model is limited (finite cell size), the results would not be totally correct. That is why the correlation function is split into different parts as suggested later in equation 3.6.

But first, in this calculation a common approximation is to only consider a neighbour list (all the spins $j \in J$ whose distance to the spin $i \in I$ at initial time $r_{i-j}(t = 0)$ is smaller than half the smallest cell length: $r_{i-j}(t = 0) \leq min_{d\in\{1,2,3\}} \left\{ \frac{Cell[d]}{2} \right\}$, where $Cell[d]$ is the length of the cell size in the d^{th} direction). This reduces drastically the number of calculations to be done by the computer, and hence the time necessary for such an analysis. To do so, it is important to take care of the periodic boundary conditions. For this purpose, the system can be considered as a simulation cell surrounded by 26 ghost cells in 3D (8 in 2D as shown in figue 3.13). Hence, each atom in the simulation cell has also 26 ghost images. If the interest is to see the effective distance between spins i and j, all the 26+1 distances (+1 for the simulation cell) are calculated and the smallest one chosen. This is the closest neighbour j.

Only the interactions between a spin i and its neighbour list will be considered in the calculations.

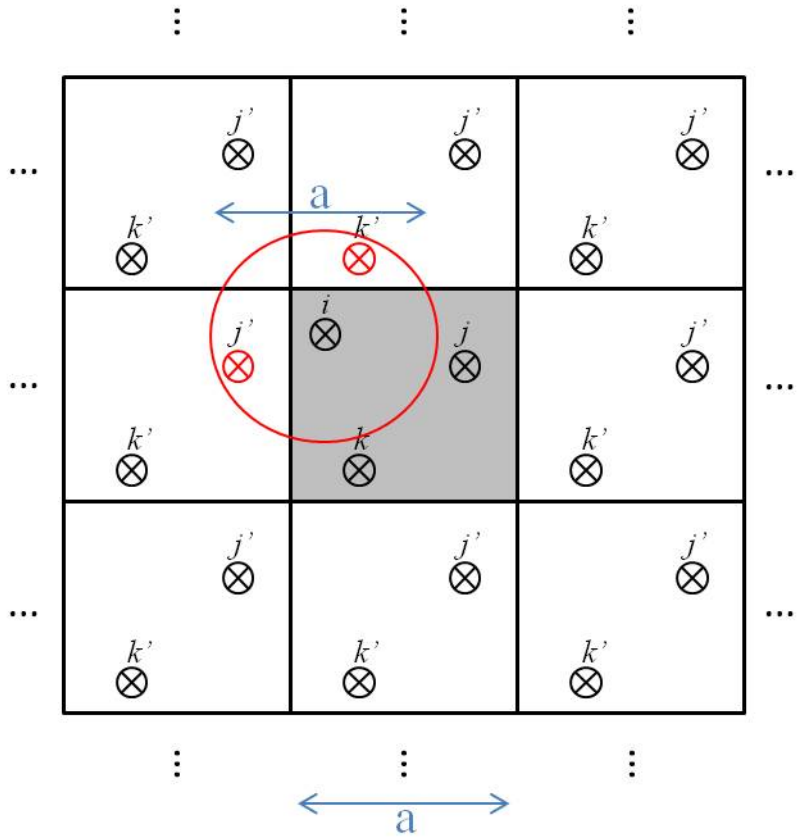

Figure 3.13: In 2D, the simulation cell is surrounded by 8 ghost cells. All the spins whose distance to a spin i are in the disc of radius $min_{d\in\{1,2,3\}}\frac{Cell[d]}{2}$ (where $Cell[d]$ is the length of the cell in the d^{th} direction) is in the its neighbour list.

The distances between a spin i and a spin j that is in its neighbour list is an element used to differentiate the kind of interaction. Indeed, spin pair interactions belong to one of the four following sets: the Near-Near (NN), the Near-Far (NF), the Far-Near (FN) and the Far-Far (FF) interactions.

The Near-Near component is calculated for each time and for all the $i-j$ pairs whose distance at time $t=0$ (first Near) and at time $t>0$ (second Near) is smaller than a distance r_{cut} (in practice, the previous distance $min_{d\in\{1,2,3\}}\frac{Cell[d]}{2}$).

The Near-Far interaction is calculated for each time and all the $i-j$ pairs whose distance is smaller than r_{cut} at time $t=0$ (Near) and greater than r_{cut} at time $t>0$ (Far). This kind of interaction only appears for $t>0$ since all the spin pairs considered here are "Near" at time $t=0$. Also, in theory, the Far-Near interaction (FN) has to be considered. How-

ever, because of the symmetry NF / FN ($r_{i-j} = r_{j-i}$), the NF interaction is the only one to be calculated and then are simply doubled (this is the reason of the factor two in equation 3.6).

The Far-Far interaction is a mathematical correction because of the finite size of the system [17]. It takes into account all the spin pairs $i - j$ whose distance is greater than r_{cut} at time $t = 0$ and at time $t > 0$. It can be generated for a 2D and 3D system subject to certain approximations. In this work, it will be only used for a pure 3D bulk water system in chapter 4 section 4.2.3.

The other results will give not exact but still good numbers (and especially a good order) for correlation functions in chapters 6 section 6.4 and 7 section 7.2.4 (for the simulations in this study, the FF component is not the main component of the correlation functions).

Hence, the correlation function can be calculated in the following way [16]:

$$G^*_{I-J}(t) = G^*_{I-J,NN}(t) + 2G^*_{I-J,NF}(t) + G^*_{I-J,FF}(t) \tag{3.6}$$

Time Selection

The calculation of the correlation function at each time would take too much computer time since the number of spin pairs scales as n^2_{spin}. This is why it will be done and averaged only for a few specific times $\{t_k,\, k \in K_{time}\}$. Then, these values will be interpolated.
As the correlation function is usually decaying quickly and for long times it is not varying so much, a choice for such a time set is:

$$K_{time} = \{0, 1, \cdots, 9, 10, \cdots, 90, 100, \cdots, 900, 1000, \cdots, 9000, 10000, 11000, \cdots, 20000\} \tag{3.7}$$

This set last value is 20000 because this will be the maximum simulation length time. Note that here, only 50 sets of coordinates are needed, which reduces significantly the time needed to generate the correlation function. Also, in this study, an arbitrary condition is that when the value of the correlation function at a time t_k is smaller than the initial value divided by 1000, then $t_k = t_{end}$, time after which all the values of the correlation function are considered to be negligible and then equal to zero in practice.

Interpolation

Then, these 50 values of the correlation function will be interpolated in order to have enough data to generate the spectral density functions. To do so, the Hermite interpolation (or spline interpolation) will be used [74]. The idea is to interpolate every two times t_k and t_{k+1} with a polynomial of order three (the k^{th} spline $S_k(t) = a_0 + a_1 t + a_2 t^2 + a_3 t^3$). The four coefficients $a_i, i \in \{1, 2, 3, 4\}$ are then calculated thanks to the values of the correlation function and its derivatives at this time (four constraints). The derivatives are not taken

from the simulations because of the noise but approximated by $\frac{dG}{dt}(t_k) \approx \frac{G(t_{k+1})-G(t_k)}{t_{k+1}-t_k}$, with for t_{end}, $\frac{dG}{dt}(t_{end}) \approx \frac{G(t_{end})-G(t_{end-1})}{t_{end}-t_{end-1}}$. In practice, the spline valid for a time $t \in [t_k, t_{k+1}]$ is decomposed on a polynomial basis of dimension 4:

$$S_k(t) = G(t_k)\phi_1(t) + G(t_{k+1})\phi_2(t) + \frac{dG}{dt}(t_k)\phi_3(t) + \frac{dG}{dt}(t_{k+1})\phi_4(t) \tag{3.8}$$

where

$$\begin{cases} \phi_1(t) = (t-1)^2(1+2t) \\ \phi_2(t) = t^2(3-2t) \\ \phi_3(t) = t(t-1)^2 \\ \phi_4(t) = (t-1)t^2 \end{cases} \tag{3.9}$$

The interest of such a spline interpolation is that when all the splines are put side to side, the final function is smooth (continue with no angles at the times t_k) that is mandatory to generate a good spectral density function.

Finally, the timestep in each interval $[t_k, t_{k+1}]$ is important. The timestep can be different in two intervals $[t_k, t_{k+1}]$ and $[t_{k'}, t_{k'+1}]$. Usually, the timestep is chosen equal to the interval length $(t_{k+1} - t_k)$ divided by a parameter "precision". However, as it will be explained in the next section, each timestep has to be smaller than a number that depends on the frequency. The number of timestep in each interval $[t_k, t_{k+1}]$ is noted T_k and $T = \cup_k T_k$ is the number of timesteps for the whole function.

3.4.5 Numerical Calculation of the Spectral Density Function and Relaxation Times

As shown in equation 2.12, the spectral density function is the Fourier transform of the correlation function $G_{I-J}(t)$. The correlation function is defined as zero for $t > t_{end}$. In practice, according to the time reversal symmetry of the correlation function, an estimation of the spectral density function is:

$$J^*_{I-J}(\omega) = 2\int_0^{t_{end}} G^*_{I-J}(t)cos(\omega t)dt \tag{3.10}$$

Such an integral can be evaluated numerically at each angular frequency in an accurate way thanks to the trapezoidal rule [74]. The basic idea is to calculate the area under a curve for all the time intervals $[t_n, t_{n+1}]$, $n \in T$. Each small area is composed by a rectangle and a triangle. The approximation of the integral of a function $f(t)$ on the interval $[t_0 = 0, t_{N_{end}} = t_{end}]$ is:

$$\int_0^{t_{end}} f(t)dt \approx \frac{1}{2}\sum_{k=0}^{N_{end}} (t_{k+1} - tk)(f(t_{k+1}) + f(t_k)) \tag{3.11}$$

Finally, applied to equation 3.12 ($f(t) = 2G(t)\cos(\omega t)$), the spectral density function becomes:

$$J^*(\omega) \approx \sum_{n=0}^{N_{end}} (t_{n+1} - t_n)(G^*(t_{n+1})cos(\omega t_{n+1}) + G^*(t_n)cos(\omega t_n)) \tag{3.12}$$

where N_{end} is the maximum time index (formally, $t_{end} = t_{N_{end}}$).

Note that, as said in the previous section, there is a condition about the timestep. Indeed, if the timestep is too big, the cos function has insufficient resolution. Actually, the product $\omega\Delta t$ has to be small enough in such a way that the cos function can be used to Fourier transform the correlation function. Usually, $\omega\Delta t \leq 0.5$ is a good approximation. Hence, the choice of the timestep Δt when $G^*_{I-J}(t)$ is interpolated as shown in the previous section depends on the angular frequency (and then the frequency $f = \frac{\omega}{2\pi}$) chosen to generate $J^*_{I-J}(\omega)$ and by extension the relaxation times.

The relaxation times are then easily generated: as shown in equations 2.13 and 2.14 only a few values of the spectral density function $J^*_{I-J}(\omega)$ for specific frequencies are necessary.

Chapter 4

Validation Of Methods In 3D Bulk Water

The purpose of this short chapter is to validate different methods discussed in chapter 3 using the bulk water benchmark. A NVT MD simulation of a pure bulk water system is described. A water potential is described. Diffusion coefficient, inter-zone translation propagation (based directly on the propagator analysis in equation 2.28) and NMR relaxation rates analyses are performed.

4.1 Bulk Water System

4.1.1 A Bulk Water Simulation Box

A bulk water simulation cell is used to validate the different methods developed in this study. An example of such a simulation box is presented in figure 4.1. Here, the water model is a three atom model, SPC/E water [75], that will be described in detail in the next section.

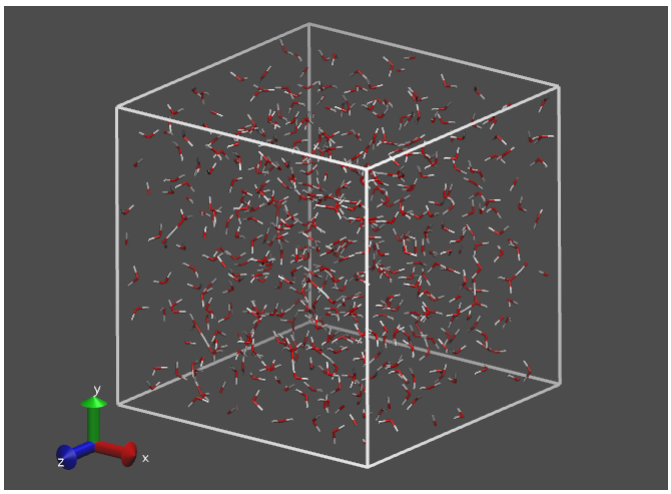

Figure 4.1: Pure Bulk water (white and red sticks) and simulation box. SPC/E water (red oxygens and white hydrogens) was used here. The simulation box size is $25 \times 25 \times 25$ $\mathring{A}^3$.

A NVT simulation was performed with all the inputs and functions described in section 3.3. However, some more specific characteristics have been used. All the water molecules were moving in the simulation box the size of which was $X = 25$ Å, $Y = 25$ Å and $Z = 25$ Å. Periodic boundary conditions were used. The temperature was set to the room temperature, 300K. The number of water molecules was chosen in order to respect the water density in this box at this temperature: $d = 1000\text{kg/m}^3$. To do so, a simple calculation was done:

$$d = \frac{M_{H_2O}}{\mathcal{N}_\mathcal{A}} = 0.033 \text{ water/Å}^3$$

where $M_{H_2O} = 18$ g/mol is the water molar mass and $\mathcal{N}_\mathcal{A} = 6.02 \times 10^{23}$ mol^{-1} is the Avogadro number. Such a calculation leads to a number of water molecules equal to $N_{H_2O} = 25 \times 25 \times 25 \times d \approx 514$ water molecules. This kind of calculation will be used in chapters 5 section 5.2.2 and 7 section 7.2.1 for the simulation of C-S-H analogues as will be explained. This is the reason why the number of water molecules was determined this way in order to introduce the technique. Another method is to run a NPT simulation with a fixed amount of water molecules, the volume varies and the density becomes stable and achieves a good density.

4.1.2 Water Representation and Atomistic Potentials

Another important element in this simulation is the representation of water that is used. In this study, as will be explained in chapter 5 section 5.3, two water atomistic potentials are considered: SPC/E and TIP4P/2005 potentials. Both of them are known to generate accurate physical properties for water, such as density and diffusivity [70, 76].

Figure 4.2 shows the basic atomistic structures of these potentials. SPC/E has 3 atoms whereas TIP4P/2005 is composed of 4 atoms. To be precise, TIP4P/2005 has one oxygen O, two hydrogens H and a pseudo atom M that is slightly shifted away from O on the bisector $\widehat{HOH}$. O is where the the mass of oxygen is located whereas M is where the charge of the oxygen is located. Hence, the Coulombic interaction between two TIP4P/2005 water oxygens is between the M of these two water molecules.

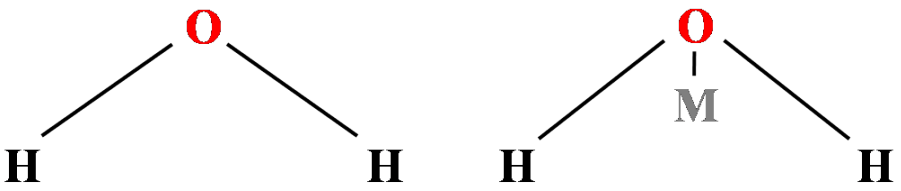

Figure 4.2: In this study, two representations of water have been considered. On both models, O stands for oxygen and H for hydrogen. On the left: SPC/E water is a three points model. On the right: TIP4P water is a four points model where M represents a pseudo atom where the oxygen charge is shifted on the bisector of $\widehat{HOH}$.

As said in chapter 3 section 3.3, the parameters of this potential have to be written in the FIELD input file. Table 4.1 sums up these potential features. These two potentials do not allow hydrogen exchanges between water molecules since the distances r_{OH} are constant. The

parameter	unit	SPC/E	TIP4P/2005
r_{OH}	Å	1.0	0.9572
r_{OM}	Å	-	0.1546
$\widehat{HOH}$	degree	109.47	104.52
q_O	e C	-0.8476	-
q_M	e C	-	-1.1128
q_H	e C	0.4238	0.5564
M_O	g/mol	15.99	15.99
M_H	g/mol	1.008	1.008
ϵ	eV	6.7429×10^{-3}	8.032×10^{-3}
σ	Å	3.166	3.1589

Table 4.1: The different parameters necessary for SPC/E and TIP4P/2005 water potentials are presented in this table: distances ($r_{OH,OM}$), angles ($\widehat{HOH}$), charges ($q_{O,H,M}$), masses ($M_{O,H}$) and Lennard-Jones parameters (ϵ and σ). Note that the Lennard-Jones potential is only considering the oxygens of two different water molecules.

water molecules are rigid. This constraint forbids hydrogen hops that would generate another diffusion process, which could have an impact on the value of the NMR relaxation times as hydrogen trajectories would be modified.

The timestep δt of this simulation (ie: the coordinates of the atoms are calculated every δt) is $\delta t = 1$fs. The coordinates of this simulation are recorded every $\Delta t = 1$ps and the simulation time is $10^5 \Delta t = 10$ ns. The coordinates are recorded every $1000\delta t$ in order to reduce the size of the outup file. Indeed, otherwise, the HISTORY file would be 1000 times bigger, which is a problem for data storage and program efficiency.

4.2 Data Analysis

4.2.1 Diffusion Coefficient

The first analysis concerns the calculation of the diffusion coefficient of pure bulk water according to Molecular Dynamics simulations. Bulk water is a homogeneous and isotropic system and the movement of a water molecule is only due to thermal fluctuations. This displacement is a stochastic process: the Brownian Motion. The mean square displacement of a water molecule varies with time. It is expected to be proportional with time as described in chapter 2 section 2.3.

The mean square displacement of water can be averaged over many initial times taken at different time points within a single simulation and all the water molecules and plotted versus time as shown in figure 4.3. Here, 100 time starts were used separated by 30 steps.

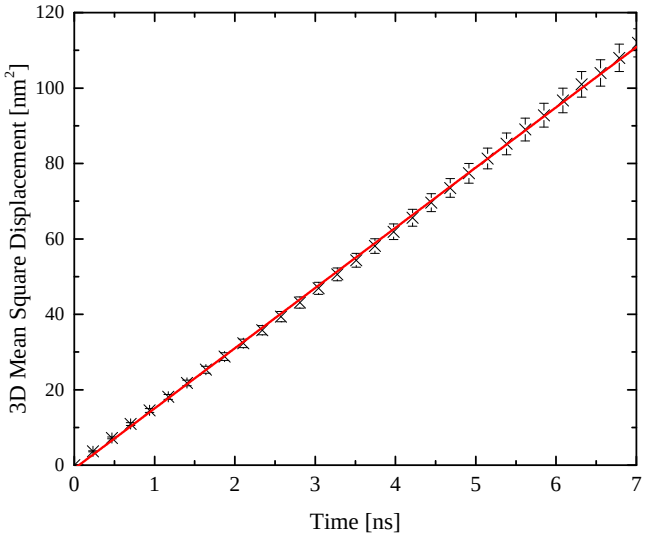

Figure 4.3: Bulk water simulated mean square displacement (black crosses) is proportional with time (t) and the slope of this curve is linked to the diffusion coefficient. It can be fitted (red full line) to a straight line. The diffusion coefficient found is $D_{sim} = 2.66 \times 10^{-9}$ $m^2.s^{-1}$ *with a standard error of* 0.01×10^{-9} $m^2.s^{-1}$. *The error bars were calculated were calculated in the mean over the average of all time starts.*

As predicted by the theory, a fit with a simple straight line can be done. The slope of such a line is $2nD = 6D$, where $n = 3$ is the number of dimensions of the system. The least squares fitting produces also a standard error. Finally, the water diffusion coefficient simulated this way is:

$$D_{sim} = 2.66 \pm 0.01 \times 10^{-9} \text{ m}^2.\text{s}^{-1}$$

This number is quite close to the experimental value, $D_{exp} = 2.597 \times 10^{-9}$ m^2s^{-1} at 303.15 K [77]. The error in the diffusion coefficient is due to error in least squares analysis and also to the periodic boundary conditions in the MD simulations (and hence to the simulation cell sizes) [78, 79].

4.2.2 Propagator Analysis

Since there is no surface in a pure bulk water system, it is not correct to speak about desorption even if the process used in MD models with surfaces to count the number of water molecules that desorbs is the same process that will be used here. The propagator is another way to describe diffusion as suggested in equation 2.28. The propagator for Brownian motion is well known and is Gaussian. It can be compared to the simulation calculations.
The main idea is to consider a population of water starting in a specific zone, say box A, at

time $t = 0$, being able to go everywhere to region Ω (Ω is the whole system and contains region A), but to only retain it in the calculation if it is in A at time t. In other words, with the notation used in the chapter 3 section 3.4.2, only the $\{A > \Omega > A\}$ water population is considered and its decay with time characterizes water propagation.

Figure 4.4 shows a box (say A as defined above) full of water molecules at $t = 0$ that start to diffuse with time. There are of course other molecules outside of this box but they are not shown.

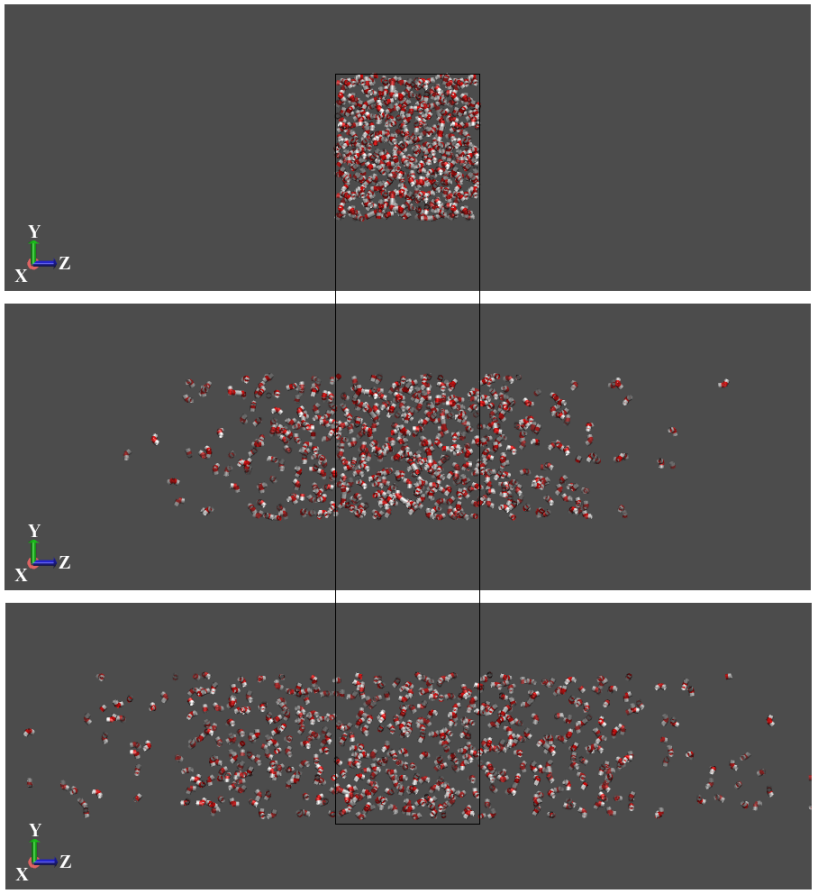

Figure 4.4: Water (red oxygens and white hydrogens) propagation from a box. Top: $t = 0$ ns; middle: $t = 0.5$ ns; bottom: $t = 1.5$ ns.

The objective is to quantify this propagation. To do so, the propagator discussion in the chapter 2 section 2.4.2 is used.
According to figure 4.4, the box is defined by two (yz) parallel plans separated by a distance $2a$ (here $2a = 25$ Å is the cell size in z direction) and the water population of interest is characterised by its position:

$$\begin{cases} x_0 \in \mathbb{R}, y_0 \in \mathbb{R}, z_0 \in [-a, a], \\ x_t \in \mathbb{R}, y_t \in \mathbb{R}, z_t \in [-a, a]. \end{cases}$$

Considering that the probability to find initially a water molecule in a specific position in the pore is $\frac{1}{2a}$ (homogeneous system), the probability a water molecule that starts in this pore and is in this pore at time t, returns allowed, is given by equation 2.28:

$$\mathcal{P}(t) \quad = \quad \text{erf}(\sqrt{\frac{a^2}{Dt}}) + \sqrt{\frac{Dt}{\pi a^2}}(e^{-\frac{a^2}{Dt}} - 1)$$

The simulated propagation curve can be fitted with this function. The only parameter that varies is the water diffusion coefficient D. The data and fit is shown in figure 4.5. The fit gives $D_{propagator} = 2.763 \pm 0.004 \times 10^{-9}$ m^2.s^{-1}. This value is only $\pm 3\%$ different to that calculated from the mean square displacement $D_{msd} = 2.66 \pm 0.01 \times 10^{-9} m^2.\text{s}^{-1}$.

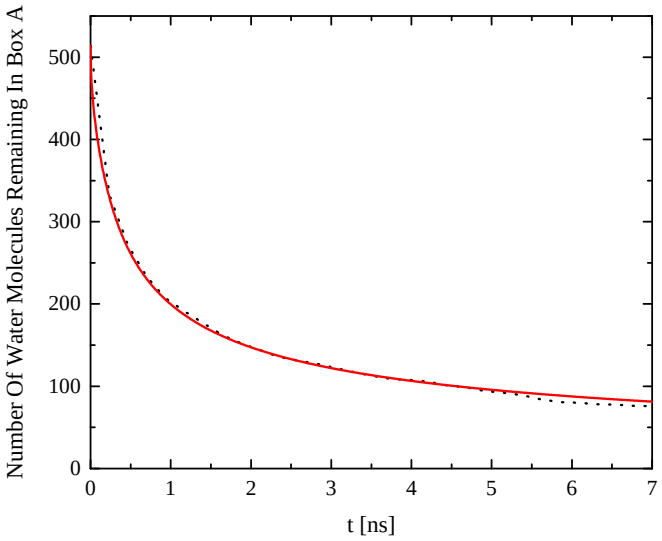

Figure 4.5: Water propagation curve versus time (t) from MD simulation (black crosses) can be fitted by the analytical formula in equation 2.28 (red solid line). This fit is good and shows the propagator is Gaussian. The varying parameter is the diffusion coefficient and is found to be $D = 2.763 \pm 0.004 \times 10^{-9}\ m^2.s^{-1}$.

4.2.3 NMR Relaxation

Proton NMR relaxation times can be generated using the methodology presented in chapter 3 section 3.4.4 . Indeed, MD simulation outputs are trajectories and the hydrogen trajectories can be used to compute correlation functions G. Equation 3.6 ($G = G_{NN} + 2G_{NF} + G_{FF}$) can be partially computed. Indeed, most of the time in this study, the G_{FF} cannot be evaluated. However, here, in the case of a 3D pure bulk system, it can be analytically calculated [17] and then added to get the actual simulated G in order to benchmark the process:

$$G^*_{FF,3D} = 4\pi N_\nu \int_0^\infty e^{-2Dtk^2} \frac{J^2_{\frac{3}{2}}(kd)}{kd^3} dk \tag{4.1}$$

where $J_{\frac{3}{2}}(x)$ is the half-integer Bessel function, D is the diffusion coefficient of bulk water, N_ν is the spin density (number of spin per unit volume) and k is the Fourier variable.

Figure 6.15 shows those simulated correlation functions from MD outputs. These results are close to those presented in [17]. If the correlation time τ_c is the time from which the ratio $\frac{G(\tau_c)}{G(0)} < 0.05$, where G=$G_{NN}$+2$G_{NF}$+$G_{FF}$, then $\tau_c = 9 \pm 1 \times 10^{-12}$ s.

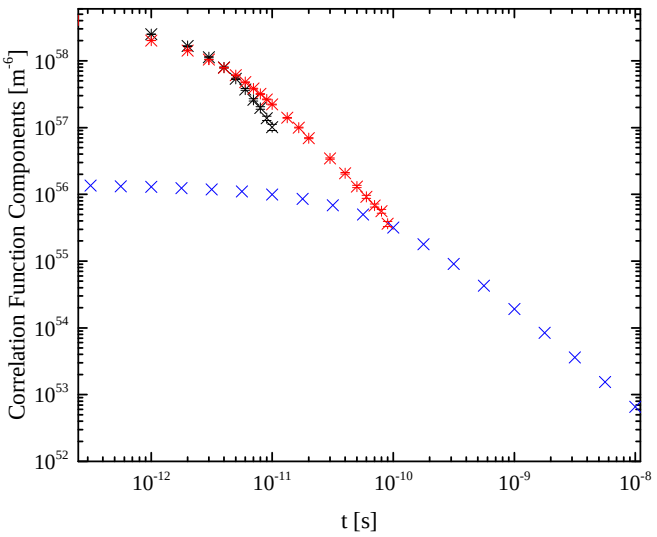

Figure 4.6: Correlation function simulated components G_{NN} (black crosses with its standard error bars), G_{NF} (red crosses and its standard error bar) and the analytical G_{FF} (blue crosses) versus time (t) in log-log space. The correlation time is $\tau_c = 9 \pm 1 \times 10^{-12}$ s.

These correlation functions (ie: G_{NN}, G_{NF} and G_{FF}) can be Fourrier transformed to produce the spectral density function components (ie: respectively J_{NN}, J_{NF} and J_{FF}). The correlation function has been calculated until its value becomes smaller, $\frac{1}{100}$ times its value at $t = 0$. Beyond this, the numerical accuracy of the data starts to decrease. The values of the different functions are set to 0 for a time $t > t_{max,i}$, where $\frac{G_i(t_{max,i})}{G_i(0)} < 0.01$. Then, the different curves are Fourier transformed and added to get the spectral density function. The curve obtained this way is flat for frequency in the range [1,100] MHz as shown in figure 4.7. Theory confirms such a flat behaviour. Indeed, using 2.17 and since the correlation time in bulk water is $\tau_c = 9 \pm 1 \times 10^{-12}$ s, the ratio between the theoretical spectral density functions at frequencies 100 MHz and 1 MHz is:

$$\frac{J_{th}(100 \text{ MHz})}{J_{th}(1 \text{ MHz})} = \frac{1 + 3.24\pi^2 10^{-6}}{1 + 3.24\pi^2 10^{-10}} \approx 1.00003$$

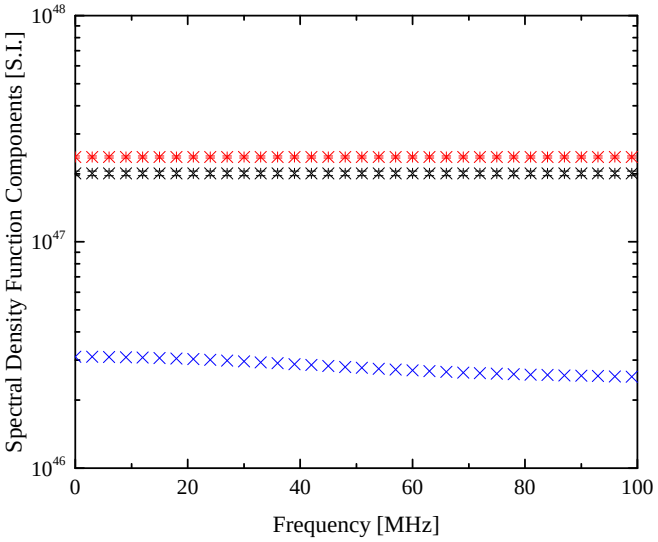

Figure 4.7: Spectral density functions J_{NN} (black crosses), J_{NF} (red crosses) and J_{FF} (blue crosses) versus frequency are shown with their respective standard errors with a frequency between 1 and 100 MHz.

As explained by the BPP theory in chapter 2 section 2.2, the inverse of a linear combination of the spectral density functions leads to the NMR relaxation times in the frequency range determined by the time space in the simulation. Since the spectral density functions are constant in this frequency range, the T_1 and T_2 are really similar. Indeed, the couple of equations 2.14 both become $\frac{1}{T_{1,2}} = \frac{10}{3}CJ^*(0)$. T_1 components curves are shown on the same frequency range in figure 4.8.

Using equations 2.13, in a frequency range of [1,100] MHz, the spin-lattice (T_1) and the spin-spin (T_2) relaxation times are found to be:

$$\begin{cases} T_1^{NN} = 11.7 \pm 1.53s, \ T_2^{NN} = 11.7 \pm 1.53s \\ T_1^{NF} = 9.9 \pm 1.04s, \ T_2^{NF} = 9.9 \pm 1.04s \\ T_1^{FF} \approx 80 \pm 10s, \ T_2^{FF} \approx 80 \pm 10s \end{cases}$$

Finally, after an harmonic average $\frac{1}{T_i} = \frac{1}{T_i^{NN}} + \frac{1}{T_i^{NF}} + \frac{1}{T_i^{FF}}$, $i = 1$ or 2, this gives:

$$T_1^{Bulk} \approx T_2^{Bulk} \approx 5.0 \pm 0.6s$$

This value is of the same order of the measured value for water at 300K of $T_{1,exp} = 3.8s$ [80]. If the $G_{FF}(t)$ component had been removed from the calculation, $J^*(0) = \int_{\mathbb{R}_+} G^*(t)dt$, which is the area under the curve, would be smaller and hence $T_{1,2}$ larger. This will be the case for the cement analogue models since G_{FF} cannot be analytically generated for such porous systems.

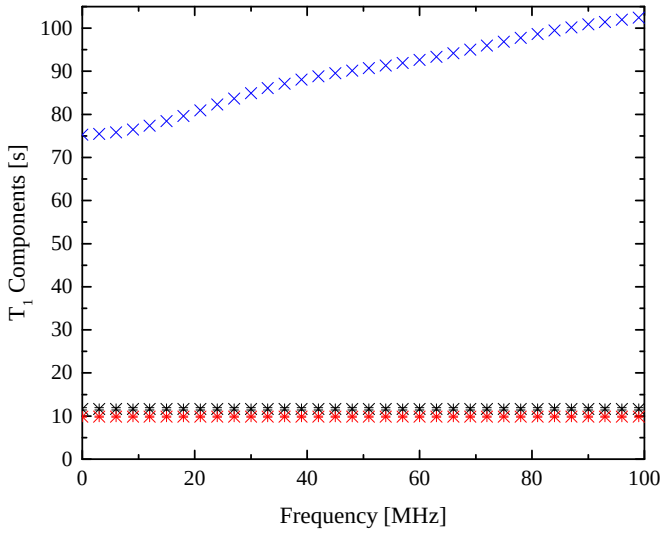

Figure 4.8: NMR relaxation time components T_1^{NN} (black crosses), T_1^{NF} (red crosses) and T_1^{FF} (blue crosses) versus frequency shown with their respective standard error.

Moreover, a major challenge in making NMR measurements is to remove all dissolved paramagnetic oxygen impurity. This will lower experimental values and may be a further cause of the observed difference between experimental and MD values.

Chapter 5

Choice Of The C-S-H Analogue Model

The purpose of this chapter is to choose a cement analogue nanoscale model on which to perform MD simulations and analyse water transport properties in the gel. First the atomistic structure will be discussed and, later, the atomistic potentials. Finally, a desorption analysis is undertaken to discriminate between the models.

5.1 C-S-H Structure

At the nanoscale, C-S-H is composed of crystallite particles of about 10 nm dimensions orientated in all the directions. Its atomistic structure during early hydration, when its calcium to silicon ratio (C/S) in the range [0.8; 2], is still under intense discussion [81, 82, 83, 84, 85]. A consensus appears in the cement community to suggest that the C-S-H nano structure at low C/S ratios is close to tobermorite [81, 83, 85, 86, 87]. Several C-S-H analogue models based on tobermorite have been proposed during the last decades [9, 81, 85, 88, 45].

The tobermorite structure is composed of layers of calcium ions sandwiched by silica Dreierketten chains (ie: with two silicate tetrahedra dimers linked by a bridging silicate tetrahedron) as shown in figure 3.1. The space between these layers is called the interlayer space. Different types of tobermorite exist and can be discriminated according to the spacing of the CaO backbone chains: tobermorite 9 Å, 11 Å and 14 Å [45]. ^{29}Si NMR experiments can be used to analyse the C-S-H crystal nanostructure. This technique classifies silicate tetrahedra according to the number of other silicate tetrahedra in their close surrounding: each silicate belongs to a population Q_n, where n is the number of neighbours.

In the 9 Å and 11 Å anomalous tobermorite systems, the layer spacing is small enough to link the two layers by a Q_3 silicate type which creates a double chain structure as shown in figure 5.1.

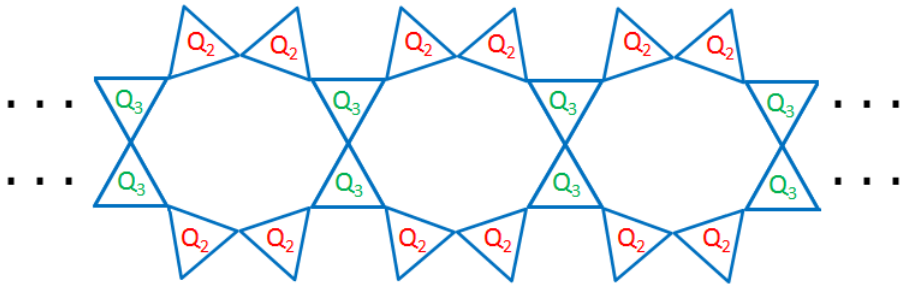

Figure 5.1: Blue triangles represent silicate tetrahedra. In tobermorite 9 Å and anomalous tobermorite 11 Å, the two silica chains are close enough to join. As a result, some silica tetrahedra are linking the two previous chains: these are the Q_3 silicates. The dots denote an infinite crystal.

In normal tobermorite 11 Å and 14 Å systems, the number of these Q_3 silicates is smaller which leads to two distinct silicate chains comprising dimers and bridging tetrahedra as shown in figure 5.2 [53, 86, 87].

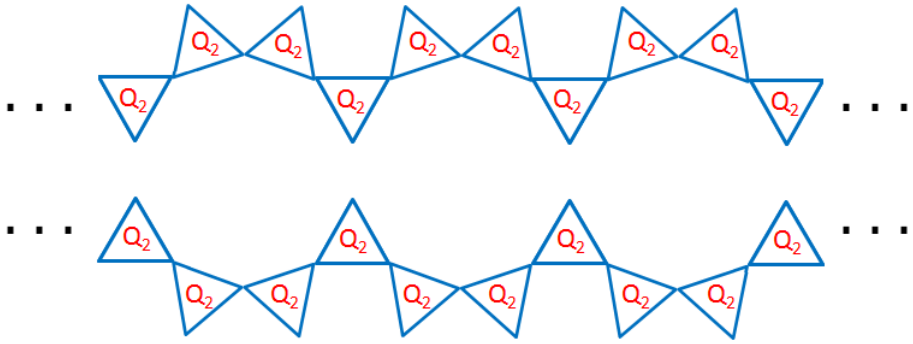

Figure 5.2: Blue triangles represent for silicate tetrahedra. In normal tobermorite 11 Å and tobermorite 14 Å, the two silicate chains are separated. As a result, there is no Q_3 silicates and only Q_2 (a lot for long chains) and Q_1 (a small amount as they only are at the extremities of the silica chains) silicates tetrahedra are present in such a structure. The dots denote an infinite crystal.

C-S-H is said to have the same layer composition as tobermorite 14 Å. The idea is to make the tobermorite system reach the C-S-H calcium to silicon ratio. To do so, the number of calcium ions in the model can be increased and/or the number of silicate groups can be decreased. ^{29}Si NMR signal shows that as the C/S ratio increases, the Q_3 signal decreases and the Q_1 signal increases, the distance between the two silica chains becomes bigger.
At C/S = 1.5, the strongest signal comes from the Q_1 silicon: the Dreierketten chain is now a chain of dimers as shown in figure 5.3 [83, 86].

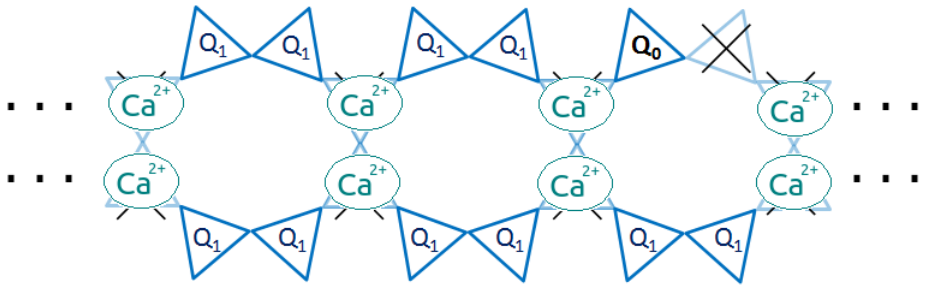

Figure 5.3: Blue triangles stand for silicate tetrahedra. In C-S-H, the Q_1 silicons are the most important silicate population. As the C/S ratio increases (some silicon tetrahedra are removed and replaced by calcium ions. Here, a Q_0 silicon is shown also. However, the number of Q_0 in such a structure is really small. The dots denote an infinite crystal.

This result is important: the structure is presented in figure 5.3. It is the skeleton of the atomistic model designed for this study as it will be shown in the next sections.

5.2 Structural Models

Nine different models were designed from a very simple silicate crystal to a more complex, and hopefully more accurate, modified tobermorite 14 Å system. They are labelled MD1 to MD9 (MD for Molecular Dynamics [Simulations]). Their atomistic structure and the potential choice are discussed here. The different models are presented in table 5.1. In this table, the desorption time τ_S is shown for each model, the calculations leading to these times are presented later in this chapter. In each case, the model comprised a crystal with periodic boundary conditions in each direction that was cut in the (xy) plane and the faces pulled apart so as to create a planar pore analogous to a cement gel pore. The pore was filled with water. The pore surfaces were treated in different ways as shown in table 5.1.

Model	Description	Potentials	τ_S [ns]
MD1	$\alpha - quartz(SiO_2)$ with Si, O mobile (100) surface terminated with O (surface O tethered) Pore size 1.0 nm - 1500 Si, 3240 O_{Si}, 886 H_2O	CLAY_FF SPC/E	0.32 ± 0.01
MD2	$\alpha - quartz(SiO_2)$ with Si, O mobile (100) surface with surface hydroxyls (H tethered) Pore size 1.0 nm - 1500 Si, 2760 O_{Si}, 480 OH, 743 H_2O	CLAY_FF SPC/E	0.15 ± 0.01
MD3	anomalous tobermorite 11 Å with Si, O mobile (100) surface with surface hydroxyls (H tethered) Pore size 1.0 nm - 768 Ca, 1152 Si, 2832 O_{Si}, 480 OH, 1512 H_2O	CLAY_FF SPC/E	0.30 ± 0.01
MD4f	tobermorite 14 Å with Si, O fixed, bridging tetrahedra replaced by Ca^{2+} (100) surface terminated with O (surface O tethered), Ca/Si=1.5 Pores sizes 1.1 nm and 3.3 nm - 192 Ca, 128 Si, 448 O_{Si}, 873 H_2O	CLAY_FF SPC/E	5.15 ± 0.02
MD4	tobermorite 14 Å with Si fixed, bridging tetrahedra replaced by Ca^{2+} (100) surface terminated with O (surface O tethered), Ca/Si=1.5 Pores sizes 1.1 nm and 3.3 nm - 192 Ca, 128 Si, 448 O_{Si}, 873 H_2O	CLAY_FF SPC/E	3.09 ± 0.01
MD5f	tobermorite 14 Å with Si, O fixed, bridging tetrahedra replaced by Ca^{2+} (100) surface terminated with O (surface O tethered), Ca/Si=1.5 Pores sizes 1.1 nm and 3.3 nm - 192 Ca, 128 Si, 448 O_{Si}, 873 H_2O	modified Freeman	7.17 ± 0.01
MD5	tobermorite 14 Å with Si fixed, bridging tetrahedra replaced by Ca^{2+} (100) surface terminated with O (surface O tethered), Ca/Si=1.5 Pores sizes 1.1 nm and 3.3 nm - 192 Ca, 128 Si, 448 O_{Si}, 873 H_2O	modified Freeman	0.14 ± 0.01
MD6f	tobermorite 14 Å with Si, O fixed, bridging tetrahedra replaced by Ca^{2+} (100) surface terminated with O (surface O tethered), Ca/Si=3.0 Pores sizes 1.1 nm and 3.3 nm - 224 Ca, 128 Si, 448 O_{Si}, 873 H_2O	CLAY_FF SPC/E	5.80 ± 0.01
MD6	tobermorite 14 Å with Si fixed, bridging tetrahedra replaced by Ca^{2+} (100) surface terminated with O (surface O tethered), Ca/Si=3.0 Pores sizes 1.1 nm and 3.3 nm - 224 Ca, 128 Si, 448 O_{Si}, 873 H_2O	CLAY_FF SPC/E	4.21 ± 0.02
MD7f	tobermorite 14 Å with Si, O fixed, bridging tetrahedra replaced by Ca^{2+} (100) surface terminated with O (surface O tethered), Ca/Si=3.0 Pores sizes 1.1 nm and 3.3 nm - 224 Ca, 128 Si, 448 O_{Si}, 873 H_2O	modified Freeman	6.84 ± 0.01
MD7	tobermorite 14 Å with Si fixed, bridging tetrahedra replaced by Ca^{2+} (100) surface terminated with O (surface O tethered), Ca/Si=3.0 Pores sizes 1.1 nm and 3.3 nm - 224 Ca, 128 Si, 448 O_{Si}, 873 H_2O	modified Freeman	0.12 ± 0.01
MD8	tobermorite 14 Å with Si, O fixed, bridging tetrahedra replaced by Ca^{2+} (100) surface with surface hydroxyls (H tethered), Ca/Si=1.5 Pores sizes 1.1 nm and 3.3 nm - 192 Ca, 128 Si, 384 O_{Si}, 64 OH_s, 873 H_2O	CLAY_FF SPC/E	0.18 ± 0.01
MD9	tobermorite 14 Å with Si, O fixed, bridging tetrahedra replaced by Ca^{2+} (100) surface terminated with O (surface O tethered) and hydroxides, Ca/Si=1.5 Pores sizes 1.1 nm and 3.3 nm - 192 Ca, 128 Si, 448 O_{Si}, 72 OH_l, 801 H_2O	CLAY_FF SPC/E	6.36 ± 0.02

Table 5.1: List of MD simulations with surface conditions (OH_s for surface hydroxyl group), different hydrated calcium ion (Ca^{2+}) densities, effect of hydroxide groups (OH_l), atomistic potentials and values of surface desorption times τ_S.

5.2.1 Previous C-S-H Analogues

The development of SiO_2 α-quartz crystal (MD1 and MD2) and the tobermorite 11 Å (MD3) models and the simulations resulting from them were performed by Jayesh Bhatt who was also in Peter McDonald's group in the department of Physics at the University of Surrey. These models are being included and presented here for completeness.

MD1 and MD2 Models: SiO_2 -Quartz Crystal.

This system is a simple α-quartz model that was cut in order to create a gel pore. The composition of such a system is well known [89].

Two SiO_2 models have been considered here: one with (100) surfaces comprising {Si-O^-} only that creates a gel pore surrounded by two negatively charged planes and another with (100) surfaces fully protonated with surface hydroxyls {Si-O-H} that creates a gel pore surrounded by two positive planes. The gel pore has a size of 1 nm and contains 886 water molecules in both models for a simulation cell of sizes $xyz = 5.5 \times 5.19 \times 3.35$ nm^3 at a temperature of 300K. The number of atoms in such a structure is 8000.
The model with surface hydroxyls is shown in figure 5.4. Periodic boundary conditions are used in the three dimensions.

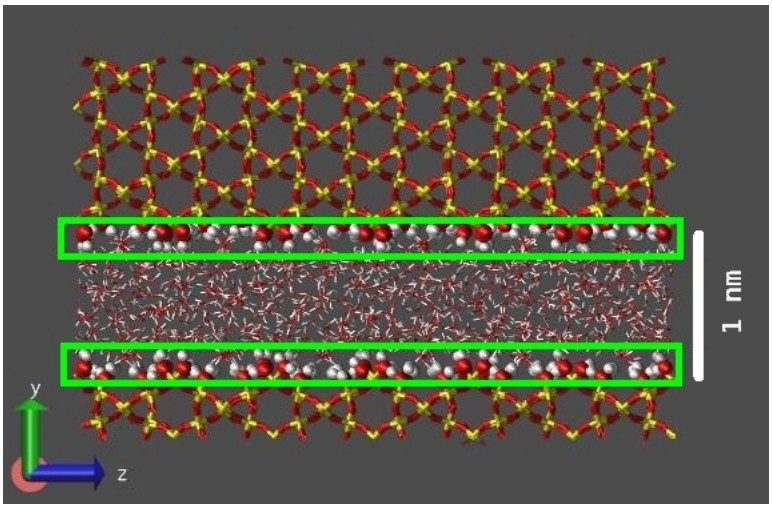

Figure 5.4: A SiO_2 α-quartz system with protonated surface creates a gel pore filled with water molecules. Red and yellow lattice: the SiO_2 crystal; red and white balls: surface hydroxyls; red and white sticks: water molecules. Here, this is a snapshot of MD2 as suggested by the protonated surface that is highlighted by the green rectangles. The white line refers to the size of the gel pore of 1 nm.

MD3 Model: Anomalous Tobermorite 11 Å

As said previously, the tobermorite structure is said to be a good candidate for the C-S-H nanostructure in the cement community. A first model based on anomalous tobermorite 11 Å has been designed by Jayesh Bhatt[87].
The main difference between this model and the SiO_2 model is the presence of layers of calcium

ions sandwiched by silica chains. The (100) surfaces are protonated. The gel pore has a size of 1 nm and contains 792 water molecules for a simulation cell of sizes $xyz = 4.55 \times 4.49 \times 5.86$ nm^3 (at room temperature and depending on the potential used). The number of atoms in such a structure is ≈ 10000.
The model is shown in figure 5.5.

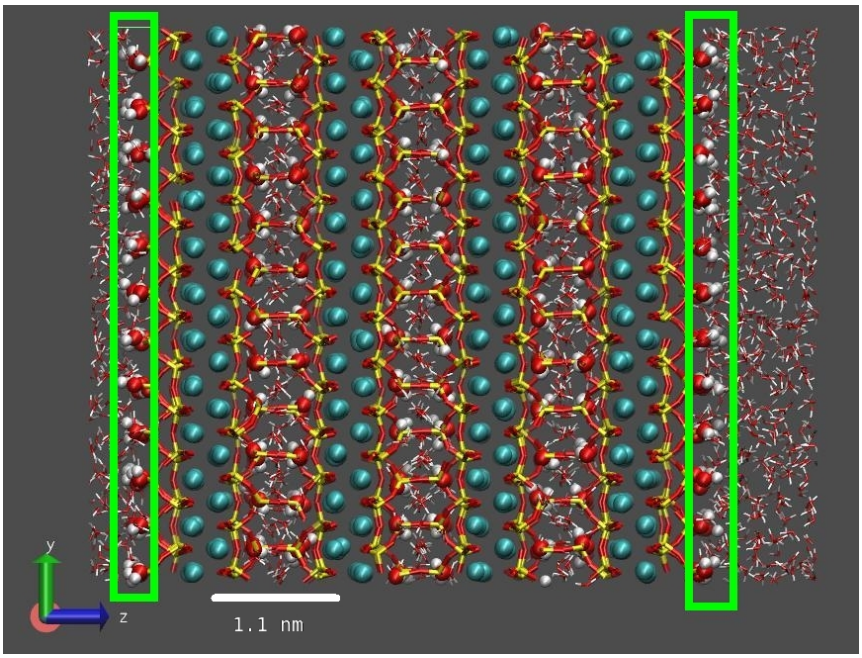

Figure 5.5: An anomalous tobermorite 11 Å system with protonated surface creates a gel pore filled with water molecules. Four pores are shown: three interlayer pores and one gel pore (that wraps around the end of the simulation cell as drawn). Red and yellow lattice: the SiO_2 crystal; red and white balls: surface hydroxyls (highlighted by the green rectangles); red and white sticks: water molecules; green ball: hydrated calcium ions. The white line refers to the size of the interlayer pore of 1.1 nm.

In this model, the Ca^{2+} ions are placed between silica chains, they are not in contact with water and they are not moving.

5.2.2 MD4 to MD9 Models: Modified Tobermorite 14 Å

C-S-H is known to have a similar layer composition to tobermorite 14 Å. The structure of tobermorite 14 Å was described by Bonaccorsi et al. [90]. However, a few structure modifications have to be undertaken in order to accommodate the Q_n distribution experimental data described in section 5.1 and which suggest C-S-H surfaces are composed of chains of silicate dimer at a C/S ratio of 1.5 [81].
The crystal surfaces that surround the interlayer and gel pores were designed from tobermorite 14 Å as follows. First, the bridging silicate tetrahedra have to be removed. This way, the (100) surfaces are formed of silicate dimers. The $\{Si_{dimer}\text{-}Si_{bridge}\}$ connections between the dimers and the bridging tetrahedra are replaced by $\{Si_{dimer}\text{-}O\}$ connections. The empty spaces between dimers are bridged with hydrated Ca^{2+} ions in order to reach a C/S ratio of 1.5. This process is presented in figure 5.6.

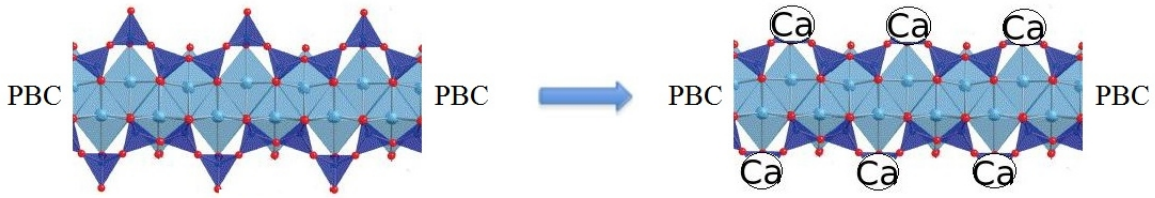

Figure 5.6: This figure is a simple illustration of the transformation of tobermorite 14 Å to the system with good Q_n and C/S ratio values. Dark blue triangles represent silicon tetrahedra; red balls are oxygens, light blue balls are calciums in layers and "Ca" in circles represent the hydrated calcium ions added to the system. The silicate dimer chains can then be easily seen. Here, this chain is infinite (ie: PBC means periodic boundary conditions). This figure is adapted from Richardson [45]

.

Contrary to earlier models, the size of the gel pore is chosen to be 3.3 nm in accordance with the ^{1}H NMR experimental value [36]. In the same way, the size of the interlayer pore is chosen to be 1 nm. The number of water molecules is chosen to be 745 for a simulation cell of size $xyz = 2.25 \times 2.96 \times 5.25$ nm^3 (at room temperature and depending on the potential used). Some atom positions can be fixed depending on the simulation (as will be explained later). The number of atoms in such a structure is 3500 (smaller than previous models in order to reach a longer simulation time).

A slight difference between MD1-4 models and this one is how to determine the number of water molecules in the gel but also in the interlayer pores. To do so, the following rule is implemented: according to some thermogravimetry experiments performed in Dijon, the water to silicon ratio (W/Si) in the interlayer is 2 [81]. This is the reason why some atom positions can be fixed. This way, the two assumptions of the W/Si ratio and the interlayer pore size are respected regardless the potential used in the simulation (the forces acting on the atoms would then determine a new volume for the interlayer).

A second rule is to look at the bulk density to determine the number of water molecules in the gel pore. To do so, a first approximation of the number of water molecules is made considering the volume available in the pore and the water density at room temperature of 1 kg.m^{-3}. A simulation is run and a density profile is generated. The bulk is defined where the density profile is flat in the middle of the pore, and its density is compared to the room temperature bulk density of 1 kg.m^{-3}. If the model bulk density if smaller than 1 kg.m^{-3}, water molecules are added. If the model bulk density is bigger than 1 kg.m^{-3}, water molecules are removed. This process is repeated until a good density value is found. Note that this process is made in order to respect the chosen pores sizes. Indeed, NPT simulations (volume can change) could be run to reach this equilibrium, but the assumptions of the pore sizes (1 nm for the interlayer pore and 3.3 nm for the gel pore) would not be respected.

The modified tobermorite 14 Å model (MD4, MD4f, MD5 and MD5f) is shown in figure 5.7.

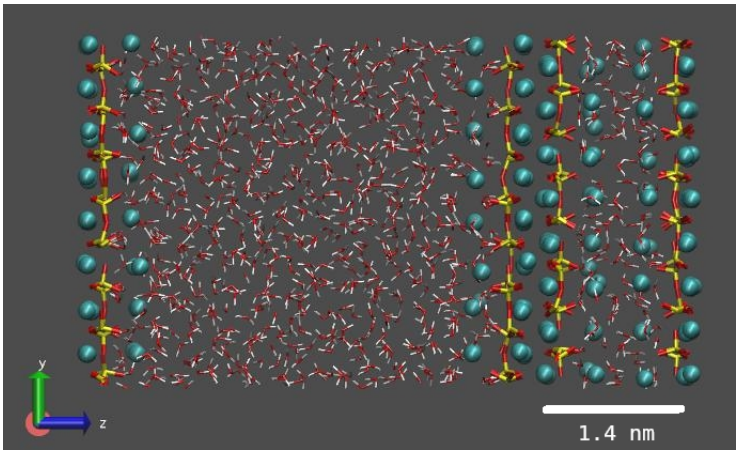

Figure 5.7: A snapshot of the simulation of the basic modified tobermorite 14 Å system is shown here (here, this is MD4 but the structure is the same for MD4f, MD5 and MD5f). Red and yellow chains are silicate dimer chains; blue balls are calciums and red and white sticks are water molecules. The gel pore is on the left and the interlayer pore on the right. The white line refers to the size of the interlayer pore of 1.4 nm.

Finally, a range of different variant models can be made from the basic MD4 structure. The initial (100) surface can be terminated by surface hydroxyls {Si-O-H} which will affect the behaviour of Ca^{2+} ions (figure 5.8). This is MD8.

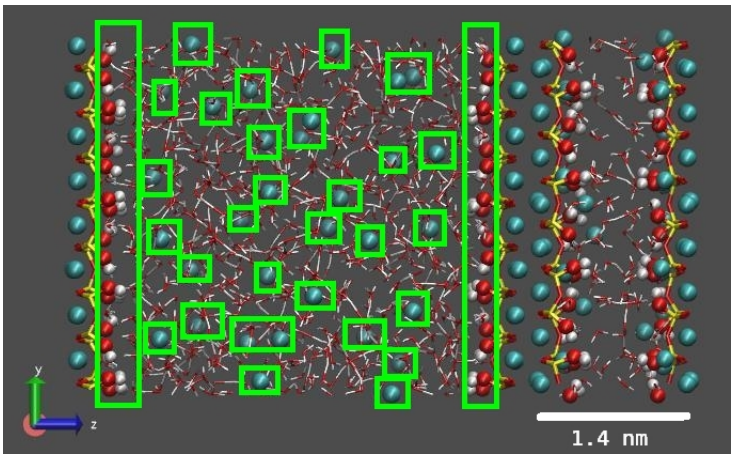

Figure 5.8: The previous modified tobermorite 14 Å system is modified here: the surface is protonated, this is MD8. As a consequence, the positive calcium ions are repelled to the bulk by the negative surface hydroxyls. The meaning of the different forms and colors are the same as in previous figure and red and white balls represent surface hydroxyls and green balls calcium ions (highlighted by green rectangles). The white line refers to the size of the interlayer pore of 1.4 nm.

The number of Ca^{2+} can be increased by adding calcium ions close to the crystal layers of the different pores. Such a model is shown in figure 5.9. This was done for models MD6, MD6f, MD7 and MD7f.

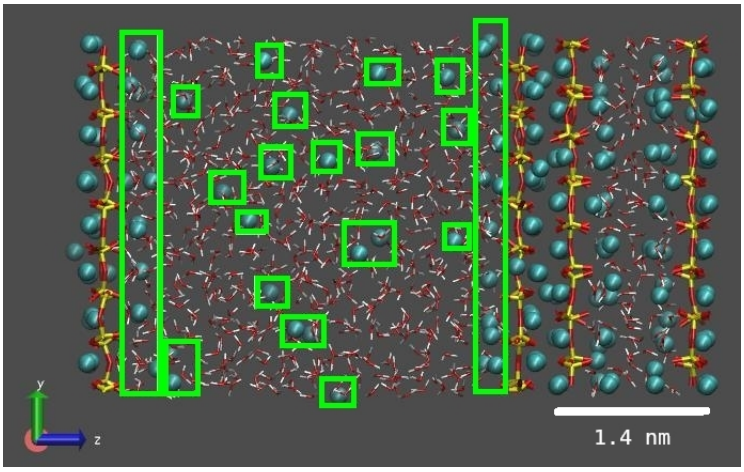

Figure 5.9: The previous modified tobermorite 14 Å system is modified here: the number of hydrated calcium ions is increased by a factor 2. Here this is a snapshot of model MD6 but the same behaviour is obtained with MD6f, MD7 and MD7f. The meaning of the different forms and colors are the same as in previous figure. The hydrated calcium ions that cannot find a stable position close to the surface (forming a negatively charged plan) are repulsed to the center of the pore. Surface stable calcium ions and the one rejected to the center of the pore are highlighted by green rectangles. The white line refers to the size of the interlayer pore of 1.4 nm.

Lastly hydroxides can be added in order to reach a charge balance of the system as can be seen in figure 5.10. This is MD9. The creation of such an hydroxide potential is discussed in the next section.

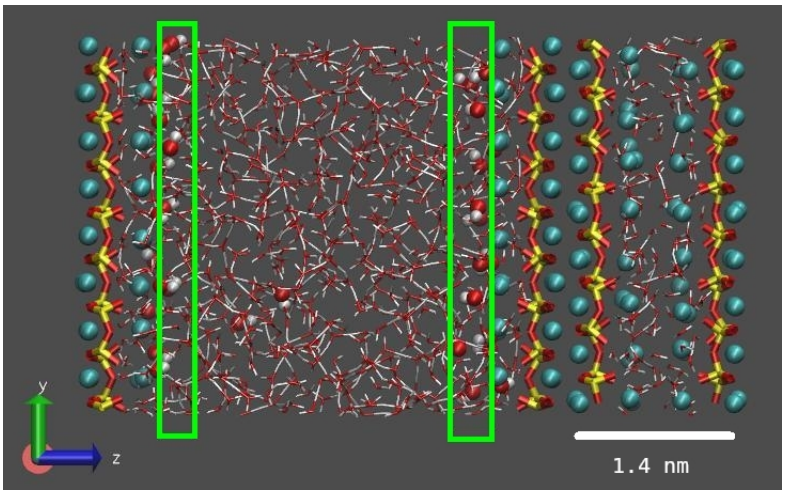

Figure 5.10: The previous modified tobermorite 14 Å system is modified here: hydroxide groups charge balance the hydrated calcium ions. This is MD9. The meaning of the different forms and colors are the same as in previous figure but here red and white balls are hydroxides. The white line refers to the size of the interlayer pore of 1.4 nm.

5.3 Atomistic Potentials

Once the atomistic configuration is made, the next step is to use an appropriate atomistic potential to run MD simulations. Unfortunately, there are no optimised potential sets for tobermorite. However, potentials have been developed for similar structures: CLAY_FF and modified Freeman potentials. A simple, but not accurate, potential for hydroxides has been designed to see their behaviour in such a system. This hydroxide potential was developed for the purpose of this study and is presented in section 5.3.1.

5.3.1 CLAY_FF and SPC/E

The CLAY_FF potential was originally designed by Cygan et al [69] for the simulations of hydrated and multicomponent mineral systems with interface with hydrated media. Such a potential is described here and is based on Lennard Jones potentials. Atoms have, in most cases, partial charges. The atoms and interactions of interest are developed here in tables 5.2 and 5.3.

Species	Symbol	M [g/mol]	q [e]
Tetrahedral silicon	Si	27.9000	2.1000
Hydroxide calcium	CaS or Cal	39.8800	1.0500
Hydrated calcium	CaL	39.8800	2.0000
Bridging oxygen	OSm or OSf	15.8000	−1.0500
Water oxygen	OW	15.9900	−0.8200
Water hydrogen	HW	1.0080	0.4100
Hydroxyl (surf) oxygen	Ohs	15.8000	−0.9500
Hydroxyl (surf) hydrogen	Hos	0.8000	0.4250

Table 5.2: The species used in the models are defined in this table. Their CLAY_FF molar masses M and charges q are given.

Species Interacting	Potential Type	Variables	
CaL-CaL	lj (E_0,r_0)	4.3384×10^{-3}	2.8720
CaL-{Cal or CaS}	lj (E_0,r_0)	3.0769×10^{-3}	4.2168
CaL-Si	lj (E_0,r_0)	1.8612×10^{-5}	3.0870
CaL-{OX}	lj (E_0,r_0)	5.4083×10^{-3}	3.0190
{Cal or CaS}-{Cal or CaS}	lj (E_0,r_0)	2.1821×10^{-7}	5.5615
{Cal or CaS}-Si	lj (E_0,r_0)	1.3200×10^{-7}	4.4317
{Cal or CaS}-{OX}	lj (E_0,r_0)	3.8356×10^{-5}	4.3638
Si-Si	lj (E_0,r_0)	7.9849×10^{-8}	3.3019
Si-{OX}	lj (E_0,r_0)	2.3202×10^{-5}	3.2340
{OX}-{OX}	lj (E_0,r_0)	6.7419×10^{-3}	3.1660

Table 5.3: The potential interactions between the different atoms involved in this study "CLAY_FF" simulations are shown here. Only the Lennard-Jones (lj) potential is used where E_0, in [eV], stands for the dissociation energy between the two atoms interacting and r_0, in [Å], is the equilibrium bond distance as described in equation 3.3. Here, {OX}={OSm or OSf or Ohs or OW}.

Hydroxide Potential

An hydroxide potential has been also partially developed. This potential has to be considered very carefully: it was calibrated in order to reproduce the calcium/water radial distribution function and to have a global charge of -e in order to charge-balance the system. MD4 is not charge balanced because CLAY_FF was not designed for modified tobermorite 14 Å system. No other physical property was tested. The basic idea was to see where the hydroxyl groups, if any in C-S-H, would go in the modified tobermorite 14 Å structures. Note that the SPC/E water potential and also TIP4P does not allow H exchange between water or with surface, and then do not take into account the hydroxide groups. The main features of such a potential are listed in tables 5.4 and 5.5.

Species	Symbol	M [g/mol]	q [e]
Hydroxide oxygen	Oh	15.9900	−1.4238
Hydroxide hydrogen	Ho	1.0080	0.4238

Table 5.4: The hydroxide ion features are defined here: molar masses M and charges q are shown. The total charge of an hydroxide is -1 in such a way that two of them can charge balance the hydrated Ca^{2+} ions that have an integer +2 charge.

Species Interacting	Potential Type	Variables	
CaL-Oh	lj (E_0,r_0)	5.2061×10^{-3}	3.2000
CaS-Oh	lj (E_0,r_0)	3.7822×10^{-5}	4.6808
Si-Oh	lj (E_0,r_0)	2.2879×10^{-5}	3.5510
{OSm or OSf}-Oh	lj (E_0,r_0)	6.6480×10^{-3}	3.4827
OW-Oh	lj (E_0,r_0)	6.7419×10^{-3}	3.2000
Oh-Oh	lj (E_0,r_0)	6.5554×10^{-3}	3.8000

Table 5.5: The potential interactions between the hydroxide and the different atoms involved in this study simulations using CLAY_FF potential are listed. Only the Lennard-Jones (lj) potential is used where E_0, in [eV], stands for the dissociation energy between the two atoms interacting and r_0, in [Å], is the equilibrium bond distance as described in equation 3.3.

5.3.2 Modified Freeman and TIP4P Potentials

Another candidate is the modified Freeman potentials. This potential was originally designed by Freeman et al [71] to model organic and mineral systems like clays. However, this potential yielded a flattened crystal interface for the tobermorite system which is unphysical and was only partially corrected by modifications proposed by Galmarini [91]. This modified potential is based on Lennard Jones, Buckingham, Morse and screened harmonic potentials that were defined in the chapter 3 section 3.3.2. Atoms can have integer or partial charges. The atoms and interactions are listed in tables 5.6 and 5.7.

Species	Symbol	M [g/mol]	q [e]
Tetrahedral silicon	Si	28.0850	4.0000
Hydroxide calcium	Ca	39.8800	2.0000
Bridging oxygen	OS	16.0000	−2.0000
Water oxygen	OW	15.9996	0.0000
Water pseudo atom	OM	0.0000	−1.1128
Water hydrogen	HW	1.0080	0.5564
Hydroxyl oxygen	Oh	16.0000	−1.4000
Hydroxyl hydrogen	Ho	1.0080	0.4000

Table 5.6: The species used in the models are defined in this table. Their "Freeman" molar masses M and charges q are listed.

Species Interacting	Potential Type	Variables				
Si-OS	buck (A,ρ,C)	1283.9073	0.3205	10.6616	-	-
Si-OW	buck (A,ρ,C)	1283.9073	0.3205	10.6616	-	-
Si-Oh	buck (A,ρ,C)	983.5560	0.3205	10.6616	-	-
Ca-OS	buck (A,ρ,C)	1090.4000	0.3437	0.0000	-	-
Ca-OW	buck (A,ρ,C)	1186.6000	0.2970	0.0000	-	-
Ca-Oh	buck (A,ρ,C)	2251.0500	0.2970	0.0000	-	-
OS-OS	buck (A,ρ,C)	22764.0000	0.1490	27.8800	-	-
OS-OW	buck (A,ρ,C)	22764.0000	0.1490	28.9200	-	-
OS-HW	buck (A,ρ,C)	396.2700	0.2500	0.0000	-	-
OS-Oh	buck (A,ρ,C)	22764.0000	0.1490	13.9400	-	-
OS-Ho	n-m (E_0,n,m,r_0)	0.0073	9	6	2.7100	-
OW-OW	lj (E_0,r_0)	8.0314×10^{-3}	3.1589	-	-	-
OW-Oh	n-m (E_0,n,m,r_0)	0.0013	9	6	4.6300	-
OW-Ho	n-m (E_0,n,m,r_0)	0.0556	9	6	1.81712	-
Oh-Oh	buck (A,ρ,C)	22764.0000	0.1490	6.9700	-	-
Oh-Ho	mors (E_0,r_0,k)	7.0525	0.9429	3.1749	-	-
Si-OS-Si	shrm (k,θ_0,ρ_1,ρ_2,r_c)	15.4963	132.0000	1.6000	1.600	3.000
Si-Oh-Ho	shrm (k,θ_0,ρ_1,ρ_2,r_c)	15.4963	141.5000	1.6000	1.200	2.600
OS-Si-OS	shrm (k,θ_0,ρ_1,ρ_2,r_c)	15.4963	109.4667	1.6000	1.600	3.000
Oh-Si-OS	shrm (k,θ_0,ρ_1,ρ_2,r_c)	15.4963	109.4667	1.6000	1.600	3.000
Oh-Si-Oh	shrm (k,θ_0,ρ_1,ρ_2,r_c)	15.4963	109.4667	1.6000	1.600	3.000

Table 5.7: The potential interactions between the different atoms involved in the simulations using modified Freeman potentials are shown here. For the Buckingham potential, A is in [eV], ρ is in [Å] and C is in [eV/Å^6]. For the $n-m$ potential, E_0 is in [eV], r_0 is in [Å] and n and m are integers with no unit. For the Lennard-Jones potential, E_0 is in [eV] and r_0 is in [Å]. For the Morse potential, E_0 is in [eV], r_0 is in [Å] and k is in [Å^{-1}]. Finally, for the screened harmonic angular potential, $\rho_{1,2}$ are in [Å], r_c is the cutoff distance for this interaction in [Å], θ is in [degree] and k is in [degree^{-2}]. Details of all these parameters can be found in chapter 3 section 3.3.2.

5.4 Simulation Details

Only NVT simulations are run. Indeed, to reach equilibrium with a chosen set of potentials, it was necessary to fix the positions of some atoms in the crystal. However, this means that the NPT ensemble (which allows the volume to change during a simulation) is not available. This is why some water molecules were added or remove in order to reach the correct bulk water density. MD4f, MD5f, MD6f and MD7f were run with some crystal atoms positions fixed (silicon and oxygen). MD4, MD5, MD6, MD7, MD8 and MD9 were run with only the silicons positions fixed. MD1, MD2 and MD3 were run without any atoms positions fixed.

All the simulations run in this study use orthorhombic periodic boundary conditions as seen in chapter 3 section 3.3.3. The simulation temperature is 300K, and the target pressure is 0 Bar. The simulations last 3 ns and coordinates are recorded every ps. Also, most of the modified tobermorite 14 Å models are not charge-balanced. This causes an error (of unknown significance) as the Ewald summation procedure was used to compute the charge contribution to the energies. Ideally, the Ewald technique should be used on a charge neutral system.

5.5 Model Selection

The different structural models presented in this chapter were associated with a different potential set. MD simulations output data were treated and detailed here: a desorption analysis was performed in order discriminate the models.

5.5.1 Density Profiles and Surface Desorption

The different modified tobermorite simulations run to determine which model should be used to analyse water dynamic properties and ^{1}H NMR relaxation times are shown here. The gel pore density profiles and the surface desorptions are also shown. The surface is defined by the closest distinct peaks to the surfaces. The link between peak and surface border can be seen in the figures. The interesting results and features of the first C-S-H analogues studied before this work (SiO_2 α-quartz crystal surface protonated or not with CLAY_FF potential simulation called MD1 and MD2 [17, 18], and anomalous tobermorite 11 Å with CLAY_FF potential simulation called MD3) will be only presented in a summary table.

All the density profile figures are on the left and the color code is as follows: the yellow solid lines show the silicate crystal, the green solid lines represent the gel hydrated calcium ions, the solid red and black lines refer respectively to the water oxygens and hydrogens, and finally, in one figure, the solid blue line represents the hydroxide oxygen. Surface hydroxyls are not shown here to simplify the figures as they are attached to the crystal surface. The surface layers are defined by the closest two peaks from the crystal of the water oxygen density profile for MD4-7 and MD9 and by the closest peak from the crystal for MD8 since only one peak is identified. With the notation previously introduced, the $\{SL > SL > SL\}$ set of water molecules is considered here.

All the desorption curves are on the right of the figures and are associated directly to the density profiles on the left where the surface layers are defined. The black dots curves represent the simulation data and the red solid lines refer to the decaying exponential fits from which the desorption times, τ_S, are deduced.

The two first sets of density profiles and desorption curves (figures 5.11 and 5.12) represent the modified tobermorite 14 Å systems with crystal atoms positions fixed (ie: silicate dimers and associated oxygen atoms cannot move during the simulation). The first set uses the CLAY_FF potential (MD4f) whereas the second was performed with the modified Freeman potentials (MD5f). In these conditions, the results seem to be simular. However, freezing the whole crystal is a constraint that may not represent the surface oxygen displacements and their effects on water.

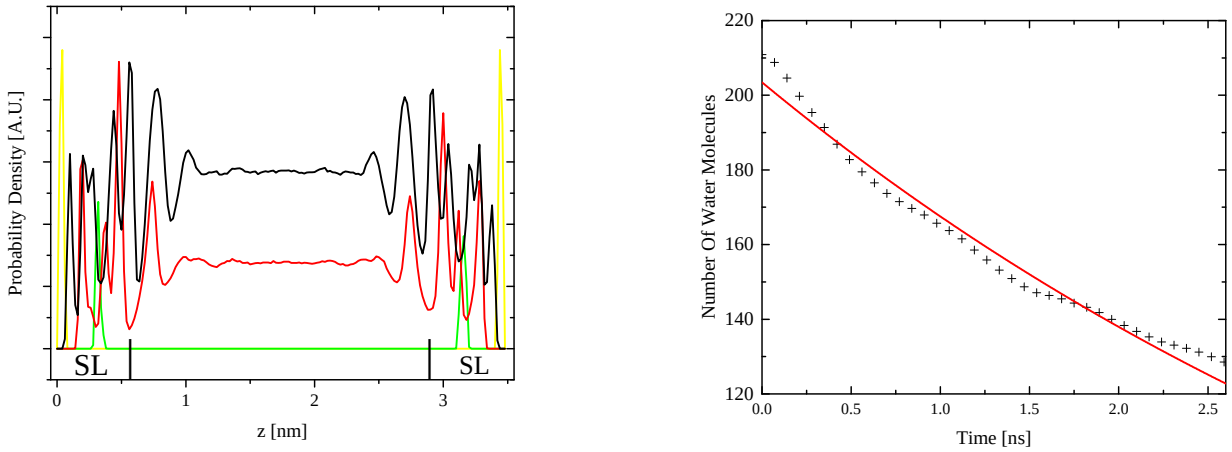

Figure 5.11: MD4f: Modified tobermorite 14 Å simulation with the whole crystal atoms positions fixed and CLAY_FF potential used. Left: density profile; right: surface desorption. $\tau_S = 5.15 \pm 0.02$ *ns as listed in table 5.1. On the left, yellow stands for silicate, green stands for calcium, red stands for water oxygen and black stands for water hydrogen. On the right, black crosses are the simulated desorption data and the solid red line is its exponential fit. The surface layers (SL) are limited by the silicate peaks and the bars on the abscissa.*

The two following sets of curves (figures 5.13 and 5.14) represent the same modified tobermorite 14 Å systems but this time with only fixed silicate atoms (ie: surface oxygen can move now). The first set uses CLAY_FF potential whereas the second one was performed with modified Freeman potentials.

The difference is striking: the desorption in the first case (with CLAY_FF potential: MD4) is comparable to when surface oxygens positions are fixed with a marginally lower desorption time whereas in the second case (with modified Freeman potentials: MD5), the water molecules desorb much faster. It seems that when the crystal atoms positions are fixed, in the case of Freeman potential, some water molecules are "trapped" in the lattice created by the fixed surface, even if water is mobile.

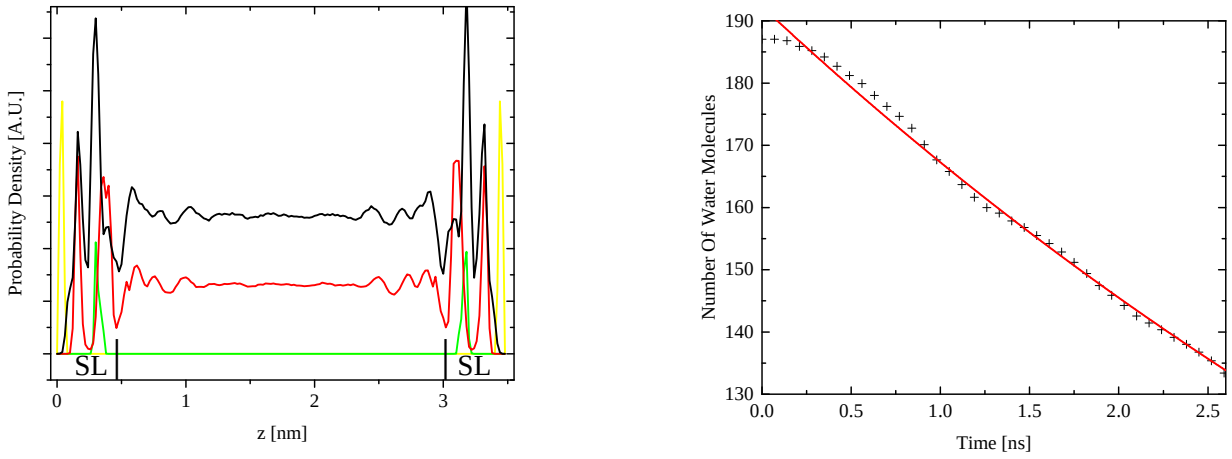

Figure 5.12: MD5f: Modified tobermorite 14 Å simulation with the whole crystal atoms positions fixed and modified Freeman potentials used. Left: density profile; right: surface desorption. $\tau_S = 7.17 \pm 0.01$ *ns as listed in table 5.1. On the left, yellow stands for silicate, green stands for calcium, red stands for water oxygen and black stands for water hydrogen. On the right, black crosses are the simulated desorption data and the solid red line is its exponential fit. The surface layers (SL) are limited by the silicate peaks and the bars on the abscissa.*

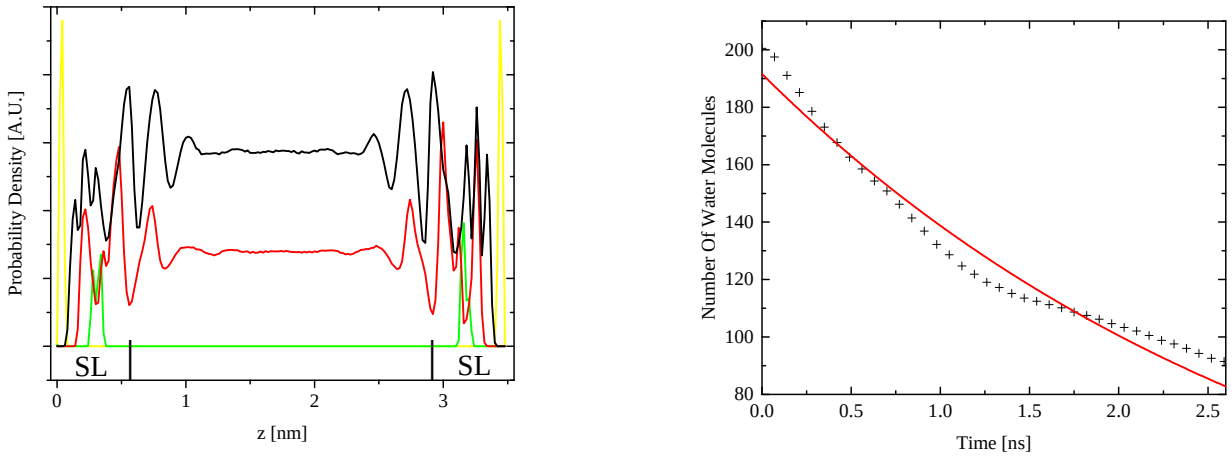

Figure 5.13: MD4: Modified tobermorite 14 Å simulation with only silicate atoms positions fixed and CLAY_FF potential used. Left: density profile; right: surface desorption. $\tau_S = 3.09 \pm 0.01$ *ns as listed in table 5.1. On the left, yellow stands for silicate, green stands for calcium, red stands for water oxygen and black stands for water hydrogen. On the right, black crosses are the simulated desorption data and the solid red line is its exponential fit. The surface layers (SL) are limited by the silicate peaks and the bars on the abscissa.*

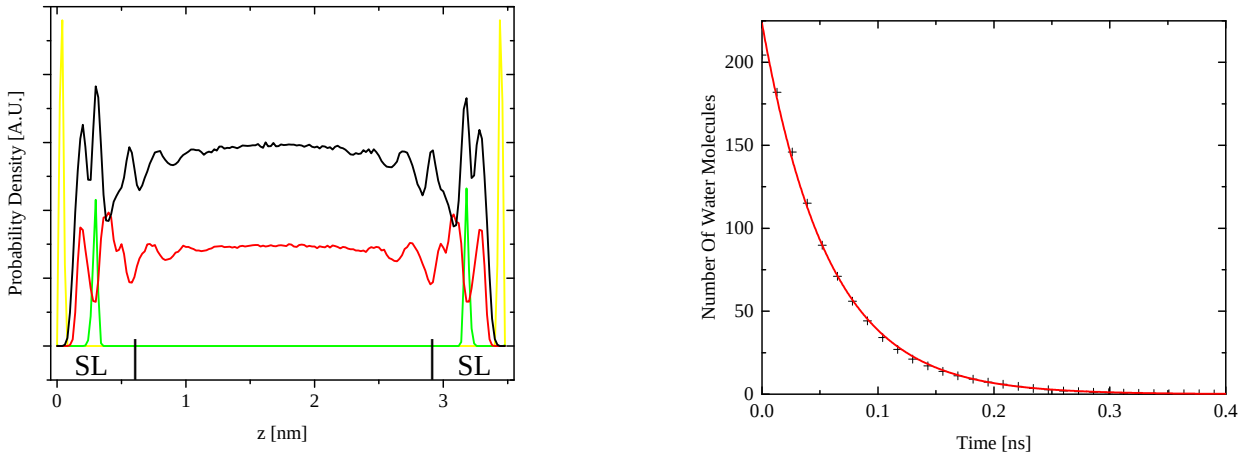

Figure 5.14: MD5: Modified tobermorite 14 Å simulation with ony silicate atoms positions fixed and modified Freeman potentials used. Left: density profile; right: surface desorption. $\tau_S = 0.14 \pm 0.01$ *ns as listed in table 5.1. On the left, yellow stands for silicate, green stands for calcium, red stands for water oxygen and black stands for water hydrogen. On the right, black crosses are the simulated desorption data and the solid red line is its exponential fit. The surface layers (SL) are limited by the silicate peaks and the bars on the abscissa.*

The four following sets of curves (figures 5.15 to 5.18) show the density profiles and surface desorption curves for the modified tobermorite 14 Å systems where the number of hydrated calcium ions was multiplied by two to see the effect on their layout close to the surface if the Ca/Si ratio in the pores was doubled. As a result, all the added calcium ions are repelled to the center of the gel pore: the lattice of the former bridging tetrahedra describes a set of stable positions for hydrated calcium ions and this set seems to be the only one close to the surface. This can be seen on the density profiles by a solid green line that is not vanishing in the middle of the pore.

The results are quite similar to the ones obtained previously when the Ca/Si ratio was 1.5. The freezing of the crystal or only the silicon is seen the same way: with the freezing crystal assumption, the CLAY_FF (MD6f) and modified Freeman potentials (MD7f) simulations have respectively a desorption time of τ_S=5.88 ns and 6.88ns (figures 5.15 and 5.16); with only the fixed silicate assumption (respectively MD6 and MD7), these numbers become τ_S=4.5 ns and 0.14 ns (figures 5.17 and 5.18) as listed in table 5.1.

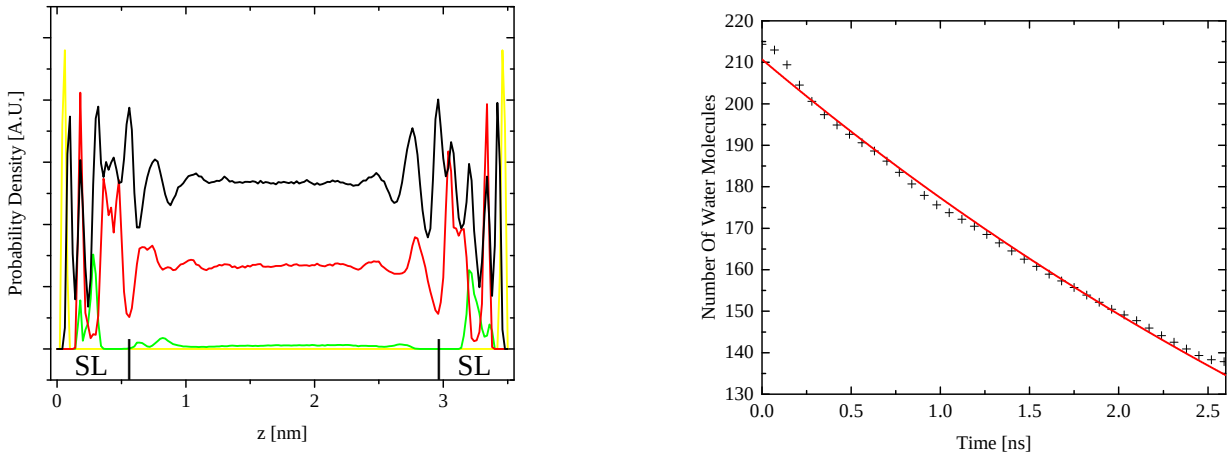

Figure 5.15: MD6f: Modified tobermorite 14 Å simulation with the whole crystal atoms positions fixed and CLAY_FF potential used and additional hydrated calcium ions. Left: density profile; right: surface desorption. $\tau_S = 5.80 \pm 0.01$ *ns as listed in table 5.1. On the left, yellow stands for silicate, green stands for calcium, red stands for water oxygen and black stands for water hydrogen. On the right, black crosses are the simulated desorption data and the solid red line is its exponential fit. The surface layers (SL) are limited by the silicate peaks and the bars on the abscissa.*

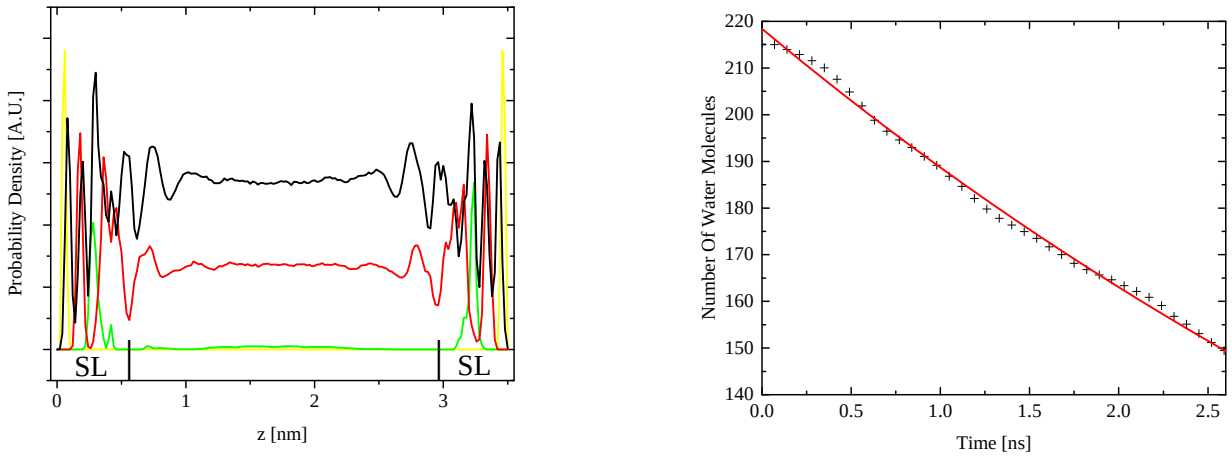

Figure 5.16: MD7f: Modified tobermorite 14 Å simulation with the whole crystal atoms positions fixed and modified Freeman potentials used and additional hydrated calcium ions. Left: density profile; right: surface desorption. $\tau_S = 6.84 \pm 0.01$ *ns as listed in table 5.1. On the left, yellow stands for silicate, green stands for calcium, red stands for water oxygen and black stands for water hydrogen. On the right, black crosses are the simulated desorption data and the solid red line is its exponential fit. The surface layers (SL) are limited by the silicate peaks and the bars on the abscissa.*

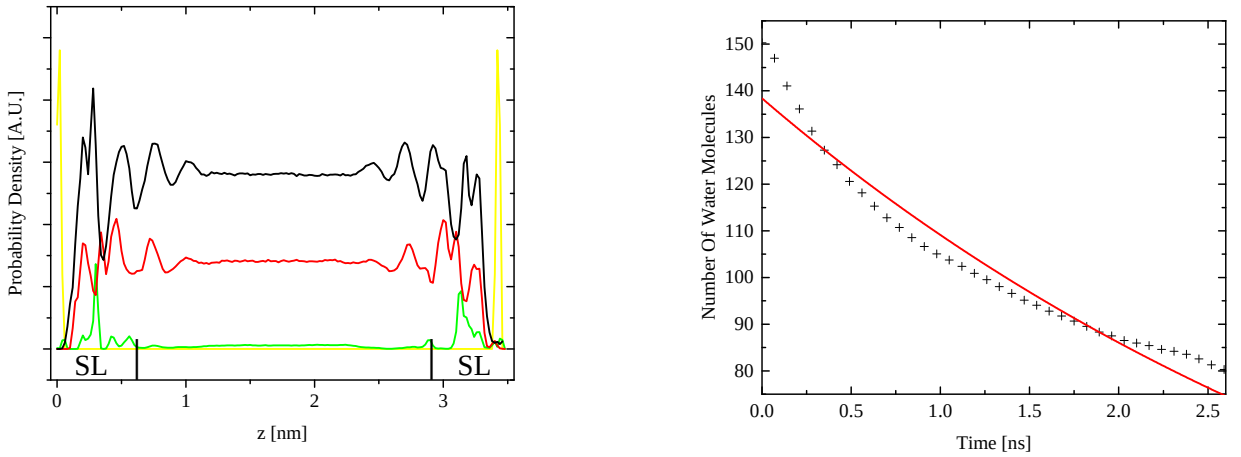

Figure 5.17: MD6: Modified tobermorite 14 Å simulation with only silicate atoms positions fixed and CLAY_FF potential used and additional hydrated calcium ions. Left: density profile; right: surface desorption. $\tau_S = 4.21 \pm 0.02$ *ns as listed in table 5.1. On the left, yellow stands for silicate, green stands for calcium, red stands for water oxygen and black stands for water hydrogen. On the right, black crosses are the simulated desorption data and the solid red line is its exponential fit. The surface layers (SL) are limited by the silicate peaks and the bars on the abscissa.*

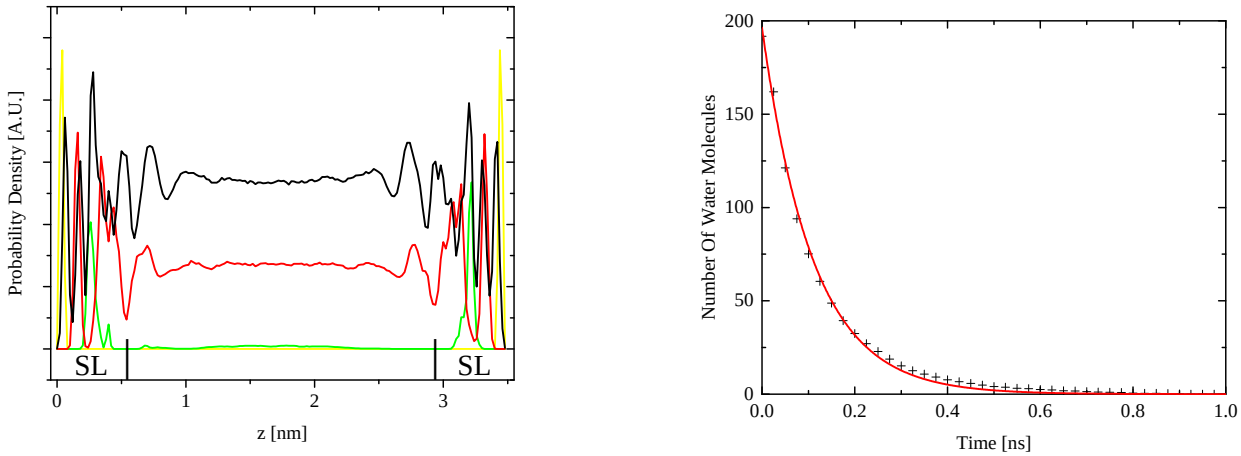

Figure 5.18: MD7: Modified tobermorite 14 Å simulation with ony silicate atoms positions fixed and modified Freeman potentials used and additional hydrated calcium ions. Left: density profile; right: surface desorption. $\tau_S = 0.12 \pm 0.01$ *ns as listed in table 5.1. On the left, yellow stands for silicate, green stands for calcium, red stands for water oxygen and black stands for water hydrogen. On the right, black crosses are the simulated desorption data and the solid red line is its exponential fit. The surface layers (SL) are limited by the silicate peaks and the bars on the abscissa.*

The next set of curves (figures 5.19) represents the modified tobermorite 14 Å systems where the surfaces are fully protonated (MD8). The effect on the calcium can be seen by the absence

of calcium peaks close to the surfaces. Indeed, the calcium ions are positively charged and are repulsed from a positively charged plane formed by the hydroxyl hydrogens directed to the center of the gel pore. As a consequence, the surface desorption time for such a system is τ_S=0.187 ns within the limits of the definition of the surface layers. Indeed, water molecules are always moving and the arbitrary choice of a plane for the surface border can be explained because of the density profle analysis but is still a simplified assumption of a more complex problem: the surface layer is defined by the zone between the crystal and the first weel, hence, it contains the closest oxygen peak.

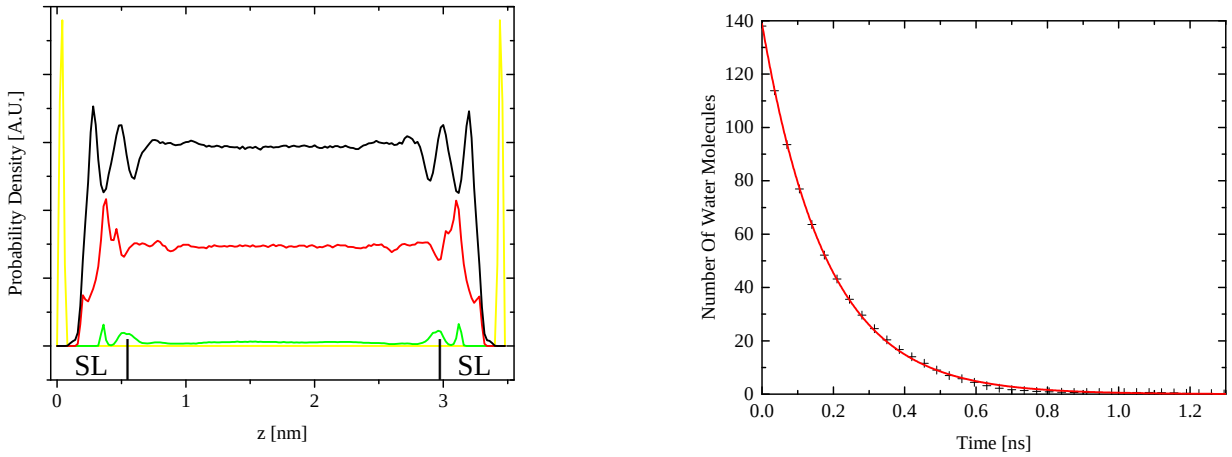

Figure 5.19: MD8: Modified tobermorite 14 Å simulation with the whole crystal atoms positions fixed and CLAY_FF potential used and surface protonated. Left: density profile; right: surface desorption. $\tau_S = 0.18 \pm 0.01$ ns as listed in table 5.1. On the left, yellow stands for silicate, green stands for calcium, red stands for water oxygen and black stands for water hydrogen. On the right, black crosses are the simulated desorption data and the solid red line is its exponential fit. The surface layers (SL) are limited by the silicate peaks and the bars on the abscissa.

Finally, a last set of curves (figures 5.20) shows the modified tobermorite 14 Å systems with hydroxide groups (called MD9): this modification was taken into account in order to charge balance the calcium in the CLAY_FF potential. Moreover, the question of the behaviour in such a system is interesting because ^{1}H NMR also sees these groups. Despite the fact that the potential of these groups has to be taken into account very carefully, the simulation shows that the hydroxides are located close to the hydrated calcium ions. Indeed, their respective charges in a neutral liquid act in such a way that they come close together as shows the blue hydroxyl peaks surround the green calcium ones. The effect of hydroxides on the surface desorption of water seems to be negligible: the desorption time here is τ_S=6.49 ns. Note that the whole crystal atoms positions are fixed.

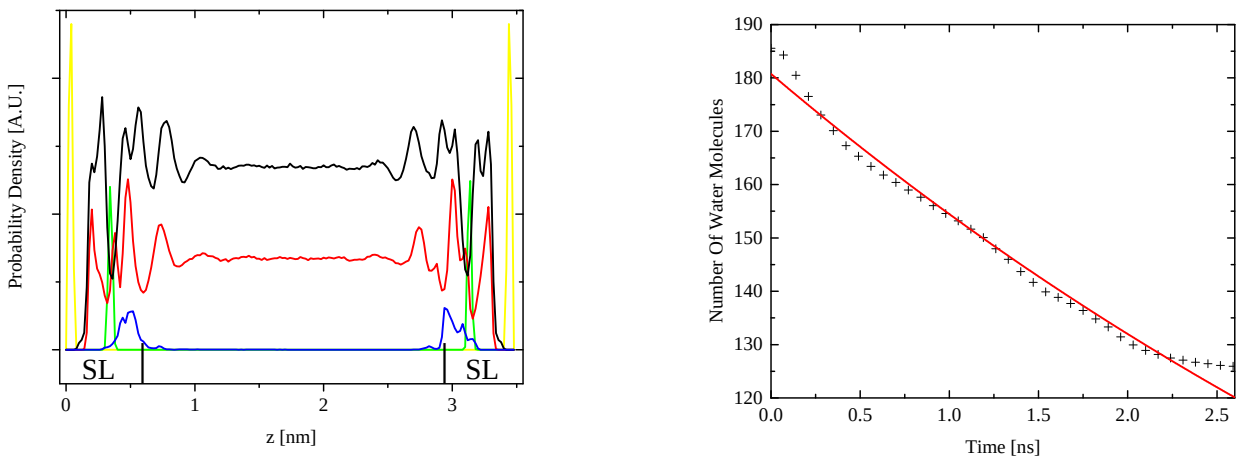

Figure 5.20: MD9: Modified tobermorite 14 Å simulation with the whole crystal atoms positions fixed and CLAY_FF potential used and hydroxide groups. Left: density profile; right: surface desorption. $\tau_S = 6.36 \pm 0.02$ ns as listed in table 5.1. On the left, yellow stands for silicate, green stands for calcium, red stands for water oxygen and black stands for water hydrogen. On the right, black crosses are the simulated desorption data and the solid red line is its exponential fit. The surface layers (SL) are limited by the silicate peaks and the bars on the abscissa.

5.5.2 Summary and Choice of the Model for Further Study

All the previous different simulations from MD1 to MD9 can be compared thanks to their desorption time as it is shown in table 5.1. As said previously, the modified Freeman potentials give smaller surface desorption times. Also, the fact to add hydrated calcium ions to the system do not change the surface desorption time. In the same way, the presence of hydroxides do not change significantly the surface desorption time contrary to protonated surfaces that negate the effect of surface calciums. Also, the surface seems to be represented in a better way if the surface oxygens are attached to silicates which can move. However, whatever the set of potentials and structures, no simulation gives a surface desorption time of the order of the one obtained by fitting NMR experimental data to Korb's model: all the models desorption times are about 2 to 5 orders of magnitude shorter than the Korb's one, which was a starting point to define a new model that is discussed in appendix.

MD1 and MD2 models do not respect the Ca/Si ratio assumptions, hence they are removed from the candidate list. MD3 model has a too small interlayer that allows the presence of Q_3 silicate tetrahedra, which is against experimental data. MD4f, MD5f, MD6f and MD7f models surface layers have fixed atoms positions which inhibited surface dynamics, hence they are removed from the candidate list. MD5 and MD7 models with modified Freeman potentials have unstable surfaces, compared to the ones that use CLAY_FF potential, and short desorption times, hence they are removed from the candidate list. MD8 model gives a short desorption time and its surfaces repelled calcium ions to the bulk which increase a lot the calcium concentration in the bulk that is not seen in the literature [81]. This is also the case for MD6 where all calcium do not find stable positions on the surface. Hence, these models are removed from the candidate list. MD9 model uses a poorly tested potential for hydroxide groups and with caution, this model is removed from the candidate list. It is noted that another recent study based more specifically on the crystal nanostructure considering defects by Kovacevic [10] can be read for more details about the modified tobermorite 14 Å structure. On this basis, MD4 model is chosen for further analysis.

Chapter 6

MD4 Analysis

The purpose of this chapter is to make a detailed analysis of the MD4 model using the methods developed and tested in earlier chapters, especially chapter 4. The density profile will be more analysed and multiple water sets will be taken into account as developped previously (ie: {A>B>C} populations). Diffusion and desorption analysis as well as NMR relaxometry calculations will be performed on these selected sets of water molecules in order to better understand water dynamics in such a system. These analyses will be used to develop a new mathematical model that will help to interpret ^{1}H NMR relaxometry in porous media at the nanoscale.

6.1 Density Profile Analysis and Layers Definition: L1, L2, TL, bulk and IL

In chapter 5 section 5.5.1, the density profile was defined: this is a diagram that shows the probability an atom (water oxygen and hydrogen, calcium ion and crystal silicate) is at a distance z from the crystal. The density profile was used to define gel water surface layers. However, much more can be said about this. Indeed, in a MD4 gel pore, it is a very first approximation to say that the water molecules are either in the surface layers or in the bulk. There is much more than one water density peak close to the surface and a flat curve in the middle of the pore. The presence of hydrated calcium ions creates a zone where the probability a water molecule stays in it is very small, as suggested by the first well in the surface layer (see figure 6.1). Actually, two peaks in the water oxygen density profile can be seen close to the surface. These peaks can be defined as two sub layers of the surface layer SL. The layer between the crystal surface and the hydrated calcium ions is called the L1 layer. The very next layer between the hydrated calcium ions and the rest of the pore is called the L2 layer.

The L2 layer raises an issue by not being clearly and easily defined. Indeed, the well between the L2 peak and the other peaks going toward bulk side is not as clear as the well that defines L1. Water exchange seems to be easier between layer L2 and the rest of the of the system than between L1 and L2. This will be confirmed later in a desorption analysis. The effect of hydrated calcium ions has a significant role on the water dynamics in this system. A comparison between the first hydration shell of gel calcium ions and L1 and L2 is discussed

in the section 6.3.3. Between L2 and Bulk, there is a zone where water molecules still feel the surface effect as the density profile is not flat but wave shaped. This is a transition layer TL. Finally, the last zone considered here is the interlayer IL. This can be separated into IL-B (for bulk in the middle) and IL-S (for surface). The interlayer zone is not in the gel pore but between CaO sheets that have not been further separated to create a gel pore. All these zones can be seen in figure 6.1 and their sizes, defined by water density peaks, are recorded in table 6.1. The distinction between IL-B and IL-S will be useful to look at the water displacement in the interlayer in the section 6.2.5.

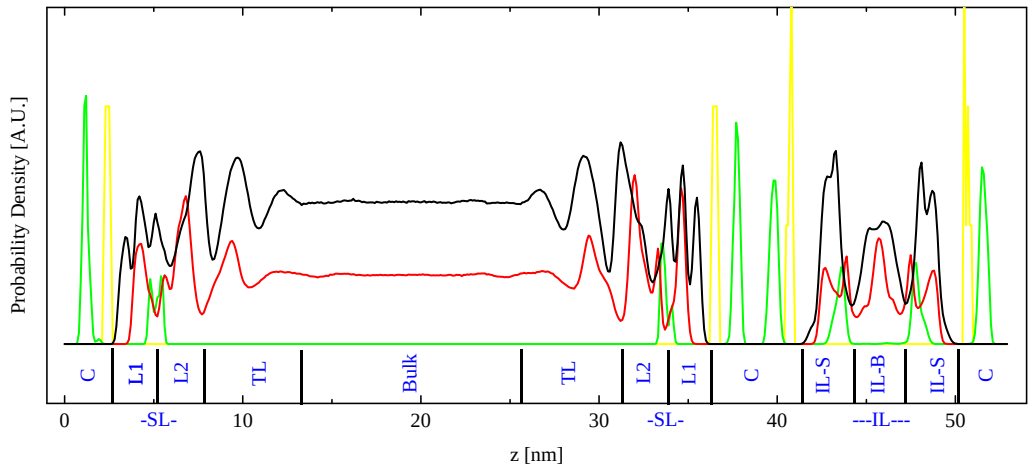

Figure 6.1: A density profile shows that MD4 can be split into multiple zones: L1, L2, TL, Bulk and IL (IL-B and IL-S). C stands for the crystal layer. The behavior of water molecules can be studied in each of these zones. Crystal layers have a strong influence on water by itself. The crystal also attracts indirectly water molecules thanks to calcium ions' influence. The calcium ions later split the surface layer into two sub layers L1 and L2 and have a strong influence on the water molecules in their surrounding. The color code is as follows: yellow line refers to silicon atoms, green line refers to calcium ions, red line refers to water oxygen atoms and black line to water hydrogen atoms.

Layer considered	Size [nm]
L1	0.23
L2	0.25
TL	0.5
bulk	1.22
IL-S	0.3
IL-B	0.3

Table 6.1: The sizes of different layers in this model are recorded here. As a comparison, the typical water size is $\approx$ 0.27 nm. There are two of each layer exept for bulk and IL-B because of the pores symmetry.

Most of the C-S-H analogues presented in chapter 5 section 5.2 were built from tobermorite that was modified in order to create the nanopores and to add hydrated calcium ions on their

surfaces. The presence of calcium ions on the surfaces in MD4 has a significant impact on water dynamics which is discussed in the section 6.1.1.

6.1.1 Calcium Effect on Water Molecules

Calcium ions in a gel pore have an important influence on surface water molecules (in L1 and L2 layers). Their positions are quite stable in this MD4 simulation: they stay around the position of the removed bridging silica tetrahedra as shown in figure 6.2. A lattice of stable calciums creates a barrier in the surface layer (and discriminates eventually L1 and L2 water molecules).

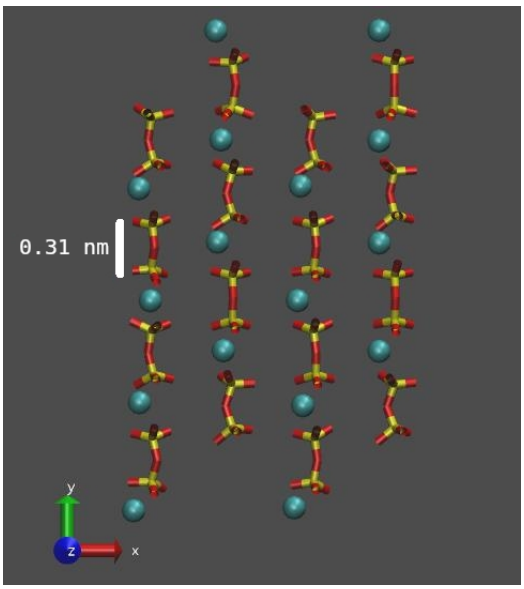

Figure 6.2: This figure represents a slice of the crystal layer silicon dimers and the gel calcium layer in the xy axis for $z \in \{SL+C\}$ as defined in figure 6.1. Calcium ions (bluish balls) are placed between silica tetrahedra dimers (yellow [for silicons] and red [for oxygens] structures) and replace the former bridging silica tetrahedra of the tobermorite 14 Å as shown in figure 5.6. These calcium ions (Ca^{2+}) create a stable lattice of a positively charged plane that splits the surface layer of water molecules into L1 and L2. The position of the gel pore calcium ions is the same as the position of the wells that split the surface layers into L1 and L2 in the density profile in figure 6.1. The white line refers to the size of a silicon dimer in the crystal layer which is 0.31 nm.

Calcium First Hydration Shell

In the MD4 model, calcium ions are not free: they are attracted by the crystal layer. A first analysis is to compare the calcium and water interaction in the presence of the crystal and in bulk water. To do so, a small simulation of one calcium ion in a pure bulk water system has been performed. The radial distribution function (RDF) that link the calcium ions and the water molecules was computed for both systems and can be seen in figure 6.3.

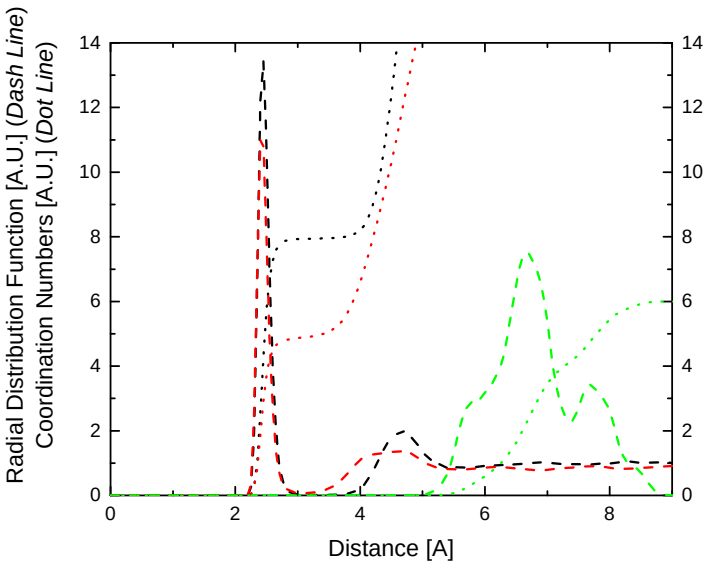

Figure 6.3: The radial distribution function that links calcium ions and the water molecules that surround them is shown here for calcium ions in the MD4 gel pore (red dash line) and in pure bulk water (black dash line). The number of water molecules in the first hydration shell is also shown for MD4 (red dot line) with ≈5 water molecules and for bulk water (black dot line) with 8 water molecules. The radial distribution function that links calcium ions to other calcium ions in MD4 gel lattices is also shown (green dash line) and the number of close calcium ions neighbours too (green dot line). It is clear here that in MD4, the average distance between two calcium ions is larger than twice the average distance between a calcium and a water molecule.

The two RDFs are slightly different and this can be explained as follows. The closest water peak (that defines the first hydration shell) in the MD4 RDF is in the same position but smaller than the bulk water system RDF. This is because of the calcium lattice. The distance between calciums is fixed and there is not enough space for all the water that is around a calcium in pure bulk water as shows in figure 6.3. The distance between two calciums in the MD4 gel ore is smaller than twice the distance between a calcium in bulk water and its first hydration shell. Only a few water molecules are sandwiched in layer L1 between the crystal and the calcium plane. This is because of an asymmetry created by the calcium plane. This is also the reason why the second RDF peak is smaller in the case of the MD4 simulation. Moreover, in MD4 model, the first hydration shell is composed of 5 water molecules on average whereas in bulk water, this number becomes 8.

To sum up, the crystal layer forms potential wells where calcium ions fit. As a result, a calcium lattice is created that traps some water molecules (in L1) and produces an asymmetry and also impacts the local distribution of freer water (in L2). The calcium first shell water desorption will be compared to the L1 and L2 desorption in the section 6.3.3.

Calcium Effect on layers L1 and L2

The probability of finding a water molecule at a given site in the different layers was analysed. Probability maps were created. To do them, every simulation timestep, the position of each water molecule was used to increment a two dimension histogram. These two dimensions define the xy plane of each layer (parallel to the crystal plane). At the end of the process, the histogram maximum value, M_{histo}), and minimum value, m_{histo}, were chosen in order to make these maps clear. These probability maps can be seen in figure 6.4. The color code for water molecule is as follows. Pink means a water molecule was at that position at least m_{histo} times. Yellow means it is a stable position for water: the value of the histogram is at least M_{histo} times. White means this position is highly improbable for water: the value of the histogram is less than m_{histo} times. For hydrated calcium ions, the color code is as follows. Green means an improbable position while blue means the probability if high. The calcium probability map overlaps the water probability map: when a calcium oscillates, it can go to a position occupied previously by water.

The calcium ions have a direct and important impact on layers L1 and L2 water molecules. The RDF distances between hydrated calcium ions and water between bulk and MD4 systems are different as shown in figure 6.3. The calcium ions are free in bulk but are trapped by the crystal layer in L1 and L2. The crystal and calcium layers create some "no-water-zones" since they occupy this space. This can be seen in the top two probability mas in figure 6.4. Also, the crystal layer and the calcium lattice presence implies the creation of a sublattice for the water molecules in their direct surrounding.

Water molecules in L1 layer are highly confined. Only a few positions are allowed because of the crystal layer and the hydrated calcium ions lattice. Also, it is clear here that L1 water molecules cannot move along the crystal if the water molecule only stays in L1, otherwise there would be some continuous colored pathways in the top left probability map in figure 6.4. Water molecules in L2 layer are no longer confined: they are freer than the ones in layer L1. The main feature of the L2 water molecules is that they are around the calciums: they form the calcium first hydration shell as can be seen in the top right probability map in figure 6.4. Water molecules in the TL layer are almost quite as free as the ones in Bulk: the only difference is that TL water still feels the crystal and hydrated calcium ions influences as the yellow dots show in the middle left probability maps in figure 6.4. Remark that the whole map is pinkish since all the positions are quasi-equally probable. Finally, the interlayer water molecules have a behaviour similar to L1 and L2 waters since these water molecules are very close to the crystal as shown in the bottom probability map in figure 6.4. The main difference between IL and the other layers is the possibility to desorb: gel zones can exchange and as a consequence, water molecules can experience different degrees of freedom. However, these exchanges can be rare, depending on the position of the considered water molecule.

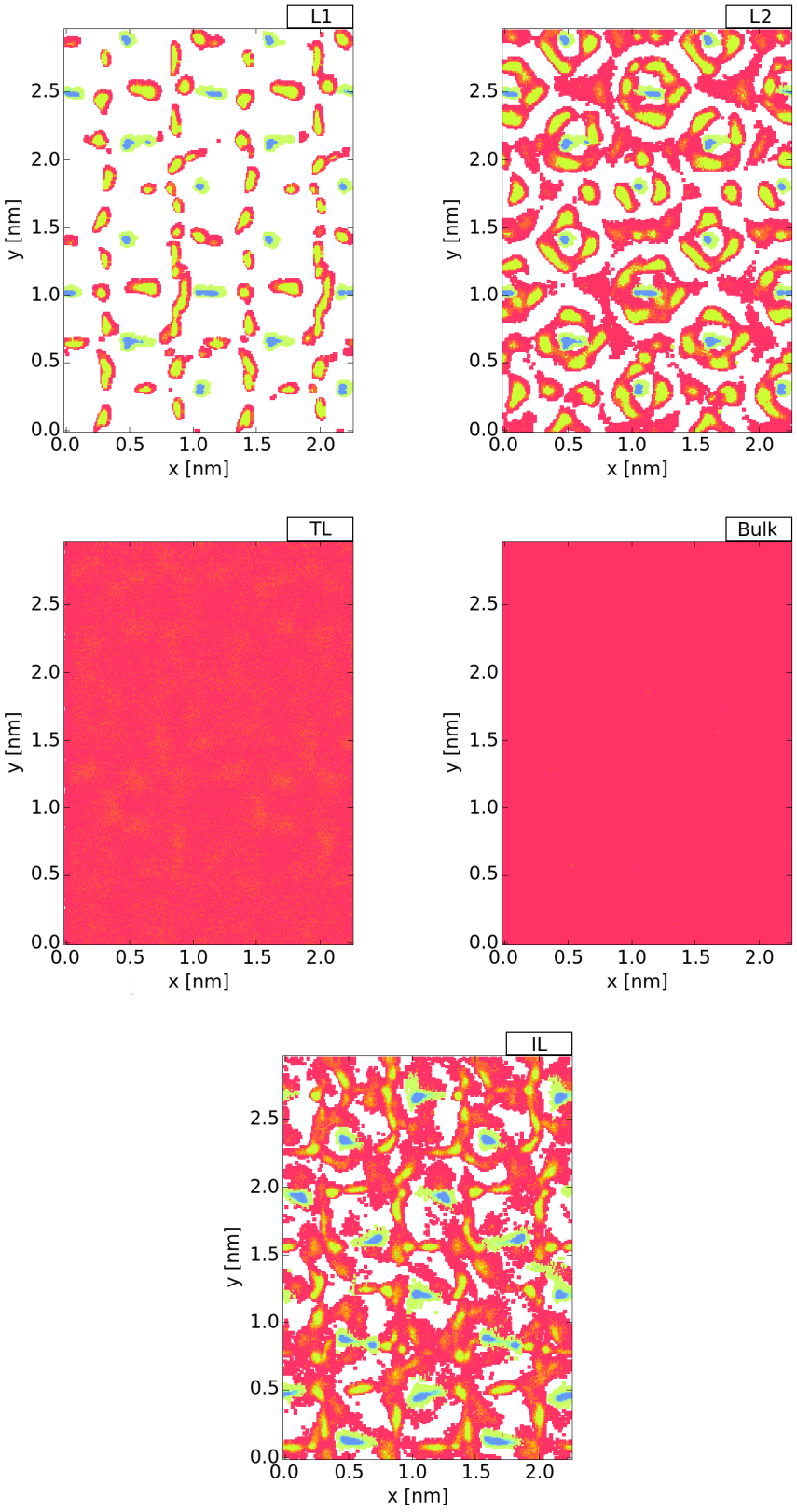

Figure 6.4: The probability of presence of water molecules in the different zones is shown here. Pink means a water molecule is not likely to stay at this position. Yellow means this is a stable position for water. White means the position is highly improbable. Green means a calcium ion can be in that position but it will be more probably in blue positions. The behaviour of water molecules is highly influenced by hydrated calcium ions that are trapped close to the surface. Top left map is for L1, top right map is for L2, middle left map is for TL, middle right map is for Bulk and bottom map is for IL.

6.2 Diffusion Analysis

The diffusion properties of water in the different layers are studied in this section. Qualitatively speaking, a large diffusion coefficient is found where water is free and a small one where water is confined. These values can be easily calculated. However, as there can be exchange between the different zones, only the water molecules that stay in a specific zone will be considered or more precisely, these water molecules will be considered during all the time that they stay in the areas in question in order to avoid vibrations around the zone border. Water molecules taken into account (actually, their oxygen atoms) are allowed to escape the considered layer up to half a water molecule diameter. Here, the {A>B>C} sets of water molecules defined in chapter 3 section 3.4.2 are used: a water starts in zone {A}, can go to zone {B} and is taken into the calculation when it is in zone {C}⊂{B}; if it leaves B, it is removed from the calculation.

6.2.1 $D_{\{B>B>B\}}$ Validation

The {B>B>B} set of water molecules is interesting because it can be compared to the results obtained in chapter 4. However, as water molecules are free, it is easy for them to leave the bulk zone to go to TL. Actually, since TL and Bulk have close properties, this leak from Bulk to TL is straightforward. Hence, the calculation will be done during a small time interval where the mean square displacement is a clear straight line. As the statistics become less and less accurate with time because the considered population of water decreases as shown in figure 6.5 (right), a range of data is selected for the mean square displacement curve in figure 6.5 (right) in order to avoid seeing the random walk of a very small number of water molecules for large time.

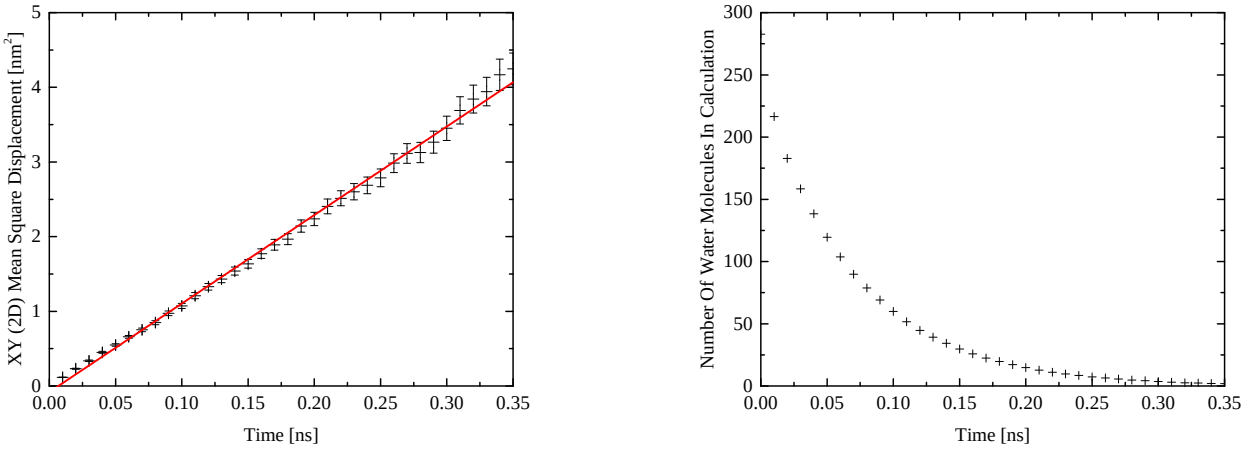

Figure 6.5: On the left, the 2D mean square displacement and its standard error (black crosses) are generated for a {B>B>B} set of water molecules. The data can be only analysed during a small time interval because of the exchange between bulk and the TL. For the same reason, the statistics become less and less accurate with time because of the decreasing population taken into account in the calculation (right). This is why a fit is done for early times (ref line). As a result, a diffusion coefficient $D_{Bulk} = 2.96 \pm 0.01 \times 10^{-9} m^2/s$ *is found.*

The 2D mean square calculations and a fit on a 0.35 ns time interval give a diffusion coefficient $D_{Bulk} = 2.96 \pm 0.01 \times 10^{-9} m^2/s$ that is close to the one found in chapter 4 in section 4.2.1 in a pure bulk water simulation system (ie: $D_{sim,Bulk\ Ch4} = 2.66 \pm 0.01 \times 10^{-9} m^2/s$).

6.2.2 $D_{\{L1>SL>L1\}}$

A second interesting set of water molecules is the {L1>SL>L1} set, where SL=L1+L2. As seen with the probability of presence in the top left probability map in figure 6.4, water molecules that stay strictly in L1 cannot diffuse but only vibrate. An hypothese could be to say a water can move along the channel formed by the crystal but as it can be seen in the same figure, there is no clear path where water molecules can go. This is the reason why the interesting set of water molecules can go to L2: it would be a transition before going back to L1, like a hop. As a result, a diffusion process can be quantified as shown in figure 6.6.

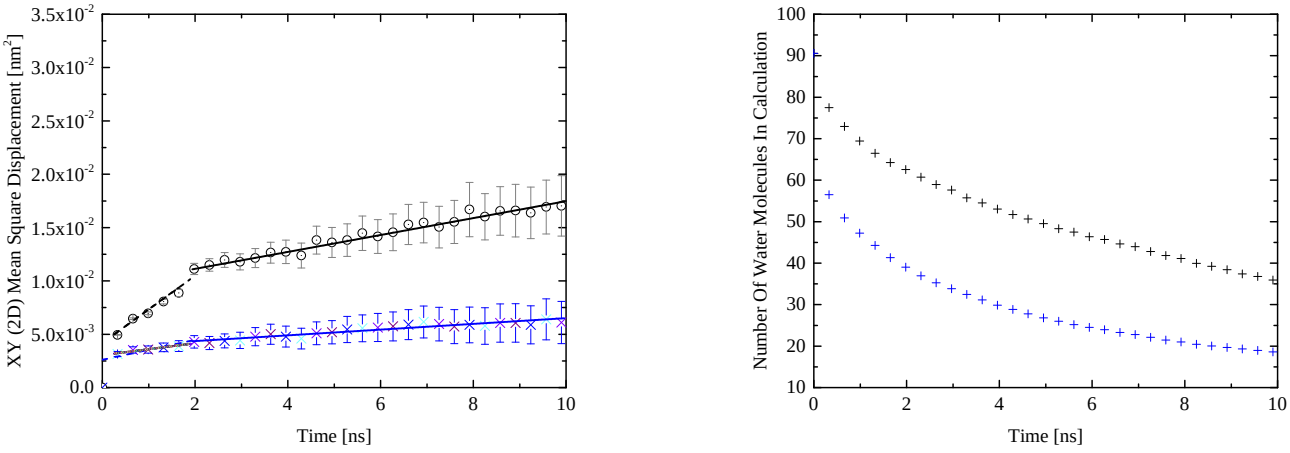

Figure 6.6: On the left, the 2D mean square displacement and its standard error (black crosses) are calculated for {L1>SL>L1} set of water molecules. These water molecules can do a hop via L2. But this hop is not straighforward and before doing it, water molecules are vibrating (black dash line). This is the reason why the curve is not considered during the short time to evaluate the diffusion process. These data are compared to {L1>L1>L1} set of water molecules to show the importance of hops (blue crosses represent for the 2D mean square displacement and its standard error). The populations taken into account in the calculation are also shown (right). As a result, the {L1>SL>L1} left curve is fitted by a straight line (black line) and a diffusion coefficient $D_{S1} = 1.98 \pm 0.01 \times 10^{-13} m^2/s$ is found.

At time less than 2 ns, the motion of the atoms is vibratory. The 2D mean square displacement is fitted on a 8 ns time interval and a diffusion coefficient is found: $D_{L1} = 1.98 \pm 0.01 \times 10^{-13} m^2/s$. It is a very small one, small enough to consider in some models that this water is fixed (especially the Faux model that will be discussed in the section 6.5). Note that if the considered set were {L1>L1>L1}, only the vibrations would have been seen and the mean square displacement slope would be negligible for long times. The hops between L1 and L2 imply a Levy walk that is discussed by Faux in his model [13] and by Levitz [92] on a 1 to 2 ns timescale.

6.2.3 $D_{\{L2>\Omega-B>L2\}}$

Layer L2 is very interesting. The influences of the crystal layer and the calcium lattice are strong so that water displacement in this layer is limited to selected paths. However, these influences are not strong enough to prevent water to easily go to TL as will be shown in the desorption analysis in the section 6.3. The set {L2>Ω-B>L2} is selected. Bulk is not allowed in the selected set in order to quantify only short excursions to TL and jumps back to L2. Also, once a water molecule reaches the bulk, there is no more a correlation with its previous state, which is not interesting for the L2 analysis.

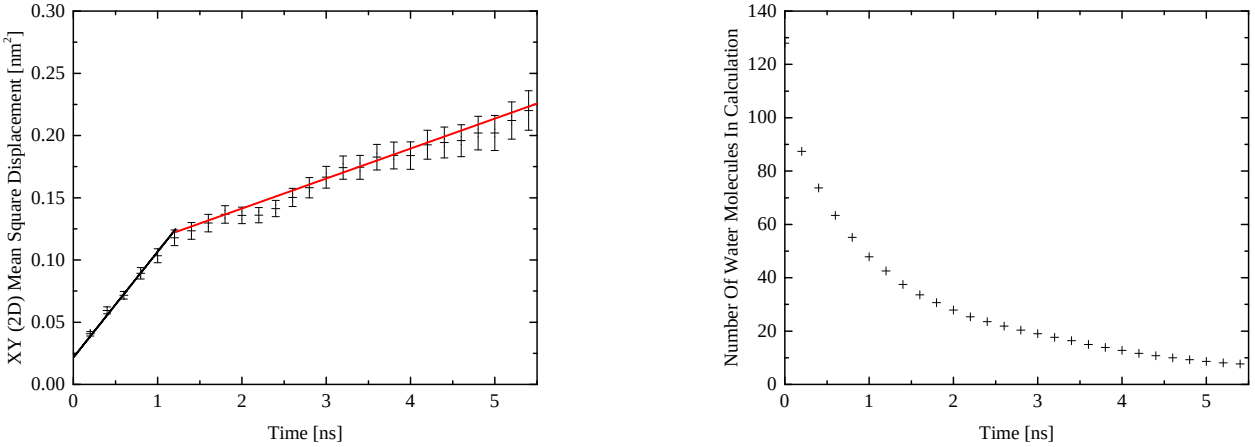

Figure 6.7: On the left, the 2D mean square displacement and its standard error (black crosses) are calculated for a {L2>Ω-B>L2} set of water molecules. These water molecules can stay in TL as long as they do not go to bulk where they lose any L2 influence. The idea is to only include jumps in TL to go to another position in L2. On the right, the decreasing {L2>Ω-B>L2} population is shown. The diffusion analysis cannot be carried out for too short times (ie: less than 1 ns) to avoid vibration effects. The curve is fitted by a straight line from 1 to 6 ns and the diffusion coefficient is calculated: $D_{L2} = 6.01 \pm 0.01 \times 10^{-12} m^2/s$.

As shown in figure 6.7, a 2D mean square calculation on a 4.5 ns time interval leads to a diffusion coefficient in L2 layer $D_{L2} = 6.01 \pm 0.01 \times 10^{-12} m^2/s$. This is one order of magnitude faster than in L1 but still three orders of magnitude smaller than in bulk, which shows the strong influence of the crystal layer and the calcium lattice. Here, contrary to what happens in L1, water is actually moving inside L2. The jumps are allowed but as it will be shown in the next section, the TL layers are much closer to the bulk than to L2, which means that the probability a jumping water stays in TL for a long time without going to the bulk or coming back to L2 is small. This is also shown by the decrease of L2 population in 6.7 on the right.

6.2.4 $D_{\{TL>TL>TL\}}$

As discussed in the previous section, the TL layer is looking like bulk as shown in Figure 6.8. A diffusion coeffient calculation on a 0.15 ns time interval gives $D_{\{TL>TL>TL\}} = 1.42 \pm 0.01 \times 10^{-9} m^2/s$, which is of the same order of the bulk one.

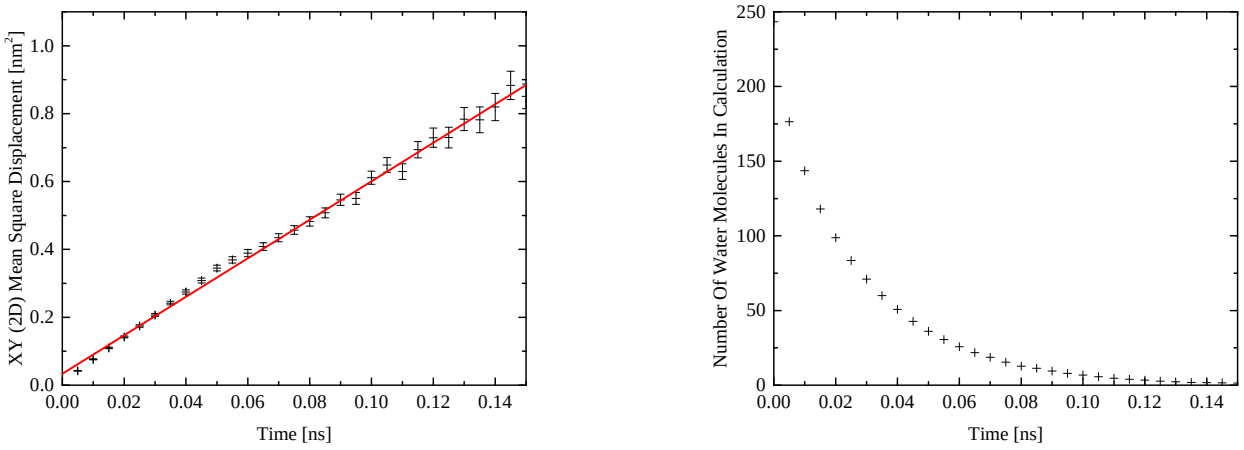

Figure 6.8: On the left, the 2D mean square displacement and its standard error (black crosses) are calculated for the {TL>TL>TL} set of water molecules. All the comments for bulk are valid for the TL. On the right, the decreasing {TL>TL>TL} population is shown. The diffusion analysis can only be done for short times (ie: less than 0.16 ns) because of the quick decrease of the number of water molecules taken into account in the calculation (right). A fit is made (red solid line on the left) and the diffusion coefficient can be calculated: $D_{TL} = 1.42 \pm 0.01 \times 10^{-9} m^2/s$.

6.2.5 $D_{\{IL>IL>IL\}}$

A first analysis about the exchange between IL-B and IL-S, defined in figure 6.1, was performed. The motion of six IL water molecules randomly chosen was investigated and their positions (ie: left surface, middle bulk or right surface) was plotted in figure 6.9. The exchange between the different layers is fast and the residency time in each layer varies widely. Water molecules are experiencing a Levy walk jumping from a layer to another.

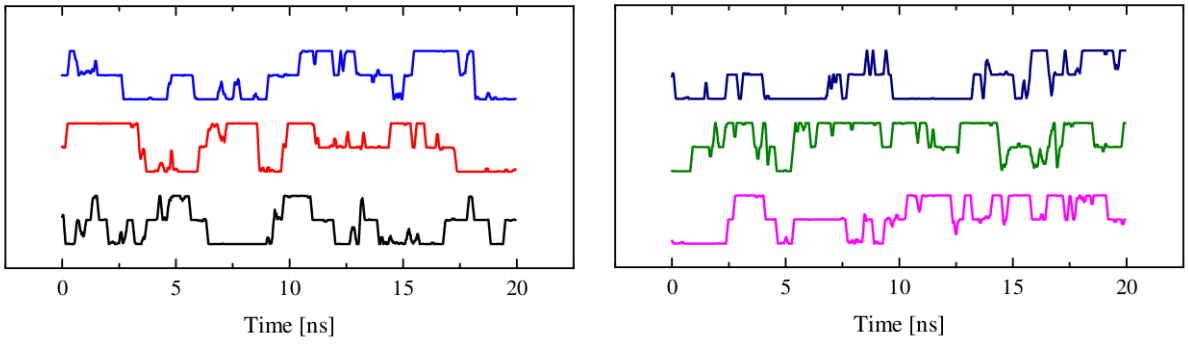

Figure 6.9: The motion of six IL water molecules randomly chosen was investigated. For each of them, three positions are allowed: left surface (top), middle bulk (middle) and right surface (bottom). The exchange between surface and bulk is fast and the residency time is varying a lot, which is a property of a Levy walk.

A diffusion analysis can be carried out. As IL and gel are not connected, the number of water in IL population does not vary and hence there is no problem with some poor statistics as shown in figure 6.10 on the right. A diffusion coefficient calculation on the whole 10 ns time interval gives $D_{IL} = 9.44 \pm 0.01 \times 10^{-11} m^2/s$.

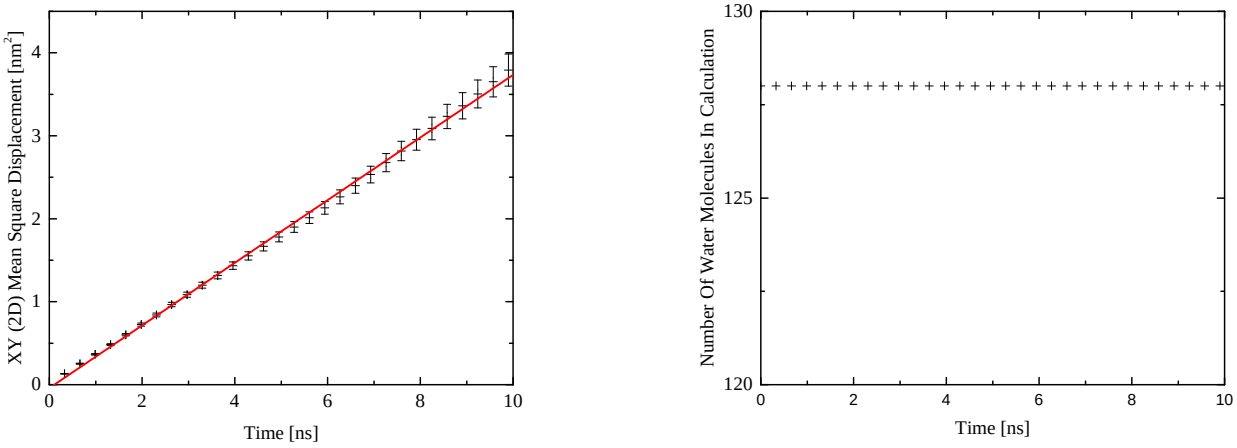

Figure 6.10: On the left, the 2D mean square displacement and its standard error (black crosses) are calculated for the {IL>IL>IL} set of water molecules. There is no decrease of the {TL>TL>TL} population because the IL is a close system in MD4: there is no exchange with other layers, the number of water molecules taken into account in the calculations is constant (right). The diffusion analysis is straightforward: a fit (red line) can easily be made and a diffusion calculation gives $D_{IL} = 9.44 \pm 0.01 \times 10^{-11} m^2/s$.

6.2.6 Diffusion Summary

The different diffusion coefficients are grouped in table 6.2:

Set of water molecules	Layer considered	Diffusion coefficient [m$^2/s$]
{L1>SL>L1}	L1	$1.98 \pm 0.01 \times 10^{-13}$
{L2>$\Omega - B >$ L2}	L2	$6.01 \pm 0.01 \times 10^{-12}$
{TL>TL>TL}	TL	$1.42 \pm 0.01 \times 10^{-9}$
{B>B>B}	bulk	$2.96 \pm 0.01 \times 10^{-9}$
{IL>IL>IL}	IL	$9.44 \pm 0.01 \times 10^{-11}$

Table 6.2: A diffusion analysis for each MD4 layer is done and diffusion cefficients are recorded in this table.

The diffusion coefficient values generated here can be compared to timescales generated by fitting NMR experimental data to Korb's model. In his model, Korb suggests that an elementary displacement time on the surface is τ_m=1.3 ns [36, 93]. With such a value and considering that the elementary displacement on the surface is typically the size of a water molecule $d_W \approx$ 2.7 Å, the diffusion coefficient on the surface according to Korb is $D_{surface} \approx d_W^2/4\tau_S \approx 10^{-11}$ m^2/s. This is bigger than L1 diffusion by 2 orders of magnitude and is bigger than L2 dif-

fusion by 1 order of magnitude. It is 10 times smaller than the IL diffusion coefficient and 100 times smaller than the TL diffusion coefficient. In short, none of the diffusion coefficients calculated for the water in C-S-H analogue remotely approach the value found from fitting Korb's model to NMR data. This is a key element. Kalinitchev found a diffusion coefficient of $\approx 10^{-11}$ m^2/s [53] for surface water but in retrospect, it is clear he was measuring vibrations since the timescale was short.

6.3 Desorption Analysis

The reason why specific sets of water molecules were used in diffusion analysis is directly related to the water exchange between zones and hence related to the desorption properties. These properties are being quantified in this section for each gel layer.

6.3.1 Desorption of {L1>SL>SL}

Layer L1 desorption is being discussed here. As developed in its diffusion analysis, a water molecule in L1 needs to go to L2 in order to move (and not vibrate). Usually, in order to avoid significant decrease in the desorption curves due to the (relatively) arbitrary frontier of a zone, vibrations around the frontier have to be neglected, and hence, the frontier is being shifted away from its original position (typically by a value of approximately half the size of the water molecule $\approx$ 0.14 nm). Here, layer L2 is $\approx$ 0.25 nm wide and is selected to allow water molecules in L1 to move in. The desorption analysis shows in figure 6.11 that a typical desorption time for such a water set for a one component exponential fit is $\tau_{s,L1} = 11.74 \pm 0.02$ ns. However, the quality of the fit is poor and a two component exponential fit leads to a fast desorption time $\tau_{s,L1,fast} = 1.52 \pm 0.01$ ns and a slow desorption time $\tau_{s,L1,slow} = 15.94 \pm 0.01$ ns. This fit is much better which can predict the presence of two different populations of water molecules in L1: those who easily go from L1 to L2 quickly and that are more likely to leave SL (fast desorption: water molecules on the frontier between L1 and L2), and the water molecules closer to the crystal that need more time to escape and desorb (slow desorption). Whatever the fit, the order of magnitude of the desorption time is the same.

6.3.2 Desorption of {L2>L2+δ>L2+δ} and {SL>SL+δ>SL+δ}

The same kind of analysis is made for L2. A small change is made here in order to consider the vibration issue discussed previously in the diffusion sections. Indeed, L2 water molecules can move to TL for a short time and come back to L2. Hence, "L2+δ" means the L2 frontier (on the TL side) is shifted a few Åaway. A desorption analysis of such a set of water gives for a one component exponential fit a typical desorption time $\tau_{s,L2} = 0.75 \pm 0.01$ ns and for a two component exponential fit $\tau_{s,L2,slow} = 1.17 \pm 0.01$ ns and $\tau_{s,L2,fast} = 0.22 \pm 0.01$ ns as shown in figure 6.12. The two fits are quite similar and hence L2 is more likely to have only one population of water molecules. Also, L2 is less correlated to the crystal so that the L2 desorption time is smaller than the one obtained for L1 (one order of magnitude less).

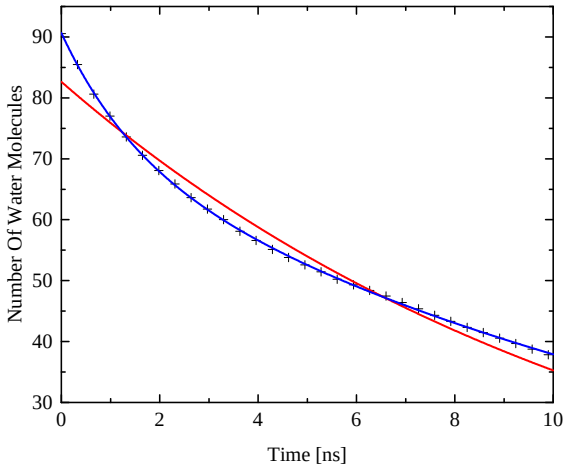

Figure 6.11: A desorption curve (black crosses), a one component exponential fit (red line) and a two component expoonential fit (blue line) show L1 waters that are accepted in L2 and desorb from SL. The one component exponential gives in a typical desorption time $\tau_s = 11.74 \pm 0.01$ *ns. A two component exponential fit gives a fast desorption time* $\tau_{s,L1,fast} = 1.52 \pm 0.01$ *ns and a slow desorption time* $\tau_{s,L1,slow} = 15.94 \pm 0.01$ *ns.*

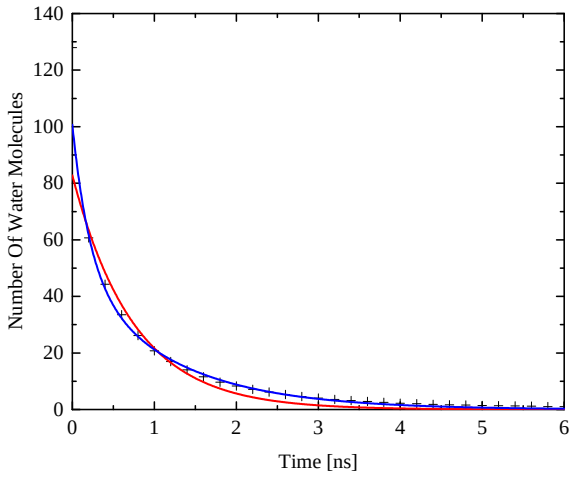

Figure 6.12: A desorption curve (black crosses), a one component exponential fit (red line) and a two component expoonential fit (blue line) show L2 water molecules desorption. The one component exponential gives in a typical desorption time $\tau_s = 0.75 \pm 0.01$ *ns. A two component exponential fit gives a fast desorption time* $\tau_{s,L2,fast} = 0.22 \pm 0.01$ *ns and a slow desorption time* $\tau_{s,L2,slow} = 1.17 \pm 0.01$ *ns.*

In the same way, if the whole surface layer is considered (SL=L1+L2), an "average" desorption time, closer to the L1 one, can be generated. For a one component exponential fit, $\tau_{s,SL} = 6.65 \pm 0.02$ ns is found and for a two component exponential fit, a fast desorption time

$\tau_{s,SL,fast} = 1.13 \pm 0.03$ ns and a slow desorption time $\tau_{s,SL,slaw} = 10.79 \pm 0.02$ ns are obtained as shown in figure 6.13. There are clearly two populations of water, L1 and L2 waters, which explains two component times: the slow one represents most of the L1 waters and the fast one the L2 waters.

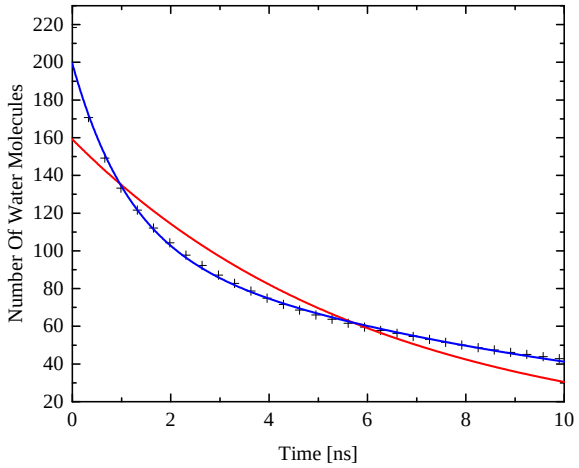

Figure 6.13: A desorption curve (black crosses), a one component exponential fit (red line) and a two component expoonential fit (blue line) show SL water molecules desorption. The one component exponential gives in a typical desorption time $\tau_s = 6.65 \pm 0.02$ ns. A two component exponential fit gives a fast desorption time $\tau_{s,SL,fast} = 1.13 \pm 0.03$ ns and a slow desorption time $\tau_{s,SL,slow} = 10.79 \pm 0.02$ ns.

6.3.3 Desorption of Gel Calcium First Hydration Shell

As suggested in the section 6.1.1, a comparison can be made between SL layer (L1 and L2) and the gel calcium first hydration shell (FHS), and more precisely corresponding to the water molecules in FHS and L1 and the water molecules in FHS and L2. Typical desorption times for these water molecules are $\tau_{s,FHS-L1} = 21.02 \pm 0.03$ ns, $\tau_{s,FHS-L2} = 2.01 \pm 0.01$ ns and for SL, a one component exponential gives $\tau_{s,FHS-SL} = 6.44 \pm 0.01$ ns and for a two component exponential $\tau_{s,FHS-SL,fast} = 1.05 \pm 0.01$ ns and $\tau_{s,FHS-SL,slow} = 21.24 \pm 0.15$ ns, respectively for FHS-L1 and FHS-L2, as shown in figure 6.14. These values are relatively close to those for L1, L2 and SL, which definitely shows once again that the calcium plane creates a stronger attachment between the water and the surface layers.

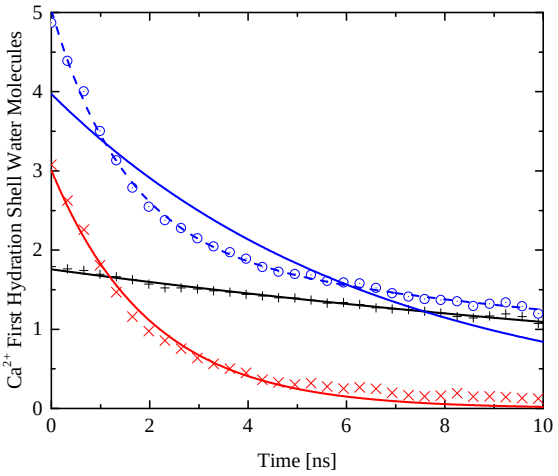

Figure 6.14: A desorption analysis is done on the calcium first hydration shell for waters in L1 (black crosses), in L2 (red crosses) and SL (blue circles) with fits by a one component exponential (respectively black, red and blue lines) and a two component exponential for the FHS-SL (blue dash line). Typical desorption times found this way are $\tau_{s,FHS-L1} = 21.02 \pm 0.03$ *ns,* $\tau_{s,FHS-L2} = 2.01 \pm 0.01$ *ns and* $\tau_{s,FHS-SL} = 6.44 \pm 0.02$ *or* $\tau_{s,FHS-SL,slow} = 21.24 \pm 0.15$ *ns and* $\tau_{s,FHS-SL,fast} = 1.05 \pm 0.01$ *ns.*

6.3.4 Desorption Summary

The different desorption times are grouped in table 6.3:

Layer considered	Desorption time [ns]	Slow desorption time [ns]	Fast desorption time [ns]
L1	11.74 ± 0.02	15.94 ± 0.01	1.52 ± 0.01
L2	0.75 ± 0.01	1.17 ± 0.01	0.22 ± 0.01
SL	6.65 ± 0.02	10.79 ± 0.02	1.13 ± 0.03
Ca FHS L1	21.02 ± 0.03	-	-
Ca FHS L2	2.01 ± 0.01	-	-
Ca FHS SL	6.44 ± 0.02	21.24 ± 0.15	1.05 ± 0.01

Table 6.3: A desorption analysis for each layer is done and desorption times are recorded in this table.

The desorption time values generated here can be compared to those found by fitting Korb's model to NMR data. In his model, Korb suggest that the residency time on the surface is τ_s=13 μs [36, 93]. There is a difference of $\approx$ 3 orders between Korb's residency time and MD4 desorption times. Faux's new model [13], introduced in the section 6.5 agrees with MD4 values.

6.4 ^{1}H NMR Relaxometry Analysis: Correlation Function

In this section, the ^{1}H NMR correlation function is generated. However, contrary to the case of a pure bulk water system, here, Fe^{3+} impurities are considered with a surface density of $\sigma_{s,th} \approx 10^{+11}$ Fe^{3+}/cm^2=10^{-10} $Fe^{3+}/\AA^2$ [49]. The actual value used in this study was $\sigma_{s,th} \approx 2.5 \times 10^{-10}$ $Fe^{3+}/\AA^2$.

The correlation function can be split into two parts: a like spin function (H-H), $G_{II}(t)$, and an unlike spin function (H-Fe), $G_{IS}(t)$. The MD4 crystal layers do not contain Fe^{3+} impurities but a simplification is to consider such an impurity anywhere in the gel surface. It is however not strictly correct because the trajectories of water molecules close to an Fe^{3+} ion would be different from the trajectories generated by simulation in this study. The smallest Fe^{3+} density that can be reached in this simulation would be $\sigma_{s,sim} = \frac{1}{2xy}$ where xy is the value of the crystal surface because of the periodic boundary conditions. The factor 2 represents the fact there are two surfaces in the gel pore. This way, the smallest impurity density would be $\sigma_{s,sim} = 7.5 \times 10^{-4}$ $Fe^{3+}/\AA^2$. If a simulation were built in order to reach $\sigma_{s,th}$, the size of the simulation cell would be too big and the simulation time too long. The idea is to consider one fictitious Fe ion in the simulation and to rescale the result by the ratio $\frac{\sigma_{s,th}}{\sigma_{s,sim}}$. Also, in order to get better statistics, the previous process can be applied for each of the 64 gel surface Si ion. Since only the $\overrightarrow{FeH}$ coordinates are used in the calculation, there are 64 different sets of coordinates.

Finally, the two functions $G_{II}(t)$ and $G_{IS}(t)$ have been computed. They can be compared to a simulated Q2D (quasi 2D) bulk slab of thickness 1.3 nm as shown in figure 6.15 based on Faux work to be published.

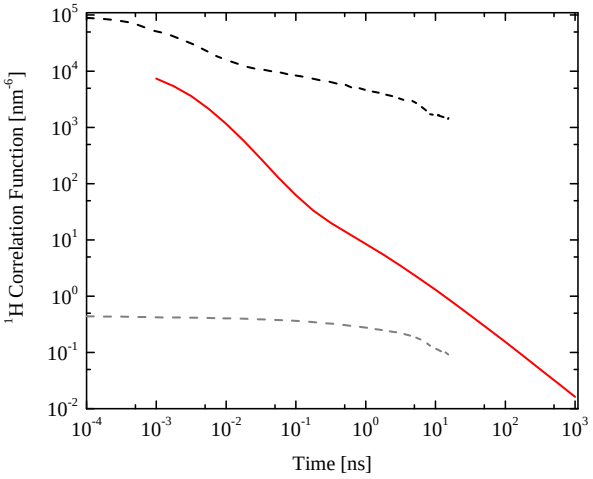

Figure 6.15: MD4 correlation function is split in a like-spin component G_{II} (top dash black line) and an unlike-spin component G_{IS} (bottom dash dark-grey line). These curves are compared to a simulated Quasi 2D bulk water slab of thickness 1.3 nm (red solid line). The initial value for the G_{IS} curve depends on the Fe^{3+} density.

Figure 6.15 represents the $G_{II}(t)$ and $G_{IS}(t)$ simulated by MD in dash lines and the correlation function of a Quasi 2D bulk water slab of thickness of 1.3 nm in solid line [17]. It is interesting to see that the G_{II} and bulk Q2D curves have a similar (but not at the same position on the abscissa) small inflection. Although the G_{II} curve is long enough to be Fourrier Transformed (last value smaller than 1% of the initial value), this is not the case for G_{IS} curve (last value $\approx 25\%$ of the initial value). MD simulation techniques have some limitations like the simulation length which also implies poor statistics and the simulation cell sizes. A more suitable simulation type such as a Monte Carlo simulation could be used. Actually, at the start of this work, this was known and it was always envisaged that MD would be used to parameterize another parallel project by a co-worker in the group (PhD of Nick Howlett [40]) that can reach long simulations times (μs) and longer cell sizes.
Here, because of such a time restriction, it was not possible to generate the spectral density functions $J(\omega)$ and the relaxation times T_1 and T_2. However, in principle, with long enough simulations, it could have been done using the BPP theory [11] just like it was done previously with bulk water in chapter 4 in section 4.2.3. The results are found to be in agreement with data and can be found in Nick Howlett's thesis [40].

6.5 To a New Model for the Interpretation of NMR Relaxometry in Hydrated Porous Silicate Materials

Throughout this work, MD simulations showed Korb's model unsustainable as the desorption time τ_s he used was not supported and nor was the surface hoping time expressed in terms of a diffusion coefficient. Therefore, Faux developed a new surface relaxation model. The details of this new model are included in appendix [13] for completeness.

Faux's new model is a two layer model. This is contrary to Korb's single layer model. In figure 6.16, the crystal surface S, where the iron impurities are located, is far from the first water layer (say L2) by a distance d_{L2} where water molecules are moving slowly with a typical time τ_{L2}. The second layer is far from the crystal by a distance d_{Beq} where water molecules are moving fast with a typical time τ_{Beq} (here, B_{eq} refers to an equivalent of the MD4 TL+B). The L1 layer is considered fixed and hence is not taken into account in this model, which implies the first moving waters are away from the surface.

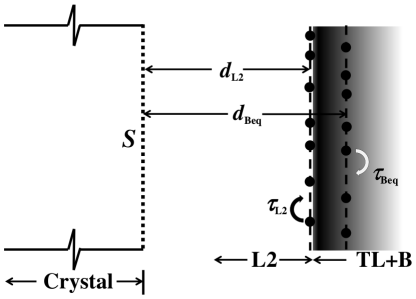

Figure 6.16: The Faux model considers two layers of water (respectively L2 and B_{eq}) distant from the surface crystal (respectively by distances d_{L2} and $d_{B_{eq}}$ with hopping rates (related to the diffusion coefficient in each of these layers). Adapted from Faux [13]

There can be exchange between the two water layers which involves a Levy walk as schematically shown in figures 6.17 and 6.18.

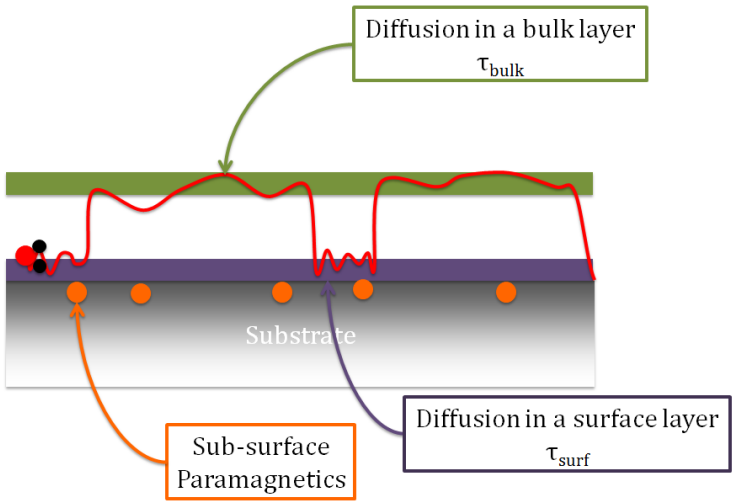

Figure 6.17: This figure represents schematically the behaviour of a water molecule in a porous media: here, the water trajectory (red solid line) start on the surface layer (ie: L2, purple zone), diffuse slowly and then goes to a bulk layer (ie: Beq, green zone) and go on diffusing, faster. Paramagnetic iron ions are represented in the surface by orange balls. This figure was extracted from a presentation by Peter McDonald.

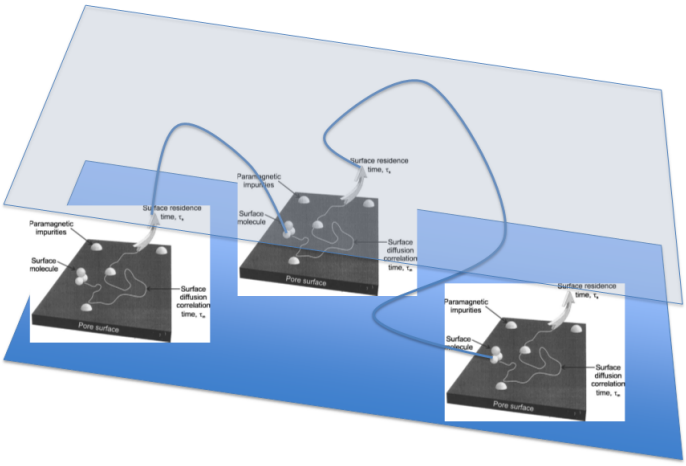

Figure 6.18: This figure represents schematically the Levy walk a water molecule performs between the two layers (dark blue plane for the surface layer and light blue plane for the bulk like layer). The three black and white pictures are extracted from [36] and represent the Korb's surface process. The dark blue line is the water trajectory that uses the bulk like layer to jump to another surface position. This figure was extracted from a presentation by Peter McDonald.

The main differences between Korb's single layer model and Faux two layer model can be listed in table 6.4:

Korb's single layer model	Faux two layer model
Can calculate T_1 and T_2 thanks to the analysis of 2D surface diffusion.	Developed an analytic model of T_1 and T_2 based on diffusion in two parallel layers.
When a water desorbs, it is removed from the calculation.	When a water desorbs, it is not removed from the calculation but can be re-absorbed.
It requires a very long residency time of the order of 10 μs.	There is no residency time problem in the calculation. Critical times are of the order of the ns.
Paramagnetic iron ions are *on* the surface.	Paramagnetic iron ions are *in* the surface.

Table 6.4: This table shows the differences between Korb's single layer and Faux two layer models.

The main similarities between Korb's single layer model and Faux two layer model can be listed in table 6.5:

Korb's single layer model and Faux two layer model
2D transport.
Same number of parameters.
Correctly get T_1/T_2 ratio.

Table 6.5: This table shows the similarities between Korb's single layer and Faux two layer models.

The Faux model respects also some experimental data as the ratio T_1/T_2=0.37±0.3; moreover, a pore lifetime parameter (that is not required) can be included in this model and would be consistent with the experimental $5ms$ pore exchange [36] and [94].
Finally, experimental data were fitted by Korb's model and the Faux model and Faux's model looks more consistent with the experimental data as shown in figure 6.19.

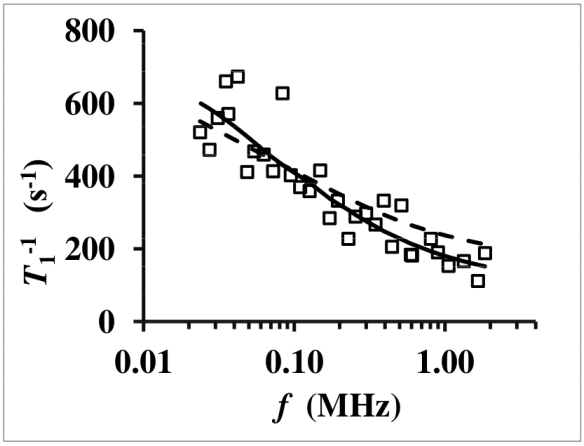

Figure 6.19: Longitudinal relaxation rates T_1^{-1} were recorded versus frequency (black squares). These data were fitted by Korb's model (dash black line) and the Faux model (solid black line). This figure is extracted from [13].

The MD results were used in support of analysis of Faux's new model. First, the structute of the different layers such as a quasi static L1 that creates a distance between the crystal and the mobile water was a key element for the model. In the same way, L2 (low mobility water) and TL and Bulk (high mobility water) defined the two layer model. Moreover, the water exchange and hops between L2 and TL showed the influence of the different layers which is different in Korb's model. And finally, the diffusion coefficients and desorption times in each of these layers were important parameters used to define the mobility of water in the model.

6.6 Summary Conclusion

To conclude, MD4 simulation was used to define different water layers in the gel and the interlayer pores: L1, L2, TL, B and IL. The presence of hydrated calcium ions in this model plays a significant role in water displacement properties. Indeed, the calcium lattice close to the surface splits the surface layer into two sub-layers: L1 where water molecules cannot move easily and L2 where water is freer and can desorb to TL. L1 water can jump to L2 to diffuse. Actually, L1 and L2 layers are directly associated with the calcium first hydration shell. The desorption times obtained here are of the order of the ns and the diffusion on the surface of the order of 10^{-13} to 10^{-12} m^2/s. Both these results are not consistent with Korb's model. Fortunately, those results helped to develop a new two layer model (Faux model) that is consistent with simulation data and experimental data. Finally, the relaxation times could not be generated here because the simulation time was too short (and not easily reachable). However, this was known from the beginning of this work and the main outputs of the MD simulations were used to feed another project that used Monte Carlo simulations that can reach longer simulation time and hence generate relaxation times.

Chapter 7

Temperature Influence and Activation Energy

The purpose of this chapter is to quantify the influence of temperature on the MD4 system. The First, a set of bulk water systems at different temperatures is analysed as a benchmark: diffusion, NMR relaxation time and their activation energies are generated. Then, diffusion and desorption on MD4 model are investigated and their activation energies are discussed. Estimates of the correlation functions for MD4 system as function of temperature are shown. These can be used by others to calibrate temperature dependence for Monte Carlo calculations for T_1 as a function of temperature.

7.1 Influence of Temperature on Bulk Water System

7.1.1 Presentation of the Simulations

The objective is to be as close as possible to experimental data to simulate the NMR and dynamic properties of bulk water system in a range of temperature from 0° to 85°. A key parameter is the water density. Takenaka et al. [95] described the variation of water density in bulk versus temperature by fitting experimental data obtained by the dilatometric method on this range of temperature. This is described by equation 7.1:

$$\frac{d_{(T)}}{d_{Max}} = 1 - \frac{(T - 277.132)^2(T + 123.035)(T - 240.862)}{609628.6(T - 190.027)(T - 242.906)} \tag{7.1}$$

where $d_{Max} = 999.973$ kg/m^3 $= 3.345 \times 10^{-2}$ Water/Å^3 is the maximum density of water and T the temperature in K.

In this study, a set of 11 pure bulk SPC/E water systems at different temperatures, containing 214 water molecules each, have been simulated. First, NPT simulations were run in order to reach a density of water molecules indicated by formula 7.1. Here, as indicated in section 4.1.1, it is useless to run NVT simulations and to vary the number of water molecules in the system since there is no crystal atom fixed. After equilibration, a NVT simulation was run for each of the 11 bulk systems for 1 ns. The densities of these 11 bulk water systems can be seen in figure 7.1.

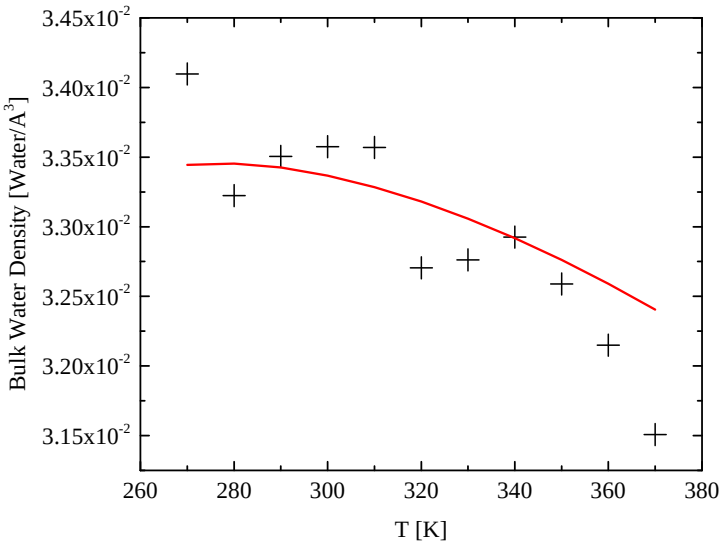

Figure 7.1: Water density versus temperature is shown in this graph. The simulation values (black crosses) seem to decrease faster than the the values obtained by a fit of the experiments [95] (red solid line). This can be explained by the relatively small number of water molecules and hence the small simulation cell sizes considered here.

The trend of water density versus temperature for the simulations is the same as what suggested by equation 7.1. Notwithstand, the decrease is faster. This can be explained by a too small number of water molecules and hence simulation cell size. These values were used for diffusion and NMR relaxation analysis as shown in the next sections.

7.1.2 Diffusion and Activation Energy

For each of these 11 simulations, the mean square displacement (MSD) of water molecules, or more precisely the MSD of the water oxygens, was calculated. The diffusion coefficients generated this way (D_{sim}) and the experimental values from literature (D_{exp}) [44] are recorded in table 7.1.

The diffusion activation energy can be generated using the Arrhenius law presented in chapter 2 section 2.7 and is shown in figure 7.2: the natural logarithm of the diffusion coefficient plot versus the inverse of temperature (in K). The slope is the activation energy divided by the gas constant $R = 8.31 J/(mol.K)$. Both simulation and experimental values are plotted.

Temperature [K]	D_{sim} [Å$^2/ns$]	D_{exp} [Å$^2/ns$]
270	113.51 ± 0.05	100
280	143.81 ± 0.02	135
290	184.90 ± 0.08	175
300	272.41 ± 0.04	185
310	281.54 ± 0.04	260
320	359.07 ± 0.04	330
330	429.56 ± 0.063	380
340	477.67 ± 0.08	460
350	526.37 ± 0.13	520
360	583.11 ± 0.14	640
370	658.70 ± 0.09	660

Table 7.1: 11 NVT simulations were used to generate the water mean square displacement and then to calculate the associated water diffusion coefficients D_{sim} and its standard error. These diffusion coefficients were compared with experimental ones D_{exp} [44]. This yields to the behaviour of water diffusion versus temperature.

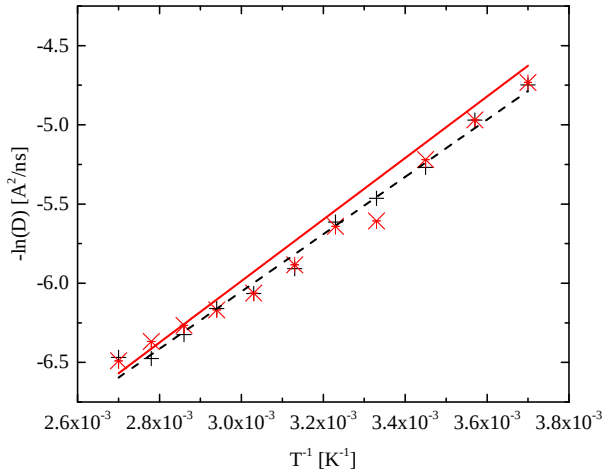

Figure 7.2: The Arrhenius law can be used to calculate the water diffusion activation energy. The natural logarithm of diffusion coefficient (simulation in red crosses and experiment in black crosses) is plotted versus the inverse of temperature in K^{-1}. The slope of the fitting straight line of these data (red solid line for simulation and black dash line for literature) is the activation energy divided by the gas constant. As a result, the water diffusion activation energy for the range of temperature 270-370 K found thanks to the 11 bulk water simulations is $E^{dif}_{a,sim} = 14.69 \pm 0.76$ kJ/mol, which is close to the activation energy from experiment $E^{dif}_{a,exp} = 16.08 \pm 0.45$ kJ/mol.

The bulk water diffusion activation energy for the simulations is $E^{dif}_{a,sim} = 14.69 \pm 0.76$ kJ/mol which is close to the measured value $E^{dif}_{a,exp} = 16.08 \pm 0.45$ kJ/mol, a relative difference of 9%. This suggests that SPC/E potential described in an accurate way the dynamic properties of water, especially for the diffusion.

7.1.3 NMR Relaxation Times and Activation Energy

The NMR relaxation time activation energy can also be calculated. For each of the 11 bulk water systems, the process explained in chapter 3 section 3.4.4 is applied: the spin pair correlation function is calculated and Fourier transformed to get the spectral density function and then the NMR relaxation times are calculated thanks to equation 2.13. Table 7.2 shows the different longitudinal relaxation times T_1 for each of the 11 temperatures for a frequency range of [10;100] MHz calculated from MD simulations. It is important to notice that a significant part of the uncertainty is due to the sensitivity to the local environment due to the $\frac{1}{r^6}$ term in the correlation function and also to the long time behavior of the correlation function that cannot be reached with MD. Despite these aspects, the order of magnitude is reasonable.

Temperature [K]	NMR relaxation time T_1 [s]
270	2.69 ± 0.54
280	3.40 ± 0.70
290	4.69 ± 0.73
300	5.63 ± 0.99
310	6.89 ± 1.56
320	8.21 ± 1.59
330	9.55 ± 1.71
340	11.17 ± 1.94
350	12.91 ± 2.46
360	14.48 ± 2.53
370	16.67 ± 2.80

Table 7.2: 11 NVT simulations were used to generate the NMR relaxation times T_1 (the T_2 is the same for this range of frequency). These results can be used to calculate the NMR relaxation time T_1 activation energy.

As for the diffusion coefficient, the Arrhenius law is used here to determine the NMR relaxation time T_1 activation energy. A plot of the natural logarithm of T_1 versus the inverse of the temperature (in K^{-1}) can be fitted by a straight line whose slope is related to the activation energy as shown in figure 7.3.

The NMR relaxation time T_1 activation energy for the simulations is $E_{a,sim}^{T_1} = 14.89 \pm 0.30$ kJ/mol whereas from an experimental study by Hindman et al [80] the activation energy is $E_{a,exp}^{T_1} = 16.51 \pm 0.14$ kJ/mol. The magnetudes are similar but the difference between these two values can be due to errors from the simulation (the far-far component used was the same for each whereas it can vary with temperature) or from the experiment. Indeed, according to Hindman, there can be a systematic error with experimental measurements but also some uncertainties associated with a correction he made for the spin-rotation constitution or even a possible correction to the inter molecular relaxation contribution arising from changes in the number density of interacting molecules around the relaxing nucleus.

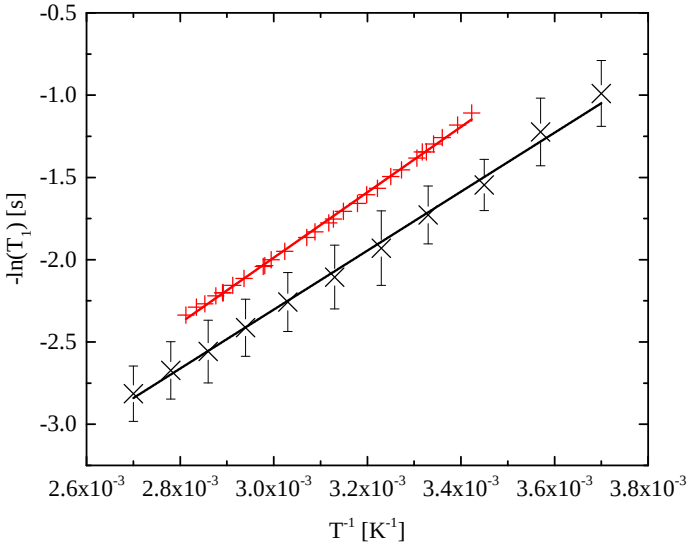

Figure 7.3: The Arrhenius law can be used to calculate the NMR relaxation time T_1 activation energy. The natural logarithm of T_1 (black crosses for simulation and red crosses for experiment [80]) is plotted versus the inverse of temperature (in K^{-1}). A straight line fits these data points (black line) and the slopes are the activation energies divided by the gas constant (black line for simulation and red line for experiment). As a result, the NMR relaxation time T_1 activation energy for the range of temperature 270-370 K found thanks to the 11 bulk water simulations is $E_{a,sim}^{T_1} = 14.89 \pm 0.30$ kJ/mol and $E_{a,exp}^{T_1} = 16.51 \pm 0.14$ kJ/mol .

7.2 Influence of Temperature on MD4 Model

In the previous section, the temperature influence on bulk water was analysed. Here, the temperature influence on NMR spin-lattice relaxation time T_1 in MD4 model is analysed. First, the preparation of the model, sligthly different than for bulk water, is discussed. Then, the diffusion of different water populations and the surface desorption activation energies are generated. Finally, the spin pair correlation functions are generated for each of the 11 temperatures.

7.2.1 Model Preparation

NVT simulations were run on the MD4 model at four different temperatures: 293.15, 313.15, 333.15 and 353.15 K (ie: 20, 40, 60 and 80 °C). The preparation of MD4 for these four temperatures is slightly different than what was done for bulk water. The same process used in chapter 5 for the choice of the model was used here. Since an NPT simulation cannot be performed because of the fixed atoms, the number of water molecules in the gel had to be changed in order to reach the required water density: the water density in the gel pore was adjusted in order to match the 3D bulk water simulation density at the same temperature since the local environment is important in the calculation of the NMR relaxation times. Also, the same water to silicon ratio (W/Si=2) was kept in the interlayer.
The different bulk densities were calibrated on the pure bulk water experimental ones [95].

7.2.2 Diffusion and Activation Energy

For these four simulations, a diffusion analysis was done. Different water populations were taken into account: {L2>Ω-B>L2}, {TL>TL>TL}, {B>B>B}, {Ω>Ω>Ω} and {IL>IL>IL}, where L1 and L2 stand for the surface layers, TL stands for the transition layer, B stands for bulk, Ω stands for the whole gel pore (ie: Ω=L1+L2+TL+B) and IL stands for the interlayer pore (in order to lighten the text, these populations will be written respectively L2, TL, B, Ω and IL). The water mean square displacement were generated for each of these populations and diffusion coefficients were calculated in the same way as in chapter 6 section 6.2. Finally, all the results are presented in table 7.3.

T [K]	D_{L2} [Å^2/ns]	D_{TL} [Å^2/ns]	D_B [Å^2/ns]	D_Ω [Å^2/ns]	D_{IL} [Å^2/ns]
293.15	0.85 ± 0.01	153.8 ± 0.1	258.8 ± 0.1	159.5 ± 0.1	7.61 ± 0.01
313.15	0.73 ± 0.01	237.5 ± 0.1	387.5 ± 0.1	236.0 ± 0.1	12.50 ± 0.01
333.15	1.04 ± 0.01	317.0 ± 0.1	500.5 ± 0.1	292.5 ± 0.1	24.38 ± 0.01
353.15	4.03 ± 0.01	387.3 ± 0.1	675.8 ± 0.1	394.8 ± 0.1	44.85 ± 0.01

Table 7.3: Four NVT simulations were used to generate different water populations (L2={L2>Ω-B>L2},TL={TL>TL>TL},B={B>B>B}, Ω={Ω>Ω>Ω} and IL={IL>IL>IL}, where {A>B>C} means that water molecules start in A, can go to B and are considered in the calculation at time t if in C) mean square displacement and to calculate the diffusion coefficients associated. They will be ploted in figure 7.4.

The natural logarithms of these diffusion coefficients can then be plotted versus the inverse of temperature. Such plots are fitted with a straight line whose slope is related to the activation energy for that process as suggested by the Arrhenius law. The {B>B>B} activation energy can be compared to the pure bulk activation energy. All of this can be seen in figure 7.4. L1 is not represented here because only vibration occurs.

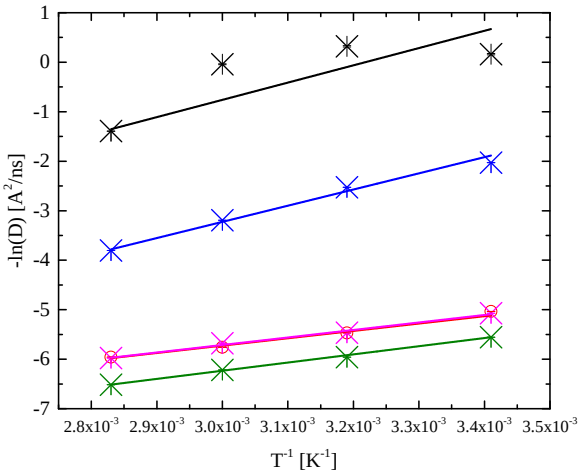

Figure 7.4: The natural logarithm of the diffusion coefficients of the different water populations are shown here. Crosses and circles represent the simulated values and the solid lines their fits by straight lines. The color code is as follows: black stands L2, purple for TL and red, just behind the green curves, for Ω, green for Bulk and blue for IL.

The different activation energies are listed in table 7.4.

Water Population	Diffusion Activation Energy [kJ/mol]
L2	20.8 ± 11.2
TL	13.3 ± 1.1
Bulk	13.5 ± 0.6
Ω	12.6 ± 0.8
IL	25.6 ± 1.9

Table 7.4: The diffusion activation energies were generated for the five different water populations (L2,TL,Bulk,Ω and IL) taking into account four temperatures from 293 to 253 K. The date presented in figure 7.4 were fited by straight lines whose slopes are the activation energies divided by the gaz constant for each water populations.

A first remark is to see that the TL and the whole gel pore Ω have the same diffusion behaviour, as if TL was an average of all the other gel water populations. Also, the MD4 bulk diffusion activation energy (13.5 ± 0.6 kJ/mol) is of the same order of the pure bulk water system activation energy (14.7 ± 0.8 kJ/mol) with a relative error of 9% which shows the weak influence of the crystal on the MD4 bulk water molecules behaviour. Finally the activation energy for L2 is bigger than that for the TL which is close to the Bulk value (one third more). This is consistent in so much as L2 is more influenced by the crystal than TL and Bulk and as TL and Bulk have close (same order of magnitude) diffusion coefficients.

7.2.3 Desorption and Activation Energy

The desorption properties also change with temperature. Qualitatively speaking, it is easier for water to desorb from a surface when the temperature is raised: the crystal fluctuates

more. Here, only the silicate oxygens are fixed in the simulation, just like the silicon atoms. The water molecules can acquire sufficient energy to overcome the barrier that otherwise that traps them on the surface thanks to stronger shocks from other water molecules. Here, the desorption of three water populations is taken into account: L1 (ie: {L1>SL>L1}), L2 (ie: {L2>L2+$\frac{\delta}{2}$>L2}) and SL (ie: {SL>SL+$\frac{\delta}{2}$>SL}), where SL=L1+L2 and δ is a water molecule size (≈ 2.8). As explained in chapter 6, the fact that a water molecule can go away from a layer by a distance of half a water molecule size is chosen in order to avoid a vibration artifact caused by the choice of the border.

The desorption times for the four temperatures are listed in table 7.5

T [K]	$\tau_{s,L1}$ [ns]	$\tau_{s,L2}$ [ns]	$\tau_{s,SL}$ [ns]
293.15	14.93 ± 0.15	2.07 ± 0.08	8.33 ± 0.06
313.15	10.31 ± 0.22	0.99 ± 0.09	6.85 ± 0.03
333.15	6.29 ± 0.25	0.65 ± 0.05	5.18 ± 0.08
353.15	4.61 ± 0.21	0.49 ± 0.06	3.89 ± 0.04

Table 7.5: 4 NVT simulations were used to generate L1, L2 and SL desorptions and the desorption times τ_s are listed here.

The natural logarithms of these desorption times can then be plotted versus the inverse of temperature. Such plots are fitted with a straight line whose slope is related to the activation energy as suggested by the Arrhenius law and shown in figure 7.5.

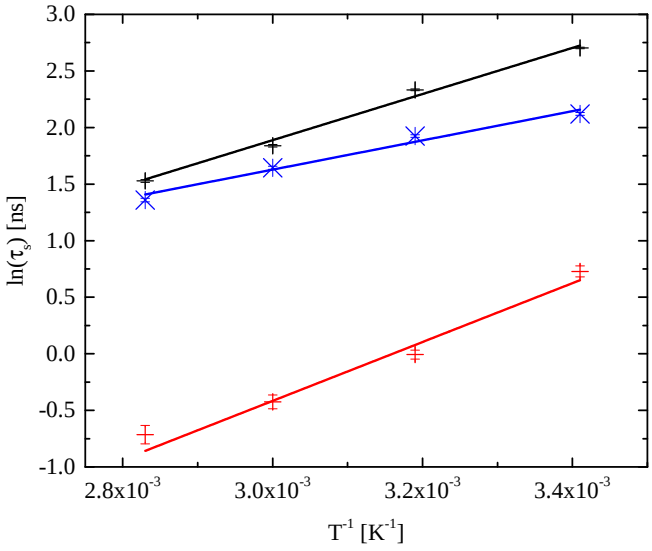

Figure 7.5: The natural logarithm of the desorption times of the different water populations are shown here. The dash lines represent the simulated values and the solid lines their fits by straight lines. The color code is as follows: black stands for L1, red stands for L2 and blue stands for SL=L1+L2.

The different activation energies are listed in table 7.6.

Surface Layer	Desorption Activation Energy [kJ/mol]
L1	16.95 ± 1.19
L2	21.61 ± 2.66
SL	10.74 ± 1.16

Table 7.6: The desorption activation energies were generated for the three different surface water populations taking into account four temperatures from 293 to 253 K.

It is interesting to notice that these results are not consistent with what could be expected: it should be more difficult for a L1 water molecule to desorb than for a L2 water molecule.

7.2.4 Correlation Functions

The last analysis that is made here is the correlation function analysis. Unfortunately, contrary to the pure bulk system, the simulation time is not big enough to generate accurate relaxation times over a frequency range which extends to the experimentally accessible regime and there is no far-far correction to add to the G(t) in this case. However, the correlation functions can be estimated for the available data. However, no genuinely quantitative analysis can be made. The four correlation functions are shown in figure 7.6.

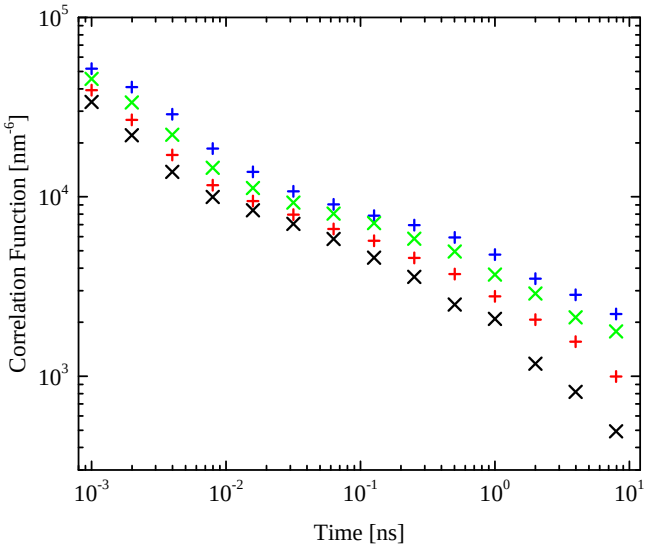

Figure 7.6: The correlation functions for MD4 model at different temperatures have been generated (dash lines). The color code is as follows: blue stands for T= 293.15K, green stands for T= 313.15K, red stands for T= 333.15K and black stands for T= 353.15K.

As shown in figure 7.6, if temperature increases the correlation time decreases (ie: the curve decreases earlier and faster), which is normal as water molecules are moving faster and the spin relaxation is faster.

Nevertheless, at the frequency t=0, all the correlation functions start at the same value

and when $t \gg 1$ ps, the typical shape of correlation functions, whatever the temperature, is theoretically $\approx \frac{1}{t}$, where t is time. Unfortunately, this cannot be seen here because of the too small amount of data. Molecular Dynamics technique is not adapted for this purpose. Nevertheless, MD can be used in order to parameterize a more suitable simulation technique: Monte Carlo simulations as said in chapter 6.

7.2.5 Experimental NMR Relaxation Times of White Cement Paste

Finally, it can be interesting to speak about the experimental NMR relaxation times. A. Gajewicz analysed in her thesis [96] the influence of temperature on NMR T_1 relaxation time on white cement paste samples. She recorded the NMR signal and used an inverse Laplace transform software in order to get the T_1 at different temperatures in the range [-20°C; 60°C]. She used a sample at 28 days of hydration and another one at 90 days of hydration. Her results for the two nanopores are shown in table 7.7:

Pore water	T_1 AE 28 days [kJ/mol]	T_1 AE 90 days [kJ/mol]
C-S-H interlayer	3.26 ± 0.29	3.12 ± 0.20
C-S-H gel	1.14 ± 0.10	0.88 ± 0.20

Table 7.7: The T_1 activation energies [AE] for C-S-H interlayer and gel pores water were measured. The values are shown for a 28 days hydration and a 90 days hydration samples are shown. These results are extracted from A. Gajewicz thesis [96].

As said in section 6.4, MD simulations cannot reach a long enough time to generate activation energies for NMR relaxation time T_1 using MD4 model. However, thanks to the MD parameters, a MC simulation could reach a long time to get results that could be compared to A. Gajevicz's data. This is a milestone for a continuation of N. Howlett's Monte Carlo project.

Chapter 8

Water Exchange between the Interlayer and the Gel Pores

The purpose of this chapter is to discuss the exchange of water between the two nanopores. Monteilhet [94] suggests an exchange time of the order of 5 ms. This number looks too big for the nanoscale. To quantify this typical exchange time, a desorption analysis of the interlayer pore is performed on a MD model based on MD4 where the interlayer and the gel pores are connected. The desorption curve generated this way is fitted and a desorption time can be found. Another analysis based on the diffusion coefficient of water molecules in the interlayer can be carried on. Finally, four hypotheses about what could happen at the edge of the interlayer are presented.

8.1 Gel-Interlayer Exchange Model

The gel-interlayer exchange model that is discussed here is based on the previous MD4 model with the same basic crystal stucture using the same interaction potentials (SPC/E water and CLAY_FF). First, all the water molecules were removed. Then, the size of the gel pore was reduced to reach the interlayer size (ie: from ≈3.5 nm to ≈1 nm). As a result, there were only two interlayer pores. The size of these interlayer pores was set to ≈5.5 nm. This model gel pore was placed on the y axis in the continuation of the two interlayers, which allows exchange. The size of this gel pore was set to the same size of the MD4 model gel pore: ≈3.5 nm. Finally, the interlayer and the gel pores were filled with water molecules in the same way as for MD4: the water to silicon ratio in the interlayer was set to 2 (W/Si=2) and an approximated number of water molecules was placed in the gel pore in order to reach a bulk density in the bulk zone of 1 kg/dm^3 as explained in section 5.2.2 in chapter 5. The model is shown in figure 8.1. The IL_E and IL_C notation is introduced in this figure and will be used in the next section.

A NVT simulation was run and the number of water molecules was adjusted in the gel bulk zone because of the exchange of water molecules between the gel and the interlayer pores. This model is composed of 4983 atoms. Also, as for MD4, the silicon atoms were fixed. The border between the interlayer and the gel is not well known. In this model, the crystal layer was just cut in such a way that the silicate dimers were not destroyed.

Once the model stabilised, a NVT simulation of 20 ns was run. The simulation temperature was set to $T = 300$K thanks to a Berendsen thermostat. The other input parameters are the same ones as in MD4 simulations: the simulation timestep was 0.001 ps, the shake algorithm and the quaternion algorithm were used with a tolerance of 10^{-5}. The Ewald summation was also used even if the system was not charged balanced which can be the source of some errors. The cutoff distance was set to 8Å.

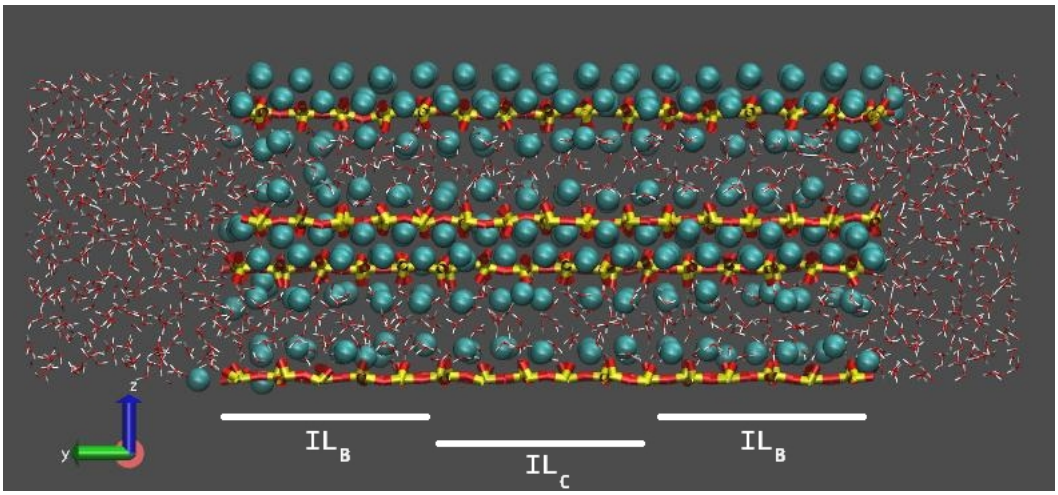

Figure 8.1: This model is composed of two interlayer pores (whose length is ≈5.5 nm) connected with a gel pore (whose length is ≈3.5 nm). The connections allow exchange between the two pores. The color code is as for MD4 model: yellow (silicon) and red (silicon oxygen) chains stand for the silica dimer chains, white (water hydrogen) and red (water oxygen) triangles stand for water molecules and blue balls stand for calcium ions. The interlayer is split into three parts: two interlayer border zones (IL_E) and one interlayer center zone IL_C.

8.2 Desorption, Exchange Time and Tortuosity

8.2.1 Interlayer Desorption

Once the simulation finished, a desorption analysis on different water populations was performed. Such curves were averaged over 50 initial times, each of them separated by a time interval of 100 ps. Each curve is fitted by a two exponential function since one can see two water populations in the interlayer: the surface one and the bulk one.

The main desorption curve is the {IL>IL>IL} that corresponds to the water molecules that were in the interlayer pore at time $t = 0$ and never moved away from it. The number of these waters is plotted in figure 8.2. This curve was fitted by an exponential function: $fit(t) = 105.72e^{-\frac{t}{4.94}} + 429.25$ waters, where the desorption time is $\tau = 4.94 \pm 0.02$ ns. This fit used a two exponential function and the second decaying time was of the order of 10^{100} ns, which implies either that there was not enough data to fit the decay of water molecules either that 429 water molecules stay in the interlayer and never exchange. A 2D diffusion analysis will show in the next section that this offset is an artifact due to the small amount

of data.

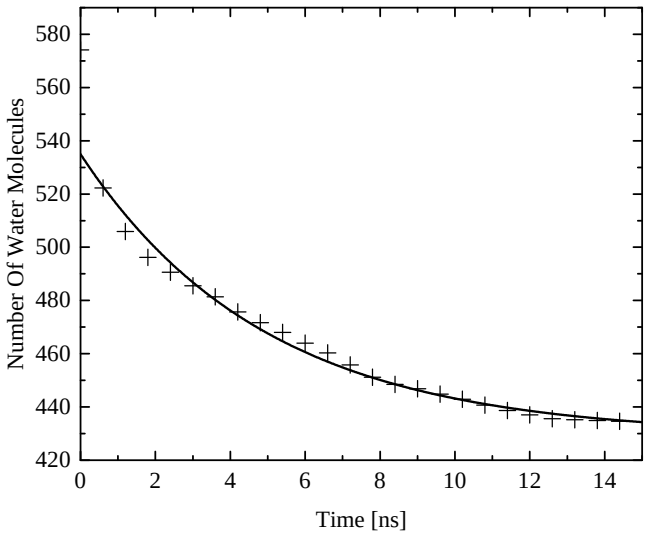

Figure 8.2: The desorption analysis of the {IL>IL>IL} set of water molecules is performed. This yields to a decaying curve (black crosses) that is fitted by an exponential function (black line) with a decaying time $\tau = 4.94 \pm 0.02$ *ns and an offset of 429 water molecules (ie:* $fit(t) = 105.72e^{-\frac{t}{4.94}} + 429.25$ *waters).*

A more detailed analysis looking at the water molecules in the interlayer center region (that can directly exchange with gel) and in the interlayer edge region is performed. These regions were defined in figure 8.1. Each of the three regions (one IL_C and two IL_E) has approximately the same amount of water which is ≈180 water molecules.

The $\{IL_C{>}IL_C{>}IL_C\}$ and $\{IL_C{>}IL{>}IL_C\}$ population desorptions are shown in figure 8.3. The $\{IL_C{>}IL{>}IL_C\}$ population does only decay after a time of ≈ 7 ns, which is consistent since the water molecules that moved to the IL_E need some time to reach the border between the gel and the interlayer. This is not the case for the $\{IL_C{>}IL_C{>}IL_C\}$ population which is fitted with a two exponential $fit(t) = 80.34e^{-\frac{t}{9.52}} + 92.71$ waters. The offset was actually the prefactor of an exponential with a decaying time of the order of 10^{100} ns like with the $\{IL > IL > IL\}$ water population. The same 2D diffusion analysis will explain this in the next section.

The $\{IL_E{>}IL{>}IL_E\}$ and $\{IL_E{>}IL_E{>}IL_E\}$ population desorptions are shown in figure 8.4. The $\{IL_E{>}IL_E{>}IL_E\}$ decays faster than the $\{IL_E{>}IL{>}IL_E\}$ since the second one allows water to go to the IL_C region. The first one is fitted by a two exponential function $fit(t) = 69.84e^{-t/3.27} + 102.57e^{-t/49.09}$ waters and the second one is also fitted by a two exponential function $fit(t) = 49.7e^{-t/4.32} + 125.91$ waters where the second decaying time is of the order of 10^{100} ns.

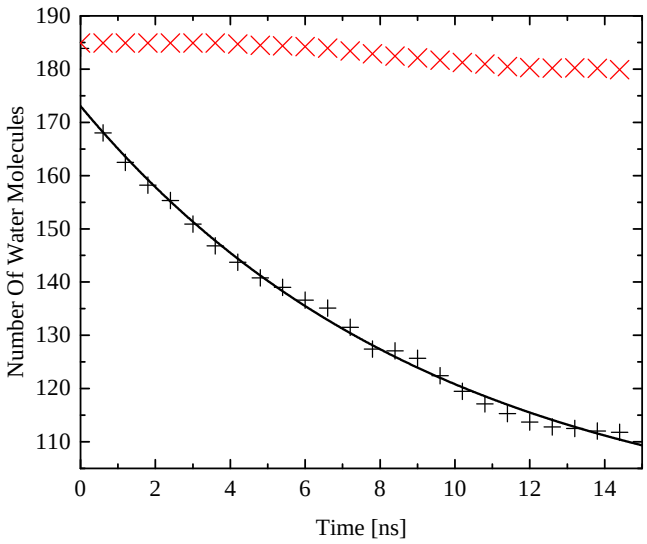

Figure 8.3: The desorption analysis of the $\{IL_C{>}IL{>}IL_C\}$ (red crosses) and $\{IL_C{>}IL_C{>}IL_C\}$ (black crosses) set of water molecules is carried out. The first one does not decay in the analysis time range since a water molecule in the center of the interlayer needs ≈ 7 ns to reach the gel. The second one is fitted (black line) by an exponential $fit(t) = 80.34e^{-\frac{t}{9.52}} + 92.71$ waters.

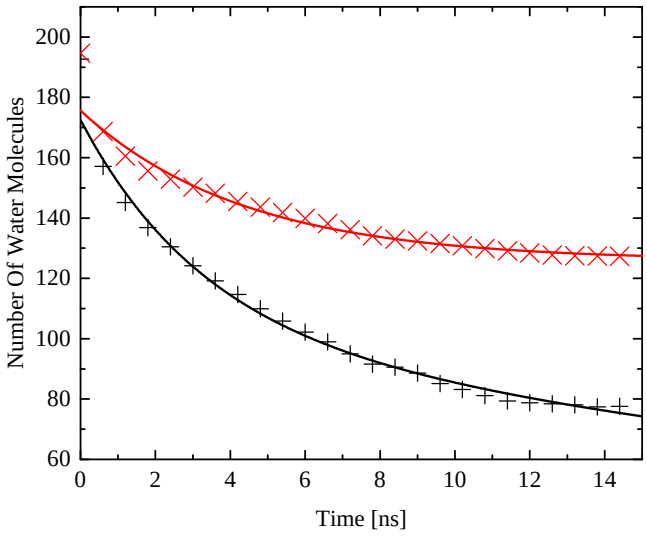

Figure 8.4: The desorption analysis of the $\{IL_E{>}IL{>}IL_E\}$ (red crosses) and $\{IL_E{>}IL_E{>}IL_E\}$ (black crosses) set of water molecules is performed. The first one is fitted (red line) by $fit(t) = 49.7e^{-t/4.32} + 125.91$ waters and the second one is fitted (black line) by $fit(t) = 69.84e^{-t/3.27} + 102.57e^{-t/49.09}$ waters.

Figures 8.3 and 8.4 show there is exchange between the three arbitrary defined zones and that water needs time to move away from the interlayer, either by the left side either by the right side. The desorption from these "sub zones" uses the other "sub zones", which increases the time necessary for desorption. Each of these curves has two behavours shown in table 8.1: a fast decay that corresponds to a decaying time in the range of $[0; 10]$ ns, and a slow decaying time bigger than 40 ns (mathematically up to infinity according to the presence of an offset in the fits). The slow decaying time is a problem since the amount of data used for this analysis is not big enough to assert such a time. However, a diffusion analysis in the interlayer is a key element to give more information about this long time.

Water population	Fast desorption time ∈ [0,10] [ns]	Slow desorption time 40 [ns]
$\{IL_C{>}IL_C{>}IL_C\}$	9.5	
$\{IL_C{>}IL{>}IL_C\}$	-	yes
$\{IL_E{>}IL_E{>}IL_E\}$	3.3	49.1
$\{IL_E{>}IL{>}IL_E\}$	4.32	

Table 8.1: The slow and fast desorption times of the four water populations $\{IL_C{>}IL_C{>}IL_C\}$, $\{IL_C{>}IL{>}IL_C\}$, $\{IL_E{>}IL_E{>}IL_E\}$ and $\{IL_E{>}IL{>}IL_E\}$ are shown in this table. When existing according to the analysis, the fast decaying time is in the range of [0,10] ns whereas nothing can be said about the slow decaying time but it is bigger than 40 ns.

8.2.2 Interlayer Diffusion versus Long Desorption Times

In chapter 6 section 6.2.5, the diffusion coefficient of water in the interlayer was calculated and was found to be $D_{IL} = 9.44 \pm 0.01 \times 10^{-11} m^2/s$. Thanks to this, an estimation of the time necessary for a water molecule in the middle of the interlayer pore (ie: IL_C) to reach the gel pore is calculated. This water molecule has to move a minimum distance of half the size of the interlayer $\frac{size}{2} = \frac{5.5}{2} = 2.75$ nm. Hence, according to the one dimension diffusion coefficient equation (in the in the y direction according to figure 8.1):

$$\tau \approx \frac{size^2}{8D} = 72.8 \text{ ns} \tag{8.1}$$

Hence, the time a water molecule in the middle of the interlayer pore needs to desorb to the gel pore is at least 72.8 ns. Indeed, here, only the shortest distance was considered (ie: the water molecule can also move along the x direction in the interlayer pore). This time agrees the criteria of a long desorption time bigger than 40 ns from the desorption analysis and is ≈69000 times smaller than Monteilhet's exchange time.

Moreover, figure 6.9 in chapter 6 section 6.2.5 shows that water molecules in the interlayer do not stay fixed on the surface. Hence, the long desorption time is finite, and the fast exchange between the surface and the middle of the interlayer pore (in the z direction) is a key element here: all the interlayer water molecules diffuse with a diffusion coefficient $D_{IL} = 9.44 \pm 0.01 \times 10^{-11} m^2/s$.

The diffusion equation can be used in a different way to see what would be the typical distance l that a water molecule in the interlayer should travel for a typical desorption time

of $\tau_{exp} = 5$ ms:

$$\frac{l}{2} = (2D\tau_{exp})^{1/2} = 9.72 \times 10^{-7} \text{ m or } l = 1943 \text{ nm} \tag{8.2}$$

This size is 350 times bigger than the expected size of the interlayer. A number of hypotheses about the interlayer connections, presented in the next section, can explain such a long desorption time with an interlayer size of ≈ 5.5 nm.

8.2.3 Possible Water Behaviour in the Interlayer

Four different hypotheses about the connection between the interlayer and the gel pores are presented in this section. They could explain the long residency time in the interlayer.

Interlayer Edge Diffusion

A first hypothesis is about the diffusion about the interlayer edge. It is certainly too simple to consider the diffusion coefficient is constant in the interlayer. Indeed, in chapter 6, the diffusion analysis was performed on an infinite interlayer. However, in real life, the gel and the interlayer pores are connected and the behaviour of water molecules around the border is not straightforward. Figure 8.5 suggests such a behaviour.

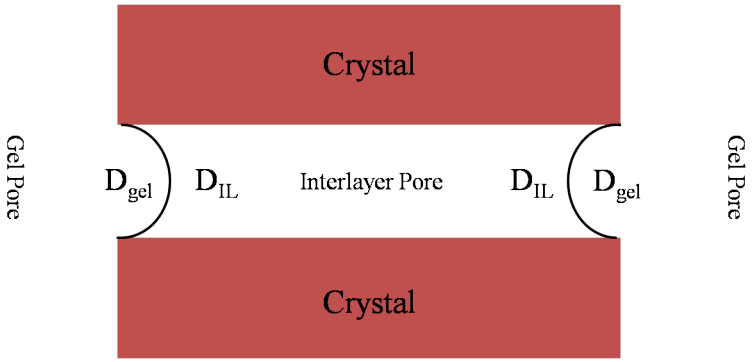

Figure 8.5: The desorption coefficient in the interlayer is not the same everywhere because of the exchange between the interlayer and the gel pore. A simple idea is to consider the gel influence is not limited to the edge of the interlayer.

Obstructed Interlayer Pore End

A second hypothesis is about the obstruction of the interlayer ends. Indeed, since there is no dominant directions for the interlayer axes, some can touch each other with an angle. This angle can influence on the exchange between the interlayer and the gel because of the opening of the connection but also because of the interaction between water molecules that try to reach the gel pore and the obstructing surface. Figure 8.6 shows such a possible layout of the different interlayers.

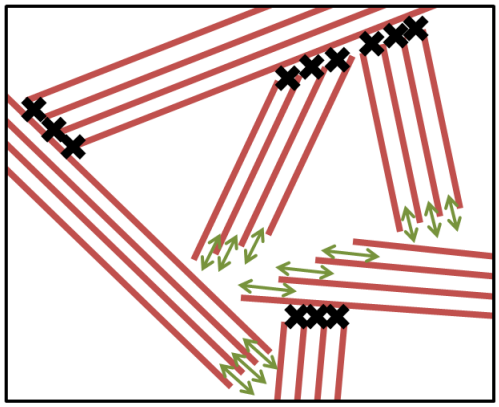

Figure 8.6: The desorption of the interlayer water molecules can be disturbed by the presence of other crystal layers obstructing the end of the interlayer. In this figure, red lines represent the crystal layers, black crosses mean water exchange is difficult whereas green double arrows show easier exchange zones.

This hypothesis is interesting because connections between the different pores is looking like the Feldman and Sereda's model (chapter 1 section 1.3.2).

Chemical Boundary at the Interlayer End

A Third hypothesis is the presence of chemical boundaries at the interlayer pores ends. Since the chemical structure used in this study is just a model and is not totally known, the actual chemical composition at the end of the interlayer can have a significant effect on the water transport properties around this region. The exchange between the two nanopores could then be influenced and a long desorption time would characterize this exchange.

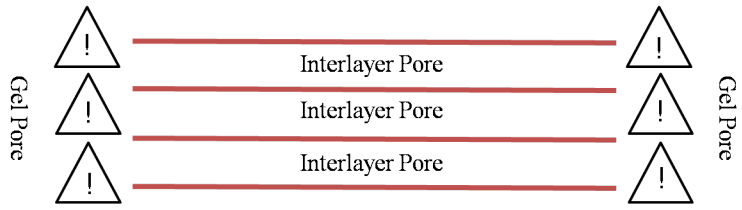

Figure 8.7: The desorption of the interlayer water molecules can be disturbed by the chemical composition of the end of the interlayer pore. However, the actual chemical structure of such a system is not well known. The red lines represent the crystal layers and the warning triangles at the ends of the interlayers suggest an unknown structure.

Interlayer Collapsing at the End

A last hypothesis discussed here is the collapse of some interlayer pores ends. For instance, if some calcium ions escape the interlayer pores, then the stability of the pore could be affected and the two crystal layers that form the interlayer could merge or at least be closer and closer from each other which would imply a more difficult exchange of water molecules between the two nanopores. Fully closed pores in another possibility.

Figure 8.8: The desorption of the interlayer water molecules can be disturbed by the collapse of the crystal layers that create the interlayer pore. The black arrows represent such collapses at different places of the model that would reduce the water exchange and the green double arrows represent an easier exchange where there is no layer collapse.

Chapter 9

Discussion And Further Work

It has been shown in this thesis that Molecular Dynamics simulations of cement analogues can provide a good amount of insight about water transport properties and ^{1}H NMR relaxometry in cement pastes at the nanoscale. This work also helped to build Faux's new two layers model that interprets in a better way the NMR experimental data than Korb's single layer model [12, 13].

This work first focused on a 3D bulk water system interacting thanks to SPC/E potential [70] in order to benchmark the methods used to analyse transport properties and NMR relaxation. The diffusion coefficient at 300 K generated thanks to this simulation was close to the experimental one ($D_{3D\ bulk,sim}$=2.66 $\times 10^{-9}$ m^2/s and $D_{3D\ bulk,exp}$=2.597 $\times 10^{-9}$ m^2/s) [77]. In the same way, a ^{1}H NMR relaxation analysis was performed based on the BPP theory [11, 29, 32, 33]. The simulated correlation function G(t) had the same characteristics of the experimental and theoretical ones. It was Fourrier transformed to get the spectral density function J(ω) and the NMR relaxation times $T_{1,2}$ that were of the same order of magnitude of the experimental ones ($T_{1,sim}$=5.0s and $T_{1,exp}$=3.8s) [80]. The differences between the simulated and experimental values were due in part to the size of the system [78, 79].

This study then focused on the C-S-H nanostructure models. Feldman and Sereda's C-S-H morphology [20, 21] suggested a set of highly connected silica layers surrounding by calcium ions and water filling the two nanopores, the interlayer and the gel pores, created by the layer lattice. This morphology and experimental data such as the Q_n analysis were used by chemists to build atomistic configurations of C-S-H analogues [9, 81]. A set of 13 C-S-H analogues MD simulations based on SiO_2 α-quartz crystal, tobermorite 11 Å and modified tobermorite 14 Å was selected and tested [87, 89, 90]. These models used either CLAY_FF+SPC/E potentials [69, 70] or modified Freeman+TIP4P potentials [71]. The MD4 model emerged as the reference from this selection. This model is based on a modified tobermorite 14Å (the bridging silica tetrahedra replaced by calcium ions) where the crystal layers form two nanopores: the gel pore (size=3.5nm) and the interlayer pore (size=1nm) filled by water [8] ($density_{Gel}$=1 kg/L; $Water/Si_{interlayer}$=2) [81]. It is important to notice that the CLAY_FF potential used for MD4 was not designed for this structure but was the best one available. Analyses of water transport properties and ^{1}H NMR relaxometry were performed.

Five different water populations, four in the gel pore and one in the interlayer pore, were defined in this model thanks to a water density profile. The gel pore is composed of bulk water in the middle B, two surfaces layers L1 and L2 and a transition layer TL between L2 and L1. This 4 layers structure is very different from the common idea of a composition of only one water surface layer and one bulk water layer. The interlayer pore is a kind of small gel pore (a size of 1 nm compared to the 3.5 nm for gel pore) and is composed of two sub-populations: the center and the surface water populations. However, since the exchange between these two sub-populations is fast on the MD simulation timescale, only one interlayer population IL is considered for this study. The gel bulk has the same properties as the 3D bulk system which is the reason of its name ($D^{300K}_{MD4,bulk}$=2.96 $\times 10^{-9}$ m^2/s and $D^{300K}_{3D\ bulk}$=2.66 $\times 10^{-9}$ m^2/s). The TL has very similar properties as bulk but the influence of the crystal can still be detected ($D^{300K}_{MD4,TL}$=1.42 $\times 10^{-9}$ m^2/s). Finally, the L1 and L2 layers are separated by calcium ions and have very different transport properties: the L1 water molecules are bound to the crystal matrix and do not really move on the simulation timescale ($D^{300K}_{MD4,L1}$=1.98 $\times 10^{-13}$ m^2/s) whereas the L2 are more free ($D^{300K}_{MD4,L2}$=6.01 $\times 10^{-12}$ m^2/s). The diffusion coefficient between L2 and TL or B are very different (3 orders of magnitude). However, these gel populations are not closed systems (which is the case for IL in MD4 or bulk and surface in Korb's model). A water molecule can move from L2 to TL and more precisely, it can use TL to do a hop and go back to L2, which is important for diffusivity. Desorption analyses were performed on the different layers to quantify these exchange times and the desorption from the surface layers did not reach the value obtained by the analysis of NMR experimental data with Korb's model which is at least 3 orders of magnitude longer than an MD simulations exchange time (τ^{300K}_{L1} 1 to 10 ns, τ^{300K}_{L1} 0.1 to 1 ns and τ_{Korb} 13 μs $\approx 10^3 \tau^{300K}_{L1}$). The gel layer properties analyses helped to build Faux's new model which considers two layers of water that can exchange: a low mobility layer (L2) that is shifted away from the crystal (because of the L1 quasi fixed water molecules) and a high mobility layer (a mix of TL and B). This new model is parameterized by MD outputs (diffusion coefficient and exchange time) and can interpret NMR data in a better way and respects experimental results [13].

The ^{1}H NMR relaxation analysis could only be partially performed. The role of the Fe^{3+} impurities in the crystal layer is important and is considered in the unlike spin correlation function part G_{IS}. Contrary to the like spin correlation function G_{II} which can be Fourier transformed, there is not enough data to Fourrier transform the G_{IS} function, and then, not enough data for the total correlation function $G=G_{II}+G_{IS}$. The MD technique is not adapted to reach a time long enough to evaluate fully G_{IS}.

The influence of the temperature was also studied. A set of 11 3D bulk water systems at different temperatures $T \in [270; 300]$ K were simulated. The diffusion coefficients and ^{1}H NMR relaxation times were generated and the associated activation energies were calculated, compared to and of the same order of the literature data ($E^{dif}_{a,sim\ 3D\ bulk}$=14.69 kJ/mol, $E^{dif}_{a,exp\ 3D\ bulk}$=16.08 kJ/mol, $E^{T1}_{a,sim\ 3D\ bulk}$=14.89 kJ/mol and $E^{T1}_{a,exp\ 3D\ bulk}$=16.51 kJ/mol) [44]. A set of four MD4 systems at 293.15, 313.15, 333.15 and 353.15 K were simulated. The diffusion coefficients and desorption times of each layer were calculated and activation energies for both were generated. The activation energy for the ^{1}H NMR relaxation times could not be calculated because of a lack of data (MD simulations roughtly reached tens of

nanoseconds).

A final analysis was to look at the exchange between the interlayer and gel pores. Monteillhet found an exchange time of the order of 10^{-4} s [94]. Another model based on MD4 was build and allowed water exchange between the interlayer and the gel pores. The length of the interlayer was set to 5.5 nm as suggested by the litterature. An exchange time in the range of $[10^{-8}; 10^{-7}]$ s was found, which is at least 3 orders of magnitude faster than Monteillhet's expectations. However, this MD model may not represent in a good way what is happening at the end of the interlayer.

Finally, even if these MD simulations helped to understand in a better way the water transport properties in cement pastes at the nanoscale, it is clear that they are limited by the available knowledge about the C-S-H nanostructure. Actually, the model of such a structure is the subject of widespread discussions in the cement community. The MD4 model is recent. There is no potential defined for this structure: CLAY_FF and Freeman potentials are designed for close structures but not for MD4. A more detailed potential could be created for such a modified tobermorite 14 Å structure. Also, more work should be done on the behavour of water at the border between the interlayer and the gel pore. Four hypotheses presented in this work can be analysed more deeply in the future. It has also been shown that even if the MD method is good to look at the details of water displacement in cement analogues, it is highly limited by the simulation time. Monte Carlo simulations can be parameterized by MD to reach longer times and generate for instance the ^{1}H NMR relaxation times for MD4 and its activation energy [40].

Appendices

PHYSICAL REVIEW E **91**, 032311 (2015)

Model for the interpretation of nuclear magnetic resonance relaxometry of hydrated porous silicate materials

D. A. Faux,* S.-H. P. Cachia, P. J. McDonald, J. S. Bhatt, and N. C. Howlett
Department of Physics, University of Surrey, Guildford GU2 7XH, United Kingdom

S. V. Churakov
Laboratory of Waste Management, Paul Scherrer Institute, CH-5232 Villigen, Switzerland
(Received 21 November 2014; published 20 March 2015)

Nuclear magnetic resonance (NMR) relaxation experimentation is an effective technique for probing the dynamics of proton spins in porous media, but interpretation requires the application of appropriate spin-diffusion models. Molecular dynamics (MD) simulations of porous silicate-based systems containing a quasi-two-dimensional water-filled pore are presented. The MD simulations suggest that the residency time of the water on the pore surface is in the range 0.03–12 ns, typically 2–5 orders of magnitude less than values determined from fits to experimental NMR measurements using the established surface-layer (SL) diffusion models of Korb and co-workers [Phys. Rev. E **56**, 1934 (1997)]. Instead, MD identifies four distinct water layers in a tobermorite-based pore containing surface Ca^{2+} ions. Three highly structured water layers exist within 1 nm of the surface and the central region of the pore contains a homogeneous region of bulklike water. These regions are referred to as layer 1 and 2 (L1, L2), transition layer (TL), and bulk (B), respectively. Guided by the MD simulations, a two-layer (2L) spin-diffusion NMR relaxation model is proposed comprising two two-dimensional layers of slow- and fast-moving water associated with L2 and layers TL+B, respectively. The 2L model provides an improved fit to NMR relaxation times obtained from cementitious material compared to the SL model, yields diffusion correlation times in the range 18–75 ns and 28–40 ps in good agreement with MD, and resolves the surface residency time discrepancy. The 2L model, coupled with NMR relaxation experimentation, provides a simple yet powerful method of characterizing the dynamical properties of proton-bearing porous silicate-based systems such as porous glasses, cementitious materials, and oil-bearing rocks.

DOI: 10.1103/PhysRevE.91.032311 PACS number(s): 82.33.Ln, 76.60.−k, 68.08.−p, 47.11.Mn

I. INTRODUCTION

Proton nuclear magnetic resonance (NMR) relaxation analysis is the most powerful technique for probing the dynamics of hydrogen-bearing molecules in porous media with applications in disciplines as diverse as petroleum engineering, catalysis, polymer science, biology, glass science, and construction materials. NMR relaxation analysis is able to provide information on the motion of hydrogen (^{1}H) protons in porous materials at the nanoscale, to infer pore-size distributions, pore surface-to-volume ratios, the time scale for pore filling and emptying, and to infer the diffusion mechanism for the mobile molecules.

According to the Bloembergen, Purcell, and Pound (BPP) model [1], the NMR spin-lattice and spin-spin relaxation times, T_1 and T_2, depend on fluctuations in magnetic dipole-dipole interactions between proton spins (usually labeled as I spins) on the same molecule (intramolecular or rotational), different molecules (intermolecular translations), and between mobile I spins and static paramagnetic impurities, labeled as S spins. Thus the interpretation of NMR relaxation experiments depends on models describing the movement of the proton-bearing fluid. Time-dependent dipole-dipole correlation functions $G(t)$ derived from a model are Fourier transformed to obtain the NMR T_1 and T_2 relaxation dispersions for comparison with experiment. One family of widely used models has been pioneered by Korb and co-workers over the last 15–20 years [2–9]. An early work [3] provided a simplified model for the relaxation associated with the I-S spin interactions between diffusing protons contained in a quasi-two-dimensional (Q2D) volume of fluid and a dilute concentration of static paramagnetic impurities on the pore surface, chiefly Fe^{3+}. Fe^{3+} ions are present in many porous silicate materials by the substitution of silicon atoms and, although concentrations are low, the I-S spin interactions dominate the dipolar relaxation at low magnetic field strengths. Therefore, models of the relaxation in cementitious materials, rocks, many glasses, and silica-based granular material include, as the primary relaxation mechanism, the interaction of the mobile I spins with the static S impurities.

The models of Korb and co-workers isolate the separate contributions to the relaxation of spins diffusing in the bulk volume of the pore and spins adsorbed to the pore surface. Assuming exchange between the pore surface and the pore bulk that is faster than the T_1^{-1} and T_2^{-1} relaxation rates (the biphasic fast-exchange regime), the experimental relaxation rates T_1^{-1} and T_2^{-1} are the average of that for the surface fluid and the bulk fluid weighted by the number of spins contributing to the relaxation in each environment [10]. In 2001, Godefroy *et al.* [4] argued that the dominant contribution to the dipolar relaxation in silica carbide granular media was associated solely with the interaction between adsorbed mobile I spins and the electronic spin associated with rare Fe^{3+} paramagnetic impurities located on the surface of the pore. The surface I-S interaction was shown to dominate due to a t^{-1} dependence of the dipolar correlation function $G(t)$ at long times compared to a t^{-2} dependence due to the dipolar interaction between bulk

*Corresponding author: d.faux@surrey.ac.uk

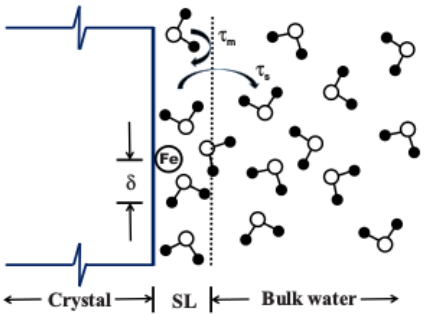

FIG. 1. (Color online) A schematic representation of the surface layer (SL) model presented by Korb and co-workers [3,4]. Water diffuses with a correlation time τ_m in the surface layer of a pore containing a dilute concentration of Fe^{3+} paramagnetic impurities. Water desorbs into the pore bulk with a characteristic time τ_s and ceases to contribute to the dipolar relaxation thereafter. $\delta \approx 0.27$ nm is the approximate distance of closest approach of a water proton to a Fe^{3+} impurity.

I spins and surface S spins. We refer to this model, illustrated in Fig. 1, as the surface-layer (SL) model.

According to the SL model, adsorbed proton-bearing molecules undergo a two-dimensional (2D) walk across the pore surface, making repeated encounters with surface paramagnetic impurities. The I-S dipolar interaction is modulated by the translational motion of spin I on the surface. The model invokes two correlation times: τ_m, the correlation time for surface hops associated with the 2D walk of the I spins on the surface, and τ_s, the surface residency time which is a measure of surface affinity. Experiments were undertaken by Godefroy *et al.* [4] on hydrated granular porous systems comprised of micron-sized grains of SiC. The pore surfaces were composed of silica (SiO_2). τ_m was obtained by fitting the SL model to the frequency dependence of T_1^{-1} and found to be 0.6 ns. τ_s was estimated from the high-frequency limit of T_1^{-1} as 1.6 μs. Later, the SL model was successfully fitted to T_1^{-1} over three orders of magnitude of frequency (20 kHz to 20 MHz) for a mortar [5] and to the ratio T_2/T_1 for white cement paste [6]. The frequency dependence of T_1^{-1} is particularly sensitive to τ_m and consistent values for τ_m are obtained for a range of porous materials with silica-based pore surfaces. For example, in the case of calcium silicate hydrates (C-S-H), the active phase in cement materials [11,12], τ_m is of the order of 1.3 ns [5]. The relaxation times *per se* are much less sensitive to τ_s, but it was nevertheless established that $\tau_s \gg \tau_m$ [4–6]. However, the ratio of T_2/T_1 depends critically on τ_s. A factor of about 0.25 at 20 MHz is typical for C-S-H and leads to an estimate of $\tau_s = 13$ μs [6], which is close to the value for the hydrated SiC granular system of Godefroy *et al.* [4].

Despite the success of the SL model in interpreting NMR relaxation data and in yielding consistent values of τ_m and τ_s for a variety of systems, the validity of the model has been questioned. The estimate of $\tau_s = 13$ μs for the surface residency time in cementitious material is long and indicates that a water molecule makes approximately 10 000 hops before desorbing. It is a challenge to devise a mechanism that allows water molecules to be sufficiently mobile to traverse distances of typically 30 nm, yet to be bound to the surface throughout. Moreover, the SL model assumes that spins which desorb to the pore bulk do not contribute to the relaxation thereafter. In other words, it is assumed that a desorbed spin does not return to the surface on a time scale much longer than the surface residency time of 13 μs. Yet, a bulk water molecule diffuses a distance of about 0.4 μm in 13 μs, a distance which is much larger than the typical pore thickness in cementitious materials where, despite uncertainty as to the morphology of mature C-S-H, most pores have sizes ranging from about 2 to 50 nm [7,13,14]. Furthermore, the fast-exchange model has limited application if $\tau_s \approx 10$ μs. For a pore of thickness equivalent to 10 surface layers, for example, mixing of surface and bulk water can only occur over time scales longer than $\approx 10 \times 10$ μs, which is similar to typical spin-spin relaxation times T_2 of ^{1}H in C-S-H, i.e., about 100 μs [14].

This work is motivated by the desire to resolve the above inconsistencies, to identify the nanoscale structure of C-S-H in cement, and, in particular, to understand the behavior of water in the nanoscale pores formed by C-S-H. This is vital if cementitious materials are to be developed with improved durability and lower carbon footprint, bearing in mind that cement production worldwide currently contributes 5–8% of global CO_2 emissions and is set to rise further as demand increases in the developing nations. The detailed morphology of C-S-H is still debated but it is widely acknowledged that C-S-H is a highly heterogeneous, nanoporous material comprised of disordered sheets of calcium and oxygen atoms and silicate tetrahedra separated by sheets of water further separated by nanosized pores, i.e., so-called gel pores, and larger capillary pores [13,15]. Although the focus of the present work is on cementitious materials, many of the conclusions are equally applicable to other nanoporous silicate-based materials such as zeolites, glasses, and quartz.

In this paper, the results of molecular dynamics (MD) simulations of hydrated cement-analogue Q2D pores are presented. Previous MD simulations of cement-analogue mineral-water interfaces have been undertaken by Kirkpatrick and co-workers [16], Pellenq and co-workers [17], Nonat and co-workers [18], and others. A good review may be found in Ref. [19]. Of particular interest is the comparison of the surface diffusion coefficient between the MD simulation and NMR experimentation [20] characterized in the SL model by a surface diffusion correlation time τ_m using a modified tobermorite 9 Å cement analog. Tobermorite is a silicate-based material with a well-characterized structure used to model stacked C-S-H layers. The surface diffusion correlation time τ_m was found to be in the range 0.1–1.1 ns (with an average of 0.2 ns), which is consistent with experiment and serves to validate both the experimental results and the MD approach.

We present results of MD simulations of water in Q2D pores confined by a silica or tobermorite crystal with a focus on the measurement of the surface residency time, τ_s. A variety of MD model systems are explored, but in all cases τ_s is found to be shorter than the value obtained by fitting the SL model to NMR results by 2–5 orders of magnitude. Furthermore, the MD simulations do not reveal large-scale surface diffusion of

water prior to desorption. Both observations conflict with the SL model.

In one MD simulation, the water is confined to a 14 Å tobermorite crystal with surfaces modified by replacing bridging SiO_2 tetrahedra by calcium ions. The Ca/Si ratio is therefore 1.5, which is close to that observed in experiment. This simulation reveals three highly structured water layers and a homogeneous region of bulklike water in the central region of the pore. Layer 1 (L1) contains adsorbed water located between the crystal surface and a layer of aqueous Ca^{2+} ions. The water in layer 2 (L2) forms the first hydration shell to the adsorbed Ca^{2+}. Layer 3 is formed by water molecules in the second hydration shell of Ca^{2+} ions referred to as the transition layer (TL).

A simplified two-layer model is presented in which the motion of the water is described by two representative 2D layers of mobile water. We refer to this model as the 2L model. The theory is developed resulting in a nearly analytic expression for the dipolar correlation function representing the interaction between mobile I spins contained in a 2D layer displaced from the static relaxation centers close to the crystal surface. It is demonstrated that the 2L model not only provides an improved fit to the experimental data presented by Barberon and co-workers [5] and McDonald and co-workers [6], but also yields estimates of physical quantities that are consistent with simulation.

The structure of the paper is as follows. The SL model is reviewed in Sec. II B. The theory for the spin-lattice and spin-spin relaxation times T_1 and T_2 associated with 2D translational diffusion of I spins in a plane displaced from the paramagnetic relaxation centers is presented in Sec. II C. Section III summarizes the key results from the MD simulations. Previous experimental results are then reanalyzed using the 2L model in Sec. IV and, finally, the key results are summarized in Sec. V.

II. THEORY

A. General background

A collection of I spins diffuse in a pore space in the presence of a static magnetic field. Nuclear spin relaxation arises due to the modulation of the dipolar interaction between the I spins and fixed paramagnetic impurities (S spins) due to the relative translational diffusion and rotational motion of spin I relative to spin S. The spin-lattice and spin-spin relaxation times associated with the translational motion of spin I with respect to spin S, i.e., $T_{1,IS}$ and $T_{2,IS}$, respectively, may be expressed in terms of the powder-average spectral density function $J(\omega)$ as [6,21]

$$T_{1,IS}^{-1} = \tfrac{1}{3}\beta_{IS}^2[7J_{IS}(\omega_S) + 3J_{IS}(\omega_I)], \quad (1)$$

$$T_{2,IS}^{-1} = \tfrac{1}{6}\beta_{IS}^2[4J_{IS}(0) + 13J_{IS}(\omega_S) + 3J_{IS}(\omega_I)], \quad (2)$$

where $\beta_{IS} = (\mu_0/4\pi)\gamma_I\gamma_S\hbar\sqrt{S(S+1)}$, and γ_I and γ_S are the gyromagnetic ratios for spin I and S, respectively, with $S = \frac{5}{2}$ for Fe^{3+}. The Larmor frequency of spin I in the applied static field is ω_I and $\omega_S = 658.21\omega_I$. The ratio of the relaxation times is therefore

$$\frac{T_{2,IS}}{T_{1,IS}} = \frac{2[7J_{IS}(\omega_S) + 3J_{IS}(\omega_I)]}{4J_{IS}(0) + 13J_{IS}(\omega_S) + 3J_{IS}(\omega_I)}, \quad (3)$$

which is Eq. (5) presented by McDonald *et al.* [6]. The powder-average spectral density function $J_{IS}(\omega)$ is obtained from the Fourier transformation of the powder-average dipolar correlation function $G_{IS}(t)$ defined as

$$J_{IS}(\omega) = 2\int_0^\infty G_{IS}(t)\,\cos\omega t\,dt. \quad (4)$$

It is therefore necessary to determine the dipolar correlation function $G_{IS}(t)$ for the translational diffusion of I spins for a chosen diffusion model.

A mobile spin confined to a pore may be located in one of two distinct environments, the surface or bulk. The observed relaxation rate may be expressed as

$$T_{1,\mathrm{obs}}^{-1} = x\,T_{1,\mathrm{surf}}^{-1} + (1-x)T_{1,\mathrm{bulk}}^{-1}, \quad (5)$$

where $x = N_{\mathrm{surf}}/N$, and $N = N_{\mathrm{surf}} + N_{\mathrm{bulk}}$ is the fraction of the total number of spins in the surface region. There is an equivalent expression for $T_{2,\mathrm{obs}}^{-1}$.

B. The surface-layer (SL) model

The SL model introduced by Korb and co-workers [3,4] is presented schematically in Fig. 1 and is applicable to systems in which the dominant relaxation mechanism is associated with the interaction between a uniform density of static S spins and a uniform density of I spins undertaking uncorrelated translational motion in the 2D surface of the pore. In the SL model, both the I spins and the S spins are confined to the same 2D surface plane. The distance of nearest approach of spin I to spin S in the 2D plane is defined as δ, which is typically in the range 0.27–0.30 nm [5]. δ acts as a convenient unit of elementary distance in the SL model, but the primary results from the model do not depend on the choice of δ.

The SL model neglects all I-I spin interactions for surface-surface interactions on the basis that $\gamma_S \gg \gamma_I$. All I-S interactions for subsurface S spins in the crystal are neglected. Contributions to observed relaxation rates due to the bulk water confined in the pores are not explicitly included in the SL model, but this contribution is included as a single frequency-independent contribution when executing a fit to relaxation time data at low magnetic field [5].

Korb and co-workers showed that the translational motion of I spins confined to a 2D layer leads to a t^{-1} dependence of the dipolar correlation function $G_{IS,\mathrm{SL}}(t)$ at long times [3,4]. Consequently, the leading term for $G_{IS,\mathrm{SL}}(t)$ at long times is of the form At^{-1}, where A is a constant which is proportional to $\sigma_S\epsilon^{-4}$, where σ_S is the areal density of S spins at the 2D pore surface and ϵ is a distance parameter of order δ. It is not possible to Fourier transform a function of the form At^{-1}. Therefore, the SL model also assumes that the I spins desorb from the surface (and cease to contribute to the relaxation) with a characteristic time τ_s. After time τ_s, the number of I spins at the surface has dropped by a factor e^{-1} compared to the number at the surface at $t = 0$. On this basis, the following expression for $G_{IS,\mathrm{SL}}(t)$ was proposed [4]:

$$G_{IS,\mathrm{SL}}(t) = \frac{A}{t}\left[\frac{e^{-t/\tau_s} - e^{-t/\tau_m}}{\tau_m^{-1} - \tau_s^{-1}}\right], \quad (6)$$

where the correlation time τ_m is the characteristic time for a move of length δ of the I spins within the 2D surface layer such

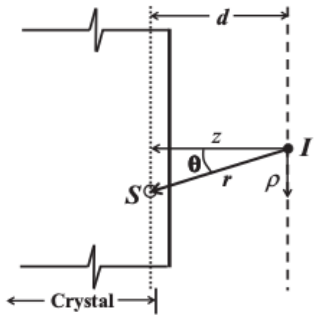

FIG. 2. A schematic diagram of a 2D layer containing diffusing I spins which interact with static paramagnetic impurities (S spins) of areal density σ_S. The separation of the two layers is d.

that the self-diffusion coefficient $D = \delta^2/4\tau_m$. The expression for $G_{IS,\mathrm{SL}}(t)$ is dependent on three parameters, i.e., A, τ_m, and τ_s. Note that A in Eq. (6) incorporates powder averaging and therefore differs from the expression in Ref. [4] by a factor $1/5$. Equation (6) may be Fourier transformed analytically to yield $J_{IS,\mathrm{SL}}(\omega)$ and hence the NMR relaxation times may be calculated using Eqs. (1) and (2).

C. $G(t)$ for a displaced 2D layer of diffusing spins

We now determine the powder-average dipolar correlation function $G(t)$ for the translational motion of I spins in a 2D plane placed parallel to a layer of S spins separated by a perpendicular distance d. A schematic diagram is presented as Fig. 2. The system is identical to the SL model illustrated in Fig. 1, except that the layer containing the diffusing spins is displaced from the layer containing the S spins. The starting point for the derivation of the correlation function $G(t)$ is the expression [22]

$$G(t) = \frac{4\pi N_{\mathrm{Fe}}}{5} \iint \left[\sum_{M=-2}^{2} \frac{Y_{2M}(\theta_0,\phi_0)\, Y^*_{2M}(\theta,\phi)}{r_0^3 r^3} \right] \times P(\mathbf{r},t|\mathbf{r}_0) d^3\mathbf{r}_0 d^3\mathbf{r}, \tag{7}$$

where $P(\mathbf{r},t|\mathbf{r}_0)$ is the probability density function (or diffusion propagator) for a pair of spins separated by $\mathbf{r}$ at time t *given* the spin pair was separated by $\mathbf{r}_0$ at $t = 0$. N_{Fe} is the volume density of S spins at the surface of the crystal, usually expressed as $N_{\mathrm{Fe}} = \sigma_S/\delta_{\mathrm{Fe}}$, where σ_s is the areal density of S spins contained in a thickness δ_{Fe} of crystal. The Y are the spherical harmonic functions of order two and the presence of the asterisk superscript on the Y indicates the complex conjugate. The powder average has been taken resulting in the factor $1/5$ [22].

The probability density function appropriate for the diffusion of I spins relative to fixed S spins where the I spins are confined to a layer of thickness δ may be written

$$P(\mathbf{r},t|\mathbf{r}_0) = \frac{1}{\delta} \frac{1}{4\pi Dt} e^{-|\boldsymbol{\rho}-\boldsymbol{\rho}_0|^2/4Dt}, \tag{8}$$

where the appearance of $1/\delta$ arises due to the assumption of a uniform density of I spins across the layer thickness δ, where δ is taken to be the approximate distance of nearest approach of protons on different water molecules. The $\boldsymbol{\rho}$ represents a vector in the plane of the layer. D is the 2D self-diffusion coefficient of the I spins, which may be expressed in terms of a characteristic diffusion correlation time τ by

$$D = \frac{\delta^2}{4\tau}. \tag{9}$$

Thus, τ is the mean time for a move of distance δ in the 2D plane. Note that this definition is slightly different from that for the SL model. In the SL model, δ is the I-S distance of nearest approach [5], although the numerical value is the same in each model, namely, 0.27 nm.

Equation (8) is replaced by its well-known Fourier integral with Fourier variable $\mathbf{k}$ and then substituted into Eq. (7) to yield

$$G(t) = \frac{4\sigma_S\delta}{5\pi\delta_{\mathrm{Fe}}} \iint \sum_{M=-2}^{2} \frac{Y_{2M}(\theta_0,\phi_0) Y^*_{2M}(\theta,\phi)}{\left(\rho_0^2+d^2\right)^{3/2}(\rho^2+d^2)^{3/2}} \times \left[\int e^{-Dtk^2} e^{i\mathbf{k}\boldsymbol{\rho}} e^{-i\mathbf{k}\boldsymbol{\rho}_0} d^2\mathbf{k} \right] d^2\boldsymbol{\rho}_0 d^2\boldsymbol{\rho}, \tag{10}$$

where $r^2 = \rho^2 + d^2$, $d^2\boldsymbol{\rho} \equiv \rho\, d\rho\, d\phi$ and the integrations over z and z_0 have been completed. The exponential functions are replaced using the Jacobi-Anger expression and the functional forms for the spherical harmonic functions inserted. Integrals involving $M = \pm 1$ vanish and the integration over the azimuthal angles ϕ and ϕ_0 may be undertaken explicitly. Simplifications lead to the following expression:

$$G(t) = \frac{\pi\sigma_S\delta}{4\delta_{\mathrm{Fe}}} \int_0^\infty k\, e^{-Dtk^2} \left[6I_2^2(k) + 2I_0^2(k) \right] dk, \tag{11}$$

where

$$I_0(k) = \int_0^\infty \frac{\rho(2d^2-\rho^2)}{(\rho^2+d^2)^{3/2}} J_0(k\rho) d\rho, \qquad I_2(k) = \int_0^\infty \frac{\rho^3}{(\rho^2+d^2)^{3/2}} J_2(k\rho) d\rho, \tag{12}$$

and where the subscripts on I_0 and I_2 reflect their origin as $M = 0$ and $M = 2$ terms, respectively. Here, J_0 and J_2 are Bessel functions of the first kind. Changing variables to dimensionless quantities based on a distance ϵ, such that $\kappa = k\epsilon$, $p = \rho/\epsilon$, and $\xi = d/\epsilon$, and executing the integrations with the aid of Gradsteyn and Ryzhik [23], gives

$$I_0(k) = \frac{\kappa e^{-\xi\kappa}}{\epsilon}, \quad I_2(k) = \frac{\kappa e^{-\xi\kappa}}{3\epsilon}. \tag{13}$$

Substituting these expressions into Eq. (11) and use of Eq. (9) yields the final expression for $G(t)$,

$$G(t) = \frac{2\pi\sigma_S}{3\epsilon^4} \frac{\delta}{\delta_{\mathrm{Fe}}} K(t,\tau), \qquad K(t,\tau) = \int_0^\infty \kappa^3 e^{-\kappa^2 t/4\tau} e^{-2\xi\kappa} d\kappa. \tag{14}$$

The behavior of the correlation function at long times may be found by setting the upper limit on the integration to Δ and

making the substitution $v = \kappa\sqrt{t}$ to yield

$$K(t \to \infty,\tau) = \frac{1}{t^2}\int_0^{\Delta\sqrt{t}} v^3 e^{-v^2/4\tau} e^{-2\xi v/\sqrt{t}}\, dv. \quad (15)$$

Executing the integral and setting $t \to \infty$ produces a leading term for $G(t \to \infty)$ of the form

$$G(t \to \infty) = \frac{16\pi\sigma_S\delta\tau^2}{3\epsilon^4\delta_{Fe}t^2}, \quad (16)$$

which is independent of both Δ and ξ. Equation (16) is fundamentally different from the equivalent expression for the SL model as given by Eq. (6) due to the displacement of the 2D layer containing I spins from the layer containing the relaxation centers. If all I-S spin vectors are contained in a plane, $\theta = \pi/2$, and the spherical harmonic functions are simplified, resulting in a leading term proportional to t^{-1}. This simplification is not valid when the diffusing spins are displaced from the S spins and the leading term at long times becomes proportional to t^{-2}. This t^{-2} dependence was effectively obtained by Korb and co-workers in their analysis of I-S spin relaxation in Q2D pores [3].

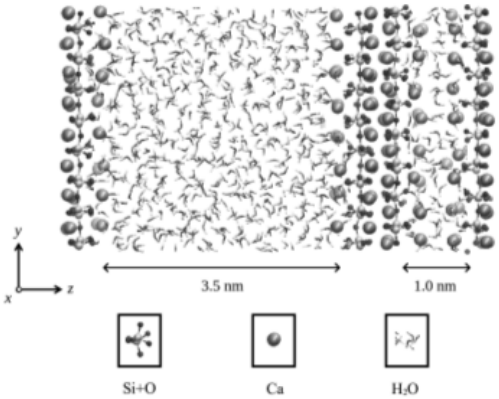

FIG. 3. A simplified image taken from molecular dynamics model MD4 showing a pore with water confined in the z direction by modified tobermorite 14 Å surfaces. The Si atoms are fixed, the surface oxygen atoms are tethered, and Ca^{2+} ions are present near the surfaces and are mobile.

III. RESULTS OF MOLECULAR DYNAMICS SIMULATION

The aim of the present MD simulations is to elucidate the atomic-scale dynamics of water on cement-analogue surfaces, thereby testing the validity of the assumptions of the SL models. MD simulations of hydrated silicate-based pores were undertaken exploring a range of crystals, surface morphologies, pore sizes, and potential energy functions, as summarized in Table I. The five simulations are labeled MD1–MD5. The confining crystals were silica, tobermorite 14 Å, or tobermorite 11 Å [24–26]. Tobermorite has a well-characterized crystal structure and is frequently used as an analog for stacked C-S-H layers [19]. Water was confined by the crystal to a Q2D pore with thicknesses ranging from 1.0 to 5.0 nm. As an example, model MD4 is illustrated in Fig. 3. The MD simulations were performed using the DL_POLY package [27,28] with periodic boundary conditions applied in all three directions. Water molecules in the pore thus experience confinement in the z direction, while the x-y plane is infinite due to the periodic boundary conditions. The SPC/E [29] or TIP4P [30] potential was used for the water-water interactions and the CLAYFF [31] or modified Freeman [32–35] potential was applied for interactions within the crystal. The Lorentz-Berthelot mixing rules [36] were applied to model the crystal-water interface. Some details of models MD1 and MD2 have been published elsewhere [22,37].

Each system was equilibrated using the isothermal-isobaric ensemble to a target temperature of 300 K and a pressure of 0 Pa. Water molecules were added or removed from the pore to match the bulk water density in the middle of the

TABLE I. List of molecular dynamics simulations with surface conditions, interatomic potentials, and results for the surface residency time τ_s. Some details of models MD1 and MD2 have been published [22,37].

Model	Description	Potentials	τ_s (ns)
MD1	alpha-quartz (SiO_2) with Si, O mobile (100) surface terminated with O Pore 1.0 nm containing 886 H_2O	CLAYFF SPC/E	0.32
MD2	alpha-quartz SiO_2 with Si, O mobile. (100) surface with surface hydroxyls (H tethered) Pore 1.0 nm containing 886 H_2O	CLAYFF SPC/E	0.15
MD3	11 Å anomalous tobermorite with Si, O mobile (100) surface with surface hydroxyls (H tethered) Pore 1.0 nm containing 792 H_2O	CLAYFF SPC/E	0.03
MD4	14 Å tobermorite, Si/O frozen, bridging tetrahedra replaced by Ca^{2+} (100) surface terminated with O (surface O tethered) Pore 3.3 nm containing 745 H_2O, Ca/Si = 1.5	CLAYFF SPC/E	12
MD5	14 Å tobermorite, Si/O frozen, bridging tetrahedra replaced by Ca^{2+} (100) surface with surface hydroxyls (H tethered) Pore 3.3 nm containing 745 H_2O, Ca/Si = 1.5	modified Freeman TIP4P	0.08

pore at equilibrium. A cutoff distance of 10.0 Å was applied to the Lennard-Jones potentials and the Ewald summation method [38] was used to incorporate long-range Coulombic interactions. Each of these systems was then simulated under the NVT conditions (constant number of particles, volume, and temperature) using the Hoover thermostat [39] to obtain a MD trajectory up to 20 ns long.

A full analysis of the MD results will be reported elsewhere. Here we focus on the results for the physical quantities relevant to the models presented in Sec. IIC and, for this purpose, we focus on model MD4 as the model C-S-H structure most suitable for later comparison with NMR relaxation results. However, our broad conclusions are not model (MD1–MD5) dependent. MD4 comprises a tobermorite 14 Å surface in which the bridging tetrahedra have been replaced by Ca^{2+} ions. The calcium ions yield a Ca/Si ratio of 1.5, which is close to the experimental value of about 1.8 typical of cementitious materials. The silicon atoms in the crystal are frozen, but the surface oxygen atoms are mobile and tethered.

The surface of C-S-H carries a positive permanent charge due to the deprotonation of Si-OH surface sites. This surface charge causes structuring of water and adsorption of aqueous Ca^{2+} ions at the C-S-H surface [40]. The density distribution of water and aqueous Ca^{2+} ions in a 3.3 nm pore for the model MD4 is shown in Fig. 4. Three highly structured water layers within 1 nm to the surface and a homogeneous region of bulklike water can be clearly distinguished. These regions are referred to as layer 1 and 2 (L1, L2), transition layer (TL), and bulk (B), respectively. Analysis of current classical MD simulations and our former results from *ab initio* modeling of C-S-H [40] and tobermorite [25,26] suggest that L1 is formed by H_2O molecules adsorbed on the crystalline surface of C-S-H and water coordinating adsorbed aqueous Ca^{2+} ions. The L2 layer is formed by water in the first hydration shell of adsorbed Ca^{2+} ions. The maximum of the aqueous Ca^{2+} density profile is on the L1/L2 boundary. The TL is dominated by water molecules forming the second hydration shell of the adsorbed Ca^{2+} ions. The density profile of water oxygen next to the surface is consistent with that obtained by Cheng and co-workers from a hydrated mica surface using x-ray reflectivity [41] and in accord with the MD simulations of Kalinichev and co-workers [19].

The 2D self-diffusion coefficient for the water in each layer was determined from the gradient of $\langle x^2+y^2\rangle$ as a function of t for model MD4. Model MD4 is of 20 ns duration and statistical averaging is taken over MD trajectories every 0.025 ns. The calculation of the 2D self-diffusion coefficient is performed at time t for water which is located in the specific layer throughout the time period 0–t. Thus, a spin that leaves the specified layer is excluded from the calculation even if it has returned to the layer at time t.

The water molecules contained in L1 are bonded to the surface of the crystal and to the aqueous Ca^{2+} ions. Thus the calcium ions located on the surface increase the surface affinity of the water contained in L1, as predicted in Ref. [19]. Water molecules in L1 remained immobile within the 20 ns simulation time.

The water molecules in L2 form the first hydration shell of adsorbed Ca^{2+} ions. The density of water-oxygen atoms in L2 and the aqueous Ca^{2+} ions are presented in Fig. 5, which clearly identifies the regions occupied by the water. Density also exists in circular regions which arises due to the cooperative movement of groups of water molecules mediated by the calcium. A more detailed analysis of this unusual diffusion mechanism will be published elsewhere. The

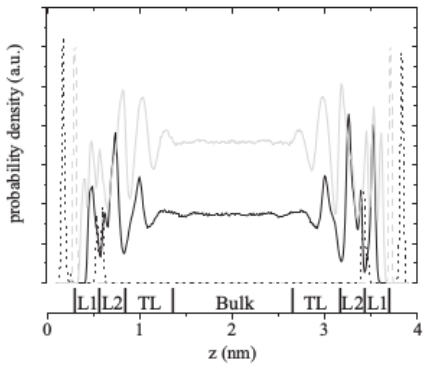

FIG. 4. The particle density is presented as a function of z for the surface silicon atoms (gray dashed line), calcium in the crystal and pore (black dashed line), and the water-oxygen (black solid line) and the water-hydrogen (gray solid line) atoms in the pore. The water exhibits four layers labeled L1 (layer 1), L2 (layer 2), transition layer (TL), and bulk (B).

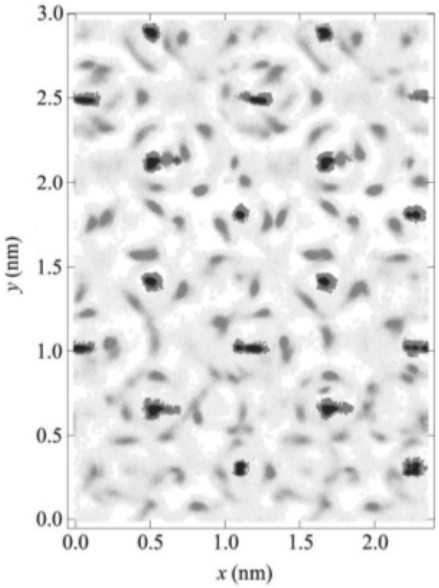

FIG. 5. The probability density of the water-oxygen atoms (light-gray shading) and calcium ions (dark-gray shading) in layer L2 for model MD4.

diffusion coefficient for the water in layer L2 is found to be approximately 2×10^{-12} m^2/s. The corresponding diffusion correlation time τ_{L2} defined as $\delta^2/4D$, where $\delta = 0.27$ nm, is 9 ns, which is broadly consistent with values of τ_m from fits to experimental data using the SL model [4,5]. We speculate that it is the water in L2 rather than L1 which dominates the dipolar relaxation in cementitious systems.

The water contained in the TL is fast moving, the particle probability density is uniform, and the diffusion coefficient of 1.4×10^{-9} m^2/s is of the same order as bulk water. The corresponding diffusion correlation time τ_{TL} is 13 ps. Finally, the diffusion coefficient for the bulk water in region B is found to be 2.7×10^{-9} m^2/s, which is larger than the experimental diffusion coefficient of bulk water at room temperature, 2.2×10^{-9} m^2/s [42], but consistent with MD simulations of bulk water using the same interatomic potential with a similar cell size [22,43]. The corresponding diffusion correlation time is about 7 ps.

The results for the surface residency time τ_s are presented in Table I for all models. For all models MD1–MD5, τ_s was determined by counting the fraction of spins remaining in the region L1+L2 as a function of time and executing a fit to $Ae^{-t/\tau_a} + Be^{-t/\tau_b}$. Spins leaving region L1+L2 were excluded from the remaining total even if they subsequently returned to L1+L2. The double exponential fit is chosen to accommodate different desorption rates from L1 and L2. τ_s is selected as the longest of τ_a and τ_b.

The surface residency time is found to be 0.03 ns or less in models MD1–MD3, indicating that the water molecules in L1+L2 desorb quite rapidly if the surface affinity is low. τ_s is found be 12 ns for model MD4 and 0.08 ns for MD5. The difference between the CLAYFF-SPC/E and Freeman-TIP4P potential sets of MD4 and MD5, respectively, is surprisingly large. The Freeman-TIP4P combination is normally used for clays and provided an unphysical flattened crystal interface, which was only partially corrected by modifications proposed by Galmarini [35]. We conclude that the CLAYFF-SPC/E potential set is the best combination for hydrated silica-based surface studies and note that this is the same potential set used for the MD simulations of Kalinichev and co-workers [19]. Finally, we note that there is no evidence of large-scale surface diffusion prior to desorption in any model.

Notwithstanding the spread of values from the MD simulations and a significant uncertainty in the surface morphology of C-S-H pore surfaces, all values of the surface residency time τ_s are approximately 2–5 orders of magnitude less than typical values of order 1–10 μs obtained by fitting the SL model to NMR relaxation measurements. The MD simulations do not therefore support the SL model in this regard.

IV. A TWO-LAYER MODEL AND REEVALUATION OF EXPERIMENTAL RESULTS

Barberon and co-workers [5] measured T_1 for a hydrated mortar at various times after hydration to about 10.5 h. This is a rare example of the full frequency dependence of T_1^{-1} for a cement system to be found in the literature where the data is not renormalized to a master curve. These authors identified a frequency-independent relaxation rate for frequencies less than 22 kHz due to the rigid lattice limit of the I spins within the solid hydrates. From 10 h after hydration, a resonance feature appears at 3–5 MHz which was associated with water molecules bound to surface Fe^{3+} impurities. Between the two, Barberon and co-workers identified a bilogarithmic dependence of T_1^{-1} on frequency. They divided the pore water into two environments, i.e., surface water and bulk water. The frequency-independent relaxation rate associated with the bulk water was estimated from the high-frequency limit of T_1 to be 55 s^{-1} and the contribution to the frequency-dependent T_1^{-1} relaxation rate due to surface water was fitted using the SL model described in Sec. II B. Consequently, over the frequency range 0.02–2 MHz, the observed relaxation rate is given by

$$T_{1,\mathrm{obs}}^{-1} = xT_{1,\mathrm{SL}}^{-1} + (1-x)T_{1,\mathrm{B}}^{-1} \approx xT_{1,\mathrm{SL}}^{-1} + T_{1,\mathrm{B}}^{-1}, \quad (17)$$

where x is the fraction of spins on the surface and $T_{1,\mathrm{B}}^{-1} = 55$ s^{-1} is the relaxation rate associated with the bulk water.

In executing the fits to the T_1^{-1} relaxation rate, Barberon and co-workers estimated the values of certain physical quantities as listed in Table II leaving three fit parameters: τ_s, τ_m, and x. These authors assumed that $\tau_s \gg \tau_m$, which simplifies Eq. (6) so that it becomes independent of τ_s. At the longest hydration time of 10.5 h, the fit yielded $\tau_m \approx 1.3$ ns and $x \approx 0.1$. Later, McDonald and co-workers [6] undertook a T_1–T_2 correlation study of hydrated cement paste. The ratio T_2/T_1 was found

TABLE II. List of parameters required to fit the SL model to NMR relaxation measurements on hydrated mortar [5] and cement paste [8].

Parameter	Best estimate	Comments
δ	0.27 nm	Estimated distance of nearest approach of a water proton to a substitutional surface Fe^{3+} impurity.
σ_s	1.8×10^{12} Fe^{3+}/cm^2	Mass density of paramagnetic impurities measured by ESR. Surface density σ_s assumes uniform density and average distance between layers of Fe^{3+} of 0.6 nm [5].
ϵ	0.38 nm	Size of water molecule.
$\chi\epsilon$	1 nm	Thickness of surface water layer estimated from calorimetry and NMR studies [47].
R_{1b}	55 s^{-1}	Estimated contribution to the relaxation rate due to bulk water [5].
$x \approx N_S/N$	$\approx$0.1	A fit parameter [5].
τ_m	1.3 ns	A fit parameter assuming $\tau_s \gg \tau_m$ [5].
τ_s	13 ± 5 μs	A fit parameter. Value from T_1–T_2 NMR correlation experiments on cement paste [6,8].

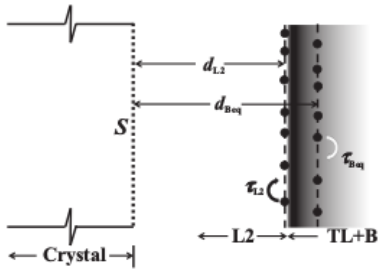

FIG. 6. A schematic representation of the two-layer (2L) model. Water diffuses with a correlation time τ_{L2} in layer L2 and τ_{Beq} in an equivalent layer which is representative of the layers TL+B combined. The shading illustrates the increasing contribution to the dipolar correlation function $G(t)$ of spins in the bulk due to the interaction with surface paramagnetic impurities.

to be approximately 0.25 and the SL model was fitted to data yielding $\tau_s \approx 13$ μs.

We now present the alternative model, the two-layer (2L) model, represented schematically in Fig. 6. The underlying principles which led to the SL model are retained in the 2L model, that is, the primary relaxation mechanism is associated with the translational diffusion of water protons moving in a 2D plane parallel to a crystal surface containing a dilute concentration of surface paramagnetic impurities.

The 2L model contains three key differences from the SL model. First, the 2L model incorporates two 2D layers of diffusing spins, i.e., one associated with slow-moving spins close to the pore surface and the second associated with fast-moving spins in the bulk of the pore. While this can likely be viewed quite generally, it is particularly appropriate to cement C-S-H where pores are believed to be substantially planar. Second, whereas the single 2D layer in the SL model contains *both* the diffusing spins *and* the Fe^{3+} ions, the 2L model displaces the two 2D layers of diffusing spins from the layer containing the paramagnetic impurities. This is an important distinction because $G(t)$ at long times, as described in Sec. II C, is of the form t^{-2} rather than t^{-1}. The third key difference between the SL model and the 2L model relates to assumptions about the behavior of spins which depart a layer. In the SL model, spins are assumed to desorb from the surface layer with a characteristic desorption time τ_s. The desorbed spins cease to contribute to the relaxation thereafter, which means that the SL model assumes that spins do not return to the surface layer over the time scale of a NMR relaxation time. Given relaxation times of the order of 100 μs and diffusivities of the order of 10^{-9} m^2/s, the implication therefore is that pore sizes must be of the order of μm. Such a large size is at odds with independent and NMR observations that suggest gel pores are nanosized [13,14]. The 2L model, by contrast, allows spins to depart the layer to return at a later time.

The 2L model is developed as follows. Consider two ensembles of spins: slow-moving spins located close to the pore surface and fast-moving spins located in the bulk of the pore. The observed relaxation rate is given by Eq. (5) in the limit of fast exchange. The 2L model identifies the slow-moving spins with layer L2 and the fast-moving spins with regions TL+B. Therefore, the observed relaxation rate $T_{1,\mathrm{obs}}^{-1}$ is given by

$$T_{1,\mathrm{obs}}^{-1} = \frac{N_{\mathrm{L2}}}{N} T_{1,\mathrm{L2}}^{-1} + \frac{N_{\mathrm{bulk}}}{N} T_{1,\mathrm{bulk}}^{-1}, \tag{18}$$

where $N \approx N_{\mathrm{L2}} + N_{\mathrm{bulk}}$ is the total number of particles in the pore and $N_{\mathrm{bulk}} \approx N$ refers to the combined number of spins contained in the TL and B layers. There is a similar expression for $T_{2,\mathrm{obs}}^{-1}$. Spins in layer L1 are temporarily neglected.

The rate $T_{1,\mathrm{bulk}}^{-1}$ contains contributions due to the I-I and I-S interactions with the relative contributions dependent on the size of the pore. For pores sufficiently large such that, over the NMR time scale, bulk water molecules do not sample the full volume of the pore, the measured relaxation rate will be dominated by $T_{1,\mathrm{bulk},II}^{-1}$. Here it is assumed that pore sizes are sufficiently small such that the relaxation due to the I-S interaction dominates the I-I contribution in both the bulk and in L2. Therefore, Eq. (18) may be written as

$$T_{1,\mathrm{obs}}^{-1} = xT_{1,\mathrm{L2},IS}^{-1} + (1-x)T_{1,\mathrm{bulk},IS}^{-1} \approx xT_{1,\mathrm{L2},IS}^{-1} + T_{1,\mathrm{bulk},IS}^{-1}, \tag{19}$$

where $x = N_{\mathrm{L2}}/N$ and, in principle, provides an estimate of the pore size. We use the results presented in Sec. II C to provide an estimate for $T_{1,\mathrm{L2},IS}^{-1}$ and $T_{1,\mathrm{bulk},IS}^{-1}$.

The 2L model is illustrated schematically in Fig. 6. Some model parameters are estimated from the MD simulation results and some quantities taken from Barberon and coworkers [5], as summarized in Table III. $T_{1,\mathrm{L2},IS}^{-1}$ is associated with the slow-moving spins in L2. The dipolar correlation function is calculated using Eq. (14) and is dependent upon the choice of τ_{L2} and $d_{\mathrm{L2}} = \epsilon\xi_{\mathrm{L2}}$, where we take $\epsilon = \delta = 0.27$ nm as the distance of closest approach of two proton spins. d_{L2} is chosen to be 2δ guided by the MD simulation results presented in Fig. 4 which show a sharp peak in the spin density

TABLE III. List of parameters required to fit the 2L model to NMR relaxation measurements on hydrated mortar [5] and cement paste [8].

Parameter	Best estimate	Comments
δ	0.27 nm	Approximate distance of nearest approach of two protons in water.
σ_s	1.8×10^{12} Fe^{3+}/cm^2	From Barberon *et al.* [5].
d_{L2}	2δ	From MD simulation, this work.
d_{Beq}	2.21δ	Calculation, this work.
x		A fit parameter, see Eq. (19).
τ_{L2}		A fit parameter.
τ_{Beq}		A fit parameter.

due to the mobile spins in L2 at a distance approximately 2δ from the crystal surface. τ_{L2} is a fit parameter.

The second 2D layer is designed to approximate $T^{-1}_{1,\mathrm{bulk},IS}$ for the combined effect of the fast-moving spins contained in both the TL and B regions. The reduction of the quasi-two-dimensional (Q2D) volume of spins to a representative equivalent 2D layer is a significant simplification forced, in part, by the absence of a full Q2D solution for the dipolar correlation function. However, we justify the simplification by noting, first, that $G_{IS}(t) \propto t^{-2}$ at long times for both the Q2D layer and 2D equivalent layer and, second, that $G_{IS}(0) \propto z^{-4}$ which means that the spins that provide the greatest contribution to the relaxation are those in a layer closest to the crystal surface.

The second layer is characterized by d_{Beq} and τ_{Beq}, where the subscript refers to a bulk equivalent layer. An estimate for d_{Beq} can be obtained by noting that $G(0) \propto z^{-4}$. If we make the assumption that the areal density of spins σ_{Beq} in the equivalent layer is the same as that in the bulk, such that $\sigma_{\mathrm{Beq}} = \delta N_v$ where N_v is the bulk volume density of I spins, it is possible to determine d_{Beq} by solving

$$\frac{\delta N_v}{d^4_{\mathrm{Beq}}} = N_v \int_{2\delta}^{\infty} z^{-4} dz, \tag{20}$$

from which $d_{\mathrm{Beq}} = 2.21\delta$. In other words, the 2D equivalent layer is placed at a position $z = 2.21\delta$ where the contribution to $G(0)$ is the same as the average contribution to $G(0)$ of the spins in the TL+B region of the pore, assuming that the areal spin density of water in the layer is characteristic of bulk water. It is emphasized that the 2L model allows all spins to contribute to the relaxation at all times. The contribution is characterized by d_{L2} and τ_{L2}, or by d_{Beq} and τ_{Beq}, depending on where the spin is located at any one time.

The 2L model is fitted to T_1^{-1} as a function of frequency over the range 0.02–2 MHz measured by Barberon and co-workers [5] for a hydrated mortar for the longest hydration time of 10.5 h. The 2L model requires three fit parameters similar to the SL model for a complete fit to the frequency dependence of T_1^{-1} and the ratio T_2/T_1. In this case, the three parameters are τ_{L2}, τ_{Beq}, and x, as summarized in Table III. To execute the fit, values of τ_{L2} and τ_{Beq} are chosen and the best fit is obtained by varying the single parameter x. The quality of fit (QoF) is obtained from an unweighted least-squares calculation. Figure 7 presents the QoF as a function of τ_{L2} and τ_{Beq} over five orders of magnitude for each diffusion correlation time. The black shading indicates a QoF in the range 138–145 (arbitrary units) and the dark gray shading corresponds to a QoF in the range 146–180. The upper QoF limit of 180 was chosen as the approximate value obtained by fitting the SL model to the same data. Other combinations of correlation times τ_{L2} and τ_{Beq} either produced poorer fits or it was not possible to produce a fit at all. A good fit to the data of Barberon and co-workers is obtained using the 2L model provided the two diffusion correlation times τ_{L2} and τ_{Beq} differ by about three orders of magnitude. The optimum fits, that is, QoF $\leqslant$ 145, are obtained for τ_{L2} in the range 40–130 ns and τ_{Beq} in the range 25–45 ps.

The ratio T_2/T_1 has been found to lie in the range 0.25–0.30 for a range of cementitious and other materials

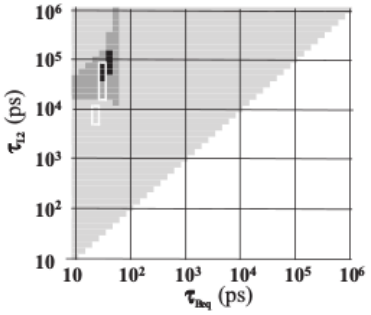

FIG. 7. The quality-of-fit (QoF) parameter (see text) is plotted as a function of τ_{L2} and τ_{Beq}. The black squares indicate QoF < 145, the dark-gray squares indicate QoF in the range 146–180, and the light-gray squares indicate QoF > 180. The white lines contain results which simultaneously have a QoF < 180 and a ratio T_2/T_2 in the range 0.25–0.30.

[6,44]. Values of T_2/T_1 in the range 0.25–0.30 are indicated by the white boundary in Fig. 7 and overlaps with the best fits to the experimental data, providing confidence in the 2L model. T_2/T_1 has a weak dependence on τ_{L2} but a strong dependence on τ_{Beq}. A similar observation was made by McDonald and co-workers [6] in applying the SL model with regard to τ_m and τ_s, respectively. The dual requirements of a QoF $\leqslant$ 180 and T_2/T_1 in the range 0.25–0.30 are satisfied by $\tau_{L2} = 18$–75 ns and $\tau_{\mathrm{Beq}} = 28$–40 ps. Both results are strikingly consistent with the results of simulation MD4 presented in Sec. III which yielded diffusion correlation times of 9 ns and 13 ps for layers L2 and TL, respectively.

The SL model fitted to the same data of Barberon *et al.* [5] yields a QoF of 181 over the same frequency range using $\tau_m = 1.3$ ns. A comparison of the two models is presented in Fig. 8. We make the observation that the SL model also provides a fit that is a weak function of τ_m. Although Barberon *et al.* quoted 1.3 ns as the surface diffusion correlation time, a value of τ_m in the range 0.5–1.3 ns also provides a fit of similar quality over the frequency range 0.02–2 MHz.

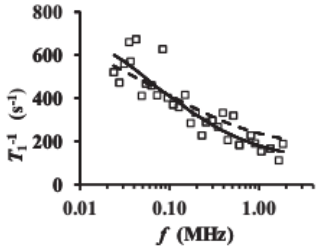

FIG. 8. T^{-1} is plotted as a function of NMR frequency. The experimental data (□) are taken from Barberon and co-workers [5] for a hydrated mortar. The fit obtained using the SL model (dashed line) and 2L model (solid line) are shown.

It is tempting to associate the fit parameter x in Eq. (19) with the fraction of spins located in the surface region following Eq. (5) thereby allowing an estimate of typical pore size. The combined requirement of QoF < 180 and T_2/T_1 in the range 0.25–0.30 produces x in the range 0.0015–0.0047, suggesting typical pore sizes of 100 nm or more. Barberon and co-workers obtain a value of about 20 nm which is closer to measured estimates [13,45]. However, Barberon and co-workers set $\epsilon = 0.38$ nm [5] and if we assume $\epsilon = 0.38$ nm for the 2L model, the revised fits also yield an estimate of 20 nm. ϵ is a distance unit which scales $G(t)$ and, where possible, is chosen to allow the model $G(0)$ to match the value of $G(0)$ obtained from another source, for example, from MD [22]. Models for $G(t)$, including the SL and 2L models, assume a uniform spin density which is a poor approximation at short distances where the I-I pair correlation function is highly structured. ϵ may therefore be chosen to compensate for the shortcoming of the uniform spin density approximation. If so, one would expect $\epsilon \lesssim \delta$. Notwithstanding, Barberon and co-workers set ϵ approximately equal to the "water molecule size" of 0.38 nm [5]. The physical basis for this choice is not explained.

However, we question the validity of estimating the pore size from x for other reasons. For example, there exists a significant uncertainty in the value of the density of paramagnetic impurities, σ_S. This is estimated from electron spin resonance (ESR) measurements and the surface density is deduced from the dry mass of sample. It is assumed that the surface density of impurities is the same as in the bulk. There is evidence, however, of clustering of iron in AFm and AFt phases [46] which means that the actual value of σ_S may be smaller. Moreover, although the average spin density of layer L2 is similar to bulk water, the MD simulations suggest that not all of the water molecules located in L2 are equally mobile, indicating that just a fraction of the water in L2 contributes significantly to the relaxation. Both effects would decrease the pore-size estimate obtained from x.

Finally, we reiterate that the SL model requires a surface residency time τ_s, whereas the 2L model does not. In the SL model, the spins are assumed to desorb from the surface and cease to contribute to the relaxation thereafter, with the fraction of spins remaining on the surface decaying as $\exp(-t/\tau_s)$. A motivation for the present study was that τ_s obtained using the SL model is unacceptably long. The 2L model, however, does not require the introduction of the $\exp(-t/\tau_s)$ term because $G(t)$ at long times is of the form t^{-2}, which can be Fourier transformed, whereas $G(t)$ decays as t^{-1} in the SL model (which cannot be Fourier transformed). The 2L model therefore resolves the surface residency time discrepancy.

V. CONCLUSIONS

The results of MD simulations of hydrated Q2D pores with the water confined by a silica or tobermorite crystal are presented. The water surface residency time is found to be about 2–5 orders of magnitude shorter than values that consistently emerge when the SL models of Korb and co-workers are fitted to experimental NMR relaxation rate data [2–9]. Furthermore, no MD simulation reveals large-scale surface diffusion of water prior to desorption. Both observations conflict with the SL model.

The MD simulations identify three highly structured layers for water at the surface of a tobermorite pore when the bridging tetrahedra are replaced by Ca^{2+} ions. Layer L1 contains water adhered to the surface of the pore, layer L2 is the first hydration shell of the aqueous Ca^{2+} ions located on the L1/L2 boundary, and the third layer is a transition layer. The fourth layer is bulklike water in the central region of the pore.

Guided by the MD simulations, a two-layer (2L) model is proposed and used to interpret NMR relaxation rates obtained from frequency-dependent T_1^{-1} data obtained by Barberon and co-workers [5] for a hydrated mortar and the ratio T_2/T_1 obtained from T_1–T_2 correlation studies of hydrated cement paste by McDonald and co-workers [6]. The 2L model retains the principles that underly the SL model, that is, the dipolar relaxation is associated with the interaction of diffusing I spins moving in a 2D plane with rare static paramagnetic S spins located at the surface of the confining crystal. In essence, the surface residency time τ_s and diffusion correlation time τ_m of the SL model are replaced by diffusion correlation times τ_{L2} and τ_{Beq} in the new 2L model. In the 2L model, the correlation times are associated with water diffusing in two 2D planes representative of regions L2 and the TL+bulk, respectively.

The theory is presented for the dipolar correlation function $G(t)$ for a 2D layer of diffusing spins displaced from paramagnetic relaxation centers located in the surface of the confining crystal. It is shown that the long-time behavior of $G(t)$ is proportional to t^{-2}, in contrast to the t^{-1} behavior when the relaxation centers are contained in the same plane as the diffusing spins, which forms the basis of the SL model.

Using the 2L model, a satisfactory fit to the frequency-dependent T_1^{-1} data obtained by Barberon and co-workers [5] for a hydrated mortar can only be obtained if τ_{L2} and τ_{Beq} are of the order of nanoseconds and picoseconds, respectively. The fits are significantly better than those obtained from the SL model using the same experimental data. Using this experimental data only, the best fits (QoF $\leqslant 145$) are obtained for τ_{L2} and τ_{Beq} in the range 40–130 ns and 25–45 ps, respectively. Remarkably, the values of τ_{L2} and τ_{Beq} that satisfy the stringent requirement that the ratio T_2/T_1 lies in the range 0.25–0.30 coincides with the best fits to the frequency-dependent T_1^{-1} data. This provides confidence in the validity of the model. The combined requirements and accepting fits such that QoF $\leqslant 180$ suggest that $\tau_{L2} = 18$–75 ns and $\tau_{Beq} = 28$–40 ps.

The 2L model yields NMR relaxation times which not only provide an improved fit to the experimental data compared to the SL model but yield values of τ_{L2} and τ_{Beq} broadly consistent with simulation. Model MD4 produces values of 9 ns and 13 ps, respectively. Considering the uncertainties in the morphology of C-S-H, the aqueous Ca^{2+} density, the crudeness of the interatomic potentials, the difficulty of obtaining accurate diffusion coefficients even in well-characterized systems, and other poorly known physical quantities, the agreement can be considered as good.

In conclusion, the MD simulations provide fresh insight into the dynamics of water at silicate-based surfaces and the 2L model provides a different approach to the interpretation of NMR relaxation dispersions obtained from proton-bearing porous silicate-based systems such as porous glasses, zeolites, cementitious materials, and oil-bearing rocks.

ACKNOWLEDGMENTS

N.C.H. and J.S.B. acknowledge the support of Engineering and Physical Sciences Research Council (UK) for financial support (Grant No. EP/H033343/1). S-H.P.C. acknowledges support from the European Union Seventh Framework Programme (FP7/2007-2013) under Grant Agreement No. 264448.

[1] N. Bloembergen, E. M. Purcell, and R. V. Pound, Phys. Rev. **73**, 679 (1948).
[2] J.-P. Korb, S. Xu, and J. Jonas, J. Chem. Phys. **98**, 2411 (1993).
[3] J.-P. Korb, M. Whaley-Hodges, and R. G. Bryant, Phys. Rev. E **56**, 1934 (1997).
[4] S. Godefroy, J.-P. Korb, M. Fleury, and R. G. Bryant, Phys. Rev. E **64**, 021605 (2001).
[5] F. Barberon, J.-P. Korb, D. Petit, V. Morin, and E. Bermejo, Phys. Rev. Lett. **90**, 116103 (2003).
[6] P. J. McDonald, J.-P. Korb, J. Mitchell, and L. Monteilhet, Phys. Rev. E **72**, 011409 (2005).
[7] A. Plassais, M.-P. Pomiés, N. Lequeux, J.-P. Korb, D. Petit, F. Barberon, and B. Bresson, Phys. Rev. E **72**, 041401 (2005).
[8] L. Monteilhet, J.-P. Korb, J. Mitchell, and P. J. McDonald, Phys. Rev. E **74**, 061404 (2006).
[9] J.-P. Korb, New J. Phys. **13**, 035016 (2011).
[10] K. Brownstein and C. Tarr, J. Magn. Reson. **26**, 17 (1977).
[11] A. J. Allen, J. J. Thomas, and H. M. Jennings, Nat. Mater. **6**, 311 (2007).
[12] E. Masoero, E. D. Gado, R. J.-M. Pellenq, S. Yip, and F.-J. Ulm, Soft Matter **10**, 491 (2014).
[13] H. M. Jennings, Cem. Conc. Res. **38**, 275 (2008).
[14] A. Valori, P. J. McDonald, and K. L. Scrivener, Cem. Conc. Res. **49**, 65 (2013).
[15] I. G. Richardson, Cem. Conc. Res. **34**, 1733 (2004).
[16] R. Kirkpatrick, A. Kalinichev, X. Hou, and L. Struble, Mater. Struc. **38**, 449 (2005).
[17] R. J.-M. Pellenq, A. Kushima, R. Shahsavari, K. J. Van Vliet, M. J. Buehler, S. Yip, and F.-J. Ulm, Proc. Natl. Acad. Sci. **106**, 16102 (2009).
[18] G. Kovačević, B. Persson, L. Nicoleau, A. Nonat, and V. Veryazov, Cem. Conc. Res. **67**, 197 (2015).
[19] A. G. Kalinichev, J. Wang, and R. J. Kirkpatrick, Cem. Conc. Res. **37**, 337 (2007).
[20] J.-P. Korb, P. McDonald, L. Monteilhet, A. Kalinichev, and R. Kirkpatrick, Cem. Conc. Res. **37**, 348 (2007).
[21] A. Abragam, *The Principles of Nuclear Magnetism* (Oxford University Press, Oxford, 1961).
[22] D. A. Faux, P. J. McDonald, N. C. Howlett, J. S. Bhatt, and S. V. Churakov, Phys. Rev. E **87**, 062309 (2013).
[23] I. S. Gradshteyn and I. M. Ryzhik, *Table of Integrals, Series, and Products*, 7th ed., edited by Alan Jeffrey and Daniel Zwillinger (Elsevier/Academic, Amsterdam, 2007).
[24] S. Merlino, E. Bonaccorsi, and T. Armbruster, Eur. J. Mineral. **13**, 577 (2001).
[25] S. V. Churakov, Am. Mineral. **94**, 156 (2009).
[26] S. V. Churakov, Eur. J. Mineral. **21**, 261 (2009).
[27] W. Smith and T. Forester, J. Molec. Graphics **14**, 136 (1996).
[28] I. T. Todorov, W. Smith, K. Trachenko, and M. T. Dove, J. Mater. Chem. **16**, 1911 (2006).
[29] H. J. C. Berendsen, J. R. Grigera, and T. P. Straatsma, J. Phys. Chem. **91**, 6269 (1987).
[30] J. Abascal and C. Vega, J. Chem. Phys. **123**, 234505 (2005).
[31] R. T. Cygan, J.-J. Liang, and A. G. Kalinichev, J. Phys. Chem. B **108**, 1255 (2004).
[32] N. H. de Leeuw, G. W. Watson, and S. C. Parker, J. Chem. Phys. **99**, 17219 (1995).
[33] N. H. de Leeuw, S. C. Parker, C. R. A. Catlow, and G. D. Price, Phys. Chem. Minerals **27**, 332 (2000).
[34] C. L. Freeman, J. H. Harding, D. J. Cooke, J. A. Elliott, J. S. Lardge, and D. M. Duffy, J. Phys. Chem. C **111**, 11943 (2007).
[35] S. Galmarini, Ph.D. thesis, Ecole Polytechnique Federale de Lausanne, 2014.
[36] M. P. Allen and D. J. Tildesley, *Computer Simulation of Liquids* (Oxford University Press, Oxford, 1989).
[37] J. S. Bhatt, P. J. McDonald, D. A. Faux, N. C. Howlett, and S. V. Churakov, Int. J. Quant. Chem. **114**, 1220 (2014).
[38] P. Ewald, Ann. Phys. **369**, 253 (1921).
[39] W. G. Hoover, Phys. Rev. A **31**, 1695 (1985).
[40] S. V. Churakov, C. Labbez, L. Pegado, and M. Sulpizi, J. Phys. Chem. C **118**, 11752 (2014).
[41] L. Cheng, P. Fenter, K. L. Nagy, M. L. Schlegel, and N. C. Sturchio, Phys. Rev. Lett. **87**, 156103 (2001).
[42] K. Krynicki, C. D. Green, and D. W. Salter, Faraday Discuss. Chem. Soc. **66**, 199 (1978).
[43] S. Kerisit and C. Liu, Env. Sci. Technol. **43**, 777 (2009).
[44] S. Haber-Pohlmeier, S. Stapf, D. V. Dusschoten, and A. Pohlmeier, Open Magn. Reson. J. **3**, 57 (2010).
[45] A. C. A. Muller, K. L. Scrivener, A. M. Gajewicz, and P. J. McDonald, J. Phys. Chem. C **117**, 403 (2013).
[46] H. F. W. Taylor, *Cement Chemistry* (Telford, London, 1997).
[47] J. J. Fripiat, M. Letellier, and P. Levitz, Philos. Trans. R. Soc. London A **311**, 287 (1984).

Bibliography

[1] Scalenghe R, Malucelli F, Ungaro F, Perazzone L, Filippi N, Edwards A C. *Influence of 150 years of land use on anthropogenic and natural carbon stocks in emilia-romagna region (Italy).* Environmental Science and Technology **45**(12), 5112–5117 (2011). 1

[2] Picture of the MuCEM building. `http://www.perimmo.fr/IMG/jpg/mucem.jpg`. Accessed: 25/02/2015. 1

[3] Pictures of the Louis Vuitton Foundation building. `http://www.fondationlouisvuitton.fr/l-edifice.html`. Accessed: 25/02/2015. 1

[4] World Business Council for Sustainable Development, Cement Sustainability Initiative. `http://www.wbcsdcement.org/`. Accessed: 25/02/2015. vii, 1

[5] Shams S, Kashif M, Md Al-Amin. *A comparative analysis of building materials for sustainable construction with emphasis on CO_2 reduction.* International Journal of Environment and Sustainable Development **10**(4), 364–374 (2011). vii, 2

[6] TRANSCEND project is a Marie Curie Initial Training Network funded by the European Community. `http://www.nanocem.org/index.php?id=282`. Accessed: 25/02/2015. vii, 2, 3

[7] Picture of characteristic degradation of a concrete bridge. `http://www.ozcoasts.gov.au/indicators/econ_cons_acid_sulfate_soils.jsp`. Accessed: 25/02/2015. vii, 2

[8] Muller A. *Characterization of porosity and C-S-H in cement pastes by ^1H NMR.* Thèse de Doctorat, Ecole Polytechnique Federale de Lausanne, Switzerland (2014). vii, 4, 112

[9] Pellenq R J-M, Kushima A, Shahsavari R, Van Vliet K, Buehler M J, Yip S, Ulm F-J. *A realistic molecular model of cement hydrates.* Proceedings of the National Academy of Sciences **106**(38), 16102–16107 (2009). 4, 54, 112

[10] Kovačević G, Persson B,Nicoleau L,Nonat A,Veryazov V. *Atomistic modeling of crystal structure of Ca 1.67 SiH x.* Cement and Concrete Research **67**, 197–203 (2015). 4, 73

[11] Bloembergen N, Purcell E, Pound R V. *Relaxation effects in nuclear magnetic resonance absorption.* Physical Review **73**(7), 679 (1948). 5, 12, 90, 112

[12] Korb J-P, Whaley-Hodges M, Bryant R G. *Translational diffusion of liquids at surfaces of microporous materials: theoretical analysis of field-cycling magnetic relaxation measurements.* Physical Review E **56**(2), 1934 (1997). 5, 15, 23, 112

[13] Faux D A, Cachia S-H, McDonald P J, Bhatt J S, Howlett N C, Churakov S V. *Model for the interpretation of nuclear magnetic resonance relaxometry of hydrated porous silicate materials.* Physical Review E **91**(3), 032311 (2015). xvi, 5, 81, 88, 90, 92, 112, 113

[14] Torrey HC. *Nuclear spin relaxation by translational diffusion.* Physical Review **92**(4), 962 (1953). 5

[15] Sholl CA. *Nuclear spin relaxation by translational diffusion in liquids and solids: high- and low-frequency limits.* Journal of Physics C: Solid State Physics **14**(4), 447 (1981). 5

[16] Faux D A, Ross D K, Sholl C A. *Nuclear spin relaxation by translational diffusion in solids: X. monte carlo calculation for the simple hopping model.* Journal of Physics C: Solid State Physics **19**(21), 4115 (1986). 5, 42

[17] Faux D A, McDonald P J, Howlett N C, Bhatt J S, Churakov S V. *Nuclear magnetic resonance relaxometry of water in two and quasi-two dimensions.* Physical Review E **87**(6), 062309 (2013). 5, 14, 42, 50, 51, 66, 90

[18] Bhatt J S, McDonald P J, Faux D A, Howlett N C, Churakov S V. *NMR relaxation parameters from molecular simulations of hydrated inorganic nanopores.* International Journal of Quantum Chemistry **114**(18), 1220–1228 (2014). 5, 66

[19] Powers T C. Studies of the physical properties of hardened Portland cement paste. , **43**. ACI (1946). vii, 5, 6

[20] Feldman R F, Sereda P J. *A model for hydrated Portland cement paste as deduced from sorption-length change and mechanical properties.* Materiaux et Construction **1**(6), 509–520 (1968). vii, 6, 112

[21] Feldman R F, Sereda P J. *A new model for hydrated Portland cement and its practical implications.* Engineering Journal **53**(8/9), 53–59 (1970). 6, 112

[22] Jennings H M. *A model for the microstructure of calcium silicate hydrate in cement paste.* Cement and Concrete Research **30**(1), 101–116 (2000). 7

[23] Tennis P D, Jennings H M. *A model for two types of calcium silicate hydrate in the microstructure of Portland cement pastes.* Cement and Concrete Research **30**(6), 855–863 (2000). 7

[24] Jennings H M. *Refinements to colloid model of C-S-H in cement: CM-II.* Cement and Concrete Research **38**(3), 275–289 (2008). vii, 7

[25] Allen A J, Thomas J J, Jennings H M. *Composition and density of nanoscale calcium-silicate-hydrate in cement.* Nature Materials **6**(4), 311–316 (2007). 7

[26] Cohen-Tannoudji C, Diu B, Laloe F. *Quantum mechanics*. Quantum Mechanics. Wiley (1977). 9

[27] Messiah A. *Quantum mechanics*. Number vol. 1 in Quantum Mechanics. North-Holland (1965). 9

[28] Bloch F. *Nuclear induction*. Physical Review **70**(7-8), 460 (1946). 10

[29] Abragam A. *The Principles of Nuclear Magnetism*. Oxford Science Publications (1961). 12, 13, 15, 16, 112

[30] Carr H Y, Purcell E M. *Effects of Diffusion on Free Precession in Nuclear Magnetic Resonance Experiments*. Physical Review **94**(3), 630 (1954). 12

[31] Meiboom S, Gill D. *Modified spin-echo method for measuring nuclear relaxation times*. Review of Scientific Instruments **29**(8), 688–691 (1958). 12

[32] Cowan B. *Nuclear magnetic resonance and relaxation*. Cambridge University Press (2005). 12, 14, 112

[33] Harris R K. *Nuclear magnetic resonance spectroscopy* John Wiley and Sons. (1986). 12, 112

[34] Sholl CA. *Nuclear spin relaxation by translational diffusion in solids*. Journal of Physics C: Solid State Physics **7**(18), 3378 (1974). 14

[35] Barton W A, Sholl C A. *Nuclear spin relaxation by translational diffusion in solids. III. Diffusion in FCC, BCC and SC single crystals*. Journal of Physics C: Solid State Physics **9**(23), 4315 (1976). 15

[36] McDonald P J, Korb J P, Mitchell J, Monteilhet L. *Surface relaxation and chemical exchange in hydrating cement pastes: a two-dimensional NMR relaxation study*. Physical Review E **72**(1), 011409 (2005). xvi, 15, 23, 60, 84, 88, 91, 92

[37] Blümich B. *Pt callaghan. principles of nuclear magnetic resonance microscopy. oxford university press, oxford, 1993, 492 pp,£ 25. isbn 0 198 53997 5*. Magnetic Resonance in Chemistry **33**(4), 322–322 (1995). 16

[38] Berodier E, Scrivener K L. *Evolution of pore structure in blended systems*. Cement and Concrete Research **73**, 25–35 (2015). 16

[39] Kimmich R NMR*: tomography, diffusometry, relaxometry*. , **432**. Springer Berlin (1997). 17

[40] Howlett N C. *Monte-Carlo Simulations of Magnetic Resonance Relaxation in Quasi-Two Dimensional Pores*. Thèse de Doctorat, University of Surrey, United Kingdom (2014). viii, 17, 29, 90, 114

[41] Martin P A. *Mecanique statistique avancee E*cole *P*olytechnique *F*ederale de *L*ausane. (2001-2004). 17

[42] Bain A D. *Chemical exchange in NMR.* Progress in Nuclear Magnetic Resonance Spectroscopy **43**(3), 63–103 (2003). 22

[43] Philippot S, Korb J P, Petit D, Zanni H. *Analysis of microporosity and setting of reactive powder concrete by proton nuclear relaxation.* Magnetic Resonance Imaging **16**(5), 515–519 (1998). 23

[44] Krynicki K, Green C D, Sawyer D W. *Pressure and temperature dependence of self-diffusion in water.* Faraday Discussions of the Chemical Society **66**, 199–208 (1978). xx, 24, 95, 96, 113

[45] Richardson I G. *The calcium silicate hydrates.* Cement and Concrete Research **38**(2), 137–158 (2008). xi, 26, 54, 60

[46] Sholl D, Steckel J A. *Density functional theory: a practical introduction.* John Wiley and Sons (2011). 27

[47] Churakov S V. *Hydrogen bond connectivity in jennite from ab initio simulations.* Cement and Concrete Research **38**(12), 1359–1364 (2008). 27

[48] Bonaccorsi E, Merlino S, Taylor H F W. *The crystal structure of jennite, ca 9 si 6 o 18 (oh) 6· 8h 2 o.* Cement and Concrete Research **34**(9), 1481–1488 (2004). 27

[49] Lothenbach B, Matschei T, Moschner G, Glasser F P. *Thermodynamic modelling of the effect of temperature on the hydration and porosity of Portland cement.* Cement and Concrete Research **38**(1), 1–18 (2008). 28, 89

[50] Kulik D A, Berner U R, Curti E. *Modelling chemical equilibrium partitioning with the GEMS-PSI code.* PSI Scientific Report **4**, 109–122 (2003). 28

[51] Miron G D, Kulik D A, Dmytrieva S V, Wagner T. *GEMSFITS: Code package for optimization of geochemical model parameters and inverse modeling.* Applied Geochemistry **55**, 28–45 (2015). 28

[52] Allen M P, Tidesley D J. *Computer simulation of liquids.* Physics Today **42**(3), 105–106 (2008). 28, 29, 32, 37

[53] Kalinichev A G, Wang J, Kirkpatrick R J. *Molecular dynamics modeling of the structure, dynamics and energetics of mineral–water interfaces: Application to cement materials.* Cement and Concrete Research **37**(3), 337–347 (2007). 29, 55, 85

[54] Churakov S V, Kalinichev A G. Size, structure and abundance of molecular clusters in supercritical water over a wide range of densities: Monte Carlo simulations. In *Steam, Water, and Hydrothermal Systems: Physics and Chemistry Meeting the Needs of Industry. NRC Press, Ottawa*, pages 418–425 (2000). 30

[55] Shi B, He N, Wang N, Guo Z, Guo W. Lattice Boltzmann simulations of fluid flows. In *Advanced Parallel Processing Technologies*, pages 322–332. Springer (2003). 30

[56] Zalzale M, McDonald P J. *Lattice Boltzmann simulations of the permeability and capillary adsorption of cement model microstructures.* Cement and Concrete Research **42**(12), 1601–1610 (2012). 30

[57] Bentz D P. *Three-dimensional computer simulation of Portland cement hydration and microstructure development.* Journal of the American Ceramic Society **80**(1), 3–21 (1997). 30

[58] Bishnoi S, Scrivener K L. *μic: A new platform for modelling the hydration of cements.* Cement and Concrete Research **39**(4), 266–274 (2009). 30

[59] LAMMPS molecular simulation package website. `http://lammps.sandia.gov/`. Accessed: 04/07/2015. 30

[60] Amber molecular simulation package website. `http://ambermd.org/`. Accessed: 04/07/2015. 30

[61] GROMACS molecular simulation package website. `http://www.gromacs.org/`. Accessed: 04/07/2015. 30

[62] DL_POLY molecular simulation package website. `http://www.stfc.ac.uk/SCD/research/app/ccg/software/DL_POLY/44516.aspx`. Accessed: 04/07/2015. 30, 33

[63] Ewald P P. *Die berechnung optischer und elektrostatischer gitterpotentiale.* Annalen der Physik **369**(3), 253–287 (1921). 32

[64] Ryckaert J-P, Ciccoti G, Berendsen H J C. *Numerical integration of the cartesian equations of motion of a system with constraints: molecular dynamics of n-alkanes.* Journal of Computational Physics **23**(3), 327–341 (1977). 33

[65] Buckingham R A. The classical equation of state of gaseous helium, neon and argon. , **168**, pages 264–283. The Royal Society (1938). 33

[66] Jones J E. On the determination of molecular fields. I. from the variation of the viscosity of a gas with temperature. In *Proceedings of the Royal Society of London*, pages 441–462 (1924). 33

[67] Clarke J H R, Smith W, Woodcock L V. *Short range effective potentials for ionic fluids.* Journal of Chemical Physics **84**(4), 2290–2294 (1986). 33

[68] Morse P M. *Diatomic molecules according to the wave mechanics. II. vibrational levels.* Physical Review **34**(1), 57 (1929). 33

[69] Cygan R T, Liang J-J, Kalinichev A G. *Molecular models of hydroxide, oxyhydroxide, and clay phases and the development of a general force field.* The Journal of Physical Chemistry B **108**(4), 1255–1266 (2004). 33, 63, 112

[70] Berendsen H J C, Grigera J R, Straatsma T P. *The missing term in effective pair potentials.* Journal of Physical Chemistry **91**(24), 6269–6271 (1987). 33, 46, 112

[71] Freeman C L, Harding J H. *New forcefields for modeling biomineralization processes.* The Journal of Physical Chemistry C **111**(32), 11943–11951 (2007). 33, 64, 112

[72] Forsman J, Woodward C E. *Limitations of the Derjaguin Approximation and the Lorentz- Berthelot Mixing Rule.* Langmuir **26**(7), 4555–4558 (2010). 34

[73] DL_POLY molecular user manual. `http://www.ccp5.ac.uk/DL_POLY/MANUALS/USRMAN4.pdf`. Accessed: 04/07/2015. ix, 36

[74] Press W H. *Numerical recipes 3rd edition: The art of scientific computing*. Cambridge University Press (2007). 42, 43

[75] Berendsen H J C, Postma J P M, Van Gunsteren W F, DiNola A, Haak J R. *Molecular dynamics with coupling to an external bath*. The Journal of Chemical Physics **81**(8), 3684–3690 (1984). 45

[76] Abascal J L F, Vega C. *A general purpose model for the condensed phases of water: TIP4P/2005*. Journal of Chemical Physics **123**(23), 234505 (2005). 46

[77] Holz M, Heil S R, Sacco A. *Temperature-dependent self-diffusion coefficients of water and six selected molecular liquids for calibration in accurate ^1H NMR PFG measurements*. Physical Chemistry Chemical Physics **2**(20), 4740–4742 (2000). 48, 112

[78] Tazi S, Botan A, Salanne M, Marry V, Turq P, Rotenberg B. *Diffusion coefficient and shear viscosity of rigid water models*. Journal of Physics: Condensed Matter **24**(28), 284117 (2012). 48, 112

[79] Yeh I-C, Hummer G. *System-size dependence of diffusion coefficients and viscosities from molecular dynamics simulations with periodic boundary conditions*. Journal of Physical Chemistry B **108**(40), 15873–15879 (2004). 48, 112

[80] Hindman J C, Svirmickas A, Wood M. *Relaxation processes in water. A study of the proton spin-lattice relaxation time*. Journal of Chemical Physics **59**(3), 1517–1522 (1973). xvii, 52, 97, 98, 112

[81] Nonat A. *The structure and stoichiometry of C-S-H*. Cement and Concrete Research **34**(9), 1521–1528 (2004). 54, 59, 60, 73, 112

[82] Taylor H F W. *Nanostructure of C-S-H: current status*. Advanced Cement Based Materials **1**(1), 38–46 (1993). 54

[83] Cong X, Kirkpatrick R J. *^{29} Si MAS NMR study of the structure of calcium silicate hydrate*. Advanced Cement Based Materials **3**(3), 144–156 (1996). 54, 55

[84] Richardson I G, Groves G W. *A reply to discussions by H.F.W. Taylor of the papers "models for the composition and structure of calcium silicate hydrate (C-S-H) gel in hardened tricalcium silicate pastes" and "the incorporation of minor and trace elements into calcium silicate hydrate (C-S-H) gel in hardened cement pastes"*. Advanced Cement Based Materials **23**(4), 999–1000 (1993). 54

[85] Richardson I G. *Tobermorite/jennite-and tobermorite/calcium hydroxide-based models for the structure of C-S-H: applicability to hardened pastes of tricalcium silicate, β-dicalcium silicate, Portland cement, and blends of Portland cement with blast-furnace slag, metakaolin, or silica fume*. Cement and Concrete Research **34**(9), 1733–1777 (2004). 54

[86] Renaudin G, Russias J, Leroux F, Cau dit Coumes C, Frizon F. *Structural characterization of C-S-H and C-A-S-H samples-Part II: Local environment investigated by spectroscopic analyses.* Journal of Solid State Chemistry **182**(12), 3320–3329 (2009). 54, 55

[87] Hamid S A. *The crystal structure of the 11a natural tobermorite* $Ca2.25[Si_3O_{7.5}(OH)_{1.5}]$ *-* $1H_2O$. Zeitschrift fur Kristallographie **154**(2-4), 189–198 (1981). 54, 55, 58, 112

[88] Chen J J, Thomas J J, Taylor H F W, Jennings H M. *Solubility and structure of calcium silicate hydrate.* Cement and Concrete Research **34**(9), 1499–1519 (2004). 54

[89] Deer W A, Howie R A, Zussman J. *An introduction to the rock-forming minerals.* Longman London (1992). 58, 112

[90] Bonaccorsi E, Merlino S, Kampf A R. *The crystal structure of tobermorite 14a (plombierite), a C-S-H phase.* Journal of the American Ceramic Society **88**(3), 505–512 (2005). 59, 112

[91] Galmarini S C. *Atomistic Simulation of Cementitious Systems.* Thèse de Doctorat, Ecole Polytechnique Federale de Lausanne, Switzerland (2014). 64

[92] Levitz P. *From Knudsen diffusion to Levy walks.* EPL (Europhysics Letters) **39**(6), 593 (1997). 81

[93] Barberon F, Korb J P, Petit D, Morin V, Bermejo E. *Probing the surface area of a cement-based material by nuclear magnetic relaxation dispersion.* Physical Review Letters **90**(11), 116103 (2003). 84, 88

[94] Monteilhet L, Korb J P, Mitchell J, McDonald P J. *Observation of exchange of micropore water in cement pastes by two-dimensional T2-T2 nuclear magnetic resonance relaxometry.* Physical Review E **74**(6), 061404 (2006). 92, 104, 114

[95] Takenaka M, Masui R. *Measurement of the thermal expansion of pure water in the temperature range* $0°c$*-*$85°c$. Metrologia **27**(4), 165 (1990). xvi, 94, 95, 98

[96] Gajewicz A. *Characterisation of cement microstructure and pore-water interaction by* ^1H *Nuclear Magnetic Resonance Relaxometry.* Thèse de Doctorat, University of Surrey, United Kingdom (2014). xx, 103